Laser-driven shocks of astrophysical interest

Alice Fazzini

INSTITUT POLYTECHNIQUE DE PARIS

NNT : 2022IPPAX028

Thèse de doctorat

ÉCOLE POLYTECHNIQUE

IP PARIS

Laser-driven shocks of astrophysical interest

Thèse de doctorat de l'Institut Polytechnique de Paris
préparée à École Polytechnique

École doctorale n°626 de l'Institut Polytechnique de Paris (ED IP Paris)
Spécialité de doctorat: Physique – Optique, Laser et Plasma

Thèse présentée et soutenue à Palaiseau, le 20 avril 2022, par

ALICE FAZZINI

Composition du Jury :

Martin Lemoine Directeur de Recherche, Institut d'Astrophysique de Paris, Sorbonne Université (UMR 7095)	Président
Hye-Sook Park Directrice de Recherche, Lawrence Livermore National Laboratory, US	Rapporteur
Luís Oliveira e Silva Professeur des Universités, Instituto Superior Técnico Lisboa, PT	Rapporteur
Frederico Fiuza Senior Staff Scientist, SLAC National Accelerator Laboratory, Stanford University, US	Examinateur
Derek Schaeffer Associate Professor, Princeton University, US	Examinateur
Julien Fuchs Directeur de Recherche, Laboratoire pour l'Utilisation des Lasers Intenses, École Polytechnique (UMR 7605)	Directeur de thèse

Acknowledgements / Remerciements / Ringraziamenti

I would like to thank all the people who have taken part, directly or indirectly, in this project.

Tout d'abord, j'aimerais remercier la personne sans laquelle cette thèse n'aurait pas pu être possible. Merci beaucoup à Julien Fuchs, mon directeur de thèse, pour m'avoir accueillie en thèse et guidée le long de ce parcours. Grâce à lui, je n'ai appris que des connaissances de physique, mais aussi ce que cela signifie de faire de la recherche et de se donner pour comprendre de mieux en mieux nos cas d'étude. Merci aussi pour la grande motivation et l'optimisme, qui ont poussé moi et le reste de l'équipe à ne pas abandoner quand tout semblait sombre (et pas seulement parce qu'on était en train d'aligner). Donc, merci pour m'avoir appris que seulement avec persévérance et passion on atteint des objectifs.

Many thanks to Hye-Sook Park and Luís Silva for carefully reading my manuscript, as well as to the other members of my thesis committee – Martin Lemoine, Frederico Fiuza, and Derek Schaeffer – for their interest in my work and for contributing to its improvements by highlighting interesting points.

Several people contributed from the scientific point of view to the research presented in this thesis. Un très grand merci à Emmanuel d'Humières et Xavier Ribeyre, du CELIA / l'Université de Bordeaux, pour leur importante contribution du point de vue de l'interprétation physique et des simulations FLASH. Les appels hebdomadaires (ou presque) que l'on a eus à partir du premier confinement ont été essentiels pour recevoir un avis expert et ponctuel sur le sujet des chocs astrophysiques ; de plus, ils ont aidé énormément à nous donner des points de référence temporels pour présenter des conclusions partielles et, surtout, des questions.
Thanks to Quentin and Sophia as well, for having participated to some of these calls and raised interesting questions.
I could never thank enough the two post-docs who have been part of the group during these years: Konstantin Burdonov, the Experimentalist, and Weipeng Yao, the Simulation Guy. Thank you, Kostya, for the long time shared in the lab during all the experiments, while mounting and remounting optical paths and diagnostics (especially the Thomson Scattering); thanks for the expertise shared with us in those occasions and during the data analysis; thank you as well for the sour and funny conversations that you used to start at the lunch table. Thank you, Yao, for your unstoppable desire to work and to find interesting results; thanks for giving yourself to each project you were involved in; thank you for replying quickly and in detail to any question I had, even when concerning boring coding problems.
Merci beaucoup / Grazie mille à Mickael Grech et Tommaso Vinci (du LULI), en premier lieu pour

avoir développé le code Smilei et le logiciel Neutrino, deux outils essentiels pour ma thèse, et aussi pour avoir été toujours disponibles à répondre avec clarté à tous mes doutes sur leur bonne utilisation.
Merci aussi à Pascal Loiseau et Raphaël Riquier (du CEA) pour avoir développé les logiciels qu'on a utilisés pour analyser les données du Thomson scattering et de la radiographie à protons.
Thank you, Sergey and Jenya, for helping us understand what was going on during the experiments thanks to your omnipresent FSSR. Thanks to Jenya also for sharing a desperate – but "fun" as well – trip to Toulouse to collect the famous Coil.
Grazie a Salvatore Orlando e a Marco Miceli dell'Istituto Nazionale di Astrofisica (INAF) e dell'Università di Palermo per aver condiviso con noi la loro competenza, aiutandoci a capire quale relazione potesse esserci tra i nostri esperimenti e la "vera Astrofisica".
The mornings, afternoons, and evenings spent in the lab during the experiments would have never been the same without the flow of foreign students and researchers who collaborated with us. Thank you, Amina, Adam, Stanimir, Gabriel, Abraham, Ryunosuke, Jeya, and Maxence, for spending with patience so many working hours in the lab, here and abroad; thanks for sharing your knowledge; thanks for animating the experiments with jokes and laughs, and for concluding them, in some cases, with a well-earned drink.

Among the many people from LULI I am grateful to, vorrei cominciare con il ringraziare Caterina Riconda, per avermi accolta nel suo gruppo durante il tirocinio di magistrale, facendomi scoprire il mondo della ricerca in interazione laser-plasma, esperienza che successivamente mi ha portata a proseguire qui il mio percorso con un dottorato.
Je remercie Patrick Audebert, le directeur du LULI, pour m'avoir accueillie au sein du labo durant cette thèse et pour avoir su être à l'écoute de tout le monde.
De la même façon, j'aimerais remercier toute l'équipe administrative pour nous avoir toujours guidés dans le labyrinthe bureaucratique du CNRS. De manière plus générale, je voudrais remercier tous les chercheurs passés et presents qui ont contribué au développement du laboratoire. Merci beaucoup aux équipes informatiques et techniques et aux laseristes, qui ont donné un support indispensable pour le bon déroulement des manips et pour leur préparation.

Je conserverai un bon souvenir de ces années de thèse aussi grâce à l'ambience amicale qui s'est créée au LULI.
Un grande grazie a Ambra, guida dei dottorandi perduti nei labirinti amministrativi e mentali e madre dalle mille doti organizzative e culinarie; grazie per essere stata un'amica sia dentro che fuori dal lab.
Merci beaucoup à Vincent, mon "jumeau de thèse", avec qui j'ai pu partagé avec bonne humeur toutes

les manips, les repas (veggie – ou pas) à la cantine, les cafés, les bières, et les discussions sur ce qui est juste/vrai/utile/écolo/etc dans le monde.
Un grand merci à Pierre, pour sa disponibilité et sa bonté sans fin, pour sa capacité d'écouter et d'être au même temps marrant et sage, et bien sûr pour son chocolat (!).
Merci à l'incorrigible Bruno, pour être tellement fou qu'on n'y croit presque pas et pour tous les conseils et les discussions tout à coup sérieux et experts qu'il a su me filer pendant ces années.
Merci à Yaniss per avoir revitalisé le labo avec son énergie et ses "nouvelles idées".
Merci au reste de l'"équipage" - à Livia, Fred, Paul, Luke, Anna, Hanna, Guilhem, Thibault, Gabriel, et Simon - pour avoir partagé les plaintes à propos de la cantine, les cafés brûlés, les "mots du jour", les bières parisiennes trop chères, et mille discours fondés sur solides bases scientifiques ainsi que complètement délirants. Maintenant c'est aux tout nouveaux doctorants Ronan et Isabeau de continuer l'histoire du LULI…

Outside of the lab as well there are many people who have walked by my side in this path and that I want to thank.
Un grandissimo grazie a Giordano, per il calore che hanno sempre saputo trasmettere i suoi piatti, per le mille follie che hanno reso il mio soggiorno a Parigi più che memorabile, per aver saputo aggiungere un po' di ingenuità alla mia visione del mondo quando ne mancava.
Muchas gracias, Paula, per i lunghi discorsi fatti passeggiando lungo la Senna o davanti a un cocktail, per essere così easy-going da rendere sempre semplice parlare di tutto, dalle storie passante, ai dubbi presenti, fino ai sogni e le incertezze sul futuro.
Thank you to the legendary group of friends from my first year in Paris, Max, Giordano, Linda, Adrien, and Lili, who made me feel at home here and probably contributed to the decision to remain in this place after the master for the PhD. In particolare, grazie a Linda per essere stata la prima vera amica con cui condividere mille discorsi e risate che ho trovato in questa terra straniera. Thank you to the ones who left earlier also for remaining close friends from far away.
Thank you to the Bootcamp group, led by the tireless Alex, for contributing to my physical and mental health with exercise sessions and various soirées.
Thank you to the People of Cité Universitaire, for colouring most part of my stay with wonderful experiences, meetings, and adventures; thanks for the wind of novelty and enthusiasm that one could always breath all around The CitéU.
Danke Lisa, Oli, Niki, und Max, for hosting me during the first hard lockdown; thanks for making this time not only bearable but even enjoyable.
Grazie mille alle mie "Elemelons", Ambra, Elisabetta e Karina, per essermi state vicine – nonostante

le migliaia di km di distanza – durante questi anni; grazie per avermi ascoltata, capita e fatta divertire, come sempre dai tempi della scuola; grazie per aver sempre trovato un angolo di disponibilità a vederci o sentirci non appena è stato possibile.

Un grazie immenso alla mia famiglia, senza la quale non avrei potuto fare neanche l'1% della strada percorsa fino a qui. Grazie ai miei – a mia mamma, mio babbo e Marco – per avermi sempre incoraggiata a cercare la mia strada (qualunque questa fosse) e per avermi dato la possibilità di seguirla. Un grazie speciale a mia mamma Patrizia, per avermi continuamente dato perfino di più del supporto necessario, sia affettivamente che materialmente. Grazie ai miei nonni e a mio zio Gio' che, nonostante i 60-70 anni di differenza, hanno sempre capito le mie scelte e promosso la mia istruzione. Grazie anche ai miei zii – a Nanna e Ale – per essere sempre stati disponibili a sostenermi nel caso avessi bisogno. Grazie a tutti per aver creduto nelle mie scelte e per l'affetto mai fatto mancare.
Lastly, a huge Thank You to Max (for the third time in this acknowledgements section now!), for always supporting, listening, and understanding me over the years; thank you for the countless interesting conversations-discussions we have had about any subject; thanks for taking care of me and for always being able to make a smile appear on my face. All in all, thank you for making all this journey even more special.

Contents

List of abbreviations

AGN	Active Galactic Nucleus
AMR	Adaptive Mesh Refinement
CD	Contact Discontinuity
CME	Coronal Mass Ejection
CPA	Chirped Pulse Amplification
CR	Cosmic Ray
DS	Downstream
DSA	Diffusive Shock Acceleration
ELI	Extreme Light Infrastructure
EM	Electromagnetic
EOS	Equation Of State
EPW	Electron Plasma Wave
EUV	Extreme Ultraviolet
FS	Forward Shock
FSSR	Focusing Spectrometer with Spatial Resolution
FWHM	Full Width Half Maximum
GRB	Gamma-Ray Burst
HED(P)	High-Energy-Density (Physics)
IAW	Ion Acoustic Wave
IP	Imaging Plate
JLF	Jupiter Laser Facility
LFA	Long Focal (length) Area
LHC	Large Hadron Collider
LLNL	Lawrence Livermore National Laboratory
LMC	Large Magellanic Cloud
LMJ	Laser Mégajoule
LPD	Large Plasma Device
LULI	Laboratoire pour l'Utilisation des Lasers Intenses
MHD	Magnetohydrodynamics
MPI	Message Passing Interface
NIF	National Ignition Facility
OpenMP	Open Multi-Processing
PIC	Particle-In-Cell
QED	Quantum Electrodynamics
R-H	Rankine-Hugoniot
RCF	Radiochromic Film
RS	Reverse Shock
SA	Stochastic Acceleration
SASE	Self-Amplified Spontaneous Emission
SDA	Shock Drift Acceleration
SFA	Short Focal (length) Area
SI	International System of Units
SNR	Supernova Remnants
SSA	Shock Surfing Acceleration
TNSA	Target Normal Sheath Acceleration
TS	Thomson Scattering
UHECR	Ultra-High-Energy Cosmic Ray
US	Upstream
XFEL	X-ray Free Electron Laser

Introduction

Celestial objects and phenomena have been stimulating humankind's interest for millenniums, making astronomy one of the most ancient research domains. Along centuries, scientific development made it possible to pass from naked eye observations of nearby celestial bodies to more and more detailed investigations of remote astrophysical objects. However, the *in situ* study of certain objects remains impossible due to the enormous distances that separate them from the Earth, limiting the data that could be collected. The characteristic time scale of many phenomena is very large with respect to the typical temporal scale of our observation capabilities, which makes it difficult to have a dynamical study on those systems. Furthermore, in general it is evidently impossible to have any kind of control on the parameters that characterize a certain phenomenon to test possible models.
Thanks to the more recent big advancement of computational science, the domain of numerical simulations has been developing. These can represent an important tool, thanks to their controllability and reproducibility (in spite of high costs in terms of computational hours), as they allow for a detailed description of the system. Nevertheless, simulations need precise analytical models to be based on and hence to validate, which cannot be provided by limited and incomplete observations.

Nowadays, it is possible to study distant astrophysical systems in the laboratory, under controlled conditions and with temporal and spatial scales easier to handle (Remington et al., 2006).
The laser effect discovery in 1960 (Maiman et al. 1960) and its further implementation, made High-Energy-Density physics (HEDP, i.e., with energy densities above 10^{12} erg/cm^3 (Drake, 2006b)) accessible in the laboratory. Indeed, thanks to the interaction between matter and high power lasers, it is today possible to reproduce extremely high temperatures (up to 10^8 K) and densities (up to 10^{32} part/m^3) (Drake, 2006b) and hence explore a new domain of research: *laboratory astrophysics*.
Over the last two decades, many laser-based experiments have been performed with the aim of studying various astrophysical phenomena in the laboratory. This field of research has taken various axes, ranging from the investigation of planetary interiors (Koenig et al. 2005), to collisionless shocks (Marcowith et al. 2016a), from magnetic reconnection (Yamada et al. 2010), to nuclear astrophysics (Gales

2015; Boyd et al. 2009).

Evidently, the difference in temporal and spatial scales is huge, hence, *similarity criteria* have been necessary to ensure that such experimental conditions are equivalent to the ones of the astrophysical phenomena of interest. As we will see later in a more detailed way, two systems are similar from a (magneto-) hydrodynamic point of view if they share some conditions on certain dimensionless parameters, i.e., on the Reynolds (and magnetic Reynolds) number(s) and on the Péclet number (Ryutov et al. 2000; Ryutov 2018; Falize et al. 2009b). In that case, one can relate the laser-produced plasmas to astrophysical events, as their physics is *similar*, in spite of the extreme differences in spatial and temporal scales.

Collisionless shocks are present in many astrophysical environments and are thought to be responsible for the production of the cosmic rays (CRs), which are high-energy supra-thermal particles traveling in the Universe and detectable on Earth as well (Treumann 2009).

A shock can be seen as a discontinuity of certain physical quantities, such as pressure, density, or temperature. In neutral gases, a shock forms when an obstacle moves faster than the speed of sound of the fluid, i.e., for Mach numbers $M = v/c_s > 1$, where v is the object velocity and c_s is the sound speed. It can be represented as a longitudinal (sound) wave that became highly non-linear and reached a balance between dispersion and diffusion processes. An essential characteristic of shocks is their irreversibility, as at the shock front microscopic phenomena strongly convert kinetic energy into thermal heating. On Earth, shocks mostly take place in neutral gases and are called *collisional*, since the interaction between particles occurs through binary collisions. The typical thickness of a collisional shock is indeed comparable to the collisional mean free path of the fluid particles.

In space, the situation deeply changes, as most of the matter is in the state of plasma and free charges can interact through longer-range Coulomb force. In this situation, shocks mostly occur over lengths much smaller than the mean free path and are thus called *collisionless*. The essential shock dissipation is not mediated anymore by binary collisions, but relies on collective processes able to sustain the entropy production.

Supernovae are powerful and bright stellar explosions that can be seen even with the naked eye. They mostly occur via thermal runaway in binary systems or core collapse of a single star (Woosley and Weaver 1986). In the first case, a carbon-oxygen white dwarf accumulates matter from its companion star up to a point when its core temperature is high enough to ignite carbon fusion. Such a runaway nuclear fusion makes the dwarf explode, resulting in a supernova. In the second case, the core of a massive star at the end of its lifetime can collapse when it runs out of nuclear fuel and hence nuclear fusion cannot sustain the core against its own gravity anymore. This collapse can lead to a fast ex-

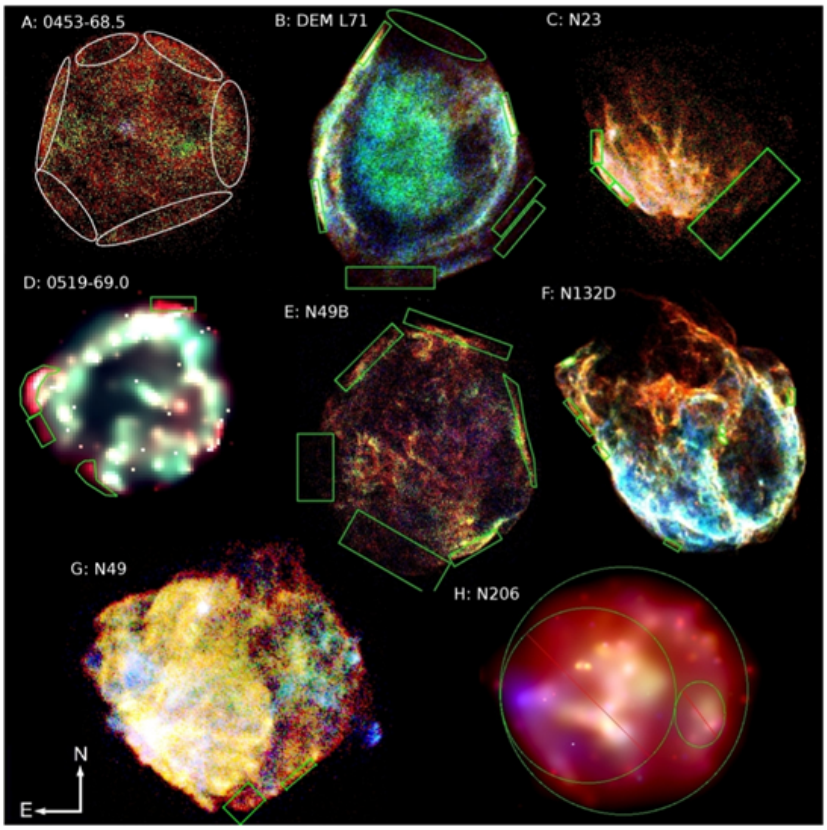

Figure 1: *Three-color maps for individual SNRs identified in the Large Magellanic Cloud (LMC) via the Chandra x-ray Telescope, as taken from Schenck et al. (2016). (Color codes are red: 300–720 eV, green: 720–1100 eV, blue: 1100–7000 eV.)*

pulsion of the outer star layer, leading to a supernova. The structure resulting from such a violent star explosion is called supernova remnant (SNR). Since it consists of very fast ejected material expanding into the interstellar medium, a forward shock forms at its boundaries. Images of some SNRs identified in the Large Magellanic Cloud (LMC) are shown in Fig. 1.

Another astrophysical environment where collisionless shocks can be found is the Earth's bow shock (Onsager and Thomsen 1991). The solar wind is a flow of charged particles – that is, protons, electron, alpha particles, and a minor fraction of heavier ions – released from the solar corona. When it encounters the Earth's magnetic field, a shock forms, separating the solar wind (upstream region) from the Earth's magnetosheath (downstream region).The Earth's bow shock is an approximately stationary structure around 90000 km from the Earth's surface. Its thickness is ~ 100 km (Bale et al. 2003), which is about one order of magnitude smaller than the solar wind free mean path, making the shock, indeed, collisionless.

While in these events shocks are non-relativistic, in the astrophysical environment shocks propagating at relativistic velocities can be found for instance in jets from Active Galactic Nuclei (AGN; Peterson 1997) or from Gamma Ray Bursts (GRBs; Piran 2005). Since this thesis is mostly focused on

non-relativistic shocks, we will not discuss further these phenomena here.

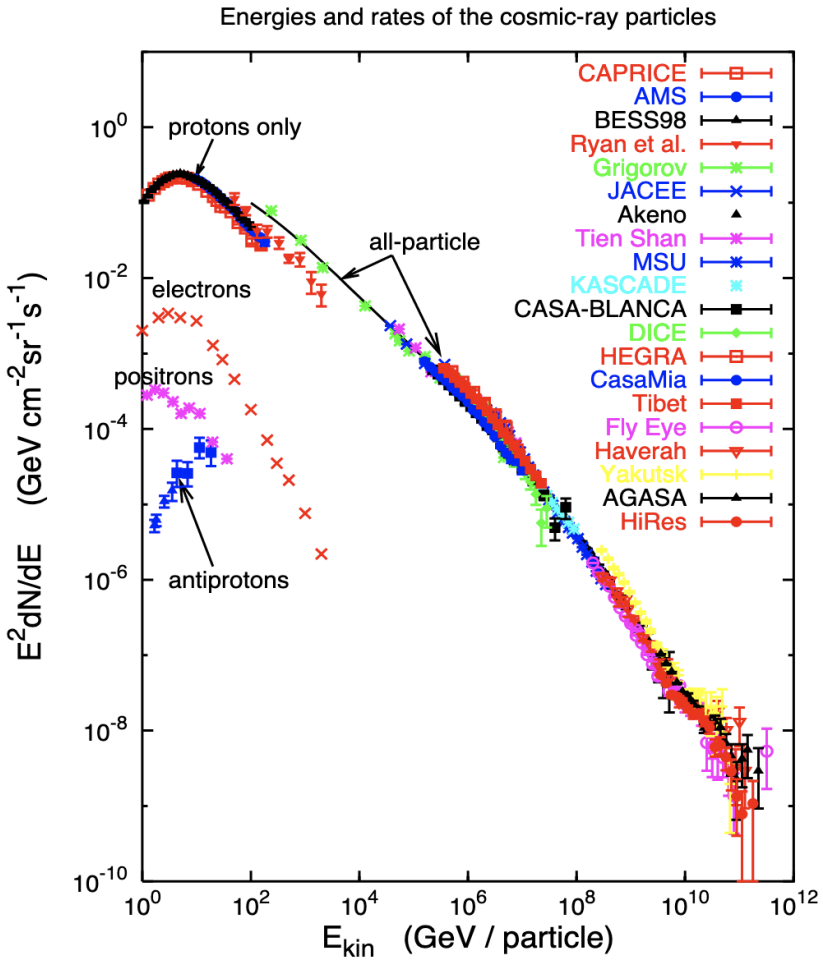

Figure 2: *Measurements of cosmic ray (CR) flux over energy per particle from different experiments. (As reported by Hillas 2006.)*

As mentioned before, the interest for astrophysical collisionless shocks is motivated also by the fact that they are held responsible for particle acceleration in space. Cosmic rays are high-energy particles traveling through space and consisting mostly of protons and alpha particles, with smaller fractions of heavier ions, electrons, positrons, and antiprotons. They are mostly produced from outside our solar system, both within our galaxy and outside, but the Sun generates them as well (Longair 1992). As is shown in Fig. 2, their kinetic energy widely ranges over many orders of magnitude, from the $\sim$ GeV/particle to around 10^{11} GeV/particle, exceeding of more than a factor 10^7 what is achievable using the nowadays most power accelerator, the Large Hadron Collider (LHC).

A full comprehension of the cosmic rays origin and propagation through the Universe is still searched by the scientific community. SNRs are believed to be the source of most part of the galactic cosmic rays (Drury 2012). However, many other astrophysical phenomena are legitimate candidates for being CRs sources, such as galactic nuclei, quasars, gamma-ray bursts, and magnetic variable stars. As we

will detail in the following sections, particle acceleration processes can take place at the shock front, the most important of which is the Fermi kind acceleration. However, this mechanism explains CRs up to $10^7 - 10^8$ GeV and suffers from a still not fully solved *injection problem*, that is, the question concerning how initially slow particles may enter into the acceleration process. The theory proposed by Blasi (2013) can explain CRs of energies up to 10^9 GeV by considering a secondary instability due to the accelerated particles, which would give rise to stronger magnetic fields able to confine much more efficiently particles at the shock front.

It has been supposed that ultra-high-energy cosmic rays (UHECRs, $E_{kin} > 10^9$ GeV) can originate from GRBs (Liu et al. 2011), neutron stars (Blasi et al. 2000), active galactic cores (Duţan and Caramete 2015), hypernovae (Wang et al. 2008b), and some more potential sources (Vannoni et al. 2011), but their origin is nowadays still very debated (Blasi 2013; Drury 2012).

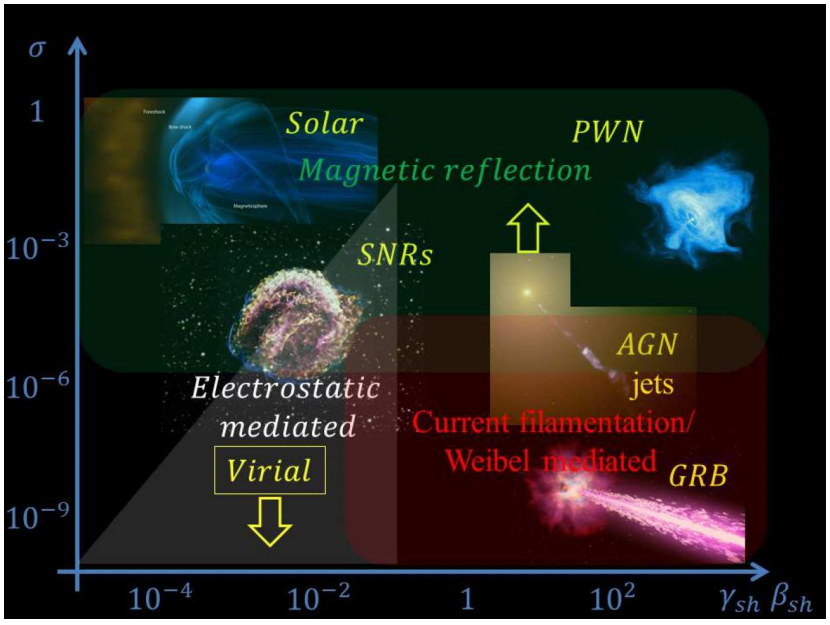

Figure 3: *Overview of collisionless astrophysical kinds, as based on their electrodynamical properties, depending on the shock energy $\gamma_{sh}\beta_{sh}$ and magnetization σ. (As reported by Moreno et al. (2019).)*

As we will see in more details later, collisionless shocks can be classified as *electrostatic* or *magnetized*, depending on their electrodynamic properties (Marcowith et al. 2016a; Treumann 2009; Sakawa et al. 2016). In general, electrostatic shocks are mediated only by an electric potential barrier, while magnetized shocks present a jump in the magnetic field as well. Weakly magnetized shocks are also said *electromagnetic* when they are mediated by an electromagnetic instability (such as the Weibel filamentation instability; Weibel 1959). Fig. 3 gives an overview of the kinds of collisionless astrophysical

shock depending on their energy $\gamma_{sh}\beta_{sh}$ and magnetization σ[1].

The first laboratory experiment investigating collisionless shocks dates back to 1971, when Dean et al. (1971) generated an electrostatic shock by making a laser-produced plasma plume propagate through an ambient plasma. Afterwards, Bell et al. (1988) produced a shock by making interact a laser-driven plasma with a spherical obstacle. These pioneering works paved the way to more sophisticated and better characterized experiments on collisionless shocks, also encouraged by the tremendous development of laser technology and the advancement in diagnostics capabilities. It is nowadays possible to generate a wide range of collisionless shocks of astrophysical interest, in particular, the study of magnetized shocks became possible thanks to intense driving laser beams and/or strong externally applied magnetic fields.

Let us expose the works conducted on various kinds of shocks. Electrostatic shocks have been more deeply investigated in further experiments by, for instance, Romagnani et al. (2008b), Ahmed et al. (2013), Kuramitsu et al. (2012), and He et al. (2019). Romagnani et al. (2008b) have carried out detailed proton-radiography measurements unveiling the electromagnetic field structure of the formed shocks and ion-solitons, as shown in Fig. 4. More recently, Ahmed et al. (2013) have characterized the initial stages of the shock formation, showing that a current free double layer may transit into a symmetric shock structure.

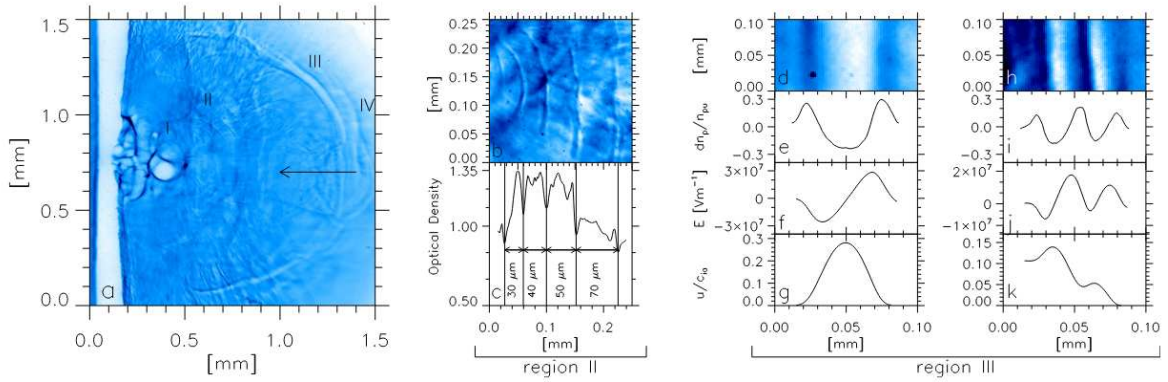

Figure 4: *Proton radiography characterization of electrostatic shocks and solitons by Romagnani et al. 2008b. Out of such measurements of probe proton density $\delta n_p/n_{pu}$, they have reconstructed the profiles of the electric field E and of the normalized ion velocity u/c_{ia}.*

The so-called electromagnetic shocks are sustained by self-generated turbulent electromagnetic fields and are supposed to take place for instance in GBRs in afterglows (Piran, 2005). The most likely candidate for the generation of such a turbulence is the Weibel filamentation instability, as proposed initially by Medvedev and Loeb (1999) and "confirmed" through PIC simulations by Kato and Tak-

[1]Where the magnetization parameter is defined as $\sigma = B^2/[4\pi(\gamma_{sh}-1)n_i m_i c^2]$, where B is the background magnetic field felt in the shock front rest frame, $\gamma_{sh} = \sqrt{1-v_{sh}^2/c^2}$ n_i is the upstream ion density, m_i is the ion mass, and c is the speed of light.

abe (2008). This kind of shock is particularly hard to experimentally produce, as it requires extremely high-energy laser beams of long duration, capable of maintaining the plasma with high temperature and high speed (to ensure its collisionless nature) for a time long enough to allow the instability formation (whose typical growth rate is $\propto \omega_p$) (Ross et al. 2017). The typical experimental setup consists of having two counter-streaming plasma flows. After the interpenetration, the Weibel-unstable plasma is supposed to stimulate the formation of two collisionless shocks propagating away from each other.

In a few experiments conducted at the OMEGA laser facility, Weibel-generated magnetic fields have been generated and characterized through proton radiography, as shown in Fig. 5 (Park et al. 2015; Huntington et al. 2015; Fox et al. 2013). Such a filamentary structure is characteristic of the early stages of the Weibel instability. However, the generation of a fully formed Weibel-mediated collisionless shock has been achieved only in a recent experiment at NIF (Swadling 2019).

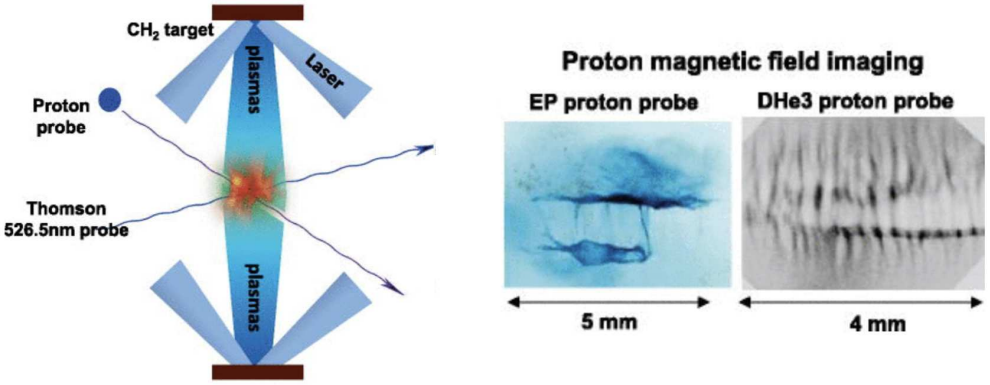

Figure 5: (*Left side.*) *Scheme of the typical Weibel-mediated shock experimental setup, as carried out by Park et al.* (*2015*). (*Right side.*) *Proton radiography images showing magnetic field filamentation.*

Magnetized (or magnetohydrodynamic (MHD)) shocks are associated with many astrophysical phenomena, such as the above mentioned SNRs and planetary bow shocks, where external magnetic fields are present. The earliest experiments involving magnetized collisionless shocks date back to the '60s, when Paul et al. (1965) and Paul et al. (1967) have reported measurements of the shock structure and electron temperature in magnetized shocks created by the compression of a linear Z-pinch. More recently, Niemann et al. (2014) have described the formation of magnetized shocks, generated by coupling a laser-driven expanding plasma plume with a large magnetized ambient plasma at the Large Plasma Device (LPD). Schaeffer et al. (2017b,a) have performed experiments at the OMEGA laser facility showing the formation and evolution of a high-Mach-number magnetized shock, unveiling the crucial role played by the magnetic piston to efficiently transfer the laser energy to the background plasma (see Fig. 6). The work from Meinecke et al. (2014) has revealed magnetic field turbulent am-

plification during the interaction between a shock and dense clumps in the ambient medium, which represents one of the candidate mechanisms for the production of strong fields at the outer shocks of SNRs.

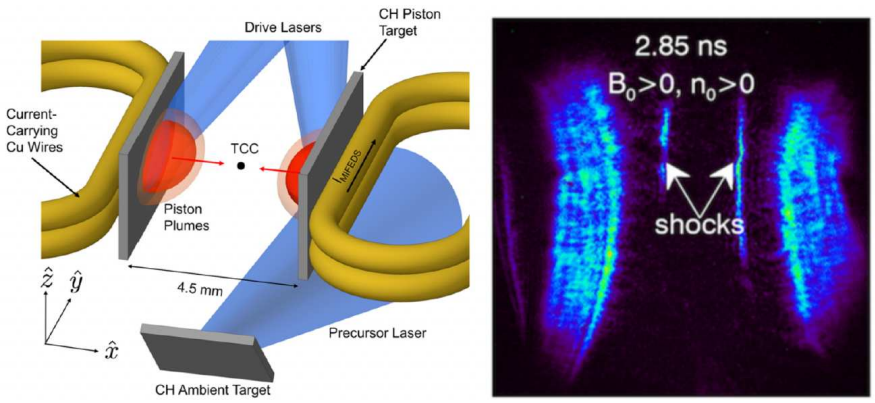

Figure 6: (*Left side.*) *Experimental setup of the experiment performed of magnetized shock by Schaeffer et al. 2017b,a.* (*Right side.*) *Angular filter refractometry image, showing the formation of a shock in the presence of an externally applied magnetic field and ambient plasma.*

While the above mentioned shocks concern only ion-electron plasma, it is worth to mention that collisionless shocks in positron-electron plasmas have been investigated as well. The generation of positron-electron beams has been reported by Sarri et al. (2013) opening the way for the study of astrophysical leptonic jets in the laboratory, while the next generation of high-intensity laser facilities, such as ELI, has been identified as possible source of pairs (Ridgers et al. 2012).

This work concerns the generation and evolution of laser-driven collisionless magnetized shocks, firstly produced and characterized in the laboratory, then modeled and more deeply understood via numerical simulations, and finally related to their astrophysical counterparts.

Chapter 1 introduces the key physical concepts necessary to comprehend this work. The essentials of laser-matter interaction are presented in the light of the use we are going to make. The physics of shocks and the acceleration mechanisms taking place at the (collisionless) shock front are also explained, with references to space events as well. Finally, similarity criteria allowing for an equivalence between experiments and astrophysical phenomena are briefly discussed.

Chapter 2 gives an overview of the experimental and numerical tools employed to perform this research. The characteristics of the laser facilities where we performed our experiments (TITAN/JLF and LULI2000) are presented, as well as the diagnostics exploited in such occasions accompanied by the programs or analysis techniques used later to treat the data. Moreover, the numerical codes (hydrodynamic or MHD) FLASH and (Particle-In-Cell, PIC) SMILEI are presented within a larger

overview of the various plasma models.

Chapter 3 presents the results of two experimental campaigns having for object the interaction between a laser-driven magnetized piston expanding through an ambient plasma and an externally applied strong magnetic field. We will focus on the characterization of the resulting supercritical collisionless shock and on the related particle acceleration processes. The shock formation and evolution will be modeled via MHD simulations with the code FLASH and PIC simulations with the code SMILEI, leading to the identification of shock surfing acceleration (SSA) as most likely candidate for the background plasma energization. Moreover, an overview of the astrophysical environments to which such results might be applicable is given.

Chapter 4 is dedicated to the study of the interpenetration between two shocks, generated with the same experimental setup as for the single shock presented in Chapter 3. We will characterize their interpenetration, occurring when such shocks have transited to subcritical, and focus on the effects of the collisionless shock superposition on the enhancement of the particle energization. Such events will be modeled as well via numerical simulations run with both FLASH and SMILEI codes. Moreover, we will present the results of additional PIC simulations modeling the interaction between two supercritical shocks, which could give an outlook for further experimental investigations. Finally, the astrophysical interest of such a research will be exposed as well.

Chapter 5 presents the concluding remarks upon this work and proposes possible directions for future research, also in the light of the recent Apollon commissioning campaign results.

Chapter 1

High-power laser-plasma interaction and its applications

1.1 Basics of laser-matter interaction

The domain of high-power laser-plasma interaction has remarkably grown over the last decades, with application ranging from laser-driven particle acceleration and fusion to laboratory astrophysics.
High-power lasers can deliver pulses of more than 200 TW, focused on relatively small areas such that the on-target intensity (= power/surface) is high enough to ionize the matter and hence produce a plasma. The intensity threshold for such a phenomenon is around 10^{10} W/cm^2, but nowadays laser facilities can deliver up to 10^{22} W/cm^2 (Danson et al. 2019; Mulser and Bauer 2020). The duration of these laser beams extends over several order of magnitude, from attoseconds ($\sim 10^{-18}$ s) to tens of nanoseconds ($\sim 10^{-8}$ s). Nanosecond lasers are characterized by moderate intensities ($\lesssim 10^{16}$ W/cm^2), while picosecond lasers allow for intensities up to 10^{20} W/cm^2, and with femtosecond lasers one can reach intensities up to 10^{22} W/cm^2. Laser pulses of attoseconds are composed of high harmonics providing a broad bandwidth and are nowadays mostly used to probe ultra-fast phenomena instead of driving them, as it is often the case for high-intensity lasers (Chopineau et al. 2021).
In general terms, laser development follows two different aims: maximizing the delivered energy or the power. These two classes of lasers correspond to different produced plasmas. High-energy lasers are characterized by "long" pulses, of the order of the ns, and generate thermal hot and dense plasmas. On the other hand, high-power lasers have duration ranging from fs to hundreds of ps and are able to produce strongly out-of-equilibrium and relativistic plasmas.
While "standard" lasers – i.e., based on the amplification of the stimulated emission from atomic or

molecular excitation (Gould et al. 1959) – have been developed since the 1960s (Maiman et al. 1960), the employment of x-ray free electron lasers (XFELs) has started around a decade ago. Based on the self-amplified spontaneous emission (SASE) of relativist electrons wiggling in an undulator (Huang and Kim 2007), XFELs can provide high-brillance high-repetition fs-pulses, suitable to give fast snapshots of fundamental processes at atomic or molecular scales.

In this thesis we will mostly focus on the experimental results obtained at the high-energy laser facilities LULI2000 (France) and Titan/JLF (United States), but we will also present the outcome of the commissioning campaign recently run on the high-power laser Apollon (France) and discuss the physics that we can envision on such a facility. The main focus will be towards the interaction between laser radiation and solid targets.

For current laser capabilities, the laser field cannot directly accelerate ions, as their mass is too large to allow them to reach velocities close the laser-light group velocity (Gibbon 2005). In our case of driving lasers with a pulse length of the order of the ns, the laser first transfers energy to the electrons, called then hot or supra-thermal, by inverse bremsstrahlung or by resonant absorption (Drake 2006a). Electrons in turn interact electrostatically with the ions, transferring energy to them, too (London and Rosen 1986; Macchi et al. 2013). Eventually, the plasma is strongly heated by the laser beam and relaxes.

1.1.1 Plasma expansion in vacuum

When a powerful laser interacts with a solid target in vacuum, the density and temperature profiles typically take the shape shown in Fig. 1.1 (Atzeni and Meyer-ter Vehn 2004), where the laser is propagating from the left to the right with intensity I_L. A plasma is formed out of the target and expands into vacuum while converting part of its thermal energy into kinetic energy. In reaction to this expansion, by the principle of conservation of the quantity of movement, a shock wave forms and propagates through the unperturbed solid (region 4), compressing and warming up the material after its passage (region 3). We will not discuss here the characteristics of shocks that form in the solid, but will only focus on the features of the front-side of the target.

We recall that electromagnetic (EM) waves can only propagate and hence deposit energy when the refractive index of the medium $N = c/v_\varphi$ is positive (where c is the speed of light and v_φ is the phase velocity). The relation of dispersion of an EM wave in an unmagnetized cold plasma is $\omega^2 = k^2c^2 + \omega_{pe}^2$ (Swanson 1989), where k is the wavenumber and $\omega_{pe} = \sqrt{n_e e^2/m_e\varepsilon_0}$ [SI] $= \sqrt{4\pi n_e e^2/m_e}$ [cgs] is the plasma frequency, n_e, e, and m_e are the electron density, charge, and mass, respectively, and ε_0 is the vacuum permittivity. An EM wave propagates indeed through plasma oscillations (Langmuir

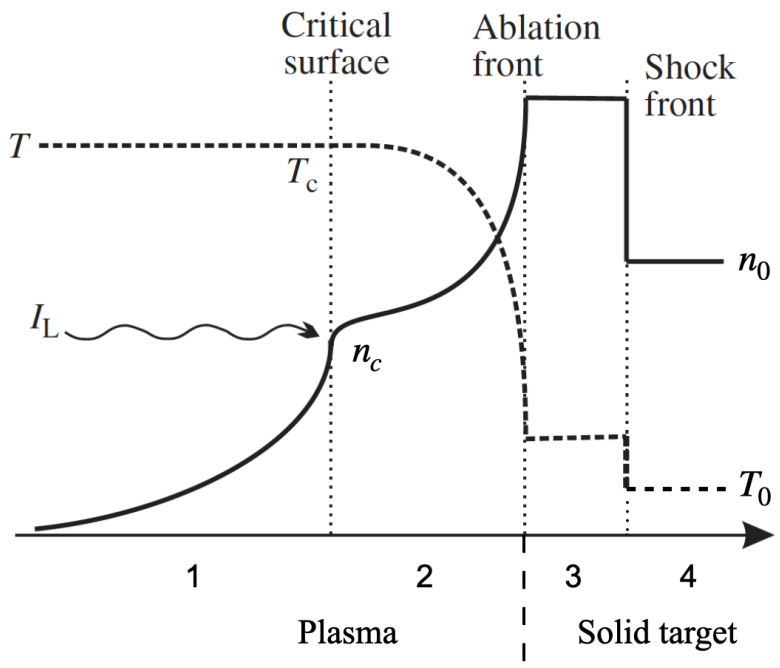

Figure 1.1: *Density (full line) and temperature (dashed line) profiles of a laser-driven ablation front from a solid target. (Adaptation from Atzeni and Meyer-ter Vehn (2004) p224.)*

waves) which affect only the electrons.

The refractive index then is:

$$N = \frac{ck}{\omega} = \sqrt{1 - \frac{\omega_{pe}^2}{\omega^2}} = \sqrt{1 - \frac{n_e}{n_c}} \tag{1.1}$$

where we have introduced the critical density n_c depending on the laser frequency ω:

$$n_c = \frac{\omega^2 m_e \varepsilon_0}{e^2}\ [\text{SI}] = \frac{\omega^2 m_e}{4\pi e^2}\ [\text{cgs}] \tag{1.2}$$

Imposing N to be a real positive number leads to a condition on the maximum electron density n_e allowed: EM waves can propagate only in an underdense plasma, i.e., for $n_e < n_c$[1].

In the formed plasma, two zones can be distinguished. An underdense transparent region (1, in Fig. 1.1), called *corona*, partially absorbs and deflects the laser radiation. Most of the relevant laser-plasma interaction phenomena, such as absorption, ionization, and nonlinear scattering, take place here, and most of the radiation in the extreme ultraviolet (EUV) and soft x-ray wavelength range (1-100 nm) comes from this region. Beyond the critical surface which reflects the laser field, we find an overdense zone (2) where the energy is transferred through thermal conductivity from the corona to the ablated solid.

[1]To be more precise, for $n_e > n_c$, EM radiation can still penetrate for a typical length of the order of $c/\omega_{pe} \equiv d_e$, called the plasma skin depth. The electromagnetic field will not have the profile of an oscillating sinusoidal wave, but will take the form of an evanescent (exponentially decreasing) wave.

1.1.2 Plasma expansion in the presence of an external magnetic field or a background gas

The characteristics of the ablated plasma expansion change drastically in the presence of an externally applied magnetic field or of a background gas.

First, let us consider the presence of an ambient gas. Depending on the laser intensity and on the gas density, the laser beam can start ionizing the gas while being focused on the solid target. Such created plasma can interact with the laser and give rise to effects such as filamentation and self-focusing (Atzeni and Meyer-ter Vehn 2004), that we will not discuss here.

During the interaction between a ns laser and matter, the corona plasma can reach temperatures ranging from tens of eV to several keV, and will, thus, emit thermal radiation. This includes a component due to the electronic transitions within the atoms (bound-bound, free-bound) present in the medium, while the presence of free electrons and ions also allows electronic transitions of free-free type (bremsstrahlung). These contributions generate a continuous emission spectrum, partially constituted of x-ray photons with energies up to several keV. The corona plasma emits in all directions and this radiation can be partly absorbed by the gas in which the target is plunged, converting it into a plasma itself. Hence, the plasma ablated from the solid target will now expand in a pre-ionized medium made of the ambient plasma at rest.

In the presence of an external magnetic field $\mathbf{B_0}$ the scene gets more complicated. To start, various modes of EM waves can exist in the plasma depending on their polarization and on the angles between $\mathbf{B_0}$ and the electromagnetic wave electric field $\mathbf{E_1}$, and between $\mathbf{B_0}$ and the wavenumber $\mathbf{k}$ (Chen 2016). These waves have dispersion relations that are different from the ones seen above for unmagnetized plasmas, hence, the critical density can differ from Eq. 1.2.

Moreover, the interaction between the ablated plasma and the external B-field may start various physical phenomena, such as plume confinement, ion acceleration, plasma instabilities, and emission enhancement (Dirnberger et al. 1994; Ripin et al. 1993; Tuckfield and Schwirzke 1969; Sudo et al. 1978; Koopman 1976).

One of the most noteworthy effects is the formation of a diamagnetic cavity (VanZeeland and Gekelman 2004; Collette and Gekelman 2010) in the case of magnetic field perpendicular to the plasma expansion velocity (which is the B-field orientation that will be discussed in this thesis). Since in many cases the electrons are magnetized and the ions unmagnetized[2], the magnetic field is tied to the electrons in the magnetohydrodynamics (MHD) framework. Hence, when we have a bulk motion of the plasma, the electrons follow the ions and advect the magnetic field along, which results

[2]A species is "magnetized" if the magnetic field affects significantly the particles motion, i.e., if their Larmor radius r_L is smaller or comparable to the length scale of the system.

"frozen-in". From a kinetic point of view, the fact that only the electrons are strongly magnetized leads to a charge separation: as the plasma expands, the ions are not "held back" by the magnetic field and surpass the electrons, which produces a net electric field pointing inwards the expansion direction $\mathbf{E_r}$. The electrons inside this expanding shell undergo an $\mathbf{E_r} \times \mathbf{B_0}$ drift which gives rise to a poloidal current that reinforces the pressure-drive $\nabla P \times \mathbf{B_0}$ diamagnetic currents. These contributions result in a local reduction of the magnetic field within the current layer, the diamagnetic cavity. Expelling the magnetic field requires energy, which is taken from the kinetic energy of the expanding plasma. Hence, with respect to the expansion into vacuum, a plasma spreading into a background magnetic field will advance more slowly and eventually stop at the so-called magnetic stopping radius, $R_B = (3N_i m_i v_i^2 / B_0^2)^{1/3}$, where N_i, m_i, and v_i are respectively the number, the mass, and the speed of the drifting ions (Schaeffer 2014).

Moreover, the spatial asymmetry, induced by the presence of the magnetic field, will shape the profile of the laser-produced plasma. In the case of vacuum, we typically have a plasma plume with a rotational symmetry around the laser axis. Now, with a magnetic field, the motion of the electrons (and hence the ions) is slowed down in the direction perpendicular to $\mathbf{B_0}$, which translates in the corresponding dimension of the plume to be smaller.

1.2 Shock formation and characteristics

Collisionless plasmas are pretty different than ordinary gases. Nevertheless, our understanding about what a shock is and how it forms and develops are mostly based on concepts coming from gas dynamics. Hence, we will first make considerations about hydrodynamic shocks, then pass to MHD and collisionless shocks.

1.2.1 Hydrodynamic shocks

In neutral gases, information can travel through the propagation of a disturbance. The perturbation takes the shape of a *sound wave*, where pressure and density oscillate in phase along the direction of propagation of the wave. The propagation of such a compressive wave is sustained by short range interactions between the molecules or atoms of the gas. At the particle scale, this interaction is naturally supplied by electromagnetic forces, but these mediate mostly binary-collisions and are relative to short-lasting induced dipoles in the molecules or atoms, while the electromagnetic fields we will refer to in later sections involve the medium in a collective way.

The *sound speed* is the velocity at which sound waves propagate in a neutral gas, independently of their frequency, and it is given by:

$$c_s = \sqrt{\frac{\partial p}{\partial \rho}} \tag{1.3}$$

where p the gas pressure and ρ is the mass density. At audio frequencies, the compression is adiabatic, i.e., the pressure changes too quickly to allow thermal conduction effects and the gas comes back to its original state after the compression wave has passed. This characteristic, together with the condition of dealing with "small" waves[3] and an ideal gas[4], allows us to calculate the sound speed as $c_s = \sqrt{\gamma\, p/\rho}$, where γ is the adiabatic index, i.e., the ratio of the specific heats c_P/c_V.
If an object moves in such a medium with a subsonical speed, it transmits momentum to the gas molecules, which convey it to other ones as a compressive wave (a sound wave). Thus, such a body can easily move as the air manages to adjust "quickly" enough around the object.
If this obstacle moves faster than the sound speed, the sound wave will not be able to reach a different part of the medium before the object itself. In this scenario, another way for information to travel is represented by shock waves. The perturbation introduced by the object leads to an irreversible compression process, which is associated with an increase of entropy and, hence, dissipation. Such a shock wave moves faster than the sound speed and modifies the state of the medium in which it travels, which results in an increase of its sound speed, making the downstream (DS) flow subsonic (with respect to the moving object).

Hence a shock can be defined as an entropy-increasing wave that causes a transition from a supersonic to a subsonic flow by irreversibly converting the kinetic energy of the upstream (US) incoming (from the point of view of the shock front) flow into thermal energy. Such a shock front takes places at widths as short as possible and is limited by viscosity and friction: it results to have thicknesses of the order of a few collisional mean free paths. Due to this thin thickness with respect to the macroscopic fluid scales, the schock-front can be seen as a "discontinuity" region that separates two fluids characterized by different state, i.e., by different pressure, temperature, flow speed, etc.
A critical quantity to consider when dealing with the motion in a certain fluid, is hence the ratio between the object velocity and the sound speed of such a medium, i.e., the so-called *Mach number*:

$$M = \frac{v}{c_s} \tag{1.4}$$

Example of hydrodynamic shocks are represented by the shock waves occurring when an aircraft

[3] In the sense that viscosity, friction, and heat conduction are negligible.
[4] A gas that follows the ideal-gas law $p = nk_BT$.

moves faster than the sound speed (Fig. 1.2[5]) or for detonations.

Figure 1.2: *Example of a shock wave formed for a jet moving at supersonic speed.*

1.2.2 Rankine-Hugoniot conditions

The macroscopic state of the US and the DS mediums can be characterized by the *Rankine-Hugoniot conditions*. They are derived by imposing the conservation of particle number, momentum, and energy across the shock and they only describe the US and DS regions supposed to be at equilibrium. Hence, they do not take into consideration the state of the thin shock front and the mechanisms taking place in there.

Let us now consider the reference frame of the shock front, i.e., where this is at rest, as sketched in Fig. 1.3.

The Rankine-Hugoniot (R-H) conditions take the integral form (Balogh and Treumann 2013):

$$\Delta(\rho v_n) = 0 \qquad \text{conservation of mass} \tag{1.5}$$

$$\Delta(\rho v^2 + p) = 0 \qquad \text{conservation of momentum} \tag{1.6}$$

$$\Delta\big(h + \frac{1}{2}v^2\big) = 0 \qquad \text{conservation of energy} \tag{1.7}$$

where ρ is the mass density, v is the flow speed in the shock front frame (for which the index n refers to the component normal to the shock front), p is pressure, $h = \epsilon + p/\rho$ is the specific enthalpy, ϵ being the internal energy. The Δ represents the difference between the value of these quantities after and before the shock passage, i.e., between the downstream and the upstream mediums.

[5]Image credit: https://aviation.stackexchange.com/questions/11936/are-we-at-peak-speed-efficiency-for-jet-airliners-at-mach-0-85.

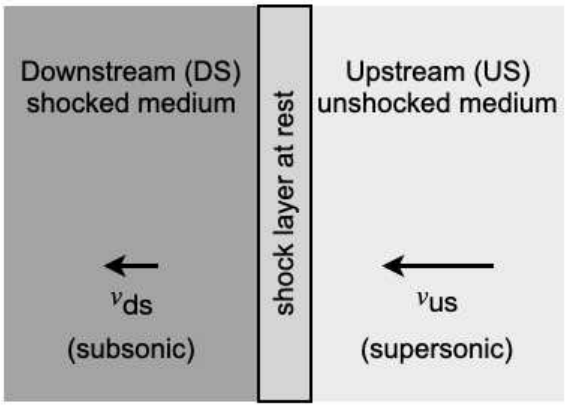

Figure 1.3: *Sketch of the shock regions and velocities in the reference frame of the shock.*

1.2.3 Magnetohydrodynamical shocks

When the fluid we deal with is a plasma, the situation becomes more complicated.

Magnetohydrodynamics (MHD) is a macroscopical and non-relativistic theory used to model plasmas. It describes the plasma as a single fluid composed of electrically charged particles of different mass (ions and electrons) but electrically neutral at the macroscopic level. Being made of charges, this fluid is conductive and undergoes induced and applied electromagnetic fields.

As will be detailed in Sec. 2.3.3, MHD is based on several assumptions that limit its validity much more than how would be required by a kinetic theory or by multi- and bi-fluid models, but it is extremely useful when these more sophisticated models would not add much in precision or when the geometry of the problem is very complex.

Plasma physical quantities and electromagnetic fields follow the MHD equations (Belmont et al. 2013):

$$\frac{\partial \rho}{\partial t} + \nabla \cdot (\rho \mathbf{v}) = 0 \tag{1.8}$$

$$\rho \left(\frac{\partial \mathbf{v}}{\partial t} + (\mathbf{v} \cdot \nabla)\mathbf{v} \right) = -\nabla p + \frac{1}{\mu}(\nabla \times \mathbf{B}) \times \mathbf{B} + \rho \mathbf{g} \tag{1.9}$$

$$\frac{\partial \mathbf{B}}{\partial t} = \nabla \times (\mathbf{v} \times \mathbf{B}) + \eta \nabla^2 \mathbf{B} \tag{1.10}$$

$$\nabla \cdot \mathbf{B} = 0 \tag{1.11}$$

Before talking about MHD shocks, let us introduce the typical kinds of wave that are possible in the MHD context, as derived by such a system of equations.

Similarly to what happens in neutral gases, there are *ion acoustic waves*, longitudinal oscillations of the ions and electrons that involve density variations. They can occur in an unmagnetized plasma or in a magnetized plasma parallel to the magnetic field. The waves are dispersionless with a propagation

speed given by:

$$c_s = \sqrt{\frac{\gamma_e Z k_B T_e + \gamma_i k_B T_i}{m_i}} \tag{1.12}$$

where k_B is Boltzmann's constant, m_i is the ion mass, Z is the charge number, T_e is the temperature of the electrons and T_i is the temperature of the ions.

Plus, in ideal[6] MHD, three fundamental waves linked also with EM-fields oscillations arise: the *Alfvén waves*, the *fast* and the *slow magnetosonic waves*. These propagate at different speeds, depending on the plasma characteristics and on the angle θ between the equilibrium magnetic field $\mathbf{B}_0$ and the propagation direction of the wave $\mathbf{k}$.

Alfvén waves are dispersionless and non compressible $(\delta\rho = 0)$ waves that involve a transverse oscillation of charge density and of magnetic and electric fields. They propagate along the equilibrium magnetic field lines at speed:

$$v_A = \frac{B_0}{\sqrt{\mu_0 \rho_0}} \tag{1.13}$$

where B_0 and ρ_0 are the unperturbed magnetic field and mass density, and μ_0 is the magnetic permeability of vacuum.

Magnetosonic waves involve oscillations of the magnetic field in phase (fast) or counter-phase (slow) with the mass density (they are hence compressible). The electric field oscillates perpendicularly to the wave propagation direction, while there is no charge density perturbation.

The group velocity for fast $(+)$ and slow $(-)$ magnetosonic waves is given by:

$$v_{ms\pm} = \sqrt{\frac{1}{2}\left[v_A^2 + c_s^2 \pm \sqrt{(v_A^2 + c_s^2)^2 - 4 v_A^2 c_s^2 \cos^2\theta}\right]} \tag{1.14}$$

where c_s is the sound speed.

They can propagate with various orientations with respect to the magnetic field, but for perpendicular propagation $(\theta = \pi/2)$ only fast waves exist. This is the case when the maximum propagation speed is reached: $v_{ms+}^{max} = \sqrt{v_A^2 + c_s^2}$.

When considering shocks inside such a conductive medium, certain jump conditions must be satisfied by the electromagnetic field, too. Then the R-H shock relations in MHD take the form of the

[6] The resistivity is neglected and the plasma is hence treated as a perfect conductor.

generalized Rankine-Hugoniot conditions (Balogh and Treumann 2013):

$$\Delta(\rho v_n) = 0 \qquad \text{conservation of mass} \tag{1.15}$$

$$\Delta(B_n) = 0 \qquad \text{no divergence of the B-field} \tag{1.16}$$

$$\Delta(v_n \mathbf{B} - \mathbf{v} B_n) = 0 \qquad \text{Faraday's law} \tag{1.17}$$

$$\rho v_n \Delta v_n + \Delta\left(p + \frac{B^2}{2\mu_0}\right) = 0 \qquad \text{conservation of perpendicular momentum} \tag{1.18}$$

$$\rho v_n \Delta \mathbf{v}_t - \frac{B_n}{\mu_0}\Delta \mathbf{B}_t = 0 \qquad \text{conservation of parallel momentum} \tag{1.19}$$

$$\frac{\rho v_n}{2}\Delta(v^2) + \frac{\gamma}{\gamma-1}\Delta(p v_n) + \frac{1}{\mu_0}\Delta(v_n B^2) - \frac{B_n}{\mu_0}\Delta(\mathbf{v}\cdot\mathbf{B}) = 0 \qquad \text{conservation of energy} \tag{1.20}$$

where the orientations n and t refer to the normal and the tangential directions, respectively, with respect to the shock front, and γ is the adiabatic index. We point out that in Eqs. 1.18–1.20 the quantities ρv_n and B_n have been brought out of the Δ because they are constant across the shock (by reason of Eqs. 1.15–1.16). For the conservation of energy, it has been supposed that the plasma has polytropic equation of state: $p/\rho^\gamma =$ constant.

Possible kinds of solutions of the generalized R-H conditions exist. Let us first distinguish between two classes: we talk about *discontinuities* when there is no change in the flow speed through the shock front ($\Delta v_n = 0$) and about *shocks* otherwise ($\Delta v_n \neq 0$). It is possible to represent these two kinds of solution in a graph where $v_{\text{ds},n}$ is represented as depending on $v_{\text{us},n}$ (see Fig. 1.4): discontinuity solutions stay on the straight line $v_{\text{us},n} = v_{\text{ds},n}$, while shocks on the other curve.

Three kinds of discontinuities can be identified:

- *Contact discontinuity* is the case with $v_{\text{us},n} = v_{\text{ds},n} = 0$ and $B_n \neq 0$. The magnetic field varies smoothly across the shock ($\Delta B = 0$), as well as does the pressure ($\Delta p = 0$). Only density and temperature present a jump ($\Delta\rho \neq 0$, $\Delta T \neq 0$), implying that the diffusion resulting from the temperature gradient makes such a discontinuity short-lived.

- *Tangential discontinuity* is the case with $v_{\text{us},n} = v_{\text{ds},n} = 0$ and $B_{\text{us},n} = B_{\text{ds},n} = 0$, which leads to a constant total pressure across the shock ($\Delta(p + B^2/2\mu_0) = 0$), while the density ρ and the tangential magnetic field $\mathbf{B}_t$ can have a jump.

- *Rotational discontinuity* represents the case when $v_{\text{us},n} = v_{\text{ds},n} \neq 0$ and $v_n^2 = B_n^2/(\mu_0\rho)$. This implies that the density, the pressure, and the strength of the tangential component of the B-field do not change across the shock ($\Delta\rho = 0$, $\Delta p = 0$, $\Delta B_t^2 = 0$). However the tangential magnetic field $\mathbf{B}_t$ is free to rotate, which gives the name to this discontinuity. Practically, this solution corresponds to an Alfvén wave-like jump: all the quantities are conserved except for

the direction of $\mathbf{B}_t$ and $\mathbf{v}_t = \mathbf{B}_t/\sqrt{4\pi\rho}$.

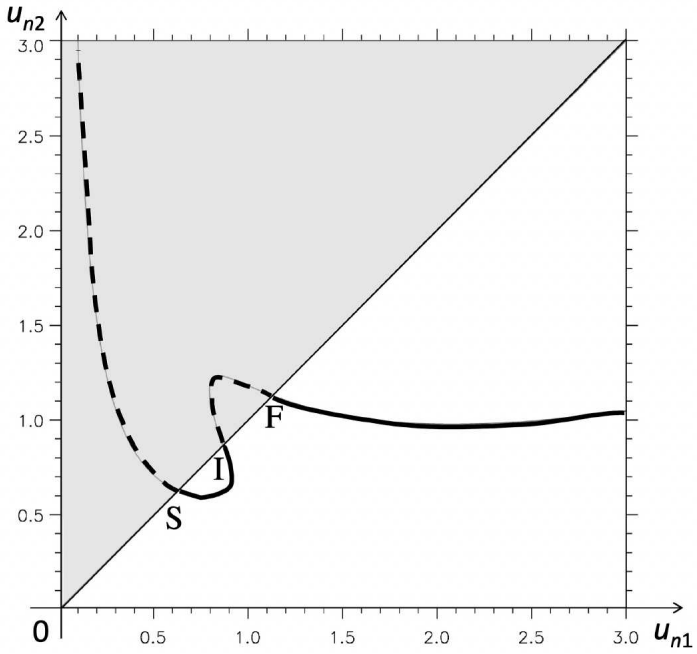

Figure 1.4: *Curves representing the possible downstream normal flow speed values $u_{ds,n}$ with respect to the upstream one $u_{us,n}$, as derived by the generalized Rankine-Hugoniot conditions (Belmont et al. 2013). Relative to $\beta_{us} = 0.8$, and $\theta_{Bn} = 30°$. The velocities are normalized to $v_{A,us}$ and the dashed line represents the values $v_{ds,n} > v_{us,n}$ not physical. The letters S, I, and F pinpoint the proximity to the linear solution corresponding to slow, intermediate (Alfvén), and fast waves, respectively.*

Shock solutions are located on the full part of the curve in Fig. 1.4, as only $v_{\mathrm{ds},n} < v_{\mathrm{us},n}$ are physical (since leading to an increase of entropy after the shock passage). The linear solutions (infinitesimal perturbations) stay in the proximity of the intersection of such a curve with the straight line $v_{\mathrm{ds},n} = v_{\mathrm{us},n}$ and correspond to the MHD waves: slow magnetosonic (S), Alfvén (or intermediate, I), and fast magnetosonic (F). In these three points $v_{\mathrm{us},n}$ coincides with the values of the corresponding MHD waves velocities: v_{ms-}, v_A, and v_{ms+}, respectively.
It is then possible to identify three kinds of shocks, departing from these linear solutions:

- *Slow shock* for upstream velocities $v_{ms-} < v_{\mathrm{us},n} < v_A$, for which only one solution is possible. In this case, the tangential B-field decreases and the pressure increases from US to DS ($\Delta|B_t| < 0$, $\Delta p > 0$).

- *Intermediate shock* for $v_A < v_{\mathrm{us},n} < v_{ms+}$, which either allows for two solutions or for none. This corresponds to a finite amplitude Alfvén solution associated with a π rotation of $\mathbf{B}_t$. If the pressure is isotropic, the density is continuous ($\Delta\rho = 0$). Such solutions are considered unstable.

- *Fast shock* for $v_{\mathrm{us},n} > v_{ms+}$, for which only one solution is allowed. Here, both the thermal and the magnetic pressure increase after the shock ($\Delta|B_t| > 0$, $\Delta p > 0$).

For further insight into MHD shocks and examples, excellent reviews are represented by Oliveira (2017) and Belmont et al. (2013).

1.2.4 Shocks in collisionless plasmas

Astrophysical plasmas are normally very different than ordinary gas.
As we said, waves and shocks in gases are supported by collisions, while most space plasma are *collisionless*. This means that their density is so low that binary Coulomb collisions are very rare and do not play an important role. This is the case when the collisional mean free path of the particles is much larger than the size of the system $\lambda_{mfp} \gg L$.
For example, the collisional mean free path in the solar wind is calculated to be around 1 AU ($= 1.5 \times 10^8$ km, i.e., the distance from Earth to the Sun), while the thickness of the Earth's bow shock is observed to be only 100–1000 km.
The absence of collisions can lead to a lack of equilibrium, normally assured by collisions, hence the need to refer to *kinetic temperatures*, as well as to the necessity of some other mechanisms capable of propagating pressure and dissipating energy. Indeed, while for hydrodynamic shocks the size of the region over which the variation of the macroscopic quantities takes place is of the order of some λ_{mfp}, in collisionless shocks the discontinuity has a much smaller thickness $\Delta_{sh} \ll \lambda_{mfp}$. A shock wave is allowed in a collisionless medium in the presence of kinetic effects playing the role of an effective dissipation at the shock front.

Shock formation: laminar and turbulent shocks

Collisionless shocks can be classified into two groups depending on how the transition between the DS and the US regions is done: laminar and turbulent shocks (Balogh and Treumann 2013).
Laminar shocks form through the steepening of finite amplitude waves. The well-known small amplitude waves (i.e., Alfvén, fast/slow magnetosonic, and ion acoustic waves) are derived from the linearization of the fluid equations (1.8–1.11). But those neglected non-linear terms may play an important role in the evolution of finite-amplitude waves. The crest of the wave may have a propagation speed $v_p + \delta v_p$ higher than the one of the zero, v_p, and of the trough, $v_p - \delta v_p$, which leads to a deformation of the wave, as sketched in Fig. 1.5 from t_1 to t_2. This brings to the formation of gradients that

are so high that the dispersive effects[7] may be so important to balance the wave steepening formation. Instead of having what is sketched in Fig. 1.5 at t_3, i.e., a wave "breaking" in a multi-valued solution of the wave equations, a steep shock front may form, as at t_4. Such an effective dissipation is due to the collective interaction between the particles and the electromagnetic field of the non-linear wave.

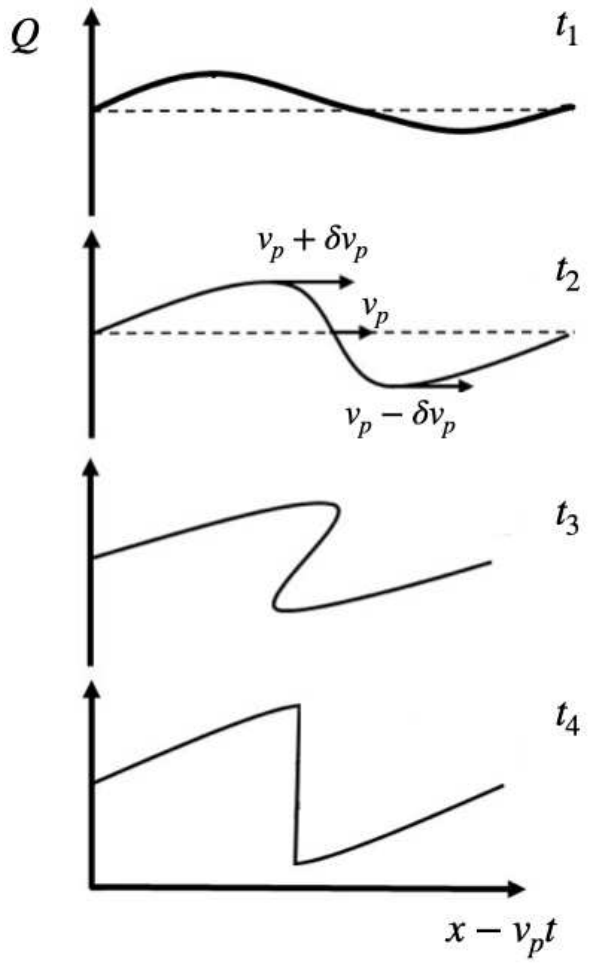

Figure 1.5: *Sketch of the self-steepening of a finite-amplitude wave associated with the oscillation of a certain physical quantity Q. In the region where the state variables of the wave would become multivalued (at t_3), irreversible processes dominate to create an abrupt, single-valued shock front. (Adapted from Chernukha (2019).)*

On the other hand, turbulent shocks form out of the amplification of turbulent electromagnetic field. Many instability mechanisms are reasonable candidates for being efficient dissipation processes in collisionless shocks (Wu 1982). Examples include the modified two-stream instability (McBride et al. 1972; Matsukiyo and Scholer 2003), cyclotron drift instability (Jiao et al. 2019), and the Weibel instability (Grassi 2017). In such cases, the instability can lead to dissipation by opening the way to smaller length scales, that is a conversion of the kinetic energy into heat, and hence an increase of temperature. Slowing down the incoming flow also means increasing its density, because of mass conservation. Thus, a zone where temperature and density change sharply is created, and has normally the size of a few tens of the particle skin depth, c/ω_{ci}.

[7] Different wavelengths have different propagation speeds.

In general, low-M_A low-β shocks are laminar, while high-M_A high-β shocks present a turbulent behavior (Formisano 1974). For example, the Earth's bow shock has been found to show both laminar and turbulent characteristics depending on the region (Formisano and Hedgecock 1973b; Greenstadt et al. 1975; Formisano and Hedgecock 1973a).

Shock characteristics

First, collisionless shocks can be classified as *electrostatic* or *magnetized*, depending on the nature of the field at the shock front. Electrostatic shocks are steep local density perturbations usually characterized by a high ion density spike surrounded by a bipolar electric field (Chen et al. 2007). They take place over scales of the order of the Debye length ($\Delta_{sh} \sim \lambda_{De}$[8]), have a tangential size of the order of the ion inertial length λ_i ($= c/\omega_{pi} = \sqrt{m_i/m_e}(c/v_e)\lambda_{De} \gg \lambda_{De}$), and can occur when the charges composing the plasma have on the average the same bulk velocity (hence there are no free electric currents) and no external magnetic field is applied (Treumann 2009).

The presence of a background magnetic field in the plasma is a common astrophysical situation and allows the formation of magnetized shocks (Stasiewicz and Eliasson 2020). For instance, the Earth's bow shock forms when the solar wind meets the Earth's magnetosphere and is characterized by a magnetic field of the order of 10^{-4} G. Similar B-field strengths are found in SNRs (Xu and Lazarian 2017), while the solar wind termination shock is accompanied by a magnetic field of the order of 10^{-6} G (Burlaga et al. 2008).

A first characteristic to consider is the orientation of the upstream ambient magnetic field $\mathbf{B}_{\text{us}}$ with respect to the shock front normal $\hat{\mathbf{n}}$, by defining the shock normal angle θ_{Bn} through

$$\tan\theta_{Bn} = \frac{\mathbf{B}_{\text{us}} \cdot \hat{\mathbf{n}}}{|\mathbf{B}_{\text{us}}|} \tag{1.21}$$

$\theta_{Bn} = 0$ is the case for *parallel shocks*, $\theta_{Bn} = \pi/2$ for *perpendicular shocks*, which are extreme cases that in reality are realized only over small portion of the shock surface. To recall the characteristics of these two special cases, one can define two other categories: we talk about *quasi-parallel shock* when $0 < \theta_{Bn} < \frac{\pi}{4}$ and about *quasi-perpendicular shocks* when $\frac{\pi}{4} < \theta_{Bn} < \frac{\pi}{2}$. In particular, shocks with $\frac{\pi}{6} < \theta_{Bn} < \frac{\pi}{3}$ are said *oblique* and show some mixed properties. While (quasi-)perpendicular shocks exhibit a sharp transition (plus a narrow foot, if supercritical), as will be detailed later, in (quasi-)parallel shocks both the upstream and the downstream media are disturbed up to larger distances (Treumann 2009). In space, the Earth's bow shock represents a case of shock transition from per-

[8]The Debye length of a plasma is a measure of the size of the region over which charge separation can naturally take place, that is the size of electrostatic fluctuations. It reads: $\lambda_{De} = \sqrt{\varepsilon_0 k_B T_e/n_e q_e^2}$ [S.I.]

pendicular to parallel: the solar wind extends over scales larger than the the Earth's magnetosphere curvature, hence, while moving along the shock, the angle between the shock normal and the magnetic field lines passes from 0° to 90° depending on the location.

Discussion on the validity of Rankine-Hugoniot conditions for collisionless shocks

It is legitimate to wonder why the Rankine-Hugoniot equations derived in the MHD frame are used also for collisionless shocks. Indeed, they suppose that the plasma has reached an equilibrium both upstream and downstream, while we previously said that the lack of "standard collisions" does not assure the fulfilment of a state where some macroscopic quantities, i.e., the temperature, can be defined.

For example, a common case of missed thermalization concerns the populations of electrons and ions. In such a case, Rankine-Hugoniot conditions have been extended to allow for separate ion and electron temperatures (see for example Sanderson and Uhrig (1978)).

However, a pseudo-state of equilibrium may still be reached if we consider zones "far enough" from the shock front.

Moreover, the R-H conditions do not take into considerations the kinetic effects into the energy balance. In spite of the fact that particle acceleration is possible at the shock front (see Sec. 1.3), previous studies have shown that the energy acquired by such non-Maxwellian particles remains small. In particular, for non-relativistic shocks, the most efficient conversion occurs at strong (quasi-)parallel shocks, where the particles kinetic energy gain accounts for up to 10-20% of the bulk kinetic energy (Caprioli and Spitkovsky 2014). In our case of perpendicular or quasi-perpendicular shocks, the efficient acceleration mechanism of diffusive shock accleration (DSA, see Sec. 1.3) is not at play anymore, and the resulting accelerated particles reach energies more than one order of magnitude smaller than in the quasi-parallel case (Caprioli and Spitkovsky 2014).

Nevertheless, R-H conditions are applicable to many cases of collisionless shocks reported in the literature (see, for instance, Grassi et al. (2017); Blandford and Eichler (1987); Bret et al. (2013); Gargaté and Spitkovsky (2011)) and, when they do not give a totally accurate result, they still represent a reasonable starting point.

Criticality

One of the most important characteristic of collisionless shocks is their criticality.

We can distinguish between *subcritical* and *supercritical* shocks depending on their magnetosonic Mach number $M_{ms} (= v_{sh}/c_{ms})$ being, respectively, smaller or larger than a certain critical Mach

number M_c. The critical Mach number M_c is defined by equating the downstream flow speed in the shock frame to the downstream ordinary sound speed and depends on the upstream plasma β and on θ_{Bn} as shown in Fig. 1.6 by Edmiston and Kennel (1984a): M_c increases with increasing shock angle θ_{Bn} and decreasing plasma β, with its highest values being ≈ 2.76, as originally inferred by Marshall (1955).

Above the critical Mach number, i.e., in supercritical shocks, resistivity alone cannot provide all

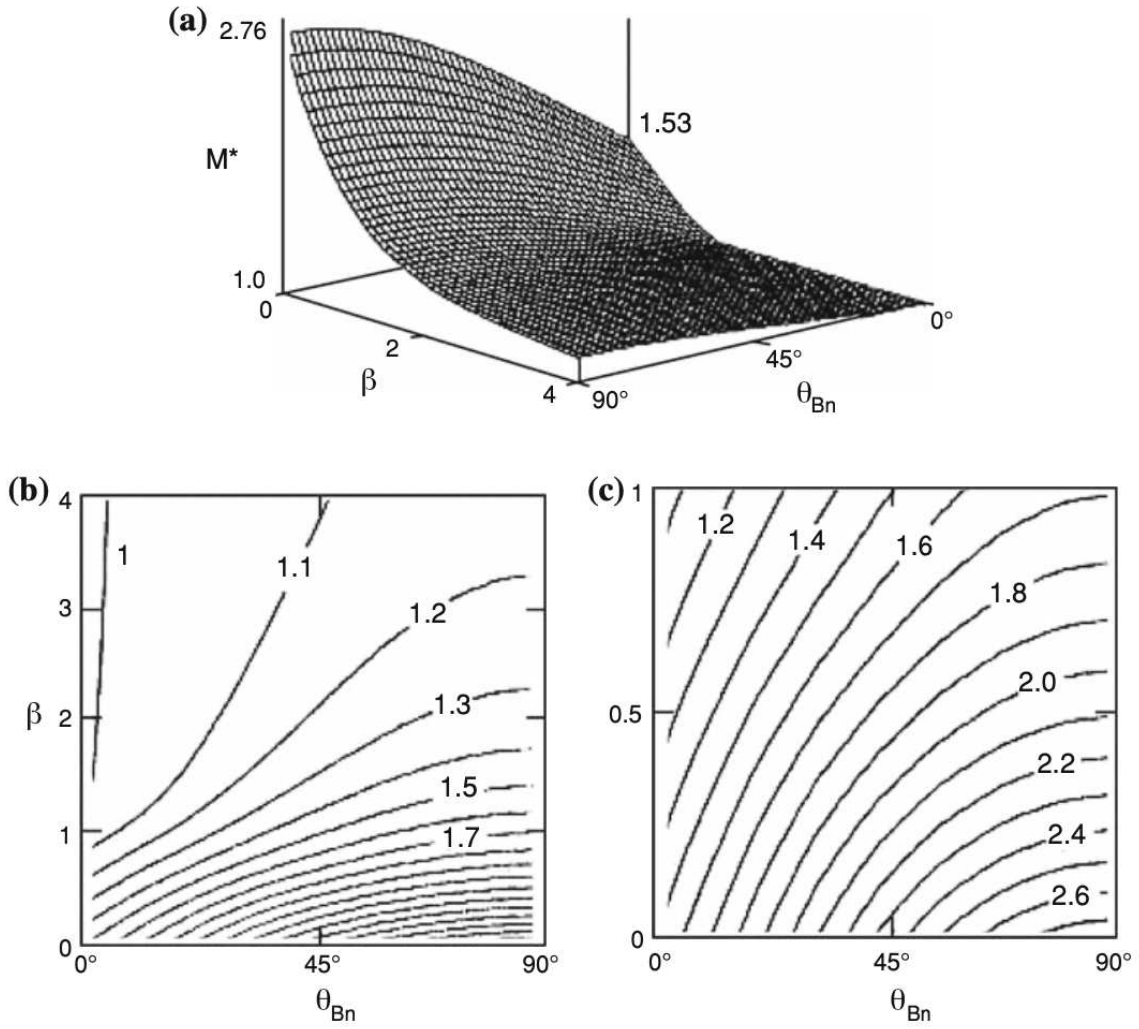

Figure 1.6: *(a) Parametric dependence of the critical Mach number M_c for a fast shock on the upstream plasma β and shock angle θ_{Bn} (between the shock normal and the upstream magnetic field) for the case of adiabatic index $\gamma = \frac{5}{3}$, as reported by Edmiston and Kennel (1984a). (b) and (c) report the contours of critical Mach numbers for two ranges of β: from 0 to 4 and from 0 to 1, respectively.*

the dissipation needed for a shock transition according to the R-H conditions, hence, other processes must provide the dissipation required for their formation. Thus, supercritical shocks are normally associated to much stronger ion heating, particle acceleration, and incoming plasma reflection than subcritical ones. Particle reflection, in particular, represents the main dissipative process, so that, the-

oretically, supercritical shocks could exist in the absence of any conventional dissipation.
On the other hand, subcritical shocks require some other kind of anomalous dissipation, which is normally provided by the contributions of resistive effects inside the shock front (i.e., energy dissipation into heat) and wave dispersion. The presence of the latter signifies that the short wavelengths responsible for the steepening would either overrun or not catch up with the wave when its profile surpasses a certain steepness. However, dispersion alone is not enough to sustain a shock, since it cannot generate the irreversible dissipation required for the heating (and thus entropy increase), hence some kind of diffusive process is always present in subcritical shock waves (Balogh and Treumann 2013).

Shock substructure

Supercritical magnetized shocks can be decomposed into several parts: the shock foot, the shock ramp and the overshoot/undershoot, as shown in Fig. 1.7. The *foot* is the small bump of magnetic field, pressure, and density located upstream of the proper shock front. It results from the accumulation of ions and/or electrons reflected by the shock ramp. The *ramp* is the part of the shock where the magnetic field and density gradients are the highest. The overshoot/undershoot structure is the magnetic field modulation in the downstream region, i.e., the B-field "overshoots" and then "undershoots" the asymptotic value. It is thought to be associated with the transmission and thermalization of ions trapped at the shock front.
In astrophysical shock waves, other features can be present. For instance, a *particle precursor* consists in a structure preceding the shock made of energetic particles that have diffused through the shock. A *radiative precursor* can also be produced by the ionizing radiation coming from the shock front.

In the case of subcritical shocks, the percentage of reflected ions is very small and neither foot nor overshoot/undershoot structures can take place. In the case of dispersive shock transition (left side in Fig. 1.8), upstream whistler steepens and makes the upstream ion beam oscillate. For resistive shock transitions (right side in Fig. 1.8) the shock forms a steep ramp without showing any upstream oscillations. The downstream B-field may develop trailing oscillations.

1.3 Shock particle acceleration mechanisms

This section aims at giving a small overview of the particle acceleration mechanisms taking place at the shock front. We will focus on the dynamics of ions.
We know that particle acceleration occurs in astrophysical systems. This stems from astrophysical

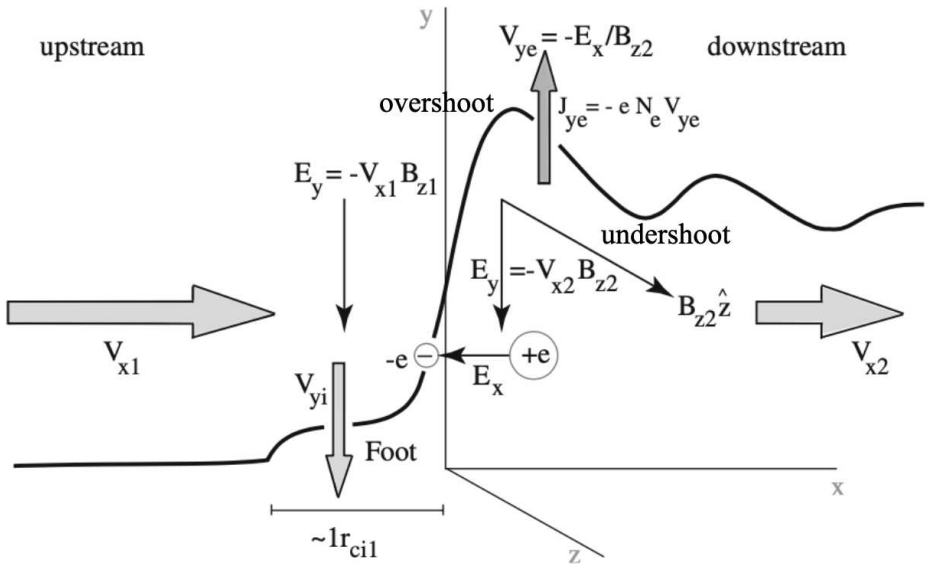

Figure 1.7: *Typical structure of a supercritical perpendicular shock front, corresponding to the profiles of magnetic field $|\mathbf{B}|$, particle density n, temperature T, and pressure p. Charge separation over lengths of the ion gyroradius r_{Li} occurs at the shock ramp generates an electric field E_x which reflects part of the incoming ions from upstream, giving rise to a foot. Such ions are accelerated by the convective electric field E_y and the resulting current causes the formation of a magnetic foot, too.* (*Adapted from Treumann* (*2009*).)

observations of high-energy particles – such as Cosmic Rays (CRs) – and radiation – such as radio emission from jets and supernova remnants (produced by GeV electron) and gamma rays (generated by TeV particles) (Gabici et al. 2019; Caprioli 2015).

Energy is transferred from fast flows and magnetic field to particles and thus to radiation via the interplay of electromagnetic fields. In the case of microscopic electric field associated with turbulent fluctuations we will talk about *stochastic acceleration* (*SA*). In the case of macroscopic fields associated with the shock, various acceleration mechanisms can take place (Marcowith et al. 2016b): *diffusive shocks acceleration* (*DSA*), *shock drift acceleration* (*SDA*), and *shock surfing acceleration* (*SSA*).

It is worth mentioning that *magnetic reconnection* is a frequent and extreme astrophysical event where the energy stored in magnetic fields is converted into heat and kinetic energy, responsible for high-energy space particles, too. For example, magnetic reconnection occuring in downstream islands plays a role in particle energization, as the cosmic rays spectra are not always explainable by diffusive shock acceleration only (Drake et al. 2006; Zank et al. 2015).

However, since this thesis is focused on shocks, we will discuss only these four kinds of acceleration relying on the presence of the shock.

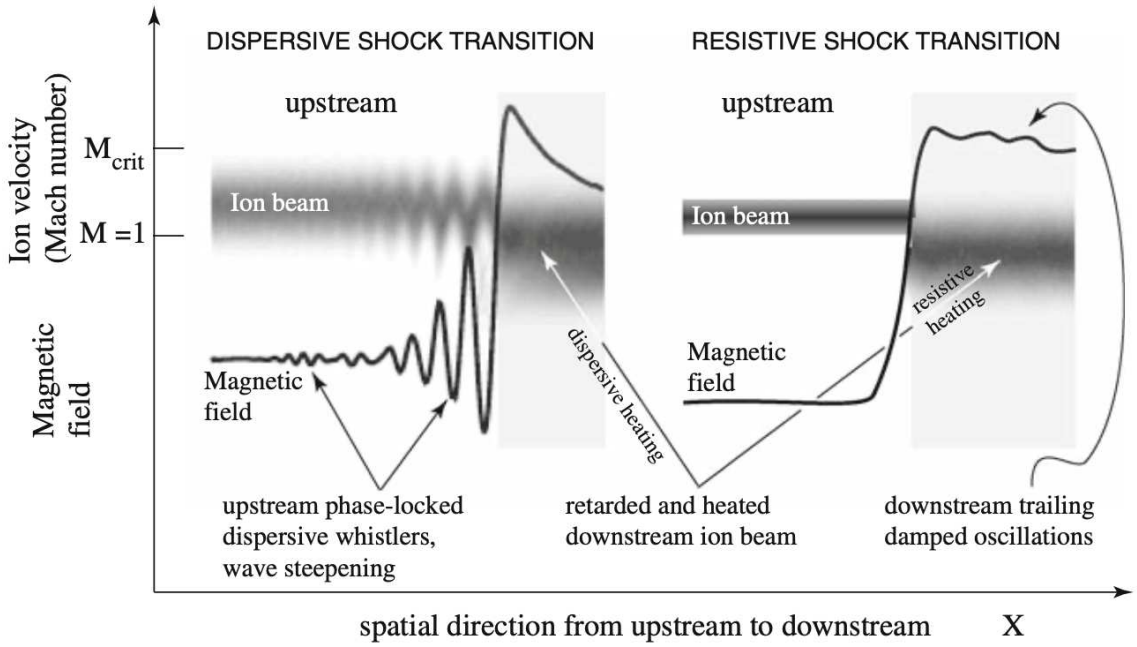

Figure 1.8: *Sketches of the ion phase space and magnetic field profiles for the two extreme types of subcritical shocks* (*Treumann 2009*).

1.3.1 Stochastic Acceleration (SA) or second order Fermi acceleration

This kind of acceleration mechanism was firstly proposed by Fermi in the late '40s as a way to accelerate cosmic particles (Fermi 1949). In the stochastic acceleration, particles gain energy by interacting repeatedly with a random distribution of scattering centers. The physics can be easily represented in a classical scenario by considering a ball with initial speed $+v$ that interacts elastically with a wall, as represented in Fig. 1.9: if the wall does not move, the ball will bounce back with a speed $-v$; if the wall moves against the ball with speed $-V$ (head-on collision), the ball will acquire energy and come back with velocity $-v-2V$; on the contrary, if the wall moves away with speed $+V$ $(< +v)$ (head-tail collision), the ball will move at the lower speed $v - 2V$.

While the ball represents a particle, the wall plays the role of "magnetic mirrors" present in moving interstellar magnetized clouds. Such "walls" can be either zones of strong magnetic field that deviate the particle along its trajectory, or a region of curved magnetic field which gradually modify the particle pitch angle. In the interstellar medium such magnetic field fluctuations are supposed to be randomly oriented and move at speeds $V \ll v$.

Eventually, a net particle acceleration takes place because the interaction between particles and magnetic walls will occur more often through head-on collisions, associated with energy gain, than head-tail ones.

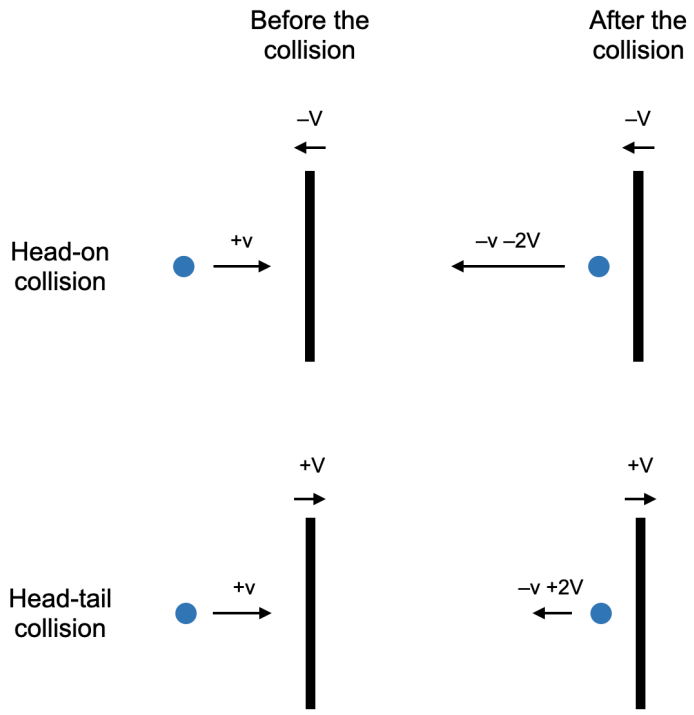

Figure 1.9: *Sketch of the principle of the stochastic acceleration for macroscopical objects. A ball with initial speed $+v$ interacts $\sim$ elastically with a massive wall moving towards the ball at speed $-V$ (top) and away from it at speed $+V$ (bottom), where $v \gg V$. In the first case, the particle gains energy, in the second one, it loses it.*

Indeed, it is possible to show that the energy gain or loss per collision is (Ferrand 2007)

$$\frac{\Delta E}{E_{in}} = -2\frac{\Delta \mathbf{v} \cdot \mathbf{V}}{c^2} \tag{1.22}$$

where E_{in} and E_{fin} are the initial and final kinetic energies of the particle, respectively, $\Delta E = E_{fin} - E_{in}$ is the difference between them, $\mathbf{\Delta v} = \mathbf{v}_{fin} - \mathbf{v}_{in}$ is the difference in velocity, and c is the speed of light. By averaging over all the collisions, we have:

$$\langle \frac{\Delta E}{E} \rangle \propto \left(\frac{V}{c}\right)^2 \tag{1.23}$$

which explains why this mechanism is also called second-order Fermi acceleration.

It possible to enlarge these considerations to proper shocks, i.e., to situations where the particle interacts with two mediums characterized by different physical quantities. One cycle is considered to be a sequence: passage through the shock layer $\rightarrow$ interaction with the DS region (characterized by a flow velocity $v_{\rm ds}$ in the shock front frame) $\rightarrow$ passage through the shock $\rightarrow$ interaction with the US region (characterized by a flow velocity $v_{\rm us} > v_{\rm ds}$). After a complete cycle, the energy change will be

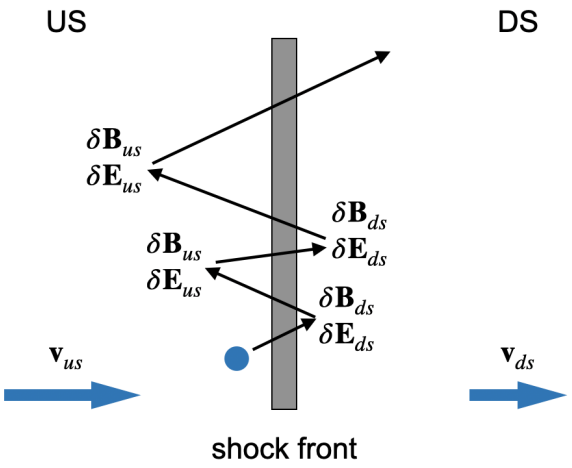

Figure 1.10: *Diagram of the SA taking place around a shock front, where a particle is scattered by magnetic turbulence associated with the DS or the US region and seen by it, statistically, as approaching. The net energy gain will eventually be positive.*

Ferrand (2007):

$$\langle \frac{\Delta E}{E_{in}} \rangle \approx \frac{4}{3} \frac{v_{in}\,(v_{\rm us} - v_{\rm ds})}{c^2} \tag{1.24}$$

and, in terms of momentum:

$$\langle \frac{\Delta p}{p} \rangle \approx \frac{4}{3} \frac{v_{\rm us} - v_{\rm ds}}{v_{in}} \tag{1.25}$$

which corresponds to a net energy gain, as the particle coming back to the shock undergoes head-on collisions in both DS and US regions.

In the MHD scenario, the energy is transferred from the bulk plasma motion to the particle, by having the fluctuating B-field lines tied to the plasma. This transfer is of course made through an electric field (as the magnetic field cannot make any work): indeed a motional electric field is associated both upstream and downstream to the turbulent magnetic field: $\delta\mathbf{E}_{\rm us} = -\mathbf{v}_{\rm us} \times \delta\mathbf{B}_{\rm us}$ and $\delta\mathbf{E}_{\rm ds} = -\mathbf{v}_{\rm ds} \times \delta\mathbf{B}_{\rm ds}$.

A sketch of the mechanism at play is shown in Fig. 1.10.

Particles have a certain probability to escape from the cloud or the shock and hence interrupt the energy gain process. This gives rise to a power-law spectrum.

The acceleration mechanism can be characterized by an acceleration time τ_{acc} (such that the particle gains kinetic energy at a rate $\partial E/\partial t \approx E/\tau_{acc}$) and by an escape time τ_{esc} (such that the number of escaped particles increases at a rate $\partial N/\partial t = N/\tau_{esc}$). Then the number of escaped particles will satisfy:

$$\frac{{\rm d}N}{{\rm d}E} = -\frac{N}{E}\left(1 + \frac{\tau_{acc}}{\tau_{esc}}\right) \tag{1.26}$$

whose solution is given by the power law (Ferrand 2007):

$$N(E) \propto E^{-s} \qquad \text{where} \quad s = 1 + \frac{\tau_{acc}}{\tau_{esc}} \tag{1.27}$$

SA plays an important role in many astrophysical phenomena, such as particle acceleration in solar flares (Petrosian 2012), in supernova remnants and their superbubbles[9] (Bykov and Fleishman 1992; Ferrand and Marcowith 2010), and in galaxy clusters (Brunetti and Lazarian 2007). However, it is unlikely that solely SA is responsible for the generation of energetic cosmic rays (CRs). Indeed, (1) the random velocities of clouds are pretty small ($V/c \sim 10^{-4}$); (2) CRs with mean free paths of the order of 0.1 pc would experience collisions only a few times per year; (3) the energy gain is second order in (V/c); all translates into a small probability of having particles gaining significant energy (Marcowith et al. 2020).

1.3.2 Diffusive Shock Acceleration (DSA) or first order Fermi acceleration

As we have seen, SA is not efficient enough to justify the observation of energetic cosmic rays. Now, if only head-on collisions take place, then the energy gain would be systematic. This is what happens in the case of Diffusive Shock Acceleration (DSA), which represents indeed a fundamental process of particle acceleration in astrophysical systems and is the more likely mechanism responsible of CRs (Malkov and Drury 2001).

Davis Jr (1956) extended and modified the SA mechanism introduced by Fermi by considering a medium where coherent magnetic fields are present in the DS and US regions, in addition to many diffusely distributed magnetic fluctuations, acting as scattering centers, in relative motion. Particles will be then scattered into all angles, giving rise to a diffuse distribution, after which this mechanism is named.

In DSA, particles gain energy by scattering around the shock on magnetic fluctuations present in both the DS and US mediums, as schematized in Fig. 1.11. Systematic energy gain occurs at every shock crossing by the particle since the scattering centers are always seen as approaching.

Let us consider a shock moving with speed v_{sh} with respect to the unperturbed upstream medium. Both the US and the DS plasmas will see the other side as approaching at speed $\Delta v = \frac{r-1}{r}\, v_{sh}$, where r is the shock compression ratio. Let us also assume that the scattering centers in both US and DS regions are efficiently isotropized by the magnetic turbulence, i.e., their mean velocity is the same as the bulk flow speed. Then a situation similar to that of SA takes place in this scenario, where the cloud

[9]Superbubbles are cavities carved out the interstellar medium by multiple supernovae and stellar winds. They are typically $\sim$ hundreds ly large and populated with hot ($\sim 10^6$ K) gas atoms less dense than the surrounding interstellar medium.

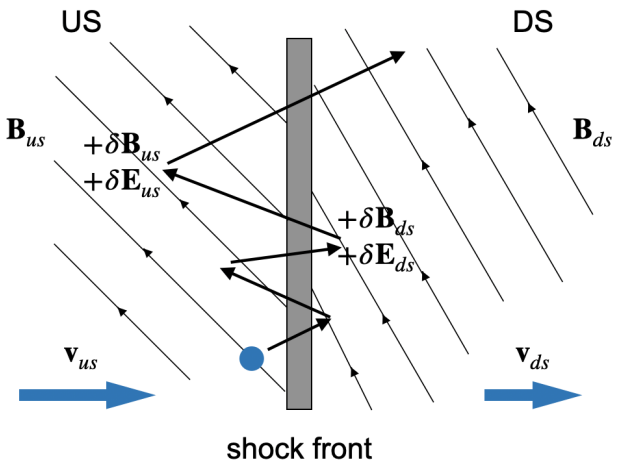

Figure 1.11: *Sketch of the trajectory of a particle bouncing over scattering centers, leading to diffusive shock acceleration.*

randomly fluctuating magnetic mirrors are replaced by magnetic waves always seen by the particle as approaching at speed Δv. By averaging over the crossing angles of the particle through the shock, one finds that the average energy change per crossing is (Ferrand 2007):

$$\langle \frac{\Delta E}{E} \rangle = \frac{4}{3} \frac{r-1}{r} \frac{v_{sh}}{c} \tag{1.28}$$

hence a gain of the first order in v_{sh}/c.

Similarly to the reasoning done for SA, by considering the probability of a particle to remain or to escape from the accelerating shock region, one would obtain again a power-law for the energy spectrum. Hence, the energy distribution of the escaped particles will take the form (Marcowith et al. 2020; Drury 1983):

$$N(E) \propto E^{-s} \quad \text{where} \quad s = 1 + \frac{\tau_{acc}}{\tau_{esc}} \tag{1.29}$$

The ratio τ_{acc}/τ_{esc} turns out to be independent of E in DSA, but only linked to the compression ratio of the shock r (Ferrand 2007; Diesing and Caprioli 2021):

$$s = \frac{r+2}{r-1} \tag{1.30}$$

The hardest spectrum that one could have is $N(E) \propto E^{-1}$, obtained in the limit of eternal confinement ($\tau_{esc} = \infty$) or for extremely strong shock ($r = \infty$).

DSA is considered as the most likely production mechanism of supra-thermal and relativistic particles in many astrophysical object, ranging from the Earth's bow shock (Blandford and Eichler 1987; Ellison et al. 1990; Jones and Ellison 1991) to shocks in clusters of galaxies (Bykov et al. 2008). This

mechanism is capable of accelerating CRs up to 10^{15} eV in SNRs (Marcowith et al. 2016b) and even higher in active radio-galaxies such as Centaurus A (Croston et al. 2009). However, it cannot explain ultra-high energy cosmic rays (UHECRs, of energies above 10^{18} eV), whose origin is still debated, even though some propositions have been advanced, such as active galactic nuclei (Abraham et al. 2007), relativistic supernovae (Chakraborti et al. 2011), gamma-ray bursts and hypernovae (Wang et al. 2008a).

Moreover, DSA works only if the velocity of the particle is much bigger than the one of the plasma flows in the DS and US regions. It is also clear that the particle must initially have a gyro-radius much larger than the shock transition layer, in order to be able to take full advantage of the difference in bulk velocity of the DS and US mediums. The so-called *injection problem* is indeed the lack of efficiency of DSA with slow particles, hence the need of another mechanism that could initially energize thermal particles.

Besides, it does not work efficiently at quasi-perpendicular shocks, as there is a lower return probability from downstream because of advection with the magnetic field lines.

Shock drift acceleration and shock surfing acceleration, which will be reviewed below, can help injecting particles in the case of perpendicular shocks.

1.3.3 Shock Drift Acceleration (SDA)

Shock drift (SDA) (Hudson and Kahn 1965; Webb et al. 1983) and shock surfing (SSA) (Sagdeev 1966; Lee et al. 1996) acceleration processes are considered to play an important role in ion (pre-) acceleration at quasi-perpendicular shocks. They both rely on the presence of an upstream coherent motional electric field $\mathbf{E} = -\mathbf{v} \times \mathbf{B}$, induced by the motion of magnetized plasma. The difference between these two mechanisms consists in the way the particles move or are confined around the shock front and in the ratio of the ion Larmor radius over the shock width (smaller for SSA and larger for SDA) (Shapiro and Üçer (2003), Yang et al. (2012)).

In SDA particles gain energy while gyrating and having their guiding center that moves along the motional electric field, as shown in Fig. 1.12.

To discuss the relevant acceleration mechanism, we should first distinguish between *subluminal* and *superluminal* shocks. We talk about subluminal (or superluminal) shocks when the intersection point between the upstream B-field and the shock front moves slower (or faster) than the speed of light c. This property can be formalized in having $\tan(\frac{\pi}{2} - \theta_{Bn}) - \frac{v_{\rm us}}{c} > 0$ for subluminal (hence, typically non-relativistic) shocks and < 0 for superluminal (hence, relativistic) ones.

In subluminal shocks, it is always possible to find a reference frame where the motional electric van-

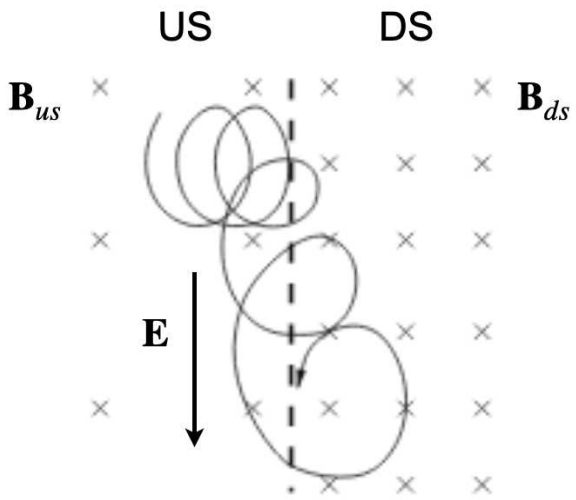

Figure 1.12: *Sketch of the trajectory of an ion undergoing SDA. In this configuration, the accelerating convective electric field* $\mathbf{E} = -\mathbf{v} \times \mathbf{B}$ *is the same in the DS and US region (in the shock reference frame) because of the R-H conditions for MHD shocks (Eq. 1.17).*

ishes, that is where the flow velocity and the magnetic field are parallel (both US and DS), which is called de Hoffmann-Teller frame (Kirk et al. 1994). In such a frame, particles move mostly along the magnetic field. When a particle drifts in the US region towards the shock, it can either be transmitted or reflected because of the higher magnetic compression. If the particle is reflected, one can derive the acquired energy by using a Lorentz transformation between the shock rest frame and the de Hoffmann-Teller frame. The maximum energy gain is obtained when the particle has a guiding center speed perpendicular to the shock front (such as the particle in Fig. 1.12) and results (Kirk et al. 1994):

$$\langle \frac{E_{fin}}{E_{in}} \rangle = \frac{1 + \sqrt{1-b}}{1 - \sqrt{1-b}} \tag{1.31}$$

where $b = B_{\rm us}/B_{\rm ds}$ is the inverse of the magnetic field compression ratio.

For transmitted particles, the energy gain is half of what obtained in case of reflection in Eq. 1.31 (Kirk et al. 1994).

In superluminal shocks, it is always possible to find a reference frame where the magnetic field and the shock front are parallel, which means that particles need to diffuse across the magnetic field if they want to cross the shock. In this case it is possible to resort to the adiabatic invariant $p_\perp/B$, which is conserved at the order of v_{sh}/v, i.e., especially for particles much faster than the shock speed. In the passage from US to DS, both B and $p_\perp$ increase. The energy gain then is maximum for a perpendicular shocks (Kirk et al. 1994):

$$\frac{E_{fin}}{E_{in}} = \frac{1}{\sqrt{b}} \tag{1.32}$$

1.3.4 Shock Surfing Acceleration (SSA)

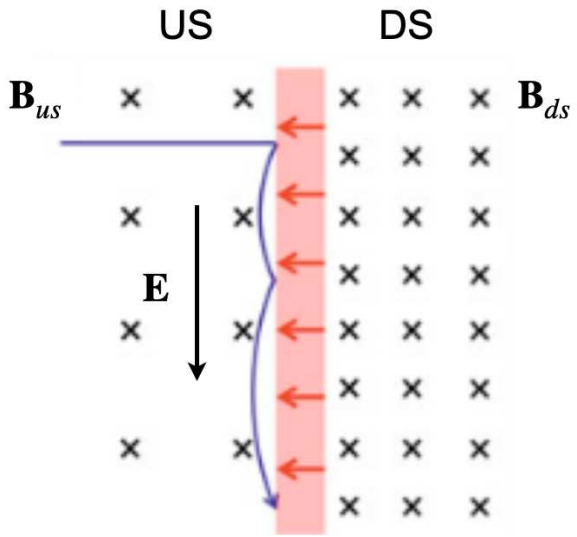

Figure 1.13: *Sketch of the trajectory of an ion undergoing SSA. In this configuration, the accelerating convective electric field* $\mathbf{E} = -\mathbf{v} \times \mathbf{B}$ *is the same in the DS and US region (in the shock reference frame) because of the R-H conditions for MHD shocks (Eq. 1.17). We point out that the initial straight trajectory of the ion is a schematization of its motion: the ion would actually gyrate because of the US magnetic field.*

Shock surfing acceleration (SSA) takes place when the shock electrostatic potential ϕ and the upstream Lorentz force trap the particle in the vicinity of the shock front. In other words, the particle (with initial velocity $v < v_{sh}$) is reflected upstream by the electrostatic field associated with the shock front, while the US Lorentz force leads the particle back to the shock front, as schematized in Fig. 1.13. The energization is then due to the convective electric field, which accelerates the particle until its kinetic energy along the shock normal surpass the shock potential (Lee et al. 1996; Shapiro and Üçer 2003; Lever et al. 2001).

SSA allows to inject particles up to energy relevant for DSA to set in (Lee et al. 1996; Zank et al. 1996) and is particularly efficient for narrow ramps.

1.4 Applications to laboratory astrophysics

The big advancements in laser technology over the last decades have allowed the investigation of the phenomena mentioned above in the laboratory, providing important insight into several mechanisms (Marcowith et al. 2016a). Applying the knowledge on laser-driven shocks to astrophysical shocks require the scaling of laboratory experiments to space events. The physical phenomena occurring on such hugely different temporal and spatial scales can indeed be compared as the equations governing their dynamics may show a certain degree of similarity.

How representative an experiment is of its astrophysical counterpart relies on the existence of certain scaling laws. These laws play a fundamental role in illustrating how comparable are systems produced in the laboratory with astrophysical phenomena. Laboratory astrophysics experiments can be classified into classes according to the type of similarity (Falize et al. 2009b; Dizière 2012), as summarized in Fig. 1.14:

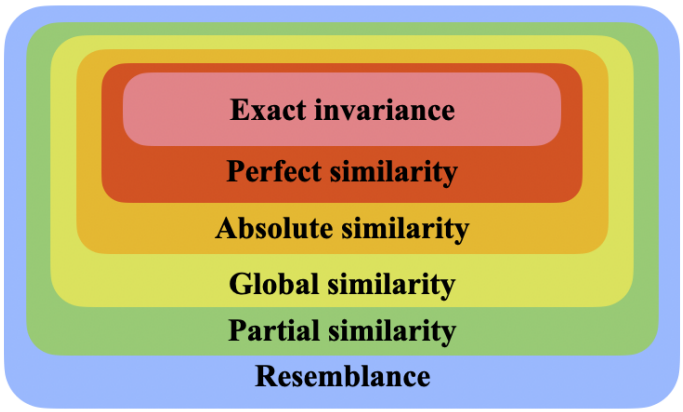

Figure 1.14: *Classification of laboratory astrophysics experiments and their reciprocal relations. (Adapted from Falize et al. (2009b).)*

1. Exact invariance (or sameness (Takabe 2001)). This is the group of the experiments aiming at reproducing the exact same thermodynamical conditions of astrophysical objects. Such experiments can be considered as "static" as they do not necessarily involve temporal or spatial scales. Typically are part of this category experiments related to the investigation of equations of state (EOS) and opacities, which are linked, for examples, to the study of matter in the planet cores, on the surface, or inside stars (see, for instance, Benuzzi-Mounaix et al. (2014); Valencia et al. (2009); Koenig et al. (1995)).

2. Similarity. These experiments (considered as "dynamical") do not try to reproduce exact same physical quantities as the astrophysical ones, but may actually take place over temporal and spatial scales much smaller than their space analogues. However, it is still possible to use scaling laws to check the the corresponding similarity properties. Several sub-categories exist:

(a) Perfect similarity: only the temporal and spatial variables are rescaled (Ryutov and Remington 2003)

(b) Absolute and global similarities: by relying on the invariance of the Lie symmetry (Olver 1995), these similarities only require the invariance of the form of the equations. In particular, they are used to adapt target configurations to different various facilities. The main difference between them is the number of free parameters used to rescale astrophysical experiments (Falize et al. 2009a).

(c) Partial similarity: here, only a part of the equations is conserved, while under study is the effect of other physical phenomena on the evolution of various quantities (Basko and Johner 1998).
Are part of this class, for example, laboratory experiments on inertial confinement fusion or on astrophysical plasma whose compositions differ from the ones in space (Falize et al. 2011).

3. Resemblance. This class includes all the experiments that reproduce processes similar to those occurring in the Universe, without being directly comparable, and can help understand the underlying physics of validate portions of numerical codes. This is the case when microscopic processes affect the hydrodynamical scales, like for radiative shocks, where, for example, the cooling process in the laboratory can be different than the one occurring in space.

As we will see, the physical processes produced in the laboratory and described in this thesis aim at the global similarity with their astrophysical counterparts.

1.4.1 Hydrodynamical similarity

Setting up scaling laws between two systems that are supposed to evolve in a similar way means imposing similarity to the equations describing these systems.
Let us first consider as hydrodynamical systems two ideal[10] polytropic[11] compressible fluids. Their evolution is hence governed by the Euler equations (Landau and Lifshitz 1987) for the conservation of mass, of momentum, and of energy:

$$\frac{\partial \rho}{\partial t} + \nabla \cdot (\rho \mathbf{v}) = 0 \tag{1.33}$$

$$\rho\Big(\frac{\partial \mathbf{v}}{\partial t} + \mathbf{v} \cdot \nabla \mathbf{v}\Big) = -\nabla p \tag{1.34}$$

$$\frac{\partial p}{\partial t} - \gamma \frac{p}{\rho} \frac{\partial \rho}{\partial t} + \mathbf{v} \cdot \nabla p - \gamma \frac{p}{\rho} \mathbf{v} \cdot \nabla \rho = 0 \tag{1.35}$$

Having Euler similarity corresponds to imposing certain relationships between the physical quantities of the two systems, i.e., their fluid velocity $\mathbf{v}$, pressure p, and mass density ρ. By defining the *Euler number* as

$$Eu = v\sqrt{\frac{\rho}{p}} \tag{1.36}$$

the two systems have a similar behavior with respect to the Euler equations if they share the same Euler number (and provided that their initial conditions are similar) (Ryutov et al. 1999).
As the sound speed of polytropic systems can be written as $c_s = \sqrt{\gamma\, p/\rho}$, the Euler number is pro-

[10] i.e., whose viscosity and thermal conductivity can be neglected.
[11] i.e., with a proportionality between the internal energy and the pressure $\epsilon \propto p$.

portional to the Mach number:

$$Eu = v\sqrt{\frac{\rho}{p}} = \sqrt{\gamma}\, v \sqrt{\frac{\rho}{\gamma p}} = \sqrt{\gamma}\, M \tag{1.37}$$

1.4.2 Validity criteria

The Euler equations govern systems behaving as hydrodynamical ideal fluids. We can summarize the conditions of validity of such equations in four points: (1) the system is collisional; (2) the heat conduction is negligible; (3) radiation flux is negligible; (4) viscosity dissipation is negligible.

Collisionality

MHD applies to collisional plasmas, i.e., whose particle (electron or ion) mean free path is comparable or even smaller to the typical length scale of the system. As discussed in the previous sections, even though this condition is not applied in many astrophysical phenomena, MHD results are still applicable to those systems up to a certain level of accuracy.

Heat conduction

The importance of diffusive heat transport is characterized by the *Péclet number* Pe (Book 1980), which corresponds to the ratio of heat convection to heat conduction. The hydrodynamic Euler equations (1.33–1.35) are valid if the Peclet number is large:

$$Pe = \frac{\text{convective transport}}{\text{thermal diffusivity}} = \frac{vL}{\chi} \gg 1 \tag{1.38}$$

where v is the fluid velocity, L the characteristic length, and χ the thermal diffusivity of electrons (Zel'dovich et al. 1967).

Radiation flux

Hydrodynamical forces have to be dominant over radiation energy fluxes. The corresponding condition depends on the mean free math of the photons, $\lambda_{mfp,\gamma}$, whose evaluation is often difficult. Let us consider two extreme cases.

If $\lambda_{mfp,\gamma} \ll L$, where L is the characteristic length of the system, then one should compare the radiation contribution to thermal diffusivity, χ_γ. In this case the corresponding Péclet number Pe_γ needs to be large:

$$Pe_\gamma = \frac{\text{thermal diffusivity}}{\text{radiative flux}} = \frac{L\nu}{\chi_\gamma} \gg 1 \tag{1.39}$$

If $\lambda_{mfp,\gamma} \gg L$, i.e., in the case of optically thin plasmas, the cooling is due to bremsstrahlung, and (at some temperatures) to line radiation. Then the required condition concerns the ratio between the radiative cooling time (optically thin emission), $\tau_{thin,\gamma}$, and a characteristic hydrodynamic time, τ_{hydro}:

$$\frac{\tau_{thin,\gamma}}{\tau_{hydro}} \gg 1 \tag{1.40}$$

Viscosity

Viscous effects are also required to be unimportant. Their influence can be quantified by the *Reynolds number* Re (Book 1980):

$$Re = \frac{\text{inertial forces}}{\text{viscous forces}} = \frac{vL}{\nu} \gg 1 \tag{1.41}$$

Presence of a magnetic field

We add that, with the inclusion of magnetic fields, similarity requires also that the effects of induction of the magnetic field by the motion of a conducting medium dominate over the magnetic diffusion. The *magnetic Reynolds number* (Book 1980), Rm, is used to describe their relative importance:

$$Rm = \frac{\text{induction}}{\text{diffusion}} = \frac{\mu_0 vL}{\eta} \gg 1 \tag{1.42}$$

where η is the magnetic diffusivity.

As we will see in the following chapters, the characterization of our laser-driven plasmas will include an evaluation of their hydrodynamical similarity to space plasmas.

Chapter 2

Experimental and numerical methods

In this chapter, we are going to present the experimental and numerical methods employed to produce and characterize the shocks. In detail, it will be articulated in three sections. In Sec. 2.1, we are going to briefly introduce the laser facilities at which the two experiments have been run: Titan/JLF at Lawrence Livermore National Laboratory (LLNL), in Livermore (US), and LULI2000 at Laboratoire pour l'Utilisation des Lasers Intenses (LULI), in Palaiseau (France). In Sec. 2.2, we will describe the diagnostics used to characterize the plasma and the programs employed to analyze the related data. Finally, in Sec. 2.3, we are going to present two kinds of codes, MHD and Particle-In-Cell (PIC), that can be used to model plasmas: in particular, we will focus on the characteristics of the MHD code FLASH and the PIC code Smilei.

2.1 Laser facilities characteristics

2.1.1 Titan/JLF

The experiment that generated single supercritical shocks was first run at the Jupiter Laser Facility (JLF) at the Lawrence Livermore National Laboratory (LLNL) in Livermore. The experimental room was Titan and is shown in Fig. 2.1.

This facility permits to couple an energetic ns-pulse and a chirped intense ps-pulse.

The short and the long pulses can be used and synchronized independently, as they have different pilots. They are both based on neodymium (phosphate) glass (Nd:Glass) lasing medium and have central wavelength $\lambda = 1053$ nm (called 1ω), that can be doubled to $\lambda = 526.5$ nm (called 2ω).

The short-pulse beam is obtained via the implementation of chirped pulse amplification (CPA) (Strickland and Mourou 1985). CPA is a technique for amplifying an ultrashort laser pulse, based essentially

Figure 2.1: *Experimental room of the Titan laser facility at LLNL (in Livermore, United States).*

on three stages: (1) temporal and spectral stretch of the laser pulse, (2) pulse amplification, (3) temporal compression, as sketched in Fig. 2.2.

The long pulse has a duration ranging from 0.35 to 20 ns and energy up to 1 kJ (or 500 J, if doubled).

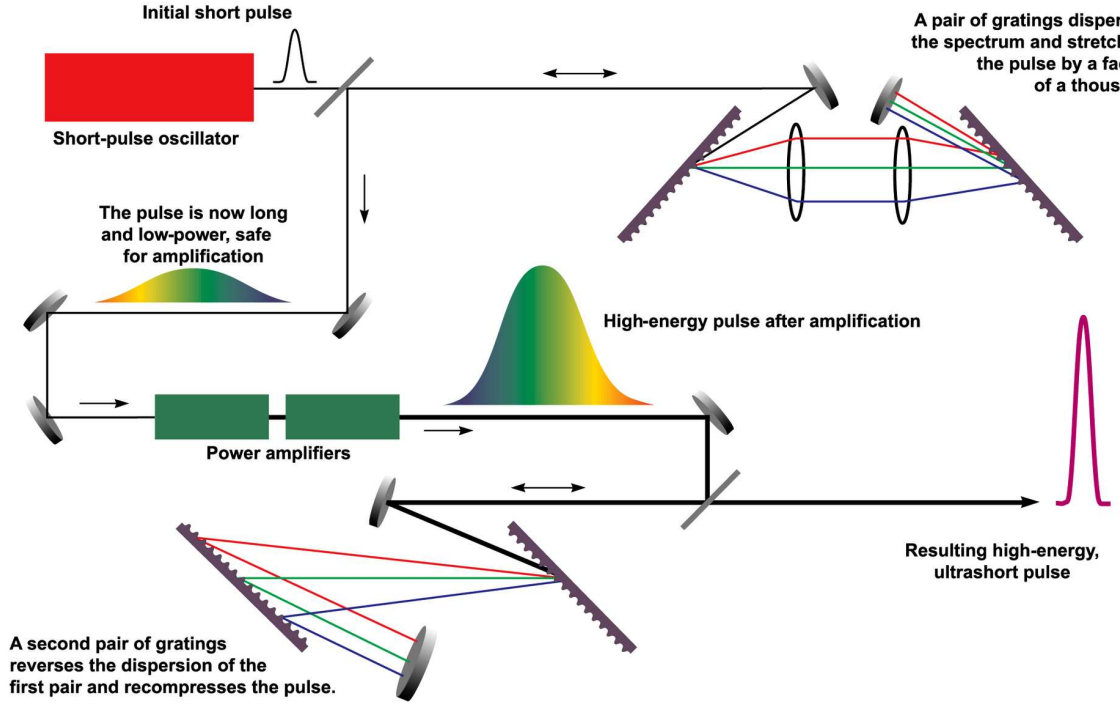

Figure 2.2: *Scheme of CPA principle. (Image adapted from LLN (1995).)*

The short pulse can last between 0.7 and 200 ps and deliver energy up to 300 J (or 50 J, if doubled). The focal spot size can be adjusted in order to obtain the desired intensity on the target (down to a minimum diameter of 20 µm for the long pulse and 8 µm for the short one).

The facility also provides an additional lower energy beam, typically used as a probe, as well as an electromagnetic pulser, used to feed magnetic coils.

Figure 2.3: *Laser hall.*

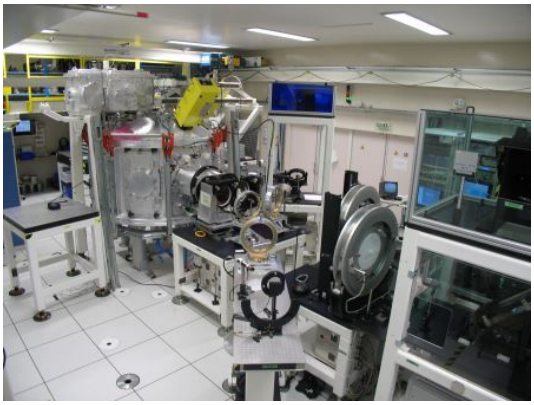

Figure 2.4: *Experimental room n.2 and interaction chamber.*

Figure 2.5: *Laser hall and experimental room n.2 of the LULI2000 laser facility at École Polytechnique (in Palaiseau, France).*

As we will see in Sec. 3.1, the long pulse was used to generate the shock, the short pulse was employed to produce via target normal sheath acceleration (TNSA) the protons to image the electromagnetic fields (i.e., proton radiography, explained in Sec. 2.2.2), and the auxiliary beam was used to perform interferometry (explained in Sec. 2.2.1).

2.1.2 LULI2000

The double shock experiment was run at LULI2000, in the experimental room n.2, shown in Fig. 2.5. The facility has four laser chains providing beams that can be independently synchronized and shaped. In the experimental room n.2, four such beams are present: two high-energy long-pulse beams (called north and south chains) and two lower energy beams, one of ns-duration (blue beam) and one of ps-duration (black beam).

Also in this case, the lasers are based on neodymium (phosphate) glass (Nd:Glass) lasing medium and have central wavelength $\lambda = 1053$ nm, that can be doubled to $\lambda = 526.5$ nm.

The "twin" north and south beams have duration ranging from 0.5 to 15 ns and energy up to 800 kJ (at 1ω). The blue beam can last, too, between 0.5 and 15 ns and deliver up to 50 J on target, while the black beam goes from 1 to 30 ps and provides up to 10 J.

Similarly to Titan, an electromagnetic pulser and auxiliary low energy (a few mJ) probe beams are provided: the Quanta-Ray and CFR200, lasting around 7 ns and with wavelength $\lambda = 1060$ nm (at 1ω) and $\lambda = 530$ nm (at 2ω).

As we will detail in Sec. 4.1, we employed the north and south beams to generate the two shocks, the blue beam to perform Thomson Scattering (explained in Sec. 2.2.3), and the Quanta-Ray to operate

interferometry.

2.2 Diagnostics

In this section we will present the working principle of the diagnostics that we have employed during our experiments and of the programs used to analyze the corresponding data. Additional information about the laboratory setup will be given in Chapters 3 and 4, when discussing specific experiments.
Laboratory diagnostics can be distinguished into *active* and *passive*. Active diagnostics make use of an external probe to investigate the state of the system. Such a probe can consist in particles or electromagnetic radiation (optical or x-ray) and ideally is not intrusive.
During our experiments, three active diagnostics helped us characterize the system:

- interferometry $\longrightarrow$ time-resolved spatially-integrated electron density
- proton radiography $\longrightarrow$ (electro)magnetic fields
- Thomson scattering $\longrightarrow$ time-resolved volumetric electron density, and ion and electron temperatures

On the other hand, passive diagnostics are based of the proper emission (of EM radiation or of particles) of the medium. We made use:

- magnetic proton spectrometer $\longrightarrow$ spectrum of the protons escaping the shock
- focusing spectrometer of x-ray self-emission with spatial resolution $\longrightarrow$ time-integrated electron density and temperature

2.2.1 Interferometry

Interferometry probing of a plasma allows for the measurement of its electron density. The principle of interferometry reposes on the "comparison" of two beams, one passing through the plasma (probing beam) and one traveling unperturbed in vacuum for the same optical length (reference beam). Once these two beams are recombined, an interference pattern (fringes) depending on their phase difference forms.

Various configurations of interferometers are possible, but during our campaigns we have used the Mach-Zehnder kind, schematized in Fig. 2.6. Here, the laser radiation is typically split into two beams which initially share the same wave-front (i.e., the same phase). Along their path, the probing beam interacting with the plasma undergoes a phase shift due to the variation of refractive index N of the

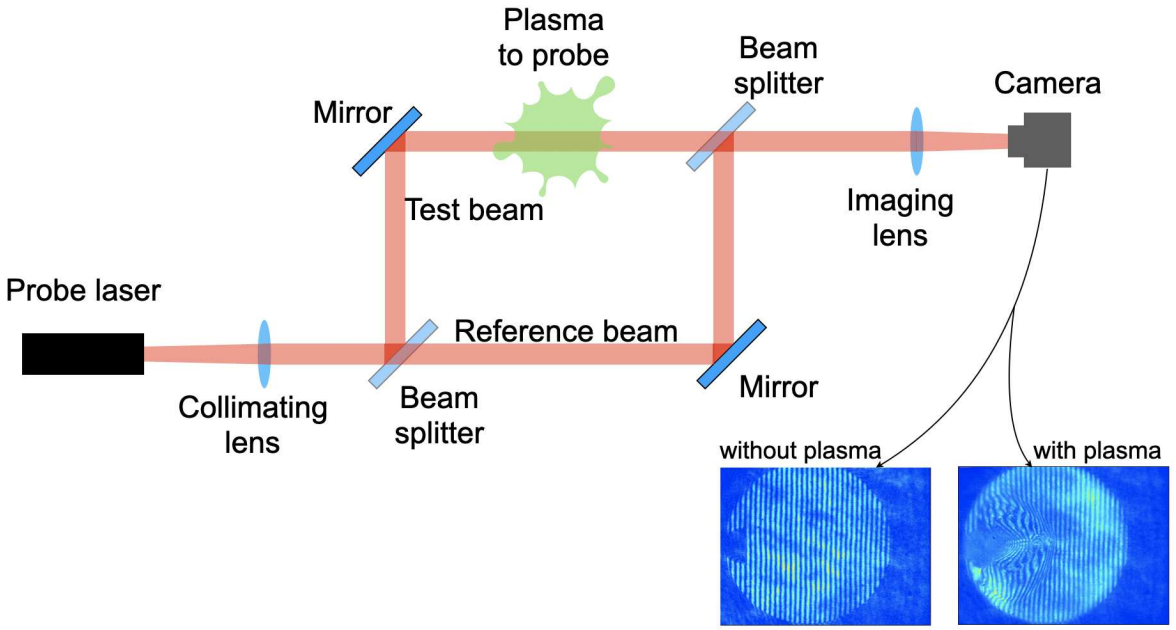

Figure 2.6: *Scheme of a Mach-Zehnder interferometry setup. We point out that, differently than what sketched here, the two beams must be not perfectly collimated after their recombination through the final beam splitter. Indeed, their orientation has to be adjusted in order to obtain exploitable interference fringes on the camera. Examples of interferometry images recorded by the camera are also shown: without any plasma, the fringes are straight and parallel to each other; in the presence of a plasma along one of the two beam paths, the fringes are distorted.*

medium, while the reference beam propagates unperturbed through a refractive index $N_0 = 1$. The phase of a wave traveling for a physical length L through a medium of refractive index N will change of a quantity

$$\Phi = \int_0^L \frac{\omega}{c} N \, dx \tag{2.1}$$

where ω is the wave frequency. The phase shift between the probing beam and the one propagating in vacuum is

$$\Delta\Phi = \int_0^L \frac{\omega}{c} (N - 1) \, dx \tag{2.2}$$

It follows from what seen in Sec. 1.1.1 that, in the case of plasma, the refractive index can be written as a function of the critical density n_c and of the electron density n_e. In particular, in the case of small electron density ($n_e \ll n_c$):

$$n = \sqrt{1 - \frac{n_e}{n_c}} \approx 1 - \frac{n_e}{2n_c} \tag{2.3}$$

which leads to a phase shift

$$\Delta\Phi \approx -\frac{\omega}{2\,c\,n_c} \int_0^L n_e \, dx \tag{2.4}$$

directly correlated to the integrated electron density found along the beam path.
The cases when $n_e(x)$ is a close to a simple 0-1-0 function (and hence when we can easily compute such an integral) are pretty rare and for sure not interesting. Most of the time, the plasma electron density changes along the probe beam, which makes it in general impossible to infer punctually the volumetric density. But when the system shows a cylindrical or spherical symmetry around an axis perpendicular to the probing direction, it is possible to extract a map the volumetric electron density. The map of $\Delta\Phi(y, z)$ and the assumed symmetry around an axis $\hat{t} = c_y\hat{y} + c_z\hat{z}$ can provide the missing information about what happens along the x-direction. This operation is done through the useful Abel transform (Bockasten 1961).
Having a magnetic field most of the time perpendicular to the optical probe and to the plasma expansion, we have been able to make little use of this trick, as the system was lacking symmetry.

In order to extract the phase shift out of the interferogram fringes, we have used the program Neutrino[1]. The phase unwrapping is made through the method of discrete wavelet transform (Heil and Walnut 1989; Berkner and Wells 1998), which uses as a base of the transform a family of functions (wavelets) built out of a Morlet wavelet function and corresponding to two parameters. The two main differences from the Fourier transform method are the fact that the wavelet coefficients depend on two parameters (instead of one) and the shape of the main wavelet function (which is not a plane wave): these allow for a better description and lower noise sensibility, but require a longer computational time (Berkner and Wells 1998).

2.2.2 Proton radiography

Proton radiography is a diagnostic aiming at mapping the electromagnetic fields of a region allowing for a certain spatial and temporal resolution (Kugland et al. 2012). It is based on the fact that protons are deflected by electromagnetic fields according to the Lorentz force $\mathbf{F} = e(\mathbf{v} \times \mathbf{B} + \mathbf{E})$ [SI].
The proton beam is generated through target normal sheath acceleration (TNSA) by a high-intensity ($I \sim 10^{18}$ W/cm^2) ps-laser focused on a thin metallic foil (in our case, 10 µm of Al). In this mechanism (Snavely et al. 2000; Wilks et al. 2001), the energy of the laser beam is deposited on the target and a part of it is transferred to hot electrons that escape from the back-side of the target. The resulting charge separation produces a strong electrostatic field that pulls back the electrons, which start oscillating at the target surface. Such oscillation takes place over a few Debye lengths and induces an electrostatic field that ionizes the atoms. Since the target bears surface contaminants, such as water,

[1] https://github.com/NeutrinoToolkit/Neutrino

the ions that are accelerated the most are the protons, as they are the lightest ones. Once they have left the target, protons follow ballistic trajectories with a $\sim 40°$ total full opening around the axis normal to the target surface (Cowan et al. 2004; Mancic et al. 2010). If they do not encounter any electromagnetic field, their trajectories are unperturbed straight lines, otherwise they are deflected according to the Lorentz force. Finally, a detector is set after their passage through the probed zone in order to image the map of their arrival. This detector normally consists in a series of RadioChromic Films (RCFs) (Bolton et al. 2014) alternated with Al filters. Protons with a certain energy distribution are naturally produced through TNSA (Karsch et al. 2003; Pfotenhauer et al. 2008), to which correspond different times of flight (between the source and the plasma) and hence different probing times. When these protons interact with the detector, their Bragg peak[2] is located at different "depths" (that is, on different RCFs of the stack). Thus, with one single shot, it is possible to probe the sample at different times, each registered on different RCFs of the stack.

For the distances and proton energies of our experiment, we typically had around 1.2 ns range of probing.

A representation of the principle of proton radiography is shown in Fig. 2.7, where the cases of unperturbed and deflected proton trajectories are sketched. The image observed on the films then indicates

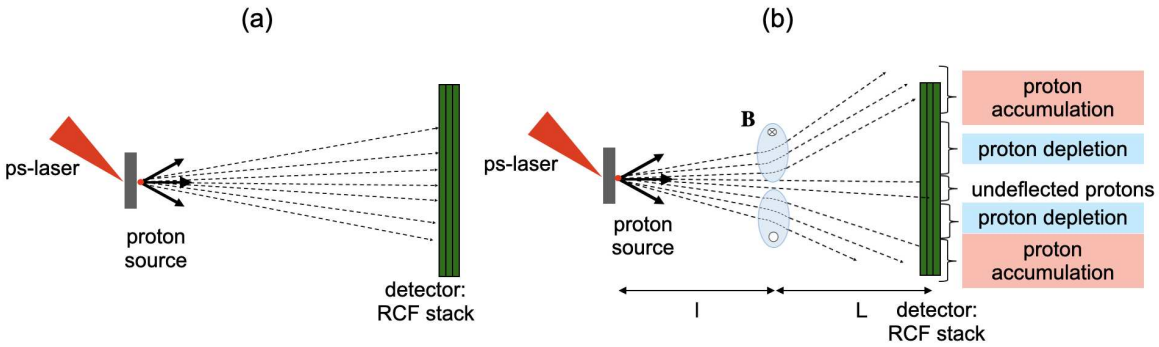

Figure 2.7: *Principle of the proton radiography. (a) Protons are created via TNSA thanks to a ps- high-intensity laser. They have straight trajectories in absence of external electromagnetic fields (and if the beam density is not too high). (b) When protons encounter a region with an electromagnetic field (in this example, a magnetic torus), they are deflected. With respect to the unperturbed case, on the detector there will be zones with higher proton concentration and zones with lower.*

the structure of the EM fields in the probed plasma, whose spatial features need to be scaled considering the magnification induced by the relative disposition of the proton source, the plasma, and the detector. By using the notation indicated in Fig. 2.7, where l and L are the distances between plasma and proton source and plasma and detector, respectively, the magnification on the films will be $M = (l + L)/l$. Thus, $1/M$ is the factor by which multiply the distances of the features imaged on

[2] i.e., the peak of energy released by the proton, which happens shortly before the are stopped (Bragg 1904).

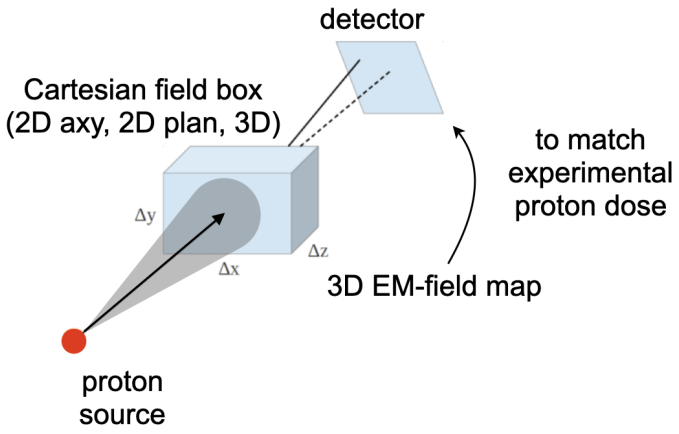

Figure 2.8: *Sketch of the ILZ principle: protons are launched on a 3D field map initialized by the user and then collected on a detector. The resulting simulated proton dose is compared to the one obtained experimentally on the RCF film corresponding to the same proton energy. The EM-field map is then changed in an iterative way and the simulation launched again.*

the RCFs to retrieve the typical distances in the plasma.

The synthetic proton radiography is then calculated through the use of a particle tracing code, ILZ (Bolanos et al. 2019), developed at LULI in the frame of previous PhDs. ILZ is a test-particle code that uses a 3D given distribution of electric and magnetic fields to simulate the trajectories of protons as they pass through the field region and then travel up to the detector, as schematized in Fig. 2.8. The working routine consists in: initializing the EM-field box $\longrightarrow$ launching the proton beam (with a certain specific energy) $\longrightarrow$ comparing the simulated proton dose on the ILZ detector with the experimental one $\longrightarrow$ adjusting the EM-field distribution to get the doses matching $\longrightarrow \ldots$
Normally, one is interested only in some features of the probed electromagnetic field, like its structure in a certain area. Then, it is common to compare not the entire 2D map of the proton dose, but only sections or single lineouts. In particular, this is what is done in our case: as we will see in Sec. 3.2.5, we considered the lineout of the proton dose collected across the shock front and tried to find via ILZ the right field that could recreate it.

Although very useful and relatively easy to set up in a laser-plasma experiments, proton radiography has some limitations (Arran et al. 2021; Graziani et al. 2017). The major one reposes on its principle: the deflection of the protons is due to the integration of the Lorenz force felt during their all trajectory in the plasma. This means that strong assumptions need to be done on the structure of both electric and magnetic fields.
Other limitations are encountered when the electromagnetic fields are too intense: this causes a strong proton deflection that makes it impossible to distinguish on the detector from where protons came as their trajectories cross. Hence, the condition of small deflections (i.e., laminar proton beam after

probing) is necessary if one wants to extract information on the fields.

2.2.3 Thomson scattering

Thomson scattering (TS) is the elastic scattering of light due to free electrons in the classical regime[3]. Indeed, an electromagnetic wave incident on a charged particle accelerates it via the Lorentz force. As the particle oscillates, it emits radiation, in turn, with the same periodicity as the incident wave. In general, scattering from ions can be neglected as they are more massive than electrons and scatter relatively little. (However, scattering from electrons associated with ion waves can be measured.)
By irradiating a plasma and collecting the (Thomson) scattered radiation, it is possible, under certain conditions, to infer information on the electron density and on the electron and ion temperatures.

Conditions on the probe beam

Let us first introduce two necessary conditions on the probe laser beam to be fulfilled before planning any measurement of TS.
On the one hand, the probe beam needs to be intense enough both in order to be able to detect the scattered light and in order to accelerate the same way the electrons along its path without being too strongly dimmed by the scattering. On the other hand, ideally it should not heat the plasma or anyhow modify its conditions. Hence, a compromise needs to be done.
The probe beam of course needs to be able to propagate through the plasma, which translate into a condition on its frequency depending on the plasma electron density n_e. That is: $\omega_i > \omega_{pe} = \sqrt{n_e e^2/m_e\varepsilon_0}$, as we saw in Sec. 1.1.1, which corresponds to $n_e < n_c$.

Collective or noncollective Thomson scattering

It essential to determine what kind of TS takes place depending on the plasma characteristics and the measurement conditions relative to our problem.
Let us consider a plasma volume V containing N free electron and N/Z ions of charge Ze. We consider an incident radiation with wavelength λ_i not too strong, so that the no particles are accelerated to relativistic speeds (hence, the contribution of the magnetic field on the charges can be neglected). The scattered radiation at a large distance R ($R \gg V^{1/3}$, λ_i) has a time-averaged power per unit solid

[3] i.e., if $h\nu \ll m_e c^2$. When this is not satisfied anymore, the emitted photons are so energetic that recoil on electrons must be taken into account, we will talk about Compton scattering. However, for mildly relativistic regimes, TS can still be employed if treated with relativistic corrections (Ross et al. 2010a).

angle (Froula et al. 2011a):

$$\frac{dP_s}{d\Omega} = \frac{cR^2}{4\pi}\left(\sum_{j=1}^{N}\mathbf{E}_{s,j}\sum_{l=1}^{N}\mathbf{E}_{s,l}\right) = \frac{cR^2}{8\pi}NE_s^2 + \frac{cR^2}{4\pi}N(N-1)\overline{(\mathbf{E}_{s,j}\cdot\mathbf{E}_{s,l})}_{j\neq l} \tag{2.5}$$

where the indexes j and l indicate the individual electrons, $\mathbf{E}_{s,m}$ is the corresponding scattered electric field, and $\mathbf{E}_s$ is the averaged scattered field by each electron (which is the same for all of them). The first term on the right side of Eq. 2.5 corresponds to the scattering due to N electrons free from the influence of the other ones. The second term depends on the interaction between the EM waves scattered by different electrons.

In order to understand the relative importance of these two contributions, let us introduce the parameter

$$\alpha \equiv \frac{1}{k\lambda_{De}} = \frac{1.07\times10^{-4}\,\lambda_i[\text{cm}]}{\sin(\theta/2)}\sqrt{\frac{n_e\,[\text{cm}^{-3}]}{T_e\,[\text{eV}]}} \tag{2.6}$$

where k is the module of the vector $\mathbf{k} = \mathbf{k}_s - \mathbf{k}_i$, $\mathbf{k}_i$ is the wave vector of the incident EM wave of wavelength λ_i ($k_i = 2\pi/\lambda_i$), $\mathbf{k}_s$ is the wave vector of the scattered light (with $|\mathbf{k}_s| \sim |\mathbf{k}_i|$, because we are considering elastic scattering in the classical regime), λ_{De} is the Debye length, n_e the electron density, T_e the electron temperature, and θ is the angle between $\mathbf{k}_i$ and $\mathbf{k}_s$.

When $\alpha \ll 1$, i.e., $\lambda_i \ll \lambda_{De}$, the wave interacts with the charged particles on a spatial scale over which they appear as free, since within the Debye length. The first term of Eq. 2.5 then dominates and we will talk in this case of *noncollective* (or *noncoherent*) scattering.

On the other hand, for $\alpha \geq 1$, that is, $\lambda \geq \lambda_{De}$, the incident wave interacts at the same time with electrons that represents the shield on each ion and electron. The second term of Eq. 2.5 will then be dominant. The resulting scattered light will depend on the collective behavior of groups of charges and will thus be called *collective* (or *coherent*).

In particular, one can safely assume to to be in a noncollective regime for $\alpha \lesssim 0.1$ (Froula et al. 2011a), while in case of $0.1 < \alpha < 1$, features of both regimes may be observed.

Before presenting the details of the two regimes, let us now show some elements valid for both. An incident beam of power P_i on a non-relativistic magnetized plasma will stimulate a scattered power P_s into a solid angle $d\Omega$ in the frequency range $[\omega_s,\, \omega_s + d\omega_s]$ (Froula et al. 2011a):

$$P_s\, d\Omega\, d\omega_s = \frac{P_i\, r_e^2\, L\, n_e}{2\pi} d\Omega d\omega_s \left(1 + \frac{2\omega}{\omega_s}\right) |\hat{k}_s \times (\hat{k}_s \times \hat{E}_{i0})|^2\, S(\mathbf{k},\omega) \tag{2.7}$$

where $r_e = e^2/(m_e c^2) = 2.82\times10^{-13}$ cm is the classical electron radius, L is the size of the TS volume in the direction of the probe beam, $\hat{k}_s$ and $\hat{E}_{i0}$ are the directions of the scattered wave vector and of the

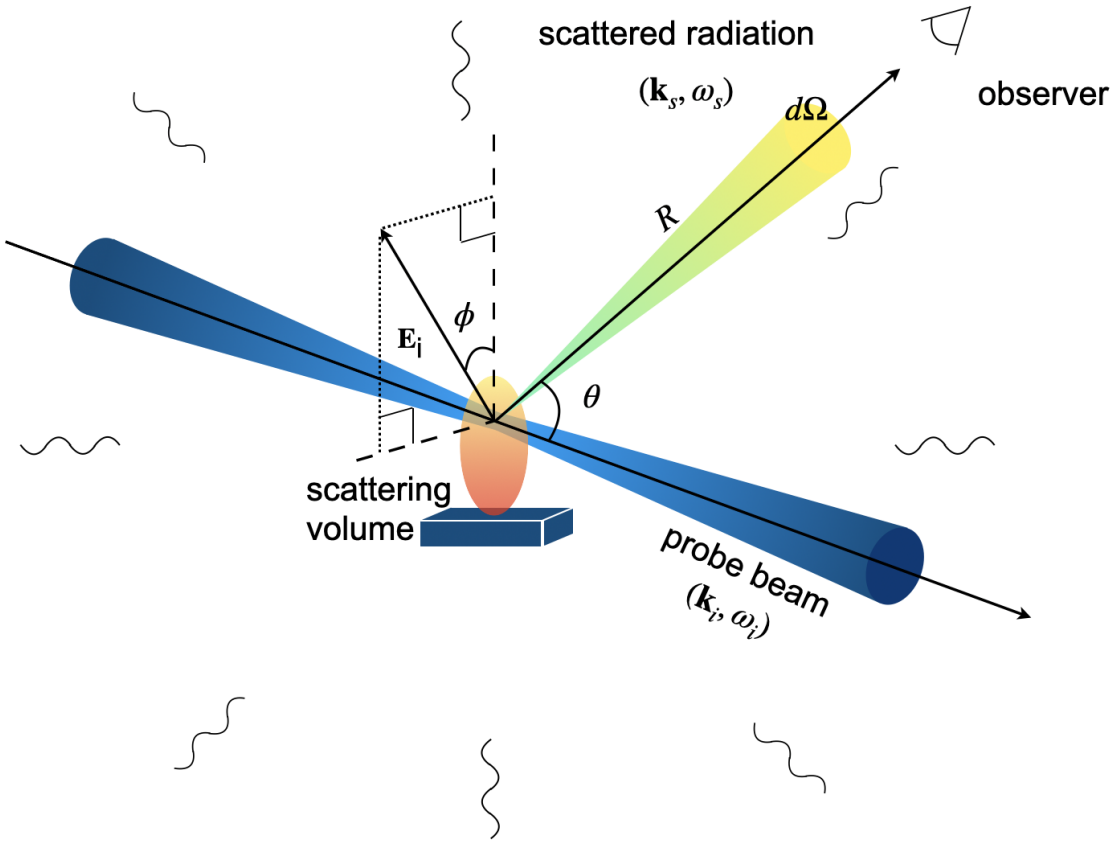

Figure 2.9: *Sketch of the Thomson scattering diagnostic setup.*

incident electric field polarization, and $S(\mathbf{k}, \omega)$ is the spectral density function. By using the scheme in Fig. 2.9, $|\hat{k}_s \times (\hat{k}_s \times \hat{E}_{i0})|^2 = 1 - \sin^2(\theta)\cos^2(\phi)$ (for polarized radiation).

Note that we have introduced the wavevector $\mathbf{k}$ and the frequency ω such that

$$\mathbf{k}_s = \mathbf{k}_i + \mathbf{k} \tag{2.8}$$

$$\omega_s = \omega_i + \omega \tag{2.9}$$

We will see that $\mathbf{k}$ and ω are linked to the plasma density fluctuations off which the incident beam interact.

As the shape of the spectral function is $S(\mathbf{k}, \omega)$ is very complicated in the general case, we will limit our discussion to the information of interest for the TS measurements of our experiments.

Noncollective Thomson scattering

The scattered wave from single electrons is Doppler shifted in frequency from the incident one by an amount ω, depending on the electron speed $\mathbf{v}_j$. The Doppler shift here is due to two effects. First, the

one due to the fact that the electron moves with respect to the source of radiation and hence feels the incident wave as Doppler-shifted by $\omega_i' = \omega_i - \mathbf{k}_i \cdot \mathbf{v}_j$. Second, the one due to the fact that the electron emits while having a velocity component in the direction of the observer.

These considerations lead to the following relationship between the scattered radiation as received by the observer (ω_s and $\mathbf{k}_s$) and the one of the incident light (ω_i and $\mathbf{k}_i$):

$$\omega_s = \omega_i + \mathbf{k} \cdot \mathbf{v}_j \quad \text{where} \quad \mathbf{k} = \mathbf{k}_s - \mathbf{k}_i \tag{2.10}$$

For a low-temperature plasma, it is reasonable to set $|k| \approx \text{constant} = 2|k_i| \sin(\theta/2)$.

The spectral function can then be written as

$$S(\mathbf{k}, \omega) = \int \int \int_{-\infty}^{+\infty} f(\mathbf{v})\, \delta[(\omega_s - \omega_i) - \mathbf{k} \cdot \mathbf{v}] dv_x\, dv_y\, dv_z \tag{2.11}$$

where the integration is made over the electron 3D velocity space.

Let us now restrict to the case with $2\omega \ll \omega_i$ and of a plasma in thermodynamic equilibrium, hence, with electrons characterized by a Maxwellian distribution function:

$$f(\mathbf{v}) = \frac{1}{(2\pi\, v_{th,e}^2)^{3/2}} \exp\left(- \frac{v_x^2 + v_y^2 + v_z^2}{2 v_{th,e}^2} \right) \tag{2.12}$$

where the mean velocity is $v_{th,e} = \sqrt{k_B\, T_e / m_e}$.

The resulting scattered spectrum will then be shifted with respect to the one of the incident beam by $\Delta\lambda = \lambda_s - \lambda_i$ (Froula et al. 2011a):

$$\frac{\Delta\lambda}{\lambda_i} = - \frac{14 v_{th,e}^2 \sin^2(\theta/2)}{c^2} \simeq -2.8 \times 10^{-5} \sin^2(\theta/2)\ T_e\,[eV] \tag{2.13}$$

In the case of externally applied magnetic field, the scattered spectrum will consist in a series of peaks with maximums following the spectrum of the nonmagnetized case. The frequency width of the peaks is $\sim k_\parallel v_{th,e}$ and their modulation is significant for

$$\frac{\Omega_e}{|k_\parallel v_{th,e}|} \geq 1 \tag{2.14}$$

In our case, such a quantity results of the order of 0.1, which confirms the fact that we do not observe this modulation in our spectra. Hence, we will not present further details about this case.

Collective Thomson scattering

In the case of collective regime, the scattering is due to the correlated motion of electrons. The major contribution to the scattered radiation comes from the plasma density fluctuations. Modeling the plasma as consisting of two fluids (electrons and ions), two kinds of charge density fluctuations occur naturally. These two plasma waves are the electron plasma wave (EPW, or Langmuir wave) and the ion acoustic wave (IAW), characterized respectively by high and low frequencies.

The EPW is a fast oscillation of the electron density and is characterized by frequencies:

$$\omega_{EPW} = \sqrt{\omega_{pe} + 3k_{EPW}^2 v_{th,e}^2} = \sqrt{\frac{n_e e^2}{m_e \varepsilon_0} + 3k_{EPW}\frac{k_B T_e}{m_e}} \tag{2.15}$$

The IAW is a longitudinal oscillation of ions and electrons and is characterized by frequencies:

$$\omega_{IAW} = k_{IAW}\sqrt{\frac{Zk_B T_e + 3k_B T_i}{m_i(1 + k_{IAW}^2 \lambda_{De}^2)}} \tag{2.16}$$

For $\alpha \gtrsim (ZT_e/3T_i - 1)^{-1/2}$, the "ion feature" becomes visible in the scattered spectrum as the IAWs are weakly dumped, while for $\alpha \lesssim (ZT_e/3T_i - 1)^{-1/2}$ the spectrum reveals the ion distribution function (Ross et al. 2010b).

Two examples of the scattered spectrum $S(\mathbf{k}, \omega)$ as a function of α are shown in Fig. 2.10.

In the collective regime, the shape of the scattered spectrum presents quasi-symmetric peaks around

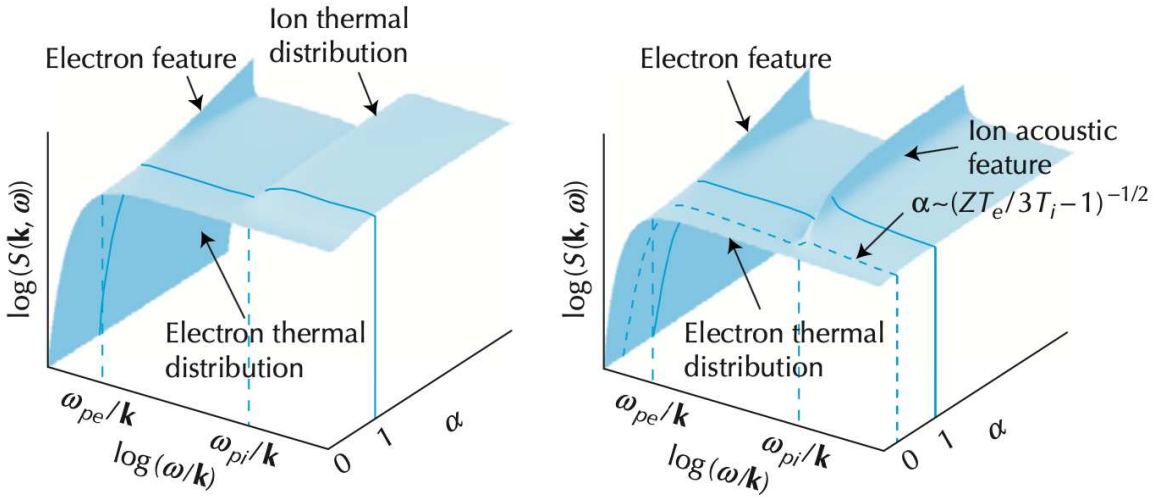

Figure 2.10: *Scattering spectral function dependence on α. Left side. $Z = 1$, $T_e/T_i = 0.1$: strongly dumped IAWs. Right side. $Z = 10$, $T_e/T_i = 10$: weakly dumped IAWs. (Image from Froula et al. (2011a).)*

the frequency of the probe beam, depending on the waves off which the radiation is resonantly scat-

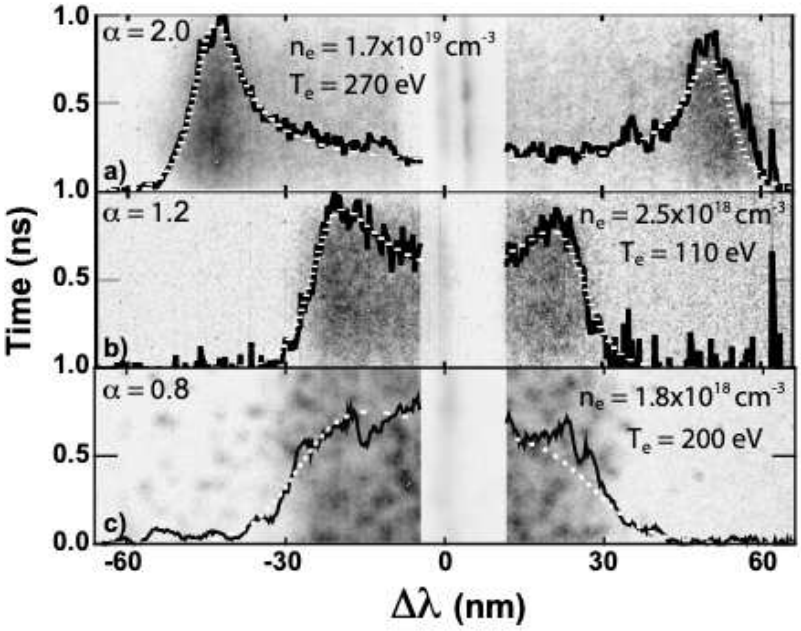

Figure 2.11: *TS spectra (black solid lines) collected with different plasma conditions and the relative simulated spectra (white dashed lines), as presented by Ross et al. (2010b). From top to bottom, the parameter α passes from 2, to 1.2, to 0.8, and the spectrum shows the transition from collective to noncollective regime.*

tered. If both EPWs and IAWs are present, two features will appear: the so-called electron and ion features.

An example of spectrum transition from noncollective to collective regime is shown in Fig. 2.11.

Scattering from high-frequency fluctuations: the "electron feature"

The scattering off the EPWs results in a spectrum with two peaks around the central probing wavelength. The distance between these two peaks is mostly sensitive to the electron density and weakly to the electron temperature. For a probing angle $\theta = 90°$ (which corresponds to our measurement conditions) the wavelength shift between the scattered feature is

$$\frac{\Delta\lambda_{EPW}}{\lambda_i} \simeq 2\sqrt{\frac{n_e}{n_{cr}} + 6\frac{v_{th,e}^2}{c^2}}\left(1 + \frac{3}{2}\frac{n_e}{n_{cr}}\right) \tag{2.17}$$

It is worth to point out that changing the electron temperature and density to best fit experimental data is a normally a solid procedure to reproduce a certain spectrum.

When relativistic effects need to be considered at least at the first order in v/c, the factor $1 + 2\omega/\omega_i$ must be left in the equation for the scattered spectrum. This leads to an asymmetry in the intensity of the peaks, like shown in Fig. 2.11.

Scattering from low-frequency fluctuations: the "ion feature"

The radiation scattered off IAWs presents two peaks around the central probing wavelength as well. Assuming that $\omega_i \gg \omega_{pe}$, the distance between the two peaks reads (Froula et al. 2011a):

$$\frac{\Delta\lambda_{IAW}}{\lambda_i} \simeq \frac{4}{c}\sin\left(\frac{\theta}{2}\right)\sqrt{\frac{k_B T_e}{m_i}\left(\frac{Z}{1+k_{IAW}^2\lambda_{De}^2}+\frac{3T_i}{T_e}\right)} \tag{2.18}$$

When various ion species are present in the plasma, multiple resonances are visible in the scattered spectrum, each of which depends only on ZT_e/T_i.

The electron features are characterized by a wider distance between the spectral peaks, hence are normally easier to identify in an experiment.

In order to measure electron and ion features, one needs optical spectrometers with very different wavelength ranges. Thus, when one wants to measure both at the same time, they split the Thomson scattered radiation coming from the interaction chamber into two beams: one sent to a spectrometer with low dispersive power to measure the electron feature, one sent to a high-dispersive power spectrometer for the ion feature. Then it is possible to send the dispersed light either to a streak camera (which will be our case), to obtain temporally resolved spectra, or to a charge-coupled device (CCD), to get spatially resolved spectra.

2.2.4 Magnetic proton spectrometer

Magnetic spectrometers are used for the measurement of the kinetic energy spectrum of certain charged particles, whose nature depends on the direction and on the strength of the magnetic field provided by the fixed magnets. The spectrometer is aligned with the axis along which the charges travels; they pass through a slit and a collimator so that when they enter the area with the magnetic field they all have their velocities perpendicular to the magnetic field lines. A particle of mass m and charge q receives an acceleration $\dot{\mathbf{v}}$ according to $\dot{\mathbf{v}} = q/m\,(\mathbf{v}\times\mathbf{B})$, hence, for particles of the same species the deflection depends only on their initial velocity.

The spectrometer we used had magnets of a length $a + b = 112$ mm proving a magnetic field of around 0.55 T, optimized for proton detection. The distribution of deflected protons was collected on an Imaging Plate (IP) (Mančić et al. 2008) set at a distance $a = 86$ mm from the beginning of the magnets, as drawn in Fig. 2.12.

By scanning the IP it is possible to see the dose of protons that reached a certain distance from the 0-order (i.e., the point on the IP aligned with the spectrometer entrance and the proton source, which

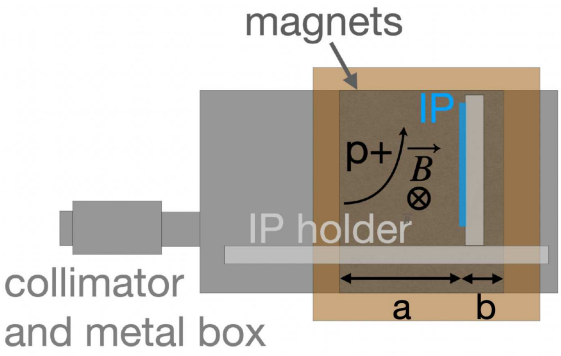

Figure 2.12: *Sketch of a magnetic spectrometer for protons. The magnetic field turns the trajectory of the protons that are initially entering through the collimator with aligned velocities perpendicular to the magnetic field. Their deflection depends on their initial kinetic energy. An Imaging Plate (IP) is set at a distance $a = 86$ mm from the beginning of the magnets to record the perpendicular proton displacement.*

corresponds to 0 deflection). The relation between such a distance and the kinetic energy could be computed if one knows all the parameters of the system with a certain accuracy. As this was not our case, we calibrated the proton spectrometer during an experimental campaign on LULI2000. For several shots, we applied on the IP different filters of known thickness and material and, hence, known proton stopping power. Thus, for each shot we linked a value of kinetic energy to a measure of distance from the 0-order, as only protons with energy higher than the filter stopping power could pass through and then be seen on the IP.

Finally, we fitted the series of such couples with the approximated function

$$\Delta y = \frac{q_e\, l_B}{\sqrt{2\, m_p\, E_k}} \left(\frac{l_B}{2} - b \right) B \tag{2.19}$$

where q_e, m_p, and E_k are the proton charge, mass, and kinetic energy, respectively, B is the strength on the magnetic field, $l_B\ (= a + b)$ is the length of the magnets, and b is the distance between the IP and the end of the magnets. Such an approximation is valid for the case of small proton deflections Δy with respect to the length of the magnet $l_B = a + b = 112$ mm, i.e. for protons of energies $E_k \gtrsim 100$ keV. We left as free parameters the magnetic field B and the distance between the IP and the end of the magnets b and, hence, obtained a calibration curve.

More details about this procedure are reported in the Appendix A.

2.2.5 Focusing Spectrometer with Spatial Resolution (FSSR)

A focusing spectrometer with spatial resolution (FSSR) consists of a bent crystal of spacing between planes suitable to diffract x-ray radiation (Faenov et al. 1994), as schematized in Fig. 2.13. Thanks to this diagnostic, it is possible to analyze the H-like (transition 2p–1s and its satellites) and He-like

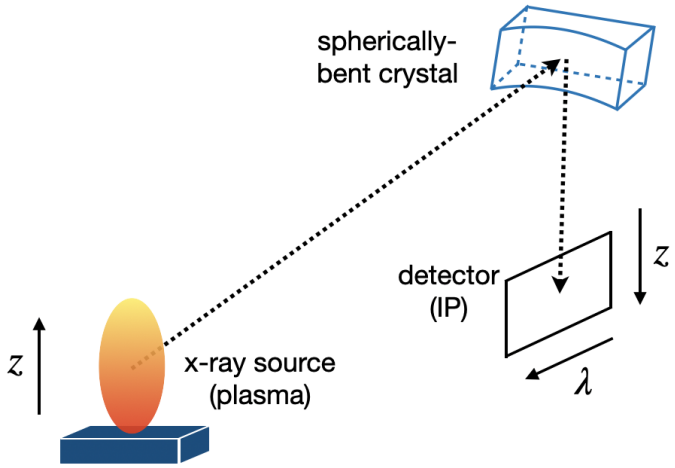

Figure 2.13: *Diagram of the FSSR principle: the x-rays due to the plasma recombination are diffracted by a spherically-bent crystal and detected by an imaging plate (IP).*

(transitions 3p–1s, 4p–1s, 5p–1s etc.) emission of Fluorine atoms (coming from our target in teflon, CF_2). The relative strength of these lines allows to estimate the electron density and temperature.
In detail, the FSSR we employed is made of a spherically bent mica crystal with a lattice spacing $2d = 19.9149$ Å and curvature radius of $R = 150$ mm. It can measure He-like and H-like lines of Fluorine in the range of wavelengths between 13 and 16 Å, with a spatial resolution about 0.1 mm and spectral resolution better than $\lambda/d\lambda = 1000$.
Such time-integrated spectra are recorded, shot by shot, on Fujifilm imaging plates (IPs) of type TR (Izumi et al. 2006). These are placed in a cassette holder protected from the visible optical radiation and located at a distance from the crystal equal to its curvature radius.

The analysis of x-ray spectra is done by comparison of the experimental line ratios with the simulated ones using the radiative-collisional code PrismSPECT (MacFarlane et al. 2003) and by comparison of emissivity profiles in different conditions.
We point out that, since this diagnostic is not time-resolved, the estimated values of electron density and temperature are weighted for times of higher emissivity, which, in turn, depends on both the plasma density and temperature.
A detailed presentation of this analysis technique is reported in Ryazantsev et al. (2015).

2.3 Plasma simulations

2.3.1 Introduction on plasma regimes

In this section we will present the numerical tools used to simulate the plasma. First, we will introduce the main physical features treated by different kinds of plasma codes. Then, we will present the codes employed for our simulations, i.e., SMILEI (Derouillat et al. 2018) and FLASH (Fryxell et al. 2000a).

The most complete description of the plasma dynamics consists in a full characterization of the particle and field state. As it is easy to imagine, when simulating real plasma systems, this approach is not realistically employable, as it would require a huge amount of memory and computational resources. Then it is natural to develop models that could describe the plasma with some approximations as long as the corresponding limitations are determined.

Plasma models (and hence plasma codes) can be categorized into two big families: the *kinetic* and the *fluid* descriptions. In a few words, the kinetic approach aims at describing the plasma conditions from the the knowledge of the microscopical interactions and motions of its constituents. On the other hand, fluid models target a macroscopical description of the system, for which the identity of individual particles is irrelevant and only the evolution of the statistical plasma parameters is considered. Various degrees of approximation reside within these two groups. Let us first explore the main features of them before discussing the codes used for our simulations.

2.3.2 Kinetic description and the PIC code Smilei

Klimontovich approach

In the *Klimontovich theory*, the full description of a plasma at a time t is given by the knowledge of the position $\mathbf{x}_i$ and the momentum $\mathbf{p}_i$ of each particle constituting the plasma. This consists in the study of the temporal evolution of the distribution function of N particles, defined as

$$f_N(t, \mathbf{x}_1, \mathbf{p}_1, \ldots, \mathbf{x}_N, \mathbf{p}_N) = \sum_{i=1}^{N} \delta[\mathbf{x} - \mathbf{x}_i(t)]\, \delta[\mathbf{p} - \mathbf{p}_i(t)] \tag{2.20}$$

where δ is the Dirac function and particles are hence modeled as point-like in space and momentum.

Vlasov approach

For real-size systems, such an exact description is computationally too demanding. This is why the *Vlasov approach* (Vlasov 1962) is commonly used to develop kinetic codes. It consists in replacing the function f_N by an ensemble averaged function $f_\alpha(t, \mathbf{x}, \mathbf{p})$, which represents the particle number density in the $(\mathbf{x}, \mathbf{p})$ 6D phase-space at a given time t for each species α constituting the plasma. This function is such

$$N_\alpha = \int f_\alpha(t, \mathbf{x}, \mathbf{p}) d\mathbf{x} d\mathbf{p}, \quad \text{where} \quad \sum_\alpha N_\alpha = N \tag{2.21}$$

The conservation of the number of particles for each species $\frac{dN_\alpha}{dt} = 0$ leads to imposing

$$\frac{df_\alpha}{dt} = 0 \implies \frac{\partial f_\alpha}{\partial t} + \mathbf{v} \cdot \nabla f_\alpha + \frac{d\mathbf{p}}{dt} \cdot \nabla_\mathbf{p} f_\alpha = 0 \tag{2.22}$$

where $\nabla = \frac{\partial}{\partial \mathbf{x}}$ and $\nabla_\mathbf{p} = \frac{\partial}{\partial \mathbf{p}}$. The term on the right side being 0 means that we do not have any gain or loss of particles of species α. The situation can be different when collisions or nuclear reactions are important; in that case and additional ad hoc term $(\frac{\partial f_\alpha}{\partial t})_C$ might be added.
In a classical plasma, $\dot{\mathbf{p}}$ is given by the Lorentz force

$$\mathbf{F} = q(\mathbf{E} + \mathbf{v} \times \mathbf{B}) \tag{2.23}$$

By substituting it in Eq. 2.22, we obtain the so-called *Vlasov equation*:

$$\frac{\partial f_\alpha}{\partial t} + \mathbf{v} \cdot \nabla f_\alpha + q_\alpha(\mathbf{E} + \mathbf{v} \times \mathbf{B}) \cdot \nabla_\mathbf{p} f_\alpha = 0 \tag{2.24}$$

In order to study the spatio-temporal evolution of the distribution function we need to couple the Vlasov equation with the Maxwell equations [SI]:

$$\nabla \cdot \mathbf{E} = \frac{\rho}{\varepsilon_0} \tag{2.25}$$

$$\nabla \cdot \mathbf{B} = 0 \tag{2.26}$$

$$\nabla \times \mathbf{E} = -\frac{\partial \mathbf{B}}{\partial t} \tag{2.27}$$

$$\nabla \times \mathbf{B} = \mu_0 \mathbf{J} + \frac{1}{c^2} \frac{\partial \mathbf{E}}{\partial t} \tag{2.28}$$

where ρ and $\mathbf{J}$ are the charge and current densities

$$\rho(t, \mathbf{x}) = \sum_{\alpha} q_\alpha n_\alpha(t, \mathbf{x}) \tag{2.29}$$

$$\mathbf{J}(t, \mathbf{x}) = \sum_{\alpha} q_\alpha n_\alpha(t, \mathbf{x}) \mathbf{u}_\alpha(t, \mathbf{x}) \tag{2.30}$$

The particle density n_α and the average velocity $\mathbf{u}_\alpha$ for the species α are two macroscopical quantities of the system obtained by the distribution function f_α:

$$n_\alpha(t, \mathbf{x}) = \int f_\alpha(t, \mathbf{x}, \mathbf{p}) d\mathbf{p} \tag{2.31}$$

$$\mathbf{u}_\alpha(t, \mathbf{x}) = \frac{1}{n_\alpha(t, \mathbf{x})} \int \mathbf{v} f_\alpha(t, \mathbf{x}, \mathbf{p}) d\mathbf{p} \tag{2.32}$$

The ensemble of Eqs. 2.24-2.28 constitutes the Vlasov system of equations. In Vlasov codes, one needs to solve, for each species α, a distribution function $f_\alpha(t, \mathbf{x}, \mathbf{p})$ depending on seven variables that need to be discretized. Even though some Vlasov codes are implemented with certain constrains (see, for instance, Vlasiator (Palmroth et al. 2013) and Impacta (Thomas et al. 2009), this approach is in most cases computationally too expensive and indeed much less adopted than the Particle-In-Cell.

Particle-In-Cell approach

Instead of using a distribution function f_α, Particle-In-Cell (PIC) codes employ "macro-particles", which are a "sample" of the complete distribution function (Pritchett 2003). The PIC method, indeed, owes its name to the discretization of the distribution function as a sum of N_α "macro-particles" (also called "super-particles" or "quasi-particles"), such that:

$$f_\alpha(t, \mathbf{x}, \mathbf{p}) = \sum_{p=1}^{N_\alpha} w_p \, S(\mathbf{x} - \mathbf{x}_p(t)) \, \delta(\mathbf{p} - \mathbf{p}_p(t)) \tag{2.33}$$

where $\mathbf{x}_p$ and $\mathbf{p}_p$ are the position and momentum of the macro-particle with index p, $S(\mathbf{x})$ is the shape-functions of all the macro-particles, and w_p is their weight, defined as:

$$w_p = \frac{n_\alpha(\mathbf{x}_p(t=0))}{N_\alpha(\mathbf{x}_p(t=0))} \tag{2.34}$$

The shape-function $S(\mathbf{x})$ describes how the δ particle charge is deposited on the simulation grid. The equations of motion of the macro-particle in the non-relativistic regime are simply:

$$\frac{d\mathbf{x}_p}{dt} = \mathbf{v}_p \tag{2.35}$$

$$\frac{d\mathbf{v}_p}{dt} = \frac{q_p}{m_p}(\mathbf{E}_p + \mathbf{v}_p \times \mathbf{B}_p) \tag{2.36}$$

where the electric and magnetic fields felt by the particles are

$$\mathbf{E}_p = \int S(\mathbf{x} - \mathbf{x}_p)\, \mathbf{E}(\mathbf{x})\, d\mathbf{x} \tag{2.37}$$

$$\mathbf{B}_p = \int S(\mathbf{x} - \mathbf{x}_p)\, \mathbf{B}(\mathbf{x})\, d\mathbf{x} \tag{2.38}$$

The PIC algorithm

Typically in a PIC simulation, the following steps are implemented (Derouillat et al. 2018; Grassi 2017). PIC simulations are initialized with the spatial profiles of the particle density n_α, the average velocity $\mathbf{u}_\alpha$, and the temperature T_α, for each species. In the so-called particle loading phase, a number N_α^{ppc} of macro-particles (as decided by the user) is created for each cell. Then the total charge $\rho(t = 0, \mathbf{x})$ and current $\mathbf{J}(t = 0, \mathbf{x})$ densities are projected on the grid. The resulting electric fields are computed by solving Poisson equation and the external electric and magnetic fields are added.
After this initialization phase ($t = 0$), the proper PIC loop starts. Each step of the loop consists in

1. interpolating the electric and magnetic fields at the quasi-particle positions
2. pushing the particles, i.e., computing the new particle positions and velocities
3. projecting the current and charge densities onto the grid
4. computing the new electromagnetic fields on the grid by solving Maxwell's equations

as schematized in Fig. 2.14.

The PIC code SMILEI

The PIC code SMILEI was developed to address kinetic simulations challenges in a way that could benefit from high-performance computing on massively parallel super-computers.

On the one hand, laser technology has improved so much over the last decades that intensities beyond 10^{22} W/cm^2 are at hand. This means that in laser-plasma interaction we need to take into account relativistic, highly nonlinear, and quantum effects. SMILEI contains ad hoc modules to treat the

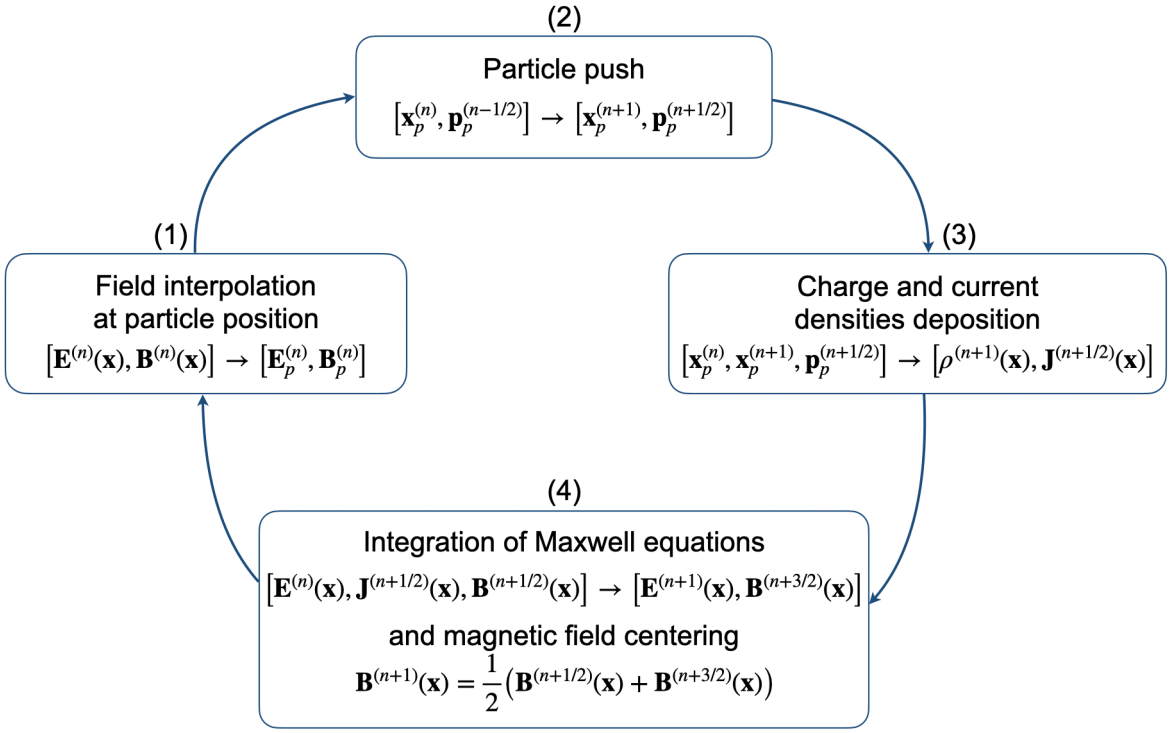

Figure 2.14: *Diagram of the typical PIC code loop: advancement from time-step* (n) *to* $(n+1)$.

difficulties encountered by other PIC codes when facing these extreme cases. The detailed discussion of these techniques can be found in Derouillat et al. (2018), in this manuscript we will limit to mention some of them. (1) For instance, SMILEI treats the grid-Cerenkov instability, which arises when dealing with ultra-relativistic particles. (2) The field ionization problem, which is not described in the standard PIC formulation, has a dedicated Monte-Carlo module in Smilei. (3) The issue of binary collisions also requires additional modules already partially developed in PIC codes; in SMILEI a few enhancements have been introduced: relativistic particles, low-temperature correction to the collision rate, and variable Coulomb logarithm.

On the other hand, the current in high-performance computing is towards an exponential increase of the number of cores available on parallel supercomputer, while the performance improvement of single microprocessors has been stagnating. Hence, SMILEI was born also with the aim to tackle this emerging complexity in an optimized way which could benefit from it.
Parallelization is commonly based on the decomposition of the simulation box in smaller domains, each one treated by a different processor. When macro-particles pass one domain to another one, information needs to be exchanged between processors. This operation is accomplished via two standard protocols: the Message Passing Interface (MPI) and the Open Multi-Processing (OpenMP) interface (Cai et al. 2003). Since the particles are carrying most of the computational work, a fixed

grid decomposition is inconvenient. It has been shown that a hybrid MPI-OpenMP parallelization enhances the code performance, hence SMILEI has implemented such a strategy. MPI processes deal with a first standard box decomposition; then, a further level of decomposition in smaller region (called "patches") is associated to the threads owned by the MPI processes. This decreases load imbalance, as the computational work of different patches can be easily shared among threads. Plus, on a higher level, neighboring MPI processes can exchange patches to dynamically optimize load unbalance.

Moreover, SMILEI's core program is written in the C++ language, while the input file that needs to be sent by the users is written in python. Indeed, on the one hand, C++ allows for an efficient and versatile way of structuring the code convenient for parallel computing. On the other hand, python is suitable for processing complex operations and supports thousands of supplementary packages advantageous for physical calculations.

2.3.3 Fluid description and the code FLASH

Derivation of the fluid equations

The fluid description of a plasma is derived by the calculation of the moments of the *Boltzmann equation*, which is the Vlasov equation (Eq. 2.22) with the additional collisional term $(\partial f_\alpha/\partial t)_C \equiv C_\alpha$ on the right side. This "manipulation" allows to retrieve fluid-like conservation laws, according to the degree of approximation chosen (multi-fluid, bi-fluid, and magnetohydrodynamic (MHD) descriptions).

Macroscopic physical quantities of the plasma can be retrieved from the distribution function f_α, as we have already seen for the particle density n_α (Eq. 2.31) and for the averaged velocity $\mathbf{u}_\alpha$ (Eq. 2.32). For each species α, we can consequently get

$$\rho_\alpha(t,\mathbf{x}) = m_\alpha n_\alpha(t,\mathbf{x}) \qquad \text{mass density} \tag{2.39}$$

$$Q_\alpha(t,\mathbf{x}) = q_\alpha n_\alpha(t,\mathbf{x}) \qquad \text{charge density} \tag{2.40}$$

$$\mathbf{J}_\alpha(t,\mathbf{x}) = Q_\alpha(t,\mathbf{x})\,\mathbf{u}_\alpha(t,\mathbf{x}) \qquad \text{current density} \tag{2.41}$$

where m_α and q_α are the mass and charge of the species α.

The mean internal thermal energy of the species α is defined (in the reference frame where the bulk

velocity of the plasma is zero) as

$$\rho_\alpha U_\alpha = \frac{m_\alpha n_\alpha}{2}\langle|\mathbf{v}'_\alpha|^2\rangle = \frac{m_\alpha}{2}\int f_\alpha(t,\mathbf{x},\mathbf{v})|\mathbf{v}'_\alpha(t,\mathbf{x})|^2 d\mathbf{v} = \frac{3}{2}\rho_\alpha v_{T\alpha}^2 = \frac{3}{2}n_\alpha k_B T_\alpha \tag{2.42}$$

$$\text{with} \quad v_{T\alpha}^2 = \frac{k_B T_\alpha}{m_\alpha} \tag{2.43}$$

where $\mathbf{v}'_\alpha = \mathbf{v}_\alpha - \mathbf{u}_\alpha$ is the relative velocity of the individual particles of the species α with respect to the bulk plasma, $v_{T\alpha}$ and T_α are the thermal speed and the temperature.

Now that we have calculated certain macroscopic quantities, let us pass to the integration of the Boltzmann equation to retrieve the conservation laws.

Via a 0-order integration over the 3D velocity space, we obtain the equation of *conservation of the mass* for each species[4]:

$$\frac{\partial \rho_\alpha}{\partial t} + \nabla\cdot(\rho_\alpha \mathbf{u}_\alpha) = 0 \tag{2.44}$$

From the moment of first order, i.e., from the integration of the Boltmann equation multiplied by $\mathbf{v}$, we obtain the equation of *conservation of momentum*:

$$\frac{\partial}{\partial t}(\rho_\alpha \mathbf{u}_\alpha) = Q_\alpha(\mathbf{E} + \mathbf{u}_\alpha \times \mathbf{B}) - \nabla\cdot(\overline{\mathbf{P}}_\alpha + \rho_\alpha \mathbf{u}_\alpha \mathbf{u}_\alpha) + \mathbf{R}_\alpha \tag{2.45}$$

where $\overline{\mathbf{P}}_\alpha$ is the pressure tensor defined as $P_{\alpha,jk} = \langle v'_{\alpha,j} v'_{\alpha,k}\rangle$ and $\mathbf{R}_\alpha = \int C_\alpha d\mathbf{v}$ is the average momentum exchanged per unity of time between particles of the species α and the ones of other species.

The moment of order 3, that is the integration of Boltzmann equation multiplied by $\mathbf{v}_\alpha^2$, gives the equation of *conservation of energy*:

$$\frac{dp_\alpha}{dt} - \gamma_\alpha \frac{p_\alpha}{\rho_\alpha}\frac{d\rho_\alpha}{dt} = (\gamma_\alpha - 1)\Big(- \nabla\cdot\mathbf{\Phi}_\alpha - \sum_j \sum_k \Pi_{\alpha,kj}\partial_k u_{\alpha,j} + H_\alpha\Big) \tag{2.46}$$

where $\mathbf{\Phi}_\alpha$ is the heat flux:

$$\mathbf{\Phi}_\alpha = \int f_\alpha \frac{m_\alpha \mathbf{v}'^2_\alpha}{2}\mathbf{v}'_\alpha \, d\mathbf{v} \tag{2.47}$$

H_α represents the rate of exchange of the energy density between particles of the species α and the others:

$$H_\alpha = \int C_\alpha \frac{m_\alpha \mathbf{u}_\alpha^2}{2} \, d\mathbf{v} \tag{2.48}$$

p_α and $\Pi_{\alpha,jk}$ are respectively the isotropic and anisotropic parts of the pressure tensor, such that:

$$P_{\alpha,jk} = p_\alpha \delta_{jk} + \Pi_{\alpha,jk} \tag{2.49}$$

[4]Under the assumption that collisions are elastic, i.e., there is no ionization etc., so that $\int C_\alpha d\mathbf{v} = 0$.

Standard fluid descriptions take up to the second order moment of the Boltzmann equation, hence, at this point we need to introduce a closure to the system, that is an approximation for the highest moment of the particle distribution equation. This is often done by imposing a condition on the heat flux through an assumption of adiabaticity or isothermality. This way, we can establish an equation of state, i.e., a relationship between pressure and density.

In the *adiabatic regime*, the heat is conducted on time-scales much larger than the typical scales of evolution of the system, thus:

$$\frac{dp_\alpha}{dt} - \gamma_\alpha \frac{p_\alpha}{\rho_\alpha}\frac{d\rho_\alpha}{dt} = 0 \quad \Longrightarrow \quad \frac{p_\alpha}{p_{\alpha 0}} = \left(\frac{\rho_\alpha}{\rho_{\alpha 0}}\right)^{\gamma_\alpha} \tag{2.50}$$

where the adiabatic index $\gamma_\alpha = (2+d)/d$ depends on the number d of degrees of freedom of the system.

At the opposite extreme, in the *isothermal regime*, heat conduction is much faster than other phenomena taking place in the plasma, hence:

$$p_\alpha = n_\alpha k_B T_\alpha \quad \Longrightarrow \quad \frac{p_\alpha}{p_{\alpha 0}} = \frac{\rho_\alpha}{\rho_{\alpha 0}} \tag{2.51}$$

Bi-fluid model

In a bi-fluid model, the plasma is considered as consisting of two species: N_e electrons and $N_i = N_e/Z$ ions. Then in Eqs. 2.44–2.46 α is substituted with either e or i and this system of six equations represents the bi-fluid model of such an ensemble of electrons and ions.

Under the circumstances where the plasma is collisionless, the distribution functions f_i and f_e are isotropic, the magnetic field effects are negligible, as well as the heat fluxes $\mathbf{\Phi}_i$ and $\mathbf{\Phi}_i$,

$$\Pi_{\alpha,jk} = 0, \qquad \mathbf{\Phi}_\alpha = 0, \qquad \mathbf{R}_\alpha = 0, \qquad H_\alpha = 0 \tag{2.52}$$

for both ions and electrons. Then, Eqs. 2.44–2.46 can be written in the simplified form:

$$\frac{\partial \rho_e}{\partial t} + \nabla\cdot(\rho_e \mathbf{u}_e) = 0, \quad \frac{dp_e}{dt} = \gamma_e \frac{p_e}{\rho_e}\frac{d\rho_e}{dt}, \quad \rho_e \frac{d\mathbf{u}_e}{dt} = Q_e\mathbf{E} - \nabla p_e \tag{2.53}$$

$$\frac{\partial \rho_i}{\partial t} + \nabla\cdot(\rho_i \mathbf{u}_i) = 0, \quad \frac{dp_i}{dt} = \gamma_i \frac{p_i}{\rho_i}\frac{d\rho_i}{dt}, \quad \rho_i \frac{d\mathbf{u}_i}{dt} = Q_i\mathbf{E} - \nabla p_i \tag{2.54}$$

Mono-fluid model

For several problems, it can be advantageous to study a plasma composed of several species α globally, as if it were a single fluid.

Out of the above defined quantities for a single species, we can calculate the corresponding ones characteristic for the mono-fluid:

$$\mathbf{u}(t,\mathbf{x}) = \frac{\sum_\alpha \rho_\alpha(t,\mathbf{x})\mathbf{u}_\alpha(t,\mathbf{x})}{\sum_\alpha \rho_\alpha(t,\mathbf{x})} \qquad \text{total plasma velocity} \tag{2.55}$$

$$n(t,\mathbf{x}) = \sum_\alpha n_\alpha(t,\mathbf{x}) \qquad \text{total particle density} \tag{2.56}$$

$$\rho(t,\mathbf{x}) = \sum_\alpha \rho_\alpha(t,\mathbf{x}) \qquad \text{total mass density} \tag{2.57}$$

$$Q(t,\mathbf{x}) = \sum_\alpha Q_\alpha(t,\mathbf{x}) \qquad \text{total charge density} \tag{2.58}$$

$$\mathbf{J}(t,\mathbf{x}) = \sum_\alpha \mathbf{J}_\alpha(t,\mathbf{x}) \qquad \text{total current density} \tag{2.59}$$

$$T(t,\mathbf{x}) = \frac{1}{n(t,\mathbf{x})}\sum_\alpha n_\alpha(t,\mathbf{x})\left(T_\alpha(t,\mathbf{x}) + \frac{m_\alpha(\mathbf{u}(t,\mathbf{x}) - \mathbf{u}_\alpha(t,\mathbf{x}))^2}{3\,k_B}\right) \qquad \text{global temperature} \tag{2.60}$$

By adding up the several equations derived by the moments of the Boltzmann equations for each species, we obtain for the mono-fluid:

$$\frac{\partial \rho}{\partial t} + \nabla\cdot(\rho\mathbf{u}) = 0 \tag{2.61}$$

$$\rho\frac{d\mathbf{u}}{dt} = Q\mathbf{E} - \nabla\cdot\overline{\mathbf{P}} + \mathbf{J}\times\mathbf{B} \tag{2.62}$$

$$\frac{dp}{dt} - \gamma\frac{p}{\rho}\frac{d\rho}{dt} = (\gamma-1)\Big(-\nabla\cdot\mathbf{\Phi} + \mathbf{E}'\cdot\mathbf{J}' - \sum_k\sum_j \Pi_{kj}\partial_k u_j\Big) \tag{2.63}$$

$$\frac{\partial Q}{\partial t} + \nabla\cdot\mathbf{J} = 0 \tag{2.64}$$

where $\mathbf{E}' = \mathbf{E} + \mathbf{u}\times\mathbf{B}$ and $\mathbf{J}' = \mathbf{J} + \mathbf{u}\times\mathbf{B}$ are the electric field and current in the reference frame moving at speed u with the mono-fluid.

In order to complete the system, we need to add a relationship between the electric field and currents. The so-called *generalized Ohm's law* expresses the electric field as a sum of terms:

$$\begin{aligned}\mathbf{E} = -\mathbf{u}\times\mathbf{B} + \frac{1}{n_e e}\mathbf{J}\times\mathbf{B} + \frac{\mathbf{J}}{\sigma} - \frac{1}{n_e e}\nabla\cdot\overline{\mathbf{P}} + \frac{m_e}{n_e e^2}\left(\frac{\partial\mathbf{J}}{\partial t} + \nabla\cdot(\mathbf{u}\mathbf{J} + \mathbf{J}\mathbf{u} - \frac{1}{n_e e}\mathbf{J}\mathbf{J})\right)\\ = \mathbf{E}_{ind} + \mathbf{E}_{hall} + \mathbf{E}_{ohm} + \mathbf{E}_{ther} + \mathbf{E}_{iner}\end{aligned} \tag{2.65}$$

where σ is the electrical conductivity, for which $\mathbf{J} = \sigma\mathbf{E}$. Here, we employ the classical expression, where σ is a scalar and not a tensor[5]: as we will see in the next section, this is the case in MHD.

In the context of MHD, such a generalized Ohm's law will be strongly simplified, as will be shown in

[5]For a more complete discussion on the electrical conductivity tensor in plasmas, refer, for instance, to Harutyunyan and Sedrakian (2016).

Eq. 2.76.

MHD model

The magnetohydrodynamic (MHD) theory models the plasma as a conducting, electrically neutral single fluid, consisting, at a microscopic level, of charges, but considered only macroscopically (Davidson 2002).
Let T, L, and V be the characteristic time, length, and velocity scales of the system, such that $V \sim L/T$; in MHD the following assumptions are made:

- Quasi neutrality of the plasma, which corresponds to the condition:

$$\frac{\omega_{ce}}{\omega_{pe}^2} \ll T \tag{2.66}$$

  where $\omega_{ce} = eB/m_e$ is the electron cyclotron frequency and $\omega_{pe} = \sqrt{e^2 n_e/\varepsilon_0 m_e}$ is the plasma frequency. Quasi neutrality means that the ratio between the total charge density Q and the charge density of a certain species – for instance, the electrons, Q_e – must be small: $|Q|/|Q_e| \ll 1$. We can rewrite: $|Q|/|Q_e| = |\varepsilon_0 \nabla \cdot \mathbf{E}|/en_e \sim \varepsilon_0 E/en_e L \sim \varepsilon_0 VB/en_e L \sim \omega_{ce}/\omega_{pe}^2 T \ll 1$.

- Non-relativistic velocities:

$$\frac{L}{T} \ll c \tag{2.67}$$

- Presence of collisions:

$$\lambda_{mfp,e}, \lambda_{mfp,i} \ll L, \qquad \tau_i \sqrt{\frac{m_i}{m_e}} \ll T \tag{2.68}$$

  where $\lambda_{mfp,\alpha}$ are the collisional mean free paths of electrons and ions and τ_i the characteristic collision time of the ions with the electrons.

- Magnetized electrons and ions:

$$\frac{r_{Li}}{L} \sim V \ll 1 \tag{2.69}$$

  where r_{Li} is the ion Larmor radius.

- (For ideal MHD) High magnetic Reynolds number:

$$Rm = \frac{\text{induction}}{\text{diffusion}} = \frac{\mu_0 VL}{\eta} \gg 1 \longleftrightarrow \frac{1}{\beta}\left(\frac{r_{Li}}{L}\right)^2 \frac{T}{\tau_i} \ll \sqrt{\frac{m_i}{m_e}} \tag{2.70}$$

  where $\beta = P_{therm}/P_{mag} = p/(B^2/2\mu_0)$ and $\eta = 1/\sigma\mu_0$ is the magnetic diffusivity

- (For resistive MHD) The electrical conductivity σ is a scalar and not a tensor, which is obtained by:

$$\omega_{ce} \gg \overline{\nu}_{ei} \tag{2.71}$$

where $\overline{\nu}_{ei}$ is the collision frequency of the electrons with the ions.

The evolution of a system in the frame of the MHD is governed by the following equations, where the terms in red (i.e., the ones where the electrical conductivity σ is present) are relative only to resistive MHD and are negligible for ideal MHD (Davidson 2002):

$$\frac{\partial \rho}{\partial t} + \nabla \cdot (\rho \mathbf{u}) = 0 \tag{2.72}$$

$$\rho \frac{d\mathbf{u}}{dt} = -\nabla p + \frac{1}{\mu_0}(\nabla \times \mathbf{B}) \times \mathbf{B} \tag{2.73}$$

$$\frac{dp}{dt} = -\gamma p \nabla \cdot \mathbf{u} + (\gamma - 1)\frac{|\nabla \times \mathbf{B}|^2}{\mu_0^2 \sigma} \tag{2.74}$$

$$\frac{\partial \mathbf{B}}{\partial t} = \nabla \times (\mathbf{u} \times \mathbf{B}) + \frac{\Delta \mathbf{B}}{\mu_0 \sigma} \tag{2.75}$$

$$\mathbf{E} = -\mathbf{u} \times \mathbf{B} + \frac{\nabla \times \mathbf{B}}{\mu_0 \sigma} \tag{2.76}$$

$$\mathbf{J} \simeq \frac{1}{\mu_0} \nabla \times \mathbf{B} \tag{2.77}$$

In spite of the many approximations that have been introduced, the MHD description is very powerful for complex systems and a good approximation even when not all the required conditions are precisely verified.
We point out that the fact that the plasma is described only by the first three moments of the Boltzmann equation does not imply that it needs to be Maxwellian or collisional.

The code FLASH

FLASH is a parallelized code for fluid plasma simulations developed by the FLASH Center of the University of Chicago (USA) (Fryxell et al. 2000b; Dubey et al. 2014). It allows for multi-dimensional hydrodynamic or MHD simulations on adaptive mesh refinement (AMR), or fixed grids, and it is mostly written in fortran90.
Originally designed for astrophysical simulations, FLASH has been extended to simulate laser energy deposition, high energy density (HED) experiments, and even some nuclear phenomena, making the code highly modular.
The material is treated as a three-temperature fluid, composed of electrons, ions, and radiation. Since

it is a hydrodynamic code, it does not follow the movements of the particles, as the PIC code SMILEI is able to.

Let us now quickly introduce two characteristics of the code FLASH we should be aware of.

The digital cells are spatially fixed and each quantity (mass, impulse,...) occupies entirely the cell. As during the system evolution the flux crosses the cell boundaries, diffusion is allowed. Such digital diffusion leads to an overestimation of the physical diffusion and of the particle speeds. This factor is crucial when studying shock evolution: if in reality a shock wave reaches a position such that it would barely "penetrate" the corresponding cell, in FLASH the shock will be present homogeneously in the entire cell, and will hence to able to reach the adjacent cell at the following time step. Hence, it is essential to find a balance for the cell size, as smaller cells would limit this effect but make the simulation heavier.

The laser radiation is treated through ray launching in the geometric optics approximation. The laser energy is deposited in cells with undercritical density through inverse Bremsstrahlung. When the beam meets a cell with overcritical density (like a solid target), FLASH "makes" it underdense and deposit its all residual energy there. Even though this modelization remains a good approximation, one needs to be aware of the fact that the energy release is much more abrupt than in reality and might be located at a wrong position.

In our case, the FLASH code has been used to simulate the overall system evolution in 3D. Indeed, the MHD "simplifications" and the modules for laser energy deposition allow us to include the laser-matter interaction initial phase and to simulate the evolution of the 3D system over a time period of the order of 10 ns.

Chapter 3

Generation of a collisionless supercritical magnetized shock

In our experimental campaigns performed at JLF/Titan and at LULI2000 we investigated shock formation combining laser-produced plasmas, a background medium, and a strong ambient magnetic field. In our setup, the expanding plasma and the magnetic field were decoupled as the higher Z piston evacuates the magnetic field and was thus unmagnetized, as will be detailed below. This allowed us to simultaneously have a highly magnetized ambient plasma (with homogeneous and steady magnetic field) and a high-β piston (as can be seen in Table 4.1, the plasma thermal β of the piston is $\beta \equiv P_{thermal}/P_{mag} \sim 14.0$). Moreover, thanks to our strong magnetic field of 20 T (Albertazzi et al. 2013), we were able to decouple more strongly the electrons from the ions (Yao et al. 2019) than in previous works (see for instance Schaeffer et al. (2017a), where their peak B-field is 8 ± 1 T), and the shock was able to fully separate from the piston, which is crucial for its characterization (Schaeffer et al. 2020). As a result, we have been able to characterize the plasma density, temperature, as well as the electric field developed at the shock front, and, more importantly, observe strong non-thermal accelerated proton populations for the first time.

In this chapter, we will first present the setup in Sec. 3.1 and show that mildly supercritical quasi-perpendicular magnetized collisionless shocks can be generated and characterized in the laboratory and detail their characteristics, in Sec. 3.2. Then, we will present the three-dimensional (3D) magnetohydrodynamic (MHD) simulations reproducing the laser-driven piston generation and the following shock formation process in Sec. 3.3.1. Afterwards, we will report on the results of kinetic particle-in-cell (PIC) simulations, which pinpoint that shock surfing acceleration (SSA) can be effective in energizing protons from the background plasma to hundred keV-level energies in Sec. 3.3.2.

Finally, we will discuss the astrophysical relevance of our laser-driven shock in Sec. 3.4 and draw the conclusions in Sec. 3.5.

3.1 Experimental setup and diagnostics

The experiments were performed at the JLF/Titan (LLNL, USA) and the LULI2000 (France) laser facilities with similar laser conditions but using complementary diagnostics, which was mostly linked with the availability of different auxiliary laser beams at each facility.

3.1.1 Laser and target conditions

In the experiment at JLF/Titan, we used a high-power laser pulse (1053 nm wavelength, 1 ns duration, 70 J energy, 1.6×10^{13} W/cm^2 intensity on target) to irradiate a solid target made of Teflon (CF_2). We used this material to exploit the x-ray emission from ionized F ions in the expanding piston plasma in order to diagnose, through x-ray spectroscopy, the properties of the laser-ablated plasma. Before the shot, a large volume hydrogen gas jet was pulsed from a nozzle, so that the whole scene was homogeneously (i.e., over larger scales than that where the system evolves) embedded in an H_2 gas of low density ($\sim 10^{18}$ cm^{-3}). The map of the volumetric plasma density is shown in Fig. 3.1, while the lineout of its profile centered on the symmetry axis is displayed in Fig. 3.2; moreover, in Fig. 3.3 is presented the FWHM of the Gaussian curve fitting the plasma density radial profile. We point out that these three graphs represent the hydrogen plasma electron density by extrapolation and are not direct measurements. Indeed, they have been obtained by performing interferometry on high pressure neutral argon and then multiplying the resulting density by $2\,p_{H_2}/p_{Ar}$, where the factor 2 is due to the fact that two electrons are released for each hydrogen atom in the plasma, p_{H_2} and p_{Ar} are the pressures of hydrogen (during our experiments at Titan and LULI2000) and argon (during such an experimental characterization of the nozzle), respectively.
Furthermore, the whole assembly was embedded in a strong magnetic field (20 T) oriented along the z-axis, which was generated by a Helmholtz coil system (Higginson et al. 2019; Albertazzi et al. 2013). The created magnetic field in our experiment is spatially uniform within 5% at the scale of shock acceleration (i.e., within 5 mm distance from the initial target surface) (Higginson et al. 2017) and typically varies by less than 1% from shot-to-shot (Albertazzi et al. 2013).

The experiment performed at LULI2000 had similar laser conditions: 1053 nm wavelength, 1 ns, 100 J, and we kept the same on-target intensity, i.e., 1.6×10^{13} W/cm^2, by adjusting the laser spot size on target. To accommodate the laser beams inside the narrow space within the magnetic field

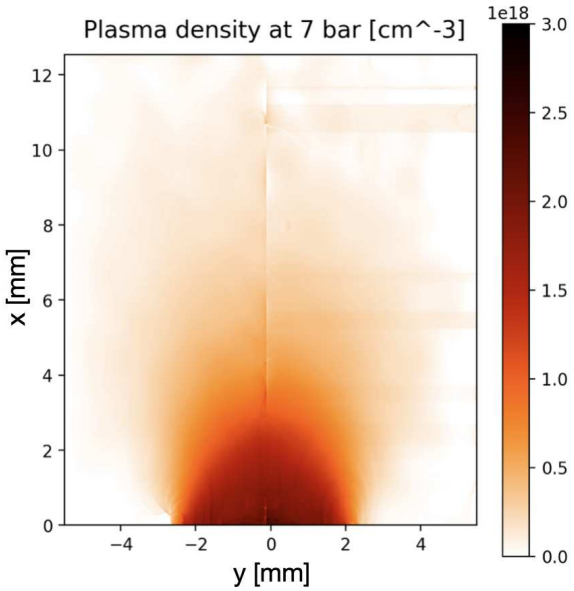

Figure 3.1: *2D map of the electron volumetric density of the hydrogen plasma, as extrapolated according to the procedure described in the text.*

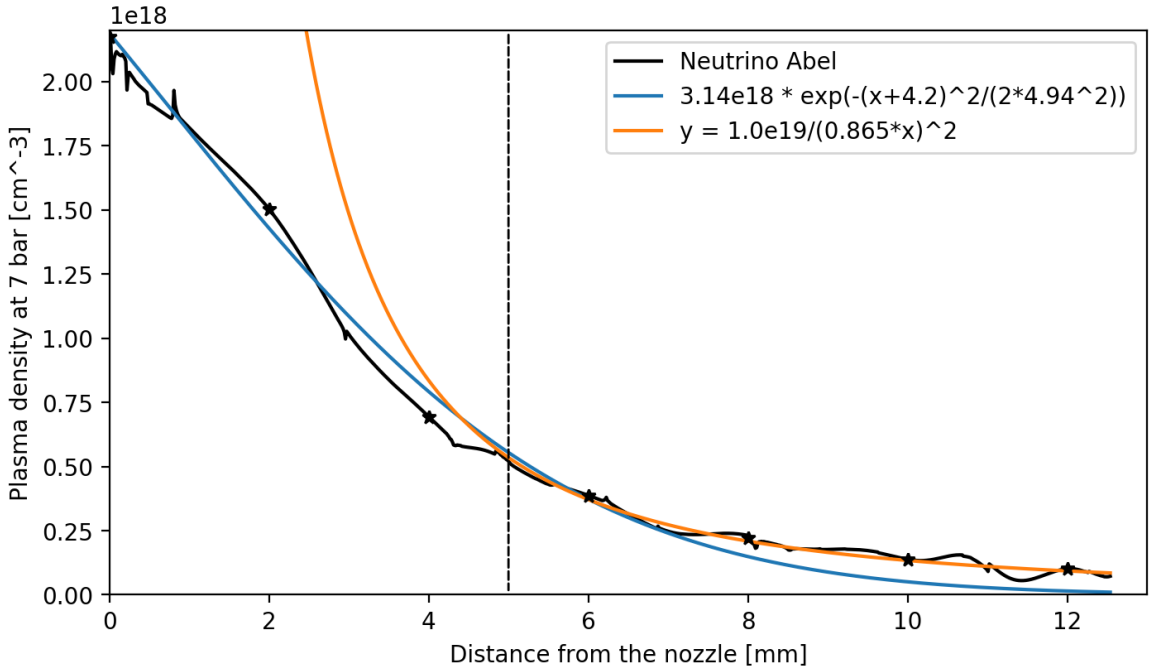

Figure 3.2: *Profile of the background plasma electron density along the axis of the gas nozzle (i.e., along the x-axis for $y = 0$ of Fig. 3.1). The experimentally retrieved black curve (Netrino Abel) is compared with the two (orange and blue) curves (whose expression is written in the legend).*

generation coil, the target had to be tilted by 45°around the z-axis and lifted up (along y). This led to the target surface to be outside the optical probing field of view of the probe beam, but allowed to see the similar development of the piston and shock wave as at JLF/Titan, and then to perform Thomson scattering (TS). The setup for the LULI2000 experiment is shown in Fig 3.4 (d).

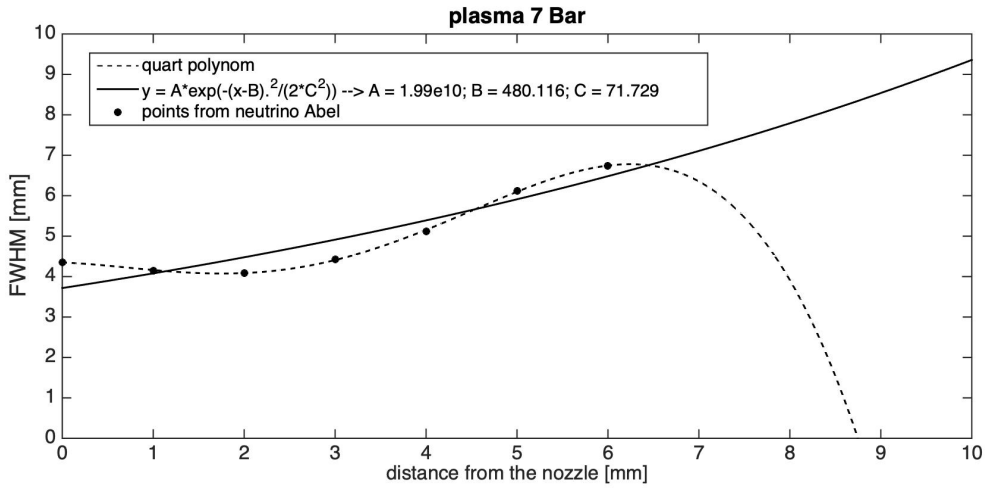

Figure 3.3: *FWHM of the Gaussian fit of the radial profile of plasma density at all heights.*

3.1.2 Optical probing

The plasma electron density was measured via interferometry by optically probing the plasma with a mJ, 1 ps auxiliary laser pulse, as detailed in Higginson et al. 2017. This allows to measure electron plasma densities in the range 10^{17} cm^{-3} to a few 10^{19} cm^{-3}, where the lower limit is given by the minimum fringe shift that can be detected and the upper limit is due to the refraction of the optical probe beam in the steep density gradients close to the initially solid target surface (where the plasma gets overcritical) (Harilal and Tillack 2004). The interferometry was set in the Mach-Zehnder configuration, as described in Sec. 2.2.1. Since the presence of the magnetic field along the z-axis breaks the symmetry of the system, we probed the plasma along two different axes (x and y), as shown in Fig. 3.4 (b) and (c). This allowed us to obtain the plasma density maps (integrated along the line of sight) in the xy- and xz-planes.

3.1.3 Proton probing

Moreover, we performed proton radiography in order to measure the local electromagnetic field at the shock. The probing protons were accelerated by the short-pulse beam of Titan (160 ± 30 J, 1053 nm, ~ 1 ps) through the Target Normal Sheath Acceleration (TNSA) process (Wilks et al. 1992) from an auxiliary target of aluminum set 60.67 mm away from the main target. They were sent parallel to the B-field, i.e., along the z-axis, as is shown in Fig. 3.4 (a). A stack of Radiochromic Film (RCF) (Chen et al. 2016) and filters was set 60 mm behind the shock, allowing to record proton radiographs of the system at different times (as explained in Sec. 2.2.2).

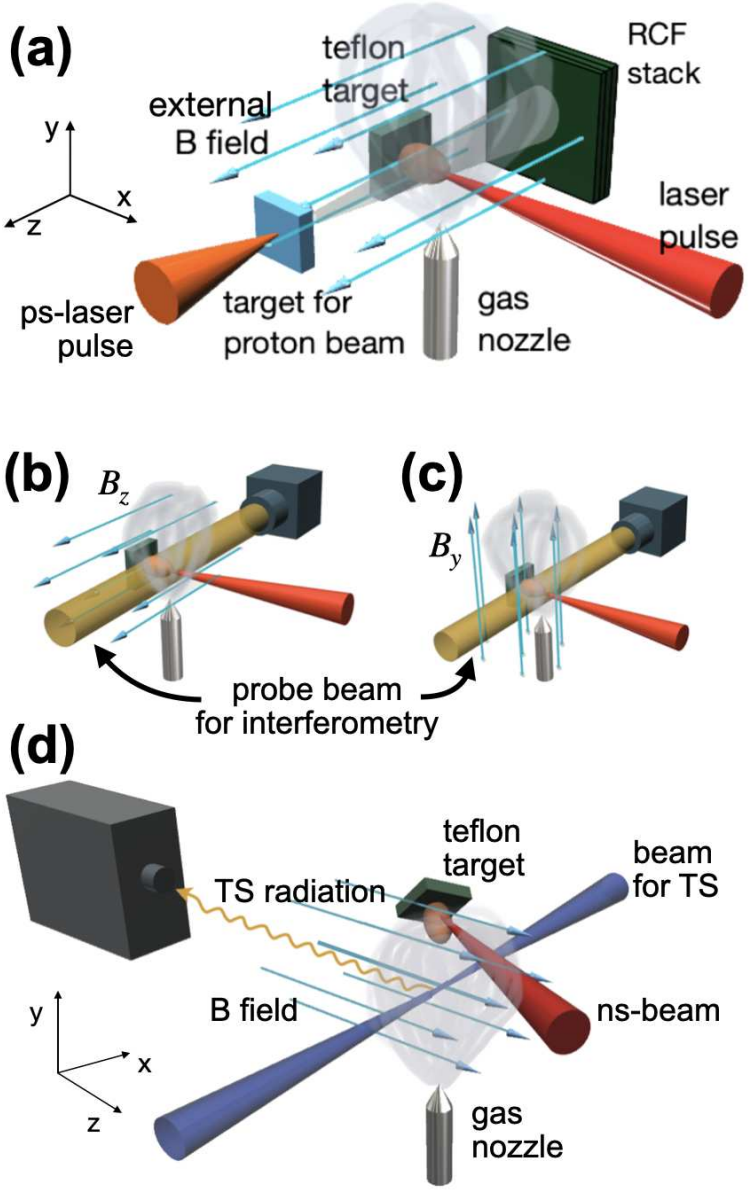

Figure 3.4: Experimental setup and diagnostics used to characterize a magnetized shock. *Proton radiography and interferometry diagnostics have been used alternatively along the axis perpendicular to the laser and to the plasma flow (i.e., the z-axis). (a) Proton radiography setup. (b-c) Interferometry setup; in this case, we could rotate the coil in order to have two different magnetic field orientations with respect to the field of view of the probe beam. (d) Thomson scattering (TS) setup at LULI2000.*

3.1.4 Thomson scattering diagnostic

At LULI2000, a second high-energy auxiliary laser (526.5 nm wavelength, 1 ns, 15 J, focused over ~ 40 μm along the z-axis and propagated throughout the plasma) was available, allowing us to perform Thomson scattering (TS) off the electron and ion waves in the plasma. TS was used in a mode where the plasma was sampled in a collective mode (Froula et al. 2011b), the collection of the scattered light being performed at 90°(along the y-axis) from the incident direction of the laser probe (the z-axis). With TS, we could access spatially and temporally resolved measurements of the plasma density and temperatures (electron and ion) in the upstream (US), as well as in the downstream (DS) region. The light scattered off the ion (TSi) and electron (TSe) waves in the plasma was analyzed by means of two different spectrometers, set to different dispersions (3.1 mm/nm for TSi and 7.5×10^{-2} mm/nm for TSe), and which were coupled to two streak-cameras (Hamamatsu for TSe, and TitanLabs for TSi, both equipped with S-20 photocathode to be sensitive in the visible part of the spectrum, and both with typical 30 ps temporal resolution), allowing us to analyze the evolution of the TS emission in time.

The central openings of both streak-cameras and spectrometers were imaging at the same location in the plasma (located 4.3 mm away from the solid target surface) within the magnetic field coil, in order to ensure that the value of the electron density obtained from the TSe analysis corresponds to the same region of the plasma that was observed in the corresponding TSi spectrum.

Thin strips of black filters were positioned at the entrance slits of both streak cameras to block the Rayleigh scattered light at the wavelength of the probing laser, for both TSi and TSe. The scattering volumes sampled by the instruments were: 120 μm along the x-axis, 120 μm along the y-axis 40 μm along the z-axis for TSi; 150 μm along the x-axis, 100 μm along the y-axis, 40 μm along the z-axis for TSe.

3.1.5 X-ray spectroscopy

The x-ray emission from the plasma was measured by a Focusing Spectrometer with high Spatial Resolution (FSSR) (Faenov et al. 1994) at both laser facilities. It was based on a spherically-bent mica crystal, with $2d = 19.9149$ Å and $R = 150$ mm, to detect H- and He-like spectral lines of fluorine ions (of the piston) in the range 750–1000 eV, as detailed in Sec. 2.2.5. The spectrometer was installed in the direction transverse to the plasma propagation, having a spatial resolution (~ 100 μm) over more than 10 mm along the plasma expansion axis. Fluorescent Fujifilm Imaging Plates (IPs) TR covered by an aluminized Mylar filter against emission in the visible range were used as a detector.

3.1.6 Ion spectrometry

Last, an ion spectrometer, having a permanent magnet of 0.5 T and equipped with a pinhole, was deployed along the axis of the magnetic field (the z-axis), 17.5 cm away from the target. It was employed in an alternate mode to the TS, as it would indeed be located in place of the collecting TS radiation diagram in Fig. 3.4 (d). The spectrometer has been calibrated precisely with a Hall probe and on many previous campaigns using filters to verify its energy dispersion. The ions were detected using absolutely calibrated IPs as detectors (Mančić et al. 2008). The fact that the spectrometer collection axis was aligned with that of the magnetic field allowed to measure the ions energized out of the plasma (Higginson et al. 2019), which otherwise could not be recorded, as they would be deflected away by the 20 T large-scale B-field. We used filters in order to eliminate the possibility that the signal observed in the dispersion plane of the spectrometer was originating from heavy ions others than protons from the ambient gas. The arrangement of the spectrometer is shown in Fig. 2.12; the protons are deflected by the magnetic field inside the spectrometer and land eventually on the IP.

3.2 Experimental results

3.2.1 Electron density measurements through interferometry

The integrated plasma electron density was obtained by optical probing the plasma at different times and with various configurations. For each shot, three different times could be probed by doubling and then splitting the probe beam into three beams ($1\omega P$, $1\omega S$, and 2ω), whose relative delay could be adjusted. 1ω and 2ω refers to the non-doubled and doubled beams, and P and S to the polarization. The analysis of the resulting interferograms was done by employing the program Neutrino, as described in Sec. 2.2.1.

Let us first consider the same time and vary the conditions imposed to the laser-driven plasma expanding from the target. In Fig. 3.5 is shown the overall electron density recorded 4 ns after the laser hits the target in three different cases: (a) and (b) with both external magnetic field B_z or B_y, respectively, and ambient H_2, (c) and (d) with only the magnetic field B_z or B_y, and (e) with only the background H_2. Moreover, (f) displays the lineouts of the integrated electron densities along the dark lines shown in the (a–d) images, allowing us to better compare them.

For the case with both ambient gas and B-field (shown in Fig. 3.6 (a) and (b)), the laser irradiation induced the expansion of a hot plasma (the piston) out of the target that propagates along the x-axis. The x-rays emitted by this plasma ionized the ambient hydrogen, creating this way a background low

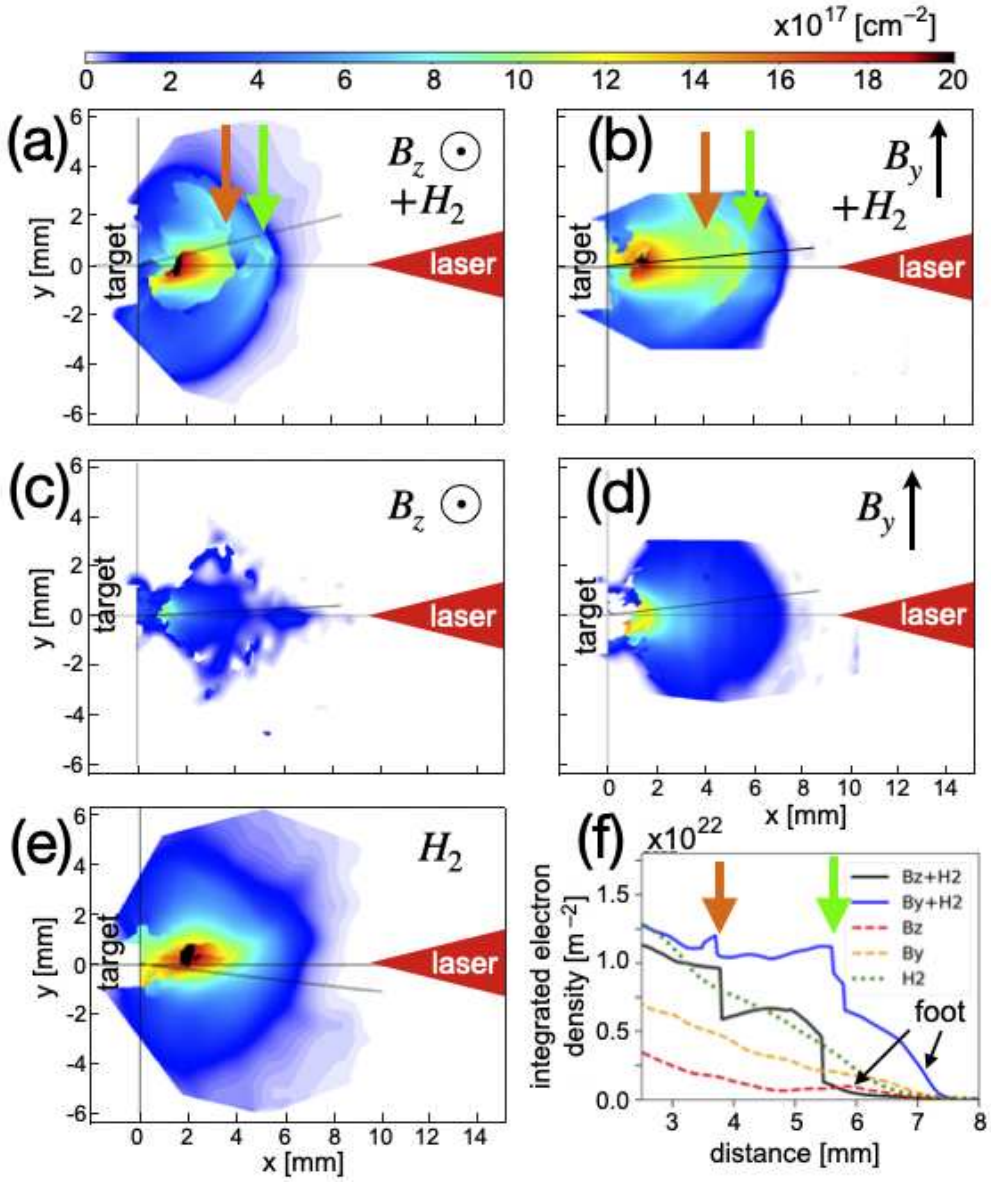

Figure 3.5: Integrated plasma electron density, as measured by optical probing at 4 ns after the laser irradiation of the target, in three different cases. *(a) and (b) Cases with both ambient gas and B-field in the xy- and xz-plane, respectively. (c) and (d) Cases with only B-field but without ambient gas (Khiar et al. 2019b; Filippov et al. 2020) in the xy- and xz-plane, respectively. (e) Cases with only ambient gas but without B-field in the xy-plane (the xz-plane will be the same). Each image corresponds to a different laser shot, while the color scale shown at the top applies to all images. The sharp edges on the top and bottom of (b) and (d) are regions blocked by the coil assembly. (f) The lineouts along the thin dark lines shown in each image. The laser comes from the right side and the piston source target is located at the left (at $x = 0$). Orange arrows indicate the piston front, while green arrows indicate the shock front.*

density hydrogen plasma. The collisionless shock is formed as a consequence of the piston propagating in the magnetized ambient plasma (Schaeffer et al. 2017a). We can clearly see both the piston front and the shock front (indicated by the orange and green arrows, respectively), and indeed they are well detached from each other, enabling us to characterize them separately.

As shown in Fig. 3.5 (f), the piston and shock fronts are also well identified by the abrupt density changes, where the piston front is steepened by the compression of the magnetic field (Khiar et al. 2019b). Besides, we can clearly see a "foot" structure ahead of the shock front in the upstream (US) region for the cases with both ambient gas and B-field, indicating the formation of the magnetized shock, as observed by satellites crossing the Earth's bow shock (Giagkiozis et al. 2017). It is due to the cyclic evolution of the plasma: the plasma in the foot is picked up to form the shock front, while the front itself is also periodically dismantled by the Larmor motion of the ions. The observed foot width is of the order 0.5-1 mm, which is comparable with the expected foot width being twice the ion inertial length (Baraka 2016) (which is here $d_i \approx 0.23$ mm), and with the width observed in our simulations shown below.
In contrast, for the case with only B-field but without ambient gas (Khiar et al. 2019b) shown in Fig. 3.5 (c) and (d), due to the lack of ambient gas, no collisionless shock was formed ahead of the piston. For the case with only ambient gas but without B-field in Fig. 3.5 (e), no shock was formed in the ambient gas, which was not dense enough to provide a suitable obstacle for shock formation. From the corresponding lineout in (f), it is clear that only a smooth plasma expansion into the ambient (the green dashed line) can then be seen.

Let us now focus on the case with both externally applied magnetic field and ambient gas and investigate the temporal evolution of the system. Fig. 3.6 shows the integrated electron density at different times. As a way of comparison, the case with only gas is also displayed in the first column. The second and third columns show the two views allowed by the interferometry setup on the case with both magnetic field and gas. Lastly, on the fourth column the lineouts of the various electron densities are shown. While the piston, the shock front, and the electron foot are well distinguishable during the first few ns, they become less clear at longer times, with the electron foot pretty disappeared after 6 ns, characteristic of a transition to the subcritical regime.

Out of this series of images, it is possible to retrieve the shock front position evolution and the corresponding velocity deduced from it, as summarized in Fig. 3.7. For the first few ns, the shock front velocity is around $v_{sh} = 1500$ km/s, corresponding to an ion-ion collisional mean-free-path $\lambda_{mfp} = v_{sh}\tau_i \approx 10$ mm, with the ion collisional time being $\tau_i \approx 6$ ns (Braginskii 1965). As both quantities are larger than the interaction spatial and temporal scales, the shock is collisionless. However, after 4-5 ns, the shock velocity decreases rapidly to about 500 km/s, thus becoming subcritical. Later we will demonstrate, with the help of kinetic simulations, that the proton acceleration happens within the first 2-3 ns of the shock evolution, i.e., when the shock is supercritical, with a front velocity above 1000 km/s.

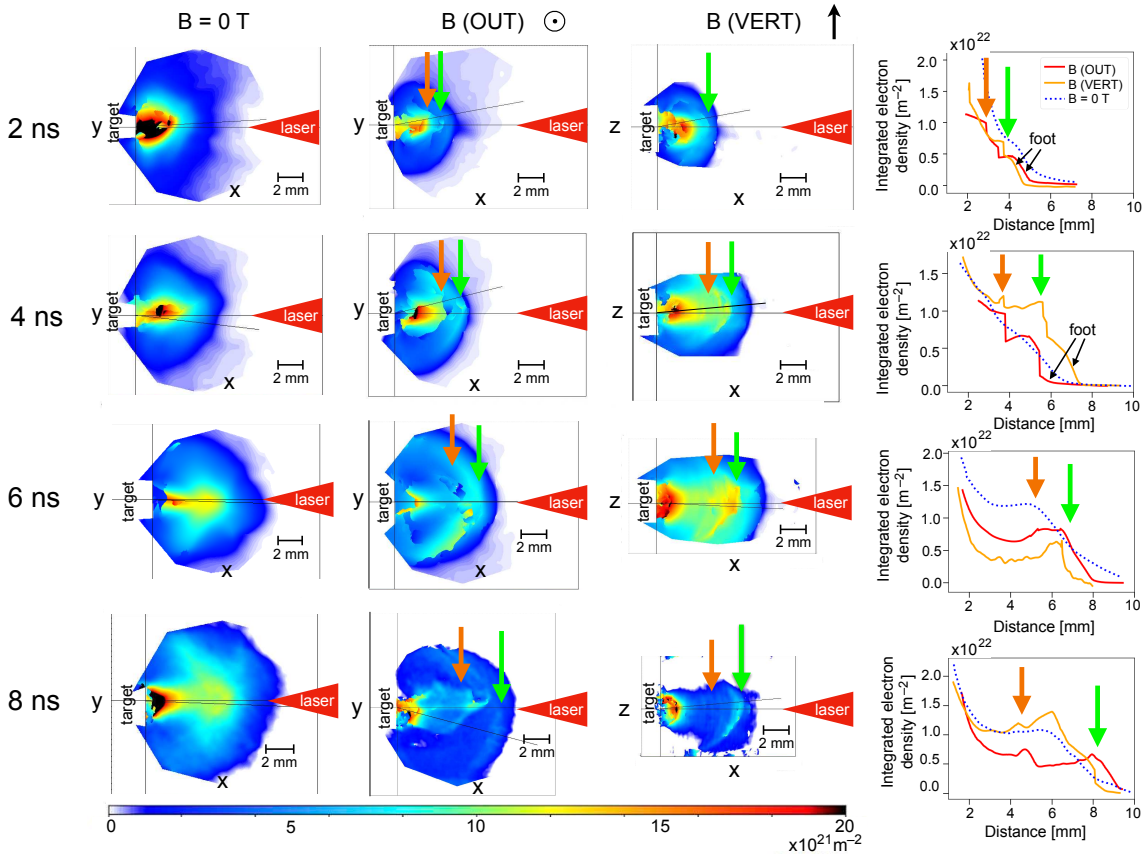

Figure 3.6: Time sequence of experimental density measurement *(integrated along the line of sight) recorded in the two different and complementary xy- and xz-planes in order to characterize in three-dimensions the overall plasma. Each image corresponds, generally, to a different laser shot. Specifically, the first column is for the case without the external magnetic field; the second and third column are for the case with the external magnetic field in the xy- and xz-plane, respectively. The color scale shown at the bottom applies to all images. The corresponding lineouts along the thin dark lines shown in each image are shown on the fourth column. From top to bottom, each row represents a different time, i.e., 2/4/6/8 ns. Magnetic field directions are indicated at the top of each column. Orange and green arrows indicate the piston and the shock front, respectively.*

3.2.2 Temperature and density characterization through Thomson scattering

The plasma temperature was measured at a fixed location (as indicated in Fig. 3.4 (d)) at different instants in time, allowing to characterize the temperature increase in the shock as it swept through the probed volume.

As detailed in Sec. 2.2.3, the analysis of the TS was performed by comparing the experimental images (recorded by the streak cameras) with the theoretical equation of the scattered spectrum for coherent TS in unmagnetized[1] and collisionless plasmas, with the instrumental function taken into an account.

[1] As seen in Sec. 2.2.3, the fact that $\Omega_{ce}/|k_{\parallel} v_{th,e}| \sim 0.1$ allows our to use an unmagnetized treatment of the TS radiation in our case.

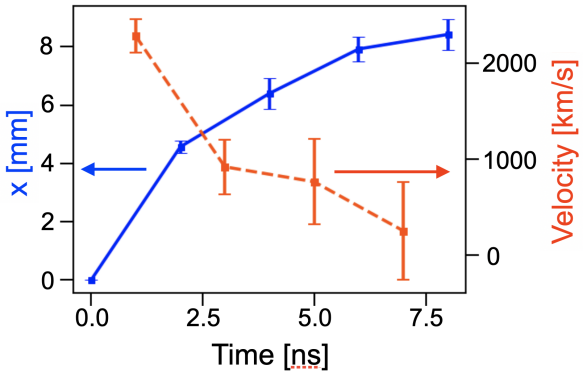

Figure 3.7: *Evolution of the shock front position along the x-axis, and the corresponding velocity. Each point corresponds to the average of the shock front of all relevant shots. The error bars on the x-position represent not only the maximum extent of the variation of the shock front position as observed in relevant shots, but they also integrate the uncertainty of the initial target surface ($x = 0$) as well as the width of the shock front. The error bars on the velocity correspond to the propagation of the errors on the position.*

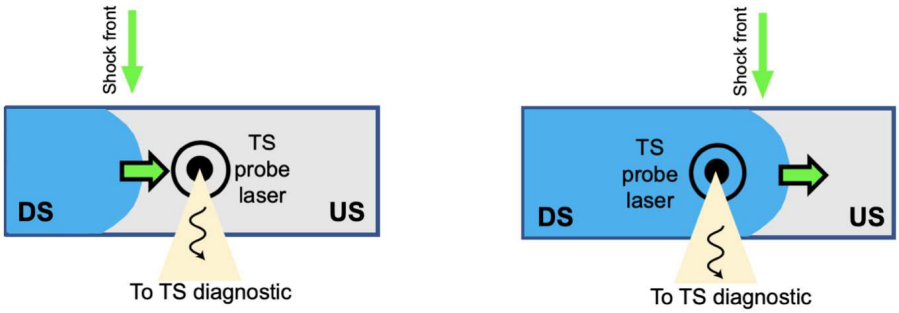

Figure 3.8: *Diagram of the region probed via Thomson scattering at different times: the upstream region (left figure) and the downstream region (right figure).*

Such an analysis allowed us to retrieve the electron density, as well as the electron and ion temperatures of the plasma in the probed volume (Froula et al. 2007, 2011b), corresponding – for different times – to the upstream (US) or the downstream (DS) region, as sketched in Fig. 3.8.

Note that the TS laser probe induces some heating in the hydrogen ambient gas. The electron temperature resulting from such heating through inverse Bremsstrahlung absorption can be analytically estimated. For this, we estimate the in-plasma intensity of the Thomson laser probe as 1.5 $\times 10^{13}$ W/cm^2, based on the fact that we see it being defocused to at least 200 μm diameter. The result is shown in Fig. 3.9 and suggests that the upper limit of the TS laser probe-induced heating is around 60 eV, that is consistent with the values we actually measure prior to the passing of the shock front in the observation location (see Fig. 3.11). Note that such value is also significantly smaller than the level of temperatures we observe induced by the shock.

Fig. 3.10 shows the TS measurements (corresponding to different shots) of electron and ion waves in the region downstream (DS) for cases with and without the external B-field. For the case without

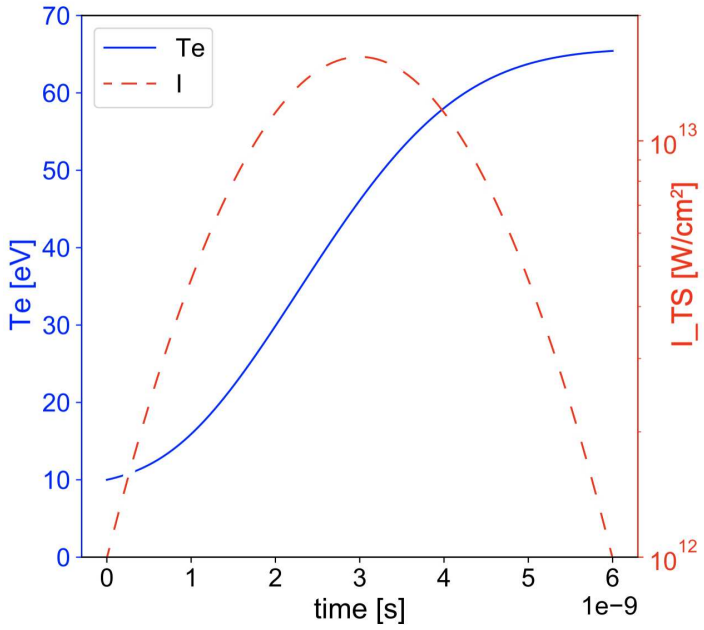

Figure 3.9: Temporal evolution of the electron temperature *obtained from the solution of* $1.5 n_e d_t T_e = \nu_B I_0 e^{-t^2/\tau^2}$. *Here,* $n_e = 1 \times 10^{18}$ *cm*$^{-3}$, ν_B *is the inverse Bremsstrahlung absorption coefficient from the NRL formulary (Book 1980). The laser energy is 15 J, with duration* $\tau = 3$ *ns, defocused focal spot* $d = 200$ *µm and wavelength* $\lambda = 526.5$ *nm, leading to an maximum intensity of* $I_0 = 1.5 \times 10^{13}$ *W/cm*^{2}, *and the initial electron temperature* $T_{e0} = 10$ *eV (left axis, blue full line). The intensity evolution of the laser* (I_{TS}) *is superimposed as a red dashed line (right axis).*

the B-field (i.e., with only ambient gas), both TSe and TSi give $n_e \sim 2.0 \times 10^{18}$ cm^{-3} and $T_e \sim 80$ eV, and TSi also gives $T_i \sim 50$ eV in the DS region, as can be seen in Fig. 3.10 (a) and (c). However, for the case with $B = 20$ T, we see strong heating in the DS region, indicated by the higher temperatures, i.e., $T_e \sim 230$ eV, and $T_i \sim 250$ eV, as can be seen in Fig. 3.10 (b) and (d).

Let us now focus on the case with both magnetic field and ambient gas and consider the overall temporal evolution of the electron and ion temperature in the probed zone. As shown in Fig. 3.11, before the shock front, the electron temperature T_e is around 70 eV (consistent with the heating induced by the Thomson scattering laser probe) and ion temperature T_i is about 20 eV. Behind the shock front, T_e is almost doubled, T_i is increased dramatically to about 200 eV, becoming larger than T_e. All of the above results are typical signs of a shock wave. Again, the formation of the shock is only possible due to the applied external magnetic field. In its absence, as shown in Fig. 3.10 (c), we witness no ion temperature increase in the same region.

3.2.3 Proton spectrum

In Fig. 3.12 is shown an example of the raw data acquired with the proton spectrometer. To verify that this signal was indeed due to protons, and not to a peculiar reflection of light that would occur

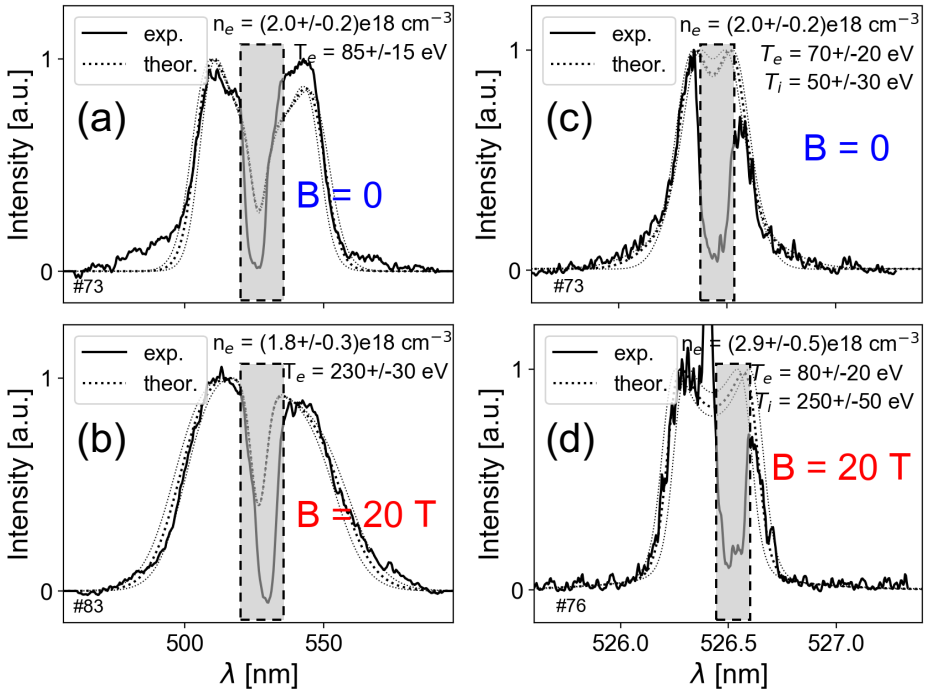

Figure 3.10: Thomson scattering measurements, of the plasma density and temperatures, in the region downstream of the shock front, and for different cases. *(a) measurement on the electron waves for $B = 0$ case (i.e., with only ambient gas), allowing to retrieve the local electron number density and electron temperature, as stated; (b) the same measurement for $B = 20$ T case (i.e., with external B-field and ambient gas). (c) measurement on the ion waves in the plasma for $B = 0$ case, allowing to retrieve the local electron and ion temperatures, as stated; (d) the same measurement for $B = 20$ T case. Solid lines are for experimental data profiles, while dashed lines are for theoretical spectra. The stated uncertainties in the retrieved plasma parameters represent the possible variation of the parameters of the theoretical fit (materialized by the thin dashed gray lines). Note that the deep central dip in the experimental spectra is related to a filter (a black aluminum stripe) which is positioned right before the entrance of the two streak cameras (recording respectively the light scattered off the electron and ion waves). This filter is used to block the very intense and unshifted laser wavelength (the Rayleigh-scattered light), which otherwise would saturate the cameras. Thus, no signal is recorded in this zone, which is materialized by the gray dashed box. The strong narrow peak at around 562.4 nm in panel (d) is caused by leakage of that strong light just at the edge of the filter. The position of the filter can change in the wavelength domain because the diagnostic can be realigned between shots.*

when both the ambient gas and the external B-field were ON, we tested applying a thin (transparent) plastic filter on half of the detector on a shot. We clearly see that no signal is observed through the filter (as expected since it stops protons having energy up to 1.8 MeV), as opposed to when the signal emerges out of the filter. Note that in Fig. 3.12, we have forced the contrast to the maximum in the zone covered by the filter to evidence that there is only noise in this zone. If we had used the same contrast as used in the zone exhibiting the signal, that zone covered by the filter would have been all black. This was how we provided an estimation for the noise level, as marked by dashed line in Fig. 3.13.

The recorded spectrum is shown in Fig. 3.13, with red dots and blue error bars (corresponding to one sigma deviation from the average of 5 shots). The cutoff energy reaches to about 80 keV, close to

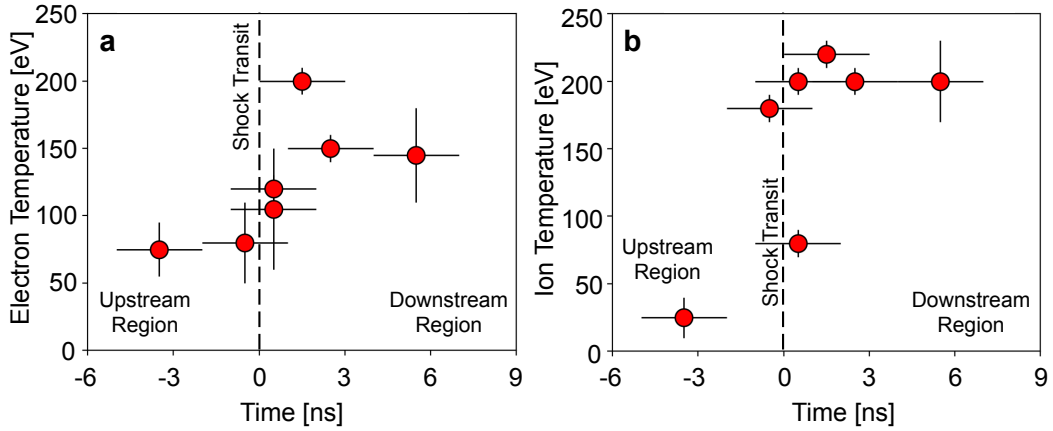

Figure 3.11: Laboratory characterization of electron and ion temperature increase in the shock. *The measurements are performed at LULI2000, using collective Thomson scattering (TS) on the electron and ion waves in the plasma, in a fixed volume 4.3 mm away from the solid target surface, and with $B = 20$ T applied. Time 0, at which a jump is identified, here corresponds to the time at which the shock is sweeping through the location of the measurement. Each data point corresponds to a shot. Panel (a) illustrates the local electron temperature inferred from both the measurements on the electron and ion waves. Panel (b) corresponds to the local ion temperature inferred from the measurement on the ion waves. The vertical error bars reflect the variations of the parameters when fitting the data with a theoretical fit, while still fitting well the data (see examples in Fig. 3.10). The horizontal bar reflects the duration (3 ns) of the laser beam used to perform the measurement.*

the Hillas limit (Hillas 1984; Drury 2012), an estimate of the maximum energy that can be gained in the acceleration region, which is around 100 keV with the velocity of 1500 km/s and the acceleration length around 3-4 mm in the first 2 ns, as shown in Fig. 3.5 (f). Without the external B-field or in the absence of ambient gas, no signal was recorded in the ion spectrometer above the experimental noise level, indicating that the non-thermal particle populations are indeed coming from the shock. We will pinpoint the underlying proton acceleration mechanism with dedicated Particle-in-Cell simulations in Sec. 3.3.2.

3.2.4 Time-integrated electron temperature and density via FSSR

The FSSR diagnostic allowed us to measure electron density and temperature profiles of the piston expansion using a quasi-stationary approach (Ryazantsev et al. 2015, 2016). The method is based on analysing the relative intensities of spectral lines of the same charge state and also takes into account the recombining plasma with a "frozen" ion charge. Fig. 3.14 summarizes the measures of electron density (a) and electron temperature (b) at different distances from the target surface and for different conditions.

We can see in Fig. 3.14 (a) that the piston encounters stronger hindrance in the case with both ambient gas (H_2) and B-field (B_z) (green diamonds), in comparison with other cases (i.e., the case with

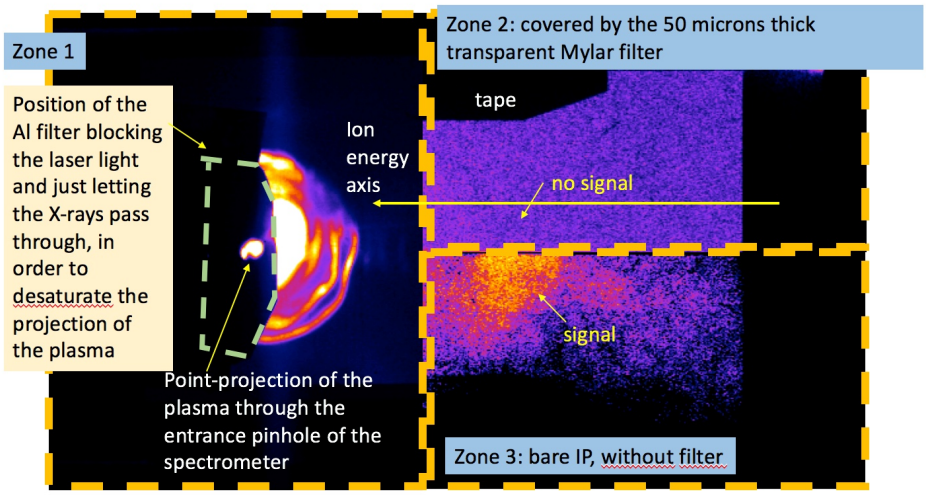

Figure 3.12: *Raw image of a scanned imaging plate (the detector used in the magnetic spectrometer), for an example shot with ambient gas and 20 T magnetic field. Here, we have on purpose treated (in contrast) in a different manner the three zones deliminated by the dashed orange rectangles, so that the signal in each zone can be seen optimally. In zone 1, which corresponds to the point-projection of the light emitted by the plasma, we can see the actual unsaturated image of the plasma through the entrance pinhole. This was unsaturated by having a filter positioned locally (deliminated by the green dashed line). The circular area around it corresponds to the opening of the coil, in which light is scattered and results also in a point-projection image. Outside of it, no light arrives on the detector, as can be observed. Then, on this shot, we have put also on the top half of the imaging plate (this is zone 2), a 50 microns thick, transparent to light, Mylar sheet. In this zone, the detector stays dark - what is shown is the very low level of noise of the detector when pushing the contrast of the image to the maximum. In Zone 3, there is however no such filter. This shows that this signal is not scattered light in the detector - otherwise it would appear through the clear filter- and is indeed due to protons - since protons are stopped in the filter up to 1.8 MeV.*

only B_z in red dots and the case with only H_2 in blue triangles). We also see in Fig. 3.14 (b) that the electron temperature in the case of B_z & H_2 becomes the highest at the piston front (between 4 and 7 mm), with respect to other cases. In addition, at the position of 4.5 mm, the evaluated electron density for the case of B_z & H_2 is around $2-3\times10^{18}$ cm^{-3} and the electron temperature is about 65 eV, which are well-reproduced by our FLASH simulations, as we will see in Sec. 3.3.1.

Similarly to the electron density data measured by optical interferometry, the x-ray spectrometer demonstrates the spatial compression of the piston when the magnetic field is applied, compared to the case of the non-magnetized ambient gas jet (see the Lyα emissivities in Fig. 3.15). The presence of He-like spectral lines of fluorine allowed us to measure the parameters of the piston. This is complementary to the Thomson scattering measurements, which characterize the shock in the hydrogen plasma.

The x-ray spectrum measured by the FSSR spectrometer is fully time-integrated, hence it deduces an average on-axis volumetric density over the few tens of ns when the plasma density and temperature are high, rather than the time-resolved and line-integrated density measured by optical interferome-

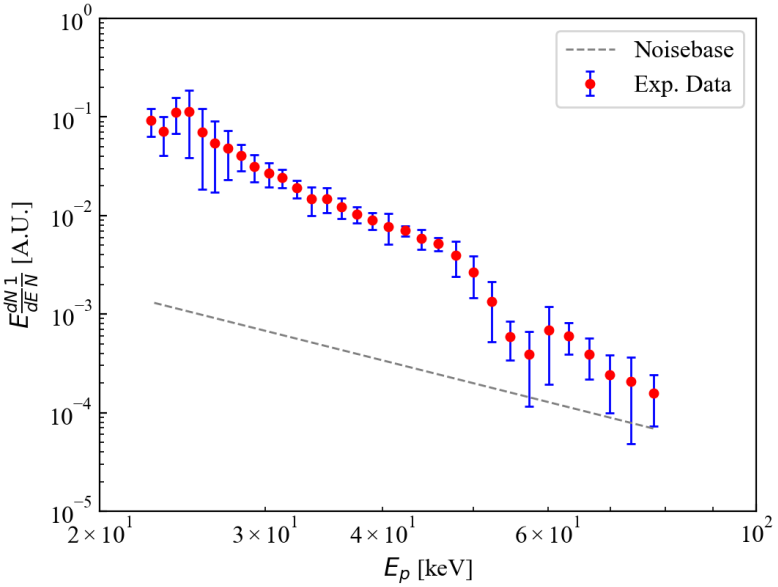

Figure 3.13: *Experimental proton spectrum (red dots) recorded with the proton spectrometer in the presence of both ambient gas and external magnetic field; the blue error bars correspond to one sigma deviation from the average of 5 shots. A noise baseline is also estimated.*

try. These two diagnostics provide complementary views of the piston.

Moreover, since the FSSR is time-integrated, we have a "blurring" effect in time. This is not so problematic since we register the most emissive part of the plasma, i.e., only when the plasma has high temperatures and densities, which is the case only over short time-scales, a few ns (Filippov et al. 2019). When the electron density drops, the plasma emissivity decreases non-linearly (Ryazantsev et al. 2015) and contributes negligibly to the total spectrum.

3.2.5 Electric field through proton radiography

In the presence of both an external magnetic field and an ambient gas, we could clearly observe the same structures of the piston front and the shock front, as shown for different times in Fig. 3.16, consistent with those observed via optical probe (see Fig. 3.5). In particular, when the radiograph is clear enough, we can see that at the shock front we have proton dose accumulation, depletion, and further accumulation (like in Fig. 3.16 (c)).

In order to infer the electromagnetic field felt by the probing protons, the particle tracing code ILZ (Bolanos et al. 2019) was used. As detailed in Sec. 2.2.2, ILZ receives as an input the parameters relative to the test particles and to the 3D map of electric and magnetic fields and simulates the particle trajectory up to the 2D detector set behind the interaction zone.

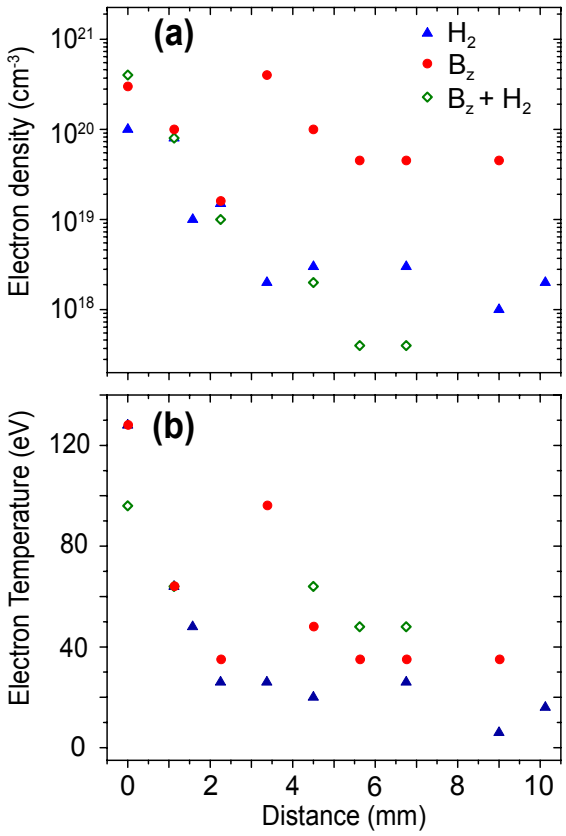

Figure 3.14: FSSR evaluation of (a) electron density and (b) electron temperature of the laser-produced piston in three different configurations (see legend) along the expansion axis. *The measurements are based on the analysis detailed in Filippov et al. (2019) of the relative intensities of the x-ray emission lines of He-like and H-like (see text) of Fluorine ions in the expanding plasma in the range of 13-16 Å. The quasi-stationary (Ryazantsev et al. 2015) approach was applied for He-like series of spectral lines assuming a "frozen" ion charge state. The 0 point corresponds to the target surface. A spatial resolution of about 100 µm was achieved. The signal is time-integrated.*

For small deflections, such a proton structure consisting in accumulation - depletion - accumulation is the sign of a bipolar electric field (see Romagnani et al. (2008a)). Hence, we used as an input for the tracing code an electric field E_x with a bipolar spatial profile along the x-axis with a hemispheric geometry in the xz-plane (where z is the axis along which the proton beam propagates) in order to mock up the experimentally observed curvature of the shock front. The same dependence on the coordinates x and z is reproduced along y over a small thickness. The electric field has only a component along x given by:

$$E_x(x,z) = \sqrt{2e}E_0 \frac{x - g(z)}{L} e^{-\frac{(x-g(z))^2}{L^2}} \tag{3.1}$$

where E_0 is the maximum field amplitude and L represents the width of the region affected by the electric field. $g(z) = -R/2 + \sqrt{R^2 - z^2}$ represents the shift of E_x along x in order to take into account

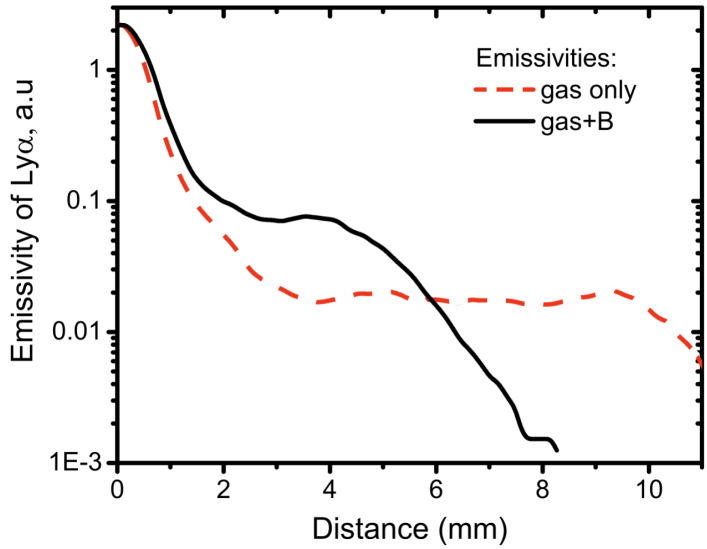

Figure 3.15: X-ray emissivity of Lyα line measured by the FSSR. *The red dashed curve represents the piston plasma emission in the range 0-10 mm in the case when the unmagnetized piston expands in the ambient gas. The black full curve represents the same but when additionally the transverse external magnetic field was applied.*

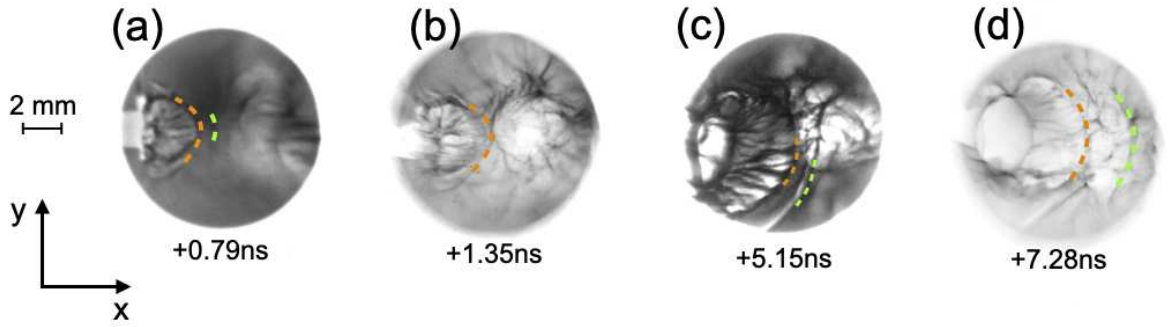

Figure 3.16: *Images of proton radiography doses at different times, relative to shots taken in the presence of both magnetic field and ambient gas. Dashed lines indicate, when visible, the piston front (in orange) and the shock front (in green).*

the hemispherical geometry in the xz-plane and derives directly from the equation of a circumference of radius R centered in $(-R/2, 0)$: $(x + R/2)^2 + z^2 = R^2$. Let us consider a time when we have obtained a clear radiograph, like $t = 5$ ns after the laser impact (as in Fig. 3.17). Then the hemispherical structure has a radius of $R = 5.1$ mm, as estimated from the experimental proton radiography relative at that time, in Fig. 3.17 (a).

We adjust E_0 and L of the ILZ input in order to match the simulated proton dose with the experimental one. The comparison between these two is shown in Fig. 3.17 (c), where the ILZ simulated modulation was obtained with the field in Eq. 3.1 with $E_0 = 4.33$ MV/m and $L = 0.12$ mm and shown in Fig. 3.17 (b).

Note that the protons are sent along the external magnetic field (i.e., in the z-direction), while the

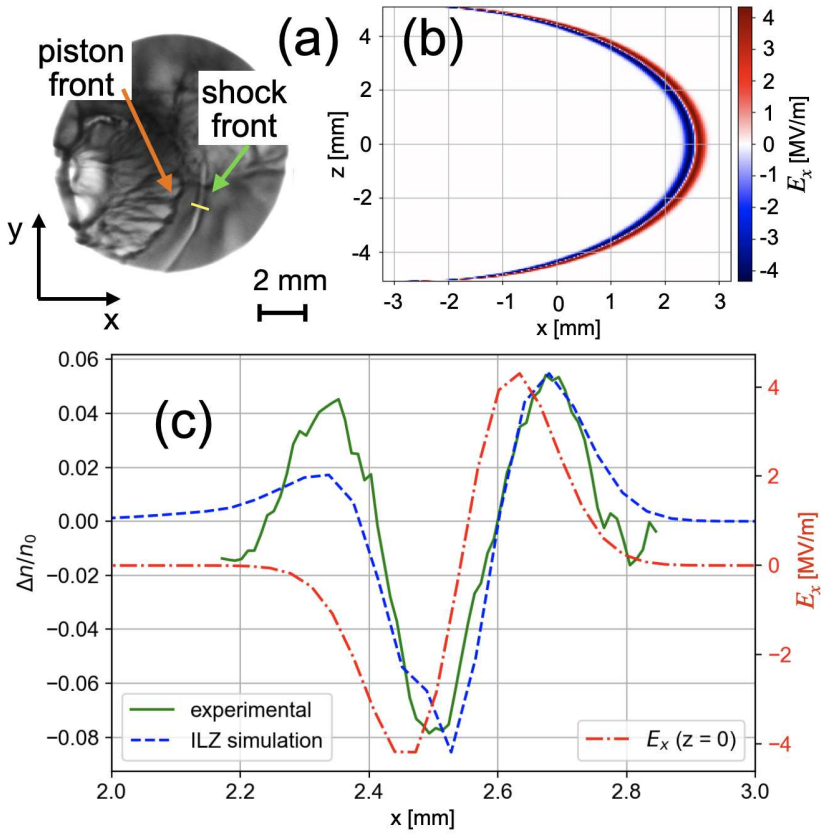

Figure 3.17: Proton radiography *obtained with the setup shown in Fig. 1, 5 ns after the laser pulse.* (a) *Raw dose collected on the RCF film corresponding to 19 MeV protons.* (b) *Hemispherical electric field* E_x *in the* xz*-plane, with a radius of* $R = 5.1$ *mm, estimated from* (a)*.* (c) *Lineout of the proton dose modulation along the yellow line indicated in* (a)*. The green full curve is the modulation from the experimental results, and the dashed blue curve is that from the ILZ simulation, which is obtained by imposing a bipolar electric field with hemispherical shape shown in* (b)*. The red dash-dotted curve represents the lineout of the field* E_x *in* $z = 0$*.*

other magnetic field components are orders of magnitude lower than the externally applied one, as shown by the PIC simulations (see Sec. 3.3.2). More importantly, B_x and B_y do no show any specific structure at the shock front, but are just fluctuating. Hence, we consider the net effect of these magnetic field components to be much smaller than that induced by the E_x electric field associated with the shock front. As a result, we interpret the proton dose modulation to be caused by the electric field only. This assumption is also supported by the fact that it yields a simulated proton deflection that is very consistent with the one recorded in the experiment, as can be seen in Fig. 3.17 (c).
The amplitude of the electric field at the shock front inferred from the synthetic proton radiography is of the order of MV/m. We will compare it with the particle-in-cell simulation results and discuss them in detail in Sec. 3.3.2.

Moreover, we compared the position of the shock structures seen in the electron density (via interferometry) with that in the electric field (via proton radiography) for the case with both external

B-field and ambient gas. For the former, we have considered the point where the electron density had a sharp jump, as shown in Fig. 3.5 (f); as for the latter, we have taken into account the external edges of the proton dose accumulation. As is shown in Fig. 3.18, the evolution of the piston front and the shock front through both diagnostics are illustrated together, and they clearly show, in both diagnostics, the slowing down of the piston and shock fronts over the first few ns after the laser pulse. Note that when the target was not clearly visible in the radiography, i.e., for the series of points around 5 ns, we made use of the interferometry results to shift all the points of the right amount, while the distances between the piston and the shock fronts were kept constant.

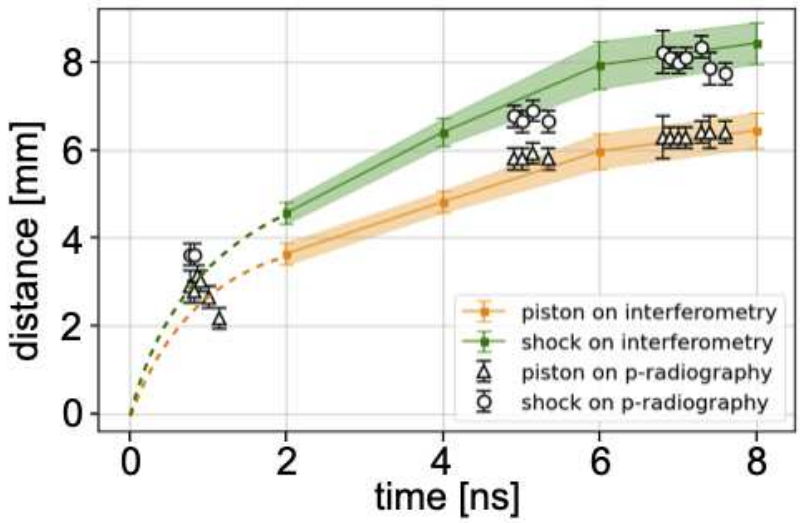

Figure 3.18: Piston and shock front position over time from the electron density (via interferometry) and from the electric field (via proton radiography). *The full green (resp. orange) line materializes the evolution of the shock (resp. piston) location as a function of time as seen on the interferometry diagnostics. It is prolonged toward time 0 by a dashed line passing through the proton radiograph data points at t∼1 ns.*

We also point out that the integration time in a given film is too short to see motion blurring of the moving shock front. The energy of the protons deposited on the RCFs that we used was always high enough to minimise the overlap of images relative to different probing times. Considering the FWHM of the proton energy spectrum relative to each film and knowing that ions deposit their energy mostly right before they stop, we can infer that the error on the probing time is negligible. Specifically, the least energetic protons we have used had an energy of 1.7 ± 0.5 MeV, which meant a time of flight of 3.4 ± 0.3 ns. Hence, 0.3 ns is the biggest error on the probing time that we have. From the following step on, the situation improves drastically, as we had protons of 5.0 ± 0.2 MeV, thus a time of flight of 1.96 ± 0.02 ns. All the following errors on the time of flight are below 10 ps. Moreover, we point out that we did not reach later probing times with lower energy protons, but by moving the timing of the ps-beam with respect to the main ns-beam responsible of the shock generation. In short, the integration time in a given film is too short to see motion blurring of the moving shock front.

Region	Piston	Shock
Characterized Plasma Conditions		
Averaged Atomic Number A	17.3	1.0
Effective Charge State Z_{eff}	8.0	1.0
Elec. Number Density n_e [cm^{-3}]	1.0×10^{19}	1.0×10^{18}
Elec. Temperature T_e [eV]	80.0	100.0
Ion Temperature T_i [eV]	40.0	200.0
Flow Velocity v_0 [km/s]	1200.0	1500.0
Local Magnetic Field Strength B [T]	5.0	60.0
Upstream Magnetic Field Strength B [T]	-	20.0
Upstream Elec. Temperature T_e [eV]	-	50.0
Upstream Ion Temperature T_i [eV]	-	20.0
Calculated Parameters		
Ion Collisional mean-free-path ($\lambda_{mfp,i}$) [mm]	6.6×10^{-4}	10.0
Ion Larmor radius ($r_{L,i}$) [mm]	5.4	0.3
Ion Collisionality ($\lambda_{mfp,i}/r_{L,i}$)	1.2×10^{-4}	37.0
Plasma Thermal Beta β_{ther}	14.0	3.4×10^{-2}
Plasma Dynamic Beta β_{dyn}	5.2×10^{3}	2.6
Mach Number M	-	14.0
Alfvénic Mach Number M_A	-	3.4
Magnetosonic Mach Number M_{ms}	-	3.3

Table 3.1: Characterized conditions of piston and shock, as well as the calculated parameters. *$\lambda_{mfp,i} = v_0\tau_i$ is the ion mean-free-path, in which the ion collisional time $\tau_i = 3m_i^{1/2}(k_BT_i)^{3/2}/(4\pi^{1/2}n_i \ln\Lambda Z^4 q_e^4)$, and $\ln\Lambda \approx 10$ is the Coulomb logarithm, q_e is the elementary charge. $r_{L,i} = m_i v_0/(Zq_eB)$ is the Larmor radius, and the ion collisionality is the ratio of them. The parameters relative to the piston are measured inside the cavity that is located behind the piston front. The thermal (resp. dynamic) beta parameter is the ratio of the plasma thermal (resp. ram) pressure over the magnetic pressure, i.e., $\beta_{ther} = P_{ther}/P_{mag} = 2\mu_0 n k_B T/B^2$, in which μ_0 is the vacuum permeability, k_B is the Boltzmann's constant; $\beta_{dyn} = P_{dyn}/P_{mag} = 2\mu_0\rho v_0^2/B^2$, in which $\rho = mn$ is the mass density. For the shock, the Mach number is the ratio of the flow velocity over the sound velocity, $M = v_0/c_s$, in which the sound velocity is $c_s = (\gamma Z k_B T_e/m_i)^{1/2}$ with $\gamma = 5/3$; the Alfvénic Mach Number is the ratio of the flow velocity over the Alfvénic velocity, $M_A = v_0/v_A$, in which the Alfvénic velocity is $v_A = B/(\mu_0 n_i m_i)^{1/2}$; and the Magnetosonic Mach number is the ratio of the flow velocity over the magnetosonic velocity (see text). For the calculation of the sound velocity and the Alfvénic velocity, we use the parameters of the upstream region.*

With all the above diagnostics, we summarize the characterization of the piston and shock conditions in Table 4.1. Note that for the collisionality, the local magnetic field strength is used. Specifically, it is taken for the piston from our FLASH simulation (in Sec. 3.3.1) and for the shock from our PIC simulations (in Sec. 3.3.2). As for the calculation of the Mach numbers for the shock, the parameters of the upstream region are used.

3.3 Numerical simulations

3.3.1 MHD simulations using the FLASH code

We used the 3D MHD code FLASH (Fryxell et al. 2000b) to study the dynamics of the plasma plume expansion and piston formation in the ambient gas with the strong magnetic field, using the same parameters as the JLF/Titan experiment. Indeed, the piston is collisional and is modeled with a MHD code here, while the shock is collisionless and is modeled with a kinetic PIC code in the next section. The simulations are initialized in 3D geometry, using three temperatures (two for the plasma, and one for the radiation) with the equation-of-state of Kemp and Meyer-ter Vehn (1998) and radiative transport, in the frame of ideal MHD and including the Biermann battery mechanism of magnetic field self-generation in plasmas (Haines 1986). Specifically, as in the experiment, the laser beam is normal to a Teflon target and has an on-target intensity of 10^{13} W/cm^2; the generated plasma plume expands in the hydrogen gas-jet having an uniform density of 10^{18} cm^{-3}. Moreover, the plasma plume expands in the uniform external magnetic field of 20 T (aligned along the z-axis, as in the experiment). Fig. 3.19 shows the FLASH simulation results, i.e., the electron density n_e in (a) and (b), the electron temperature T_e in (c) and (d), and the ion temperature T_i in (e) and (f) at t = 2 ns (after the laser irradiation), in two different cases: the upper row is for the case with only ambient gas but without B-field, while the lower row is for the case with both the ambient gas and the external magnetic field. As FLASH cannot support vacuum, we do not have the FLASH simulation for the case with only B-field but without ambient gas. We can observe that the structures of both the hydrodynamic piston and the induced shock propagating inside the ambient plasma, are qualitatively reproduced compared to the experiment. Indeed, the expanding Teflon piston produces a forward shock in the background plasma (around $x = 1.4$ mm), as well as a reverse shock inside the Teflon piston (around $x = 0.8$ mm). The electron density is $n_e \sim 1.6 \times 10^{18}$ cm^{-3} in the forward shock in the gas and increases up to $n_e \sim 5 \times 10^{19}$ cm^{-3} in the reverse shock.

The electron temperature is around 60-70 eV between the forward and the reverse shocks. This corresponds quite well to what is measured in the experiment by the FSSR (see Fig. 3.14 (b)). The ion temperature is 15 eV in the forward shock and between 80 eV and 180 eV inside the reverse shock.

Concerning the electron temperature, the FLASH simulations give a result two times lower than the TS measurements in the DS region, shown in Fig. 3.11; as for the ion temperature, the situation is worse as it is ten times less in the forward shock compared to the TS measurements. Moreover, the foot structure ahead of the shock cannot be seen in the FLASH simulations.

Such discrepancies between the MHD simulations and the experiments show the difficulties to re-

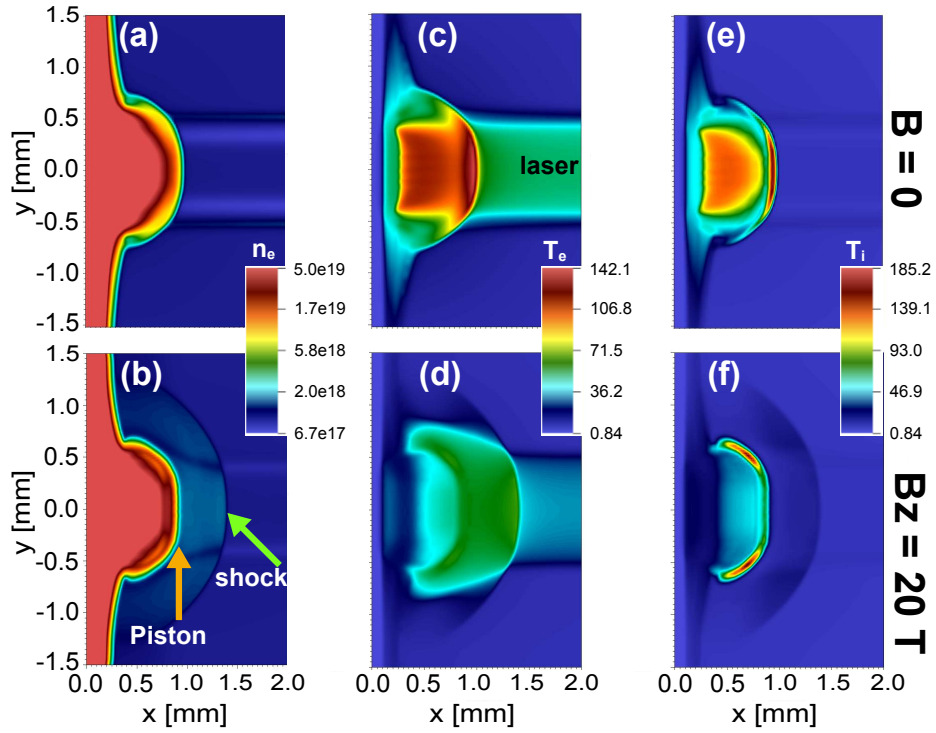

Figure 3.19: FLASH simulation investigating a single shock formation and performed in the conditions of the JLF/Titan experiment. *Maps extracted from FLASH simulations at 2 ns (after the laser irradiation) of: (a) and (b) electron density, n_e in cm^{-3}, (c) and (d) electron temperature, T_e in eV, (e) and (f) ion temperature, T_i in eV. The upper row is for the case without B-field, while the lower row is for the case with B-field. All maps are in linear scale. This xy-plane slice is cut at $z = 0$. The laser comes from the right side along $y = 0$, and the target is at the left side. The orange arrow indicates the piston edge, while the green arrow indicates the shock front.*

produce the shock condition in our case, due to the fact that the shock evolution is dominated by kinetic effects. This is why we have resorted to using PIC simulations, the initial conditions of which are taken from the experimental measurements. Nevertheless, we can still observe that the FLASH simulations reproduce well the dynamics of the piston that induces the shock.

Since FLASH has the ability to model magnetic field generation through the Biermann battery effect, it allows us to assess the importance of this effect in the present configuration. Biermann battery generation of magnetic field is typically important only close to the target surface (order of 1 mm), and it is localized over the steep temperature gradients generated by the laser beam and rapidly decays once the laser beam is off (see for example Li et al. (2006); Gao et al. (2015); Cecchetti et al. (2009); Lancia et al. (2014)). As the shock is induced by the piston in the ambient gas $\sim$ 1 mm away from the target surface after the laser is off ($\sim$ 2 ns), as shown in Fig. 3.19, the Biermann battery effect is negligible compared to that of the strong externally applied B-field.

Fig. 3.20 shows the magnetic field configuration of the expanding plasma. In particular, Fig. 3.20 (a) shows the plasma piston which expels the magnetic field, creating a bubble that is void of the

magnetic field (Khiar et al. 2019b). This piston launches a shock inside the ambient gas, with the magnetic field upstream of the shock being compressed because of magnetic flux conservation. This is clearly shown in Fig. 3.20 (b), where the magnetic field lines are plotted. Because of the three dimensional nature of the plasma flow and of the magnetic pressure, the piston and the shocked ambient plasma are more compressed by the magnetic pressure along the y-axis than along the z-axis.

From the density map at 10 ns (after the laser irradiation) of the FLASH simulation, we can still clearly see the continuously expanding plasma plume (and the compressed Teflon target) because once the laser energy is deposited on the target surface, the heat wave and the shock propagation inside the target (due to collisional effects) can last for much longer time (tens of ns) (Atzeni and Meyer-ter Vehn 2004). Such heat wave drives continuous ablation that is sustained after the laser irradiation.

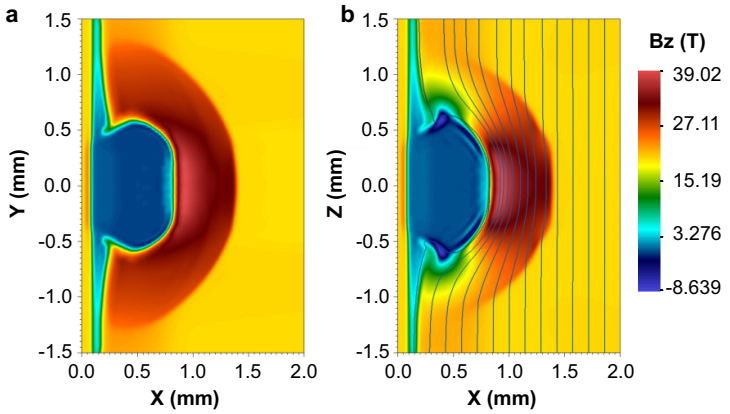

***Figure 3.20: Maps of the magnetic field in the MHD simulations**, at time $t = 2$ ns after the start of the plasma piston expansion inside the magnetized ambient medium. Shown are two-dimensional cross-section in the xy (a) and xz (b) planes, the latter with the corresponding magnetic field lines. The target is located on the left side of the box and the laser comes from the right side, as in the experiment. The colormap represents the strength of B_z.*

3.3.2 PIC simulations using the SMILEI code

Presentation of the setup

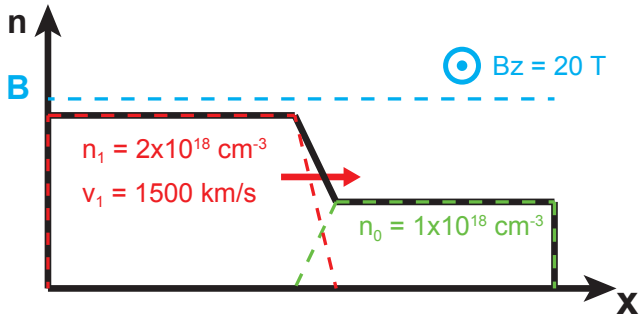

Figure 3.21: PIC simulation initialization setup. *The shocked plasma is set in the left half of the simulation box (red dashed line), drifting towards the right at speed $v_d = 1500$ km/s, while the ambient plasma lies in the right half (green dashed line). The drifting plasma has number density $n_{i1} = 2 \times 10^{18}$ cm^{-3}, while the background plasma has $n_{i2} = n_0 = 1 \times 10^{18}$ cm^{-3}. The transition between these two regions is initialized with a shock width equal to the ion inertial length $d_i = 200$ µm. A homogeneous magnetic field $B_z = 20$ T is imposed.*

The evolution of the collisionless shock is modeled with the kinetic PIC code SMILEI (Derouillat et al. 2018). These simulations focus on the dynamics of the shock front (already detached from the piston) and of its interaction with the ambient gas, using directly the parameters measured in the experiments. Since the width of the shock structure ($\sim$ mm) is much larger than the thickness of the shock ($\sim$ µm), we can treat the interaction between the shock front and the ambient plasma as quasi one-dimensional (1D) interaction, via the 1D3V version of the code.

Our 1D simulations have been initialized as sketched in Fig. 3.21: in the right half of the simulation box (Region 1) is set a hydrogen plasma drifting at speed $v_d = 1500$ km/s towards the right (x positive), while the unshocked background plasma lies in the right part of the box (Region 2). The shock width is initially imposed as the ion inertial length (Pinter 1980; Mellott 1984b) $d_i = c/\omega_{pi} = 200$ µm. Both of the two plasmas consist of electrons and protons, with the real mass ratio $m_p/m_e = 1836$. We have initialized these plasmas with parameters inferred from the TS characterization (see Sec. 3.2.2). Hence, the shocked plasma has ion and electron number densities $n_{i1} = n_{e1} = 2n_0 = 2.0 \times 10^{18}$ cm^{-3}, and temperatures $T_{i1} = 200$ eV and $T_{e1} = 100$ eV. While the ambient plasma has ion and electron number densities $n_{i2} = n_{e2} = n_0 = 1.0 \times 10^{18}$ cm^{-3}, and temperatures $T_{i2} = 20$ eV and $T_{e2} = 80$ eV. The simulation box size is $L_x = 2048\, d_e \approx 11$ mm, and the spatial resolution is $d_x = 0.2\, d_e = 1.1$ µm, in which $d_e = c/\omega_{pe} = 5.3$ µm is the plasma skin depth, and $\omega_{pe} = \sqrt{n_{e2} q_e^2/(m_e \epsilon_0)} = 5.6 \times 10^{13}$ s^{-1} is the electron plasma frequency. Here, c is the speed of light, $n_{e2} = n_0 \equiv 1.0 \times 10^{18}$ cm^{-3} is the electron number density of the ambient plasma, and m_e, q_e and ϵ_0 are the electron mass, elementary

charge, and the permittivity of free space, respectively. From the perspective of the ion Larmor motion, the simulation size is more than 10 r_{Li}, where $r_{Li} = v_1/\omega_{ci} = m_i v_1/q_e B \sim 0.8$ mm.

The magnetic field is homogeneously applied in the z-direction with $B_z = 20$ T. This means that $\omega_{ce}/\omega_{pe} = 0.06$, where $\omega_{ce} = q_e B/m_e$, while the Larmor radius is $r_{Li} = 0.8$ mm and the proton gyroperiod $\tau_{Li} = 3$ ns (for the high-velocity case of 1500 km/s in the upstream).

The simulation lasts for $1.5 \times 10^5 \omega_{pe}^{-1} \sim 2.5$ ns. Inside each cell, we put 1024 particles for each species. The boundary conditions for both particles and fields are open, and enough room is left between the boundary and the shock, so that the boundary conditions do not affect the concerned physics. The mean-free-path of the presented case is $\lambda_{mfp} \approx 1800\, d_e$, which is larger than the interaction scale, further confirming that the shock is collisionless. Given the initial low temperature of the ambient plasma in the simulation ($T_{e2} = 80$ eV), the Debye length is small compared to the grid resolution d_x, i.e., $\lambda_{De} = \sqrt{\epsilon_0 k_B T_{e2}/n_{e2} q_e^2} \approx 0.012 d_e = 0.06 d_x$. However, we have run a series of simulations with different initial temperatures, showing that the energy conservation for those cases is limited around 0.05% and the physical results are almost the same.

We have also tested a series of 1D and 2D simulations with varying resolutions ($0.1 \sim 0.5 d_e$), particle-per-cell numbers ($512 \sim 2048$), and ion-to-mass ratio ($400 \sim 1836$), all reaching similar shock behavior, which proves the robustness of the observed behavior of the quasi-perpendicular, supercritical magnetized collisionless shock investigated here.

For the calculation of the mean free path λ_{mfp}, we use $\max(v_{th,i}, v_d) \cdot \tau_i$, where $v_{th,i}$ is the ion thermal velocity, v_d is the drifting velocity, and τ_i is the ion collision time. For the drifting plasma with the observed temperature, i.e., $T_i = 200$ eV, $v_{th,i} = 140$ km/s, which is smaller than the drifting velocity.

Shock features and necessity of the magnetic field

In Fig. 3.22 are reported the results of two PIC simulations, one with and one without externally applied magnetic field, corresponding to a time $t = 2.66$ ns after the beginning of the simulation. We point out that this time does not coincide with the time after the laser hit the target in the experiments: here we are not considering the initial laser energy deposition on target and piston formation, we are starting with a discontinuity already formed and considering such a shock evolution.

For the case with the applied B-field (on the left column), typical structures of a supercritical quasi-perpendicular collisionless shock can be seen (see Sec. 1.2 and Balogh and Treumann (2013)). For example, we observe the overshoot in the downstream (DS) region (on the left of the red dashed line), the ramps in the shock fronts (both the red dashed line and the cyan dotted line), and the foot in the

upstream (US) region, as can be seen in Fig. 3.22 (a). This foot region is formed by the reflected protons at a distance within $r_{L,i}$ and modulated by the modified two-stream instability (Matsukiyo and Scholer 2003). The proton density n_i in Fig. 3.22 (e) shows a compression ratio between DS and the US regions of $n_{i,DS}/n_{i,US} \approx 4$, in agreement with the theoretical jump condition prediction (Woods 1971). This density profile, as well as that of the transverse electric field E_y (not shown here), follows the shape of the B-field B_z. The longitudinal electric field E_x in Fig. 3.22 (c) has a peak right at the ramps, providing the electrostatic cross-shock potential to trap and reflect the protons, as can be seen in the phase-space distribution in Fig. 3.22 (g). Moreover, we observe one of the periodic shock reformation (Balogh and Treumann 2013) indicated by the cyan dotted line.

On the contrary, for the case without B-field (on the right column of Fig. 3.22), the drifting plasma just

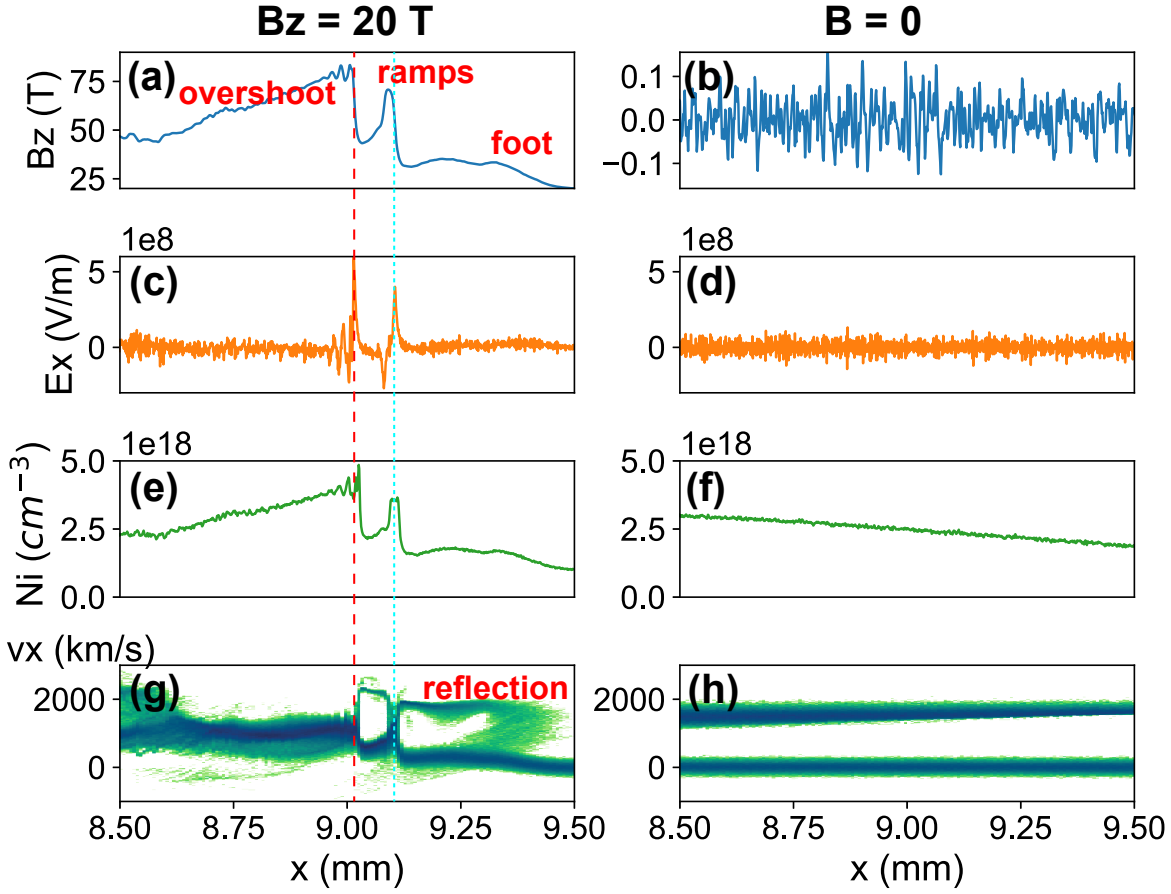

Figure 3.22: Features of the supercritical quasi-perpendicular collisionless shock structure in ion density and EM fields distribution (with and without the external magnetic field). *Specifically, (a) and (b) transverse magnetic field B_z; (c) and (d) longitudinal electric field E_x; (e) and (f) ion density profile n_i; (g) and (h) phase-space distribution x-v_x, at the end of the simulation, i.e., at $t = 2.66$ ns. The results obtained with B-field are on the left column, while those without B-field are on the right. The red dashed line and the cyan dotted line indicate the position of the shock ramps. The drifting plasma propagates from left to right.*

penetrates through the ambient one and no shock is formed, indicating that the externally imposed

magnetic field plays an essential role in the shock evolution. Thus, without it, no proton energization can take place, which is in accordance with our experimental observation.

The evolution of the phase space during the interaction between drifting and ambient protons is shown in Fig. 3.23 for two different flow velocities. The first row corresponds to the dynamics of the

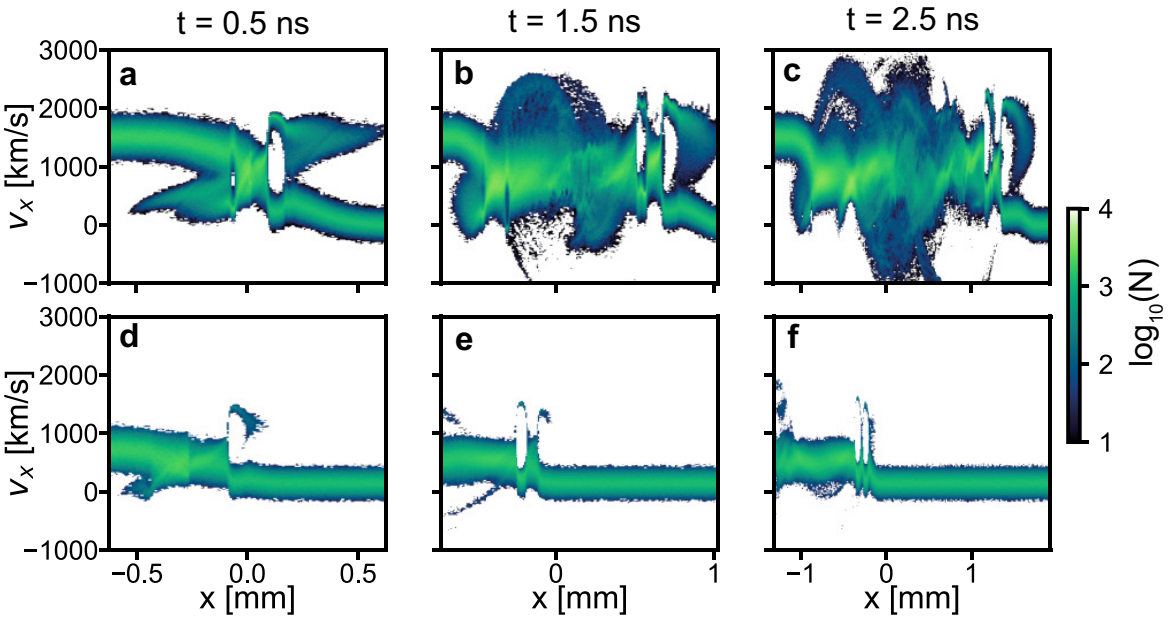

Figure 3.23: Proton phase space evolution. *The first row corresponds to the high-velocity case (with initial velocity of 1500 km/s), while the second row is for the low-velocity one (with initial velocity of 500 km/s), at (a) & (d) 0.5 ns, (b) & (e) 1.5 ns, and (c) & (f) 2.5 ns. The colorbar represents the normalized particle number N in logarithmic scale.*

high-velocity case ($v_d = 1500$ km/s), where we witness the formation of both the forward (FS) and reverse (RS) shocks at $t = 0.5$ ns in (a) and the FS reformation at $t = 1.5$ ns in (b), when protons in the DS region start to gyrate within the compressed B-field. At last, while the FS shock keeps picking up protons from the background plasma, the downstream RS becomes highly nonlinear, in (c). Comparing the first row of Fig. 3.23 with the second one, which corresponds to the low-velocity case ($v_d = 500$ km/s), it is clear that we have a lower number of reflected protons in the latter case, due to the low Magnetosonic Mach number that makes such a shock subcritical: $M_{ms} = v/\sqrt{v_A^2 + c_s^2} \lesssim 1.0 < M_{cr} \approx 2.76$. Although there is also shock reformation at $t = 1.5$ ns in (e), at last at $t = 2.5$ ns in (f) the downstream region is just heated a little bit and the FS remains in its linear stage.

Comparison between electric fields retrieved through PIC simulations and proton radiography

We note that, in the presence of magnetic field, the bipolar structure of the E_x electric field at the shock front displayed in Fig. 3.22 (c) matches the one that was retrieved from the proton radiography

data, as shown in Fig. 3.17. Such a structure seen in the 1D PIC simulations is also verified in the complementary 2D simulations that will be detailed below.

However, the PIC electric field E_x shown in Fig. 3.22 (c) does not quantitatively correspond to the one retrieved via proton radiography: the former indeed has an amplitude field $E_x \sim 5 \times 10^8$ V/m in the shock layer, which is two orders of magnitude higher than the experimentally estimated one in Fig. 3.17 (c) ($\sim 4 \times 10^6$ V/m). This discrepancy of E-field amplitude between the simulation and the experiment may be due to several reasons.

Firstly, the bipolar electric field structure obtained by proton radiography has a width of 0.4 mm, while the E_x peaks in the PIC simulations are very sharp, with widths smaller than 0.02 mm. With a time-average of the PIC simulation over 0.2 ns, the E_x profile around the shock front reaches a size of 0.4 mm, and its value drops down to 2×10^7 V/m.

Secondly, the PIC simulation represents the tip of the hemispheric expanding shock front, where the B-field is strictly perpendicular to the plasma flow and the shock is the strongest; however, the proton radiography covers the whole shock front with an integration along the z-direction. It includes all other plasma flow directions in the xz-plane, which are not perpendicular to the B-field and the corresponding shocks are weaker. This is what was already considered in the analysis of the proton radiography data, as shown in Fig. 3.17.

Lastly, the amplitude of the electric field is decreasing with time. In our 1D PIC simulation, the results shown correspond to $t = 2.66$ ns (from the beginning of the simulation); while in the experimental case, the proton radiography results are at $t = 5.0$ ns (from the laser impact). Hence, we can expect that the early-time PIC field is higher than that derived from radiographs taken at later time. Unfortunately, we cannot compare these times.

2D PIC simulations managed to partially overcome such problems and give a more realistic scenario. Indeed, the electric field amplitude becomes already one order of magnitude lower in our 2D simulation result (averaged along the y-axis) than in the 1D one. Moreover, it decreases with time, making it pretty realistic that at a later time out of our simulation possibilities such an electric field becomes of the same order of magnitude as the experimentally estimated one. The electric field E_x profile (averaged along the y-direction) at times $t = 0.25$ ns and $t = 0.70$ ns is plotted in Fig. 3.24.

SSA as acceleration mechanism

Since the shock evolves from super- to sub-critical during its evolution (as probed via interferometry), we have performed simulations with two different initial drifting velocities representative of the two phases, i.e., 1500 and 500 km/s, respectively. In order to elucidate the micro-physics responsible

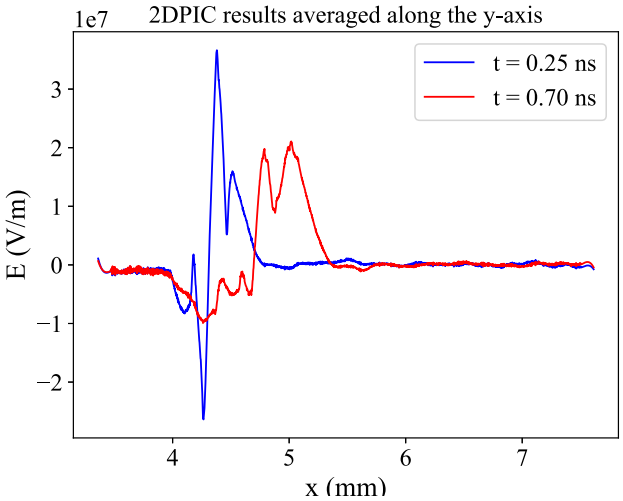

Figure 3.24: Electric field E_x profiles (averaged along the y-axis) from 2D simulations. *The blue curve is at 0.25 ns and the red one is at 0.7 ns (which is the duration of our 2D simulations, due to computational resources limits).*

for the observed non-thermal proton acceleration, a random sample of protons (10^4 out of 10^7) is followed in the simulation.

The PIC simulation results for the high-velocity case are summarized in Fig. 3.25, while Fig. 3.26 presents the experimental and the simulated proton spectra obtained with various conditions.

Fig. 3.25 (a) illustrates the proton density map in the reference frame of the contact discontinuity (CD), where we can clearly see the density pileups in the forward direction, indicating the shock formation (and periodic reformation (Balogh and Treumann 2013)). More than 2% of the tracked protons end up with energies > 40 keV, which will constitute the high-energy end of the spectrum shown in Fig. 3.26. They share similar trajectories and two representative ones (P1 and P2) are plotted in Fig. 3.25 (a). Following these trajectories, we can see that they are first picked up by the forward shock at the shock front, and then they gain energy while "surfing" along (or confined around) the shock front. Besides, while surfing along the shock front, P1 gets trapped and reflected repeatedly, with a small energy perturbation, as is shown in Fig. 3.25 (b), all of which is typical of SSA.

Typical structures of the supercritical quasi-perpendicular collisionless shock (Balogh and Treumann 2013) can also be seen in Fig. 3.25 (c), where we plot the lineout of the ion density and of the electromagnetic fields around the shock front ($0.4 < x < 1.2$ mm in the reference frame of the CD), when the shock is fully formed ($t = 1.5$ ns).

The longitudinal electric field E_x peaks right at the ramp, providing the electrostatic cross-shock potential to trap and reflect the protons with a velocity lower than that of the shock. In the corresponding x-v_x phase space in Fig. 3.25 (d), we can clearly see that, indeed, it is at the position of E_x that pro-

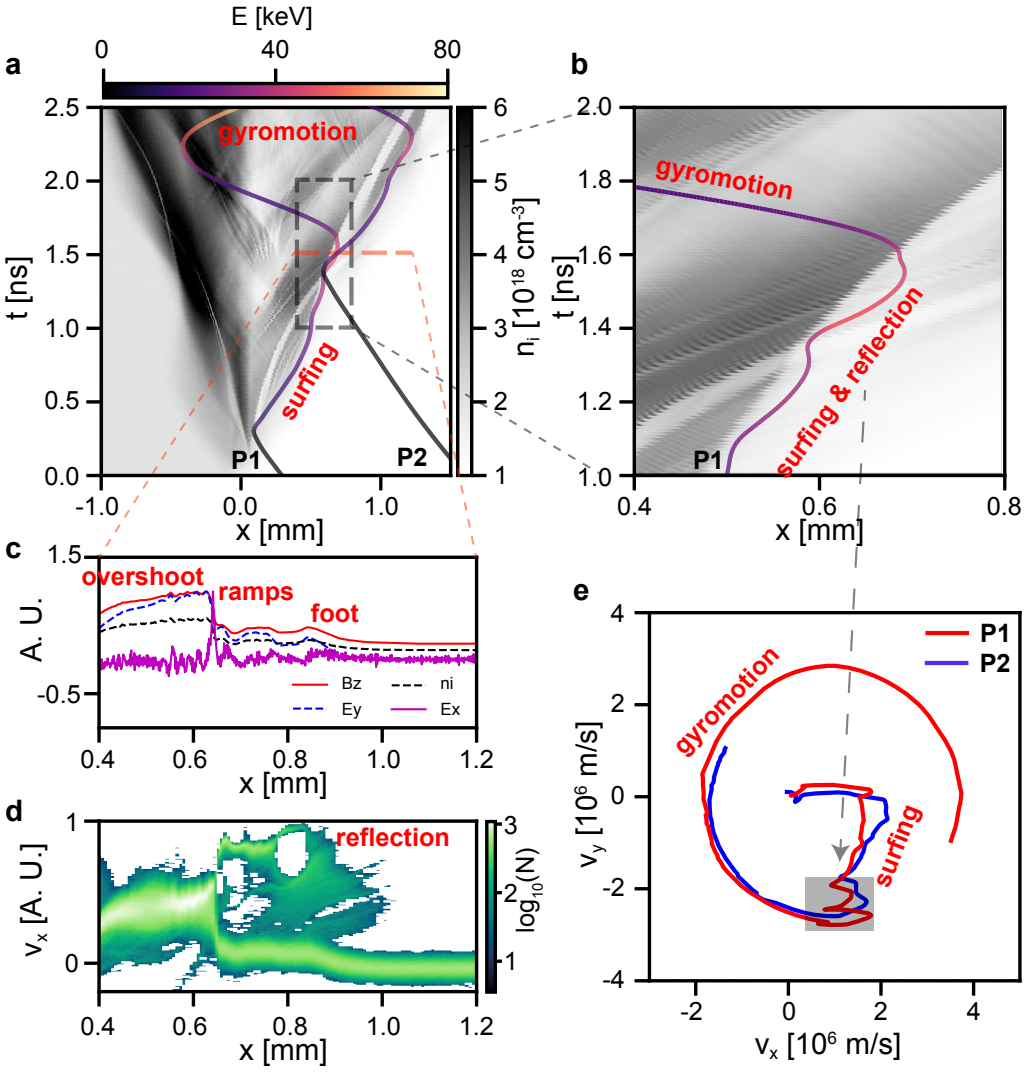

Figure 3.25: Features of a high-velocity shock and of the subsequent shock surfing proton energization as obtained through PIC simulations. *(a) Trajectories of two protons (P1 and P2, energized from the ambient gas to > 40 keV at $t = 2.66$ ns, representing 108 out of 5000 tracked particles with the "surfing/reflection/gyromotion" trajectories) in x-t diagram, overlaid on the proton density map in the reference frame of the contact discontinuity. (b) Zoom of the black dashed rectangle region in (a), showing the "surfing & reflection" of P1 along the forward shock. (c) Lineout of density and electromagnetic fields (normalized by each of their maximum value respectively) at the red dashed line in (a) ($t = 1.5$ ns, $0.4 < x < 1.2$ mm). (d) The corresponding proton x-v_x phase space diagram where the colorbar represents the normalized particle number N in logarithm scale. (e) The v_x-v_y diagram of P1 and P2. The grey shaded area corresponds to the "surfing & reflection" stage in (b).*

tons get reflected. In Fig. 3.23 we have plotted more time frames of this phase space (a–c), as well as the phase-space corresponding to the simulation performed at low velocity (d–f): the faster shock is clearly much more efficient in reflecting and energizing protons.

The fact that such reflection and energy gain happen at the peak of E_x rules out the possibility of SDA, where the ion reflection is mostly caused by the downstream compressed B-field (Zank et al. 1996).

This thesis is also sustained by the fact that the ion Larmor radius ($r_{Li} \approx 0.8$ mm) is larger than the shock width ($\Delta_s \approx 200$ µm). At last, as shown in Fig. 3.25 (e), the main contribution of the proton energy gain is due to v_y via the inductive electric field $E_y = v_x B_z$, which is again in accordance with the SSA mechanism (Matsukiyo and Scholer 2011).

The proton spectrum at $t = 2.66$ ns produced by the PIC simulated high-velocity shock (shown in Fig. 3.26 in the black solid line), is in remarkable agreement with the experimental observation. As in the experiment, no proton energization is found in the simulations performed without magnetic field or ambient medium. We note also that for the low-velocity shock (with $v = 500$ km/s), the spectrum (green dashed line) is far below the experimental noise baseline, indicating that the protons are indeed accelerated during the first $2 - 3$ ns, when the shock is in the supercritical regime.

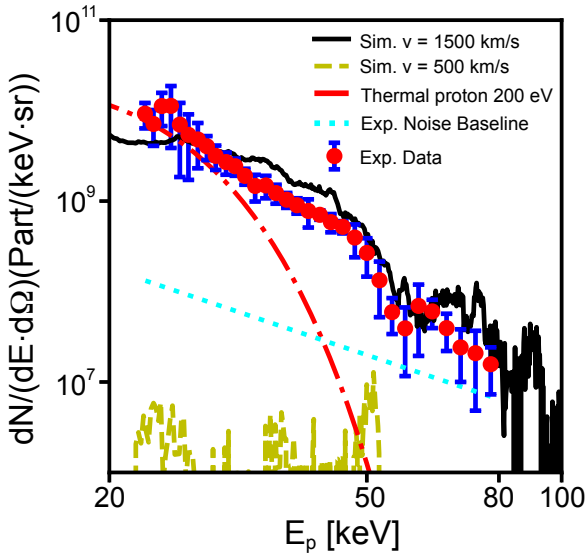

Figure 3.26: Evidence for the energization of protons picked up from the ambient medium. *Proton energy spectra of both the experiment (red dots, averaged over five shots, as measured at LULI2000) and of two PIC simulations (the black solid line for the high-velocity case with $v_d = 1500$ km/s and the yellow dashed line for the low-velocity one with $v_d = 500$ km/s, both are measured at $t = 2.66$ ns in the simulations). The red dash-dot line is the thermal proton spectrum of 200 eV. The blue error bars correspond to one sigma deviation from the average (shown by the red dots), the noise level on the diagnostic is materialized by the cyan dotted line. Note that the absolute scale in proton numbers applies only to the experimental spectrum; the simulated spectrum is arbitrarily scaled to the experiment one.*

Further analysis on the simulated proton spectra is done in order to identify the proton acceleration mechanism at play.

As shown in Fig. 3.27 (a), the energy spectrum from our experimental data can be fitted by a power-law function $\propto E^p$ with index $p = -4.28$. This is quite smaller than the usual index of shock acceleration (e.g. for DSA, $p \sim -2.3$; while for SDA, $p \sim -1.5$ (Zank et al. 1996)). The reason behind this is the fact that the shock in the experiment is short-lived. We can speculate that if the shock had lasted

for longer (e.g. if the laser driving the plasma ablation had been longer), the accelerated protons could have reached higher energies and the index could have attained higher values. We confirm that by doing a simulation lasting twice as long (see the green simulated spectrum in Fig. 3.27 (a)): at $t = 5.1$ ns the energy spectrum gets flatter and the index becomes $p = -2.27$, closer to the index inferred from the analysis of astrophysical observations (like $p \approx -1.65$ in Decker et al. (2005)).

We have also checked that the shock and the overall dynamics that are collisionless by verifying that we obtained almost identical energy spectra in simulations performed with and without ion-ion collisions (see Fig. 3.27 (b)).

In order to further corroborate the robustness of our mechanism, we have performed a series of simulations with different B-field strengths, as is shown in Fig. 3.27 (c). The acceleration efficiency becomes larger with higher strength of B-field, which is in agreement with the SSA mechanism.

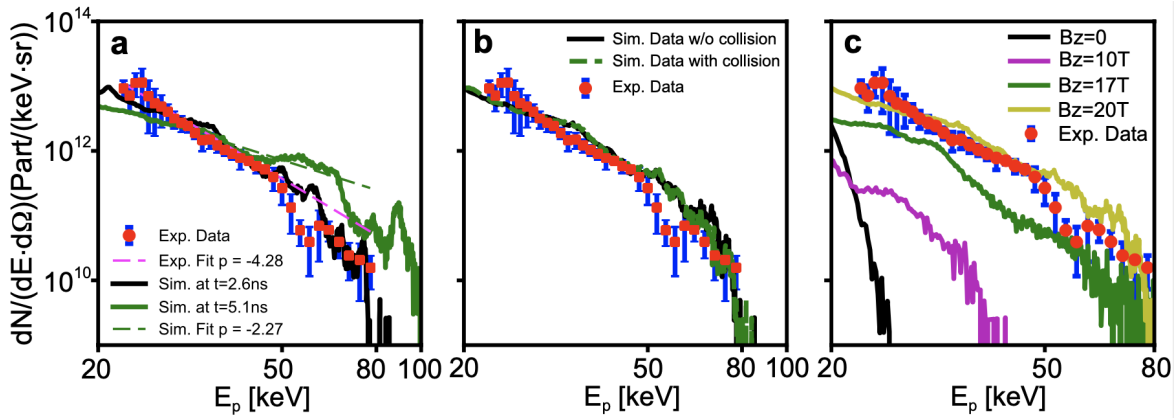

Figure 3.27: Further proton energy spectra. *(a) Experimental energy spectrum represented by red dots (averaged over 5 shots) with blue error bars (correspond to one sigma deviation from the average), fitted with a power-law function (purple dashed line) with $p = -4.28$; PIC simulated spectra at $t = 2.66$ ns (black solid line) and $t = 5.1$ ns (green solid line), where the latter is also fitted by a power-law function (green dashed line) with $p = -2.27$. Note that the absolute scale in proton numbers applies only to the experimental spectrum; the simulated spectra are adjusted to the experimental one. (b) Experimental proton spectrum (red dots), as well as the simulated one with and without ion-ion collisions (green dashed line and black solid line, respectively). (c) Experimental proton spectrum (red dots), as well as the spectra simulated in the presence of magnetic fields of different amplitude. The B-field strength is varied by modifying the angle between the B-field direction (along z) and the on-axis shock propagation direction (along x) in the xz-plane.*

Hence, a noteworthy conclusion of such an analysis is that SSA can be considered as the sole mechanism at play in picking up thermal ions and accelerating them to hundred keV-scale energies, at least for the parameters relative to our experiment and to the early stage of the shock formation and development. SSA appears to produce sufficiently energetic protons for further acceleration by DSA, as for example at the Earth's bow shock, where the threshold energy for DSA to become effective is in the range of $\sim (50 - 100)$ keV/nucleon (Balogh and Treumann 2013). Since we are limited in time in

exploring the dynamics of the protons interacting with the super-critical shock, we can only speculate that SDA might appear at a later stage, when the reflected ions acquire enough energy to cross the shock front.

2D PIC simulations taking into account non-stationarity to prove the robustness of the 1D simulations results

Multi-dimensional effects (like shock front rippling) could modify the detailed dynamics of the ion acceleration. Hence, multi-dimensional simulations are necessary to evaluate the interplay between the non-stationarity (induced by instabilities transverse to the shock propagation direction (Burgess and Scholer 2007)) and the ion reflection/acceleration.

Due to the limitation of the computational resources, we have reduced the 2D simulation scale to a manageable degree: the simulation box has dimensions $L_x = 8$ mm, $L_y = 0.8$ mm, resolution $d_x = d_y = 0.4\, d_e$, and duration $t_{end} = 0.7$ ns. Being $r_{Li} = 0.08$ mm and $\tau_{Li} = 0.05$ ns, for our 1D simulations we had $L_x \approx 136\, r_{Li}$ and duration $t_{end} \approx 53\, \tau_{Li}$. For these new 2D simulations, the transverse size is "only" $L_x \approx 10\, r_{Li}$ and the duration $t_{end} \approx 14\, \tau_{Li}$, but we believe that these values are large enough to demonstrate the effect of the non-stationarity in 2D case.

From Fig. 3.28 (a), we can clearly see that the transverse non-stationarity (front rippling) has already occurred, with 2D-stripes of magnetic field mostly positioned at/behind the shock layer. As for protons with kinetic energy above 30 keV, they mainly appear at the shock front and then travel down the negative y-direction. Fig. 3.28 (b) shows the proton energy spectra at 0.7 ns of the 1D (in red) and 2D (in black) cases, which are close to each other, with only a 2 keV difference in the highest energy cut. This can be caused by the numerical heating of the 2D case, due to the lower spatial resolution. Moreover, checking the energy evolution of the protons in the x-t map of the normalized B_z in the reference frame of the CD, it is clearly demonstrated that the accelerated proton is first reflected at (or, picked up by) the shock front in Fig. 3.28 (c), and then is surfing along the shock front while keeping gaining energy in Fig. 3.28 (d). This is exactly the same picture as we have shown for the 1D simulations (Fig. 3.25), proving that the SSA is the dominating proton acceleration mechanism at play (even in the multi-dimensional case).

Nevertheless, the non-stationarity of the shock might further accelerate the proton at a later time, especially after the protons pass through the shock front and gyrate in the DS region. But unfortunately right now we do not have the computational resources to reveal that scenario. In short, our 2D simulation shows that, at least at early times, the non-stationarity does not prevent the protons from being accelerated by SSA (reflecting and surfing).

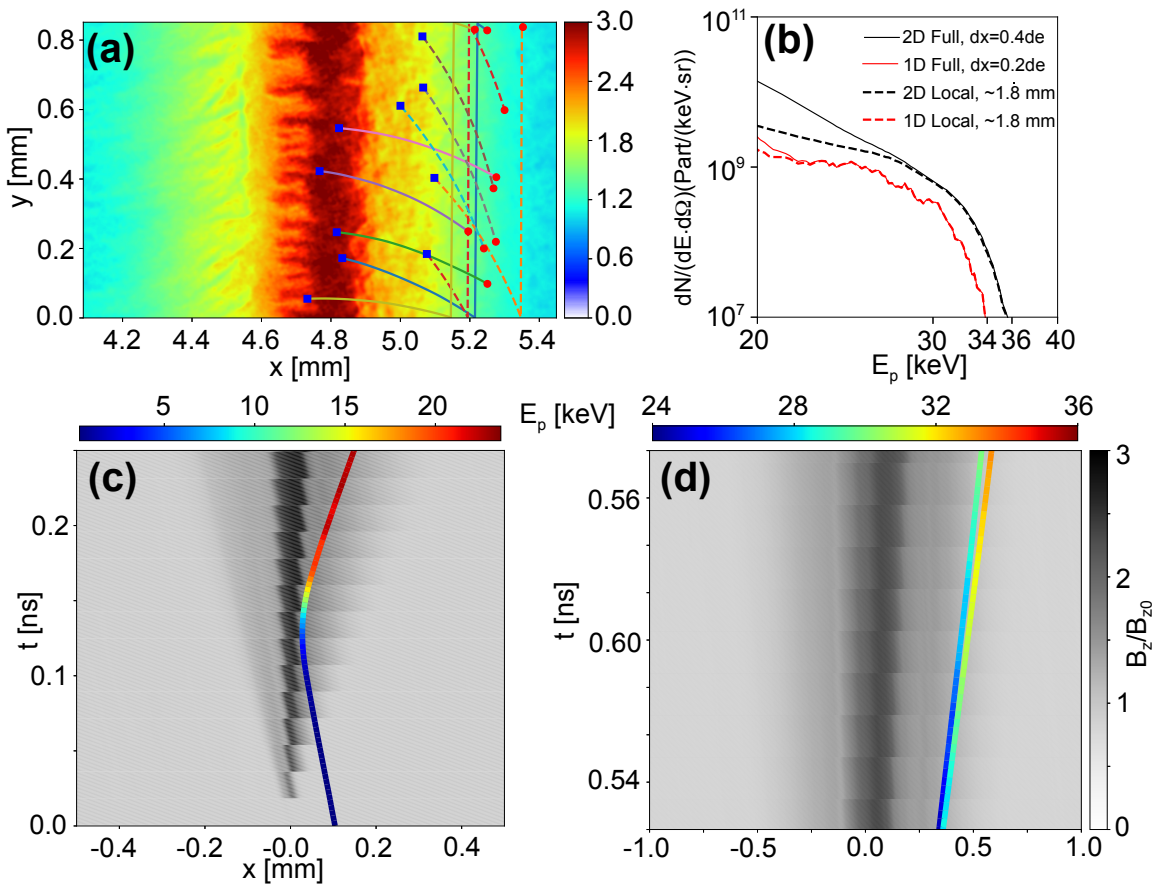

Figure 3.28: 2D simulation results. *(a) B-field maps at 0.7 ns, normalized to 20 T, with some trajectories of particles having $E_k > 40$ keV. Solid lines are from the ambient plasma and dashed ones are from the drifting plasma; blue squares are the starting position at 0.5 ns, while red dots are the ending position at 0.7 ns. (b) Energy spectra of both 1D and 2D simulation results at 0.7 ns. Red lines are for the 1D case (solid line for particles in the whole simulation box, dashed line for those lying around the shock layer in the range of 1.8 mm), while black lines are for the corresponding 2D case. (c) Trajectory of a proton reflected at the shock front in the x-t diagram, overlaid on the transversely-averaged B-field map in the reference frame of the contact discontinuity (the grey colorbar is for the B-field strength, while the colored one is for the proton kinetic energy). (d) Trajectories of two protons surfing along the shock front, also in the x-t diagram, overlaid on the transversely-averaged B-field map in the reference frame of the contact discontinuity.*

Evaluation of the Biermann battery effect

In laser-produced plasmas, there are self-generated magnetic fields. Hence, a natural question is to know whether their presence affects the system evolution.

The Biermann battery effect is typically important only close to the target surface (~ 1 mm), where there are steep temperature gradients generated by the laser beam, and thus rapidly decays once the laser beam is off (see for example Li et al. (2006); Gao et al. (2015); Cecchetti et al. (2009)). As the shock is induced by the piston in the ambient gas 1 mm away from the target surface after the laser is off (~ 2 ns), as shown in Fig. 3.19, we believe that the Biermann battery effect on the shock evolution

is negligible compared to the strong externally applied B-field.

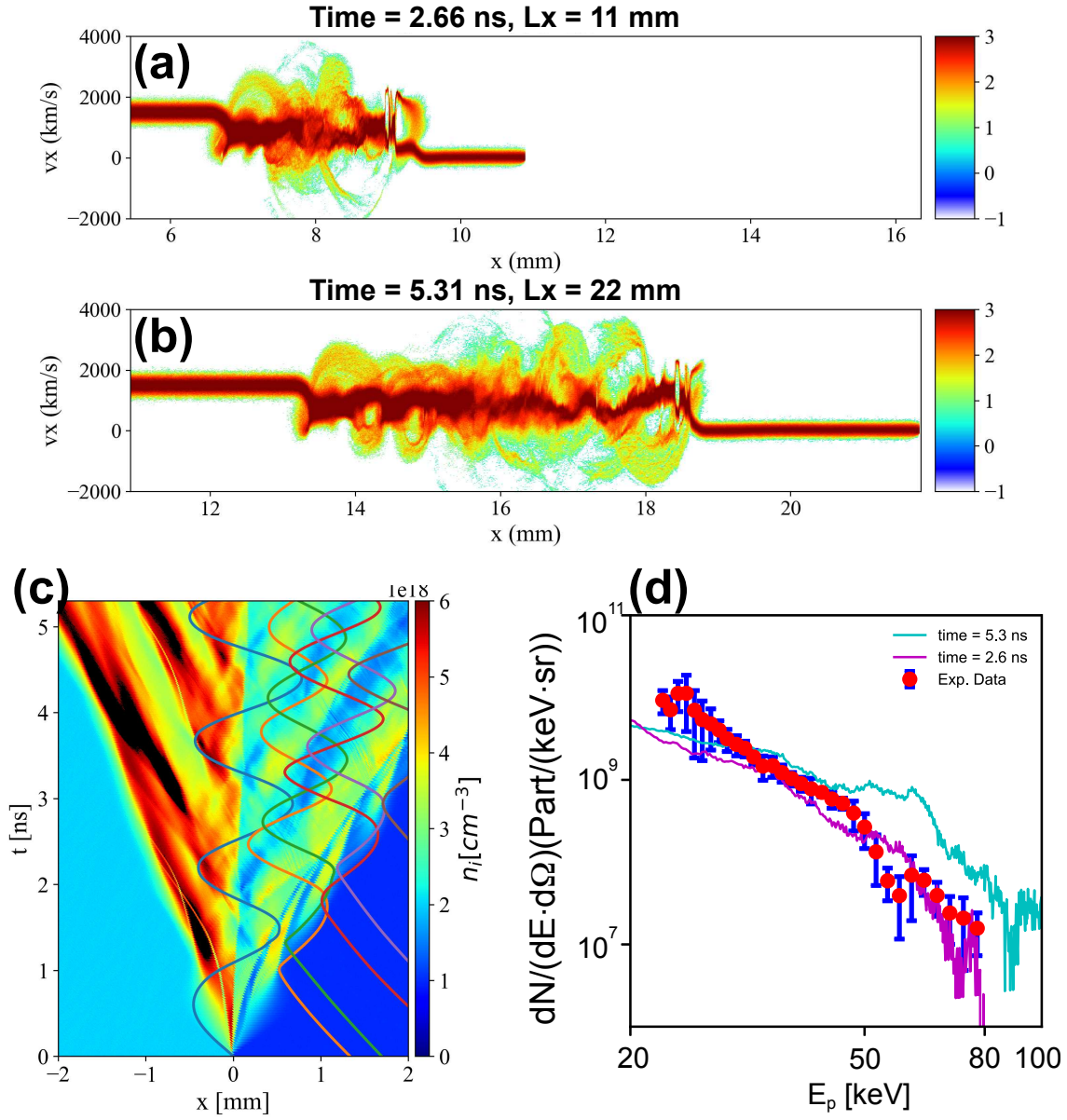

Figure 3.29: *(a) and (b) Phase-space comparison between cases with different simulation sizes and durations (as labeled). (c) Trajectories of six randomly selected protons energized from the ambient gas in the x-t diagram, overlaid on the proton density map in the contact discontinuity reference frame; all this for a simulation run over 5.31 ns, i.e., over longer time than the simulation shown in Fig. 3.25. (d) Energy spectrum for the simulation shown in Fig. 3.25 (i.e., run over 2.66 ns) and for the longer simulation (i.e., run over 5.31 ns, and with twice the box size).*

3.4 Astrophysical relevance

In this section, we will discuss the astrophysical phenomena to which our laser-produced plasma can relate.

Table 3.2 as well as the detailed version of it presented in Table 3.3 show that the shock in our experiment is relevant to the comparison with the Earth's bow shock, the solar wind termination shock, and the shock in the interaction between low-velocity supernova remnants (SNRs) and dense molecular clouds.

	M_{ms}	$\lambda_{mfp}/r_{L,i}$
Our experiment	3.1	2.2
Earth's Bow Shock	2.8	1.2×10^8
Termination Shock	4.9	7.4×10^7
Mixed-morphology SNRs	≥ 3.2	$\geq 2.0 \times 10^2$

Table 3.2: Parameters of the laboratory shocks as well as that of three shocks found in natural events. *The listed parameters for each plasma are: the Magnetosonic Mach number M_{ms} and the ratio of the collisional mean free path λ_{mfp} over the ion Larmor radius $r_{L,i}$. The first shows that all shocks are super-critical, the second shows that all shocks are collisionless, i.e., electromagnetic forces dominate over collisions since the collision mean free path is always much larger than the ion Larmor radius. The three natural events are: the Earth's bow shock, the solar wind termination shock, and low-velocity interactions of mixed-morphology SNRs (Rho and Petre 1998) with dense molecular clouds. Details on the parameters and how they are derived are given in Table 3.3.*

First, all these shocks are collisionless, since the ion mean free path λ_{mfp} is much smaller than the ion Larmor radius $r_{L,i}$ and of the width scale, which means that the system is dominated by electromagnetic collective interactions rather than binary-collisions. Moreover, all systems have Magnetosonic Mach numbers M_{ms} over the critical M_c, indicating that the plasma is qualified as supercritical (Balogh and Treumann 2013), i.e., the shock energy is dominantly dissipated through the reflection and acceleration of the upstream protons.

Besides, as shown in Table 3.3, since all systems have Reynolds numbers Re, magnetic Reynolds number R_m, and Péclet number Pe much larger than the unity, we can ensure that all systems are dominated by turbulence, that the magnetic advection dominates over magnetic diffusion, and that the flow itself is dominated by advection rather than diffusion.

Last but not least, in the case of the low-velocity SNRs interacting with dense molecular clouds, e.g., W44, the ion Larmor radius is only in the order of 10^5 cm (see Table 3.3), whereas its shock width has been measured to be much larger, i.e., in the order of $10^{17} - 10^{18}$ cm (Cosentino et al. 2019). This further supports that SSA can be more efficient than SDA in these cases.

We also note that usually detailed considerations about shock rippling and structuration are evoked in a possible competition between SSA and SDA in the solar wind (Chalov et al. 2016; Yang et al.

2012), but that these were not required here in our analysis where we simulated an idealized flat shock front. When note that in the experiment there is likely small structuring developing at the shock front induced by instabilities (Khiar et al. 2019b) (even though this is too small at this early stage to be resolved by our optical probing), but these are not required in the modeling to reproduce the experimentally observed proton energization.

In addition to the solar wind, another interesting case of shock similar to that investigated here is that of supernova remnants (SNRs) interacting with dense molecular clouds, e.g., the class of mixed-morphology SNRs (Rho and Petre 1998). A large fraction of these SNRs shows indications of low energy ($\sim$ MeV) cosmic rays (CRs) interacting with the cloud material and ionizing it (Nobukawa et al. 2019; Nava et al. 2019; Okon et al. 2020). These mildly relativistic particles are typically explained as CRs accelerated in the past at the SNR shock front that escaped the remnant and reached the cloud (Phan et al. 2020). However, our results show that in-situ generation of low energy CRs ($\sim$ MeV) could be at play, and should also be taken into account (Nobukawa et al. 2019). The in-situ acceleration would be most likely generated by the low-velocity, mildly supercritical (see Table 3.2) SNR shock interacting with the dense cloud, a scenario which is supported by our findings: since our analysis of the experiment shows that SSA is most likely behind the observed proton energization, and since the plasma parameters at play in the experiment are similar to those of the objects detailed in Table 3.3, we suggest that SSA is similarly effective in these objects.

The numbers between parentheses in Table 3.3 refer to the corresponding articles: ([1])Miceli et al. (2017). ([2])Greco et al. (2018). ([3])Slavin and Holzer (1981). ([4])Richardson et al. (2008). ([5])Velàzquez et al. (2002); Vaupré et al. (2014). ([6])Boumis et al. (2009). ([7])Frail and Mitchell (1998). ([8])Cesarsky et al. (1999); Reach et al. (2019). ([9])Stasiewicz and Eliasson (2020). ([10])Burlaga et al. (2008). ([11])Hoffman et al. (2005); Brogan (2007); Li and Chen (2010); Abdo et al. (2010); Phan et al. (2020). ([12])Koralesky et al. (1998). ([13])Claussen et al. (1997). ([14])Reach et al. (2019). ([15])Slavin and Holzer (1981). ([16])Phan et al. (2020); Okon et al. (2018). ([17])Boumis et al. (2009). ([18])Frail and Mitchell (1998). ([19])Cesarsky et al. (1999); Reach et al. (2019). ([20])Slavin and Holzer (1981). ([21])Balogh and Treumann (2013). ([22])Vaupré et al. (2014); Phan et al. (2020). ([23])Lockett et al. (1999). ([24])Frail and Mitchell (1998). ([25])Cesarsky et al. (1999); Reach et al. (2019). ([26])Bale et al. (2003); Liebert et al. (2018). ([27])Burlaga et al. (2008). ([28])Velàzquez et al. (2002). ([29])Miceli et al. (2017).

3.5 Conclusions

In conclusion, we have shown that laboratory experiments can be performed to generate and characterize globally mildly supercritical, quasi-perpendicular magnetized collisionless shocks of astro-

Parameters	Our Results	Earth's Bow Shock	Solar Wind Term. Shock	Mixed morpho. SNR W28	Mixed morpho. SNR Kes. 78 ([1])	Mixed morpho. SNR W44	Mixed morpho. SNR IC443 ([2])
Flow Velocity V [cm/s]	$\mathbf{1.5 \times 10^8}$	$\mathbf{5.0 \times 10^7}$ ([3])	$\mathbf{3.5 \times 10^7}$ ([4])	$\mathbf{(2.0 - 3.0) \times 10^6}$ ([5])	$\mathbf{1.0 \times 10^7}$ ([6])	$\mathbf{5.0 \times 10^6}$ ([7])	$\mathbf{6.0 \times 10^6}$ ([8])
Magnetic Field B [G]	$\mathbf{2.0 \times 10^5}$	$\mathbf{2.5 \times 10^{-4}}$ ([9])	$\mathbf{1.0 \times 10^{-6}}$ ([10])	$\mathbf{(0.4 - 7.0) \times 10^{-4}}$ ([11])	$\mathbf{1.5 \times 10^{-3}}$ ([12])	$\mathbf{4.0 \times 10^{-4}}$ ([13])	$\mathbf{3.0 \times 10^{-4}}$ ([14])
Electron Temperature T_e [eV]	$\mathbf{1.0 \times 10^2}$	$\mathbf{5.0}$ ([15])	$\mathbf{1.0}$	$\mathbf{0.1 - 1.0}$ ([16])	$\mathbf{1.0}$ ([17])	$\mathbf{0.1 - 1.0}$ ([18])	$\mathbf{1.0}$ ([19])
Ion Temperature T_i [eV]	$\mathbf{2.0 \times 10^2}$	$\mathbf{1.5 \times 10^1}$ ([20])					
Electron Number Density n_e $[cm^{-3}]$	$\mathbf{1.0 \times 10^{18}}$	$\mathbf{1.0 \times 10^1}$ ([21])	$\mathbf{1.0 \times 10^{-3}}$	$\mathbf{1.0 \times 10^3}$ ([22])	$\mathbf{1.0 \times 10^5}$ ([23])	$\mathbf{1.0 \times 10^4}$ ([24])	$\mathbf{1.0 \times 10^4}$ ([25])
Characteristic Length Scale L_0 [cm]	$\mathbf{1.0 \times 10^{-1}}$	$\mathbf{1.0 \times 10^7}$ ([26])	$\mathbf{6.0 \times 10^8}$ ([27])	$\mathbf{6.0 \times 10^{19}}$ ([28])	$\mathbf{6.0 \times 10^{19}}$	$\mathbf{6.0 \times 10^{19}}$	$\mathbf{6.0 \times 10^{19}}$
Sound Velocity c_s [cm/s]	2.2×10^7	6.0×10^6	1.8×10^6	$(0.6 - 1.8) \times 10^6$	1.8×10^6	$(0.6 - 1.8) \times 10^6$	1.8×10^6
Alfvénic Velocity v_A [cm/s]	4.4×10^7	1.7×10^7	6.9×10^6	$(0.3 - 4.8) \times 10^6$	1.0×10^6	8.7×10^5	6.5×10^5
Magnetosonic Velocity v_{ms} [cm/s]	4.9×10^7	1.8×10^7	7.1×10^6	$(0.6 - 4.9) \times 10^6$	2.1×10^6	2.0×10^6	1.9×10^6
Ion Thermal Velocity $v_{th,i}$ [cm/s]	1.4×10^7	4.0×10^6	1.0×10^6	$(0.3 - 1.0) \times 10^6$	1.0×10^6	$(0.3 - 1.0) \times 10^6$	1.0×10^6
Collisional Mean-Free-Path λ_{mfp} [cm]	8.8×10^{-1}	2.5×10^{14}	2.7×10^{16}	$(0.1 - 3.1) \times 10^9$	1.2×10^8	$(0.2 - 5.5) \times 10^8$	6.6×10^8
Ion Larmor Radius $r_{L,i}$ [cm]	7.8×10^{-2}	2.0×10^6	3.7×10^8	$(0.3 - 7.8) \times 10^5$	7.0×10^4	1.3×10^5	2.1×10^5
$\lambda_{mfp}/r_{L,i}$	12.2	1.2×10^8	7.4×10^7	$(1.5 - 700.0) \times 10^2$	1.7×10^3	$(0.2 - 4.2) \times 10^3$	3.2×10^3
Plasma Thermal Beta β_t	3.0×10^{-1}	1.3×10^{-1}	8.1×10^{-2}	$0.02 - 50.0$	3.6	$(0.5 - 5.0)$	9.0
Plasma Dynamic Beta β_d	2.4×10^1	1.7×10^1	5.2×10^1	$0.3 - 240.0$	1.9×10^2	6.6×10^1	1.7×10^2
Mach Number M	6.8	8.8	2.0×10^1	$1.1 - 5.3$	5.6	$(2.8 - 8.9)$	3.4
Alfvénic Mach Number M_A	3.4	3.0	5.1	$0.4 - 11.0$	9.7	5.7	9.2
Magnetosonic Mach Number M_{ms}	3.1	2.8	4.9	$0.4 - 4.8$	4.8	$2.5 - 4.7$	3.2
Reynolds Number R_e	1.5×10^2	1.2×10^2	1.0×10^2	$(2.4 - 630.0) \times 10^{13}$	4.5×10^{15}	$(0.6 - 6.0) \times 10^{15}$	5.4×10^{14}
Magnetic Reynolds Number R_{e_M}	1.8×10^5	2.8×10^{10}	1.0×10^{11}	$(2.8 - 110.0) \times 10^{19}$	4.1×10^{21}	$(0.1 - 1.9) \times 10^{21}$	2.3×10^{21}
Peclet Number P_e ([29])	3.5	3.0	2.4	$(5.6 - 1500) \times 10^{11}$	1.0×10^{14}	$(0.1 - 1.4) \times 10^{14}$	1.3×10^{13}

Table 3.3: Comparison between the parameters of the shocks produced in our experiment*, with the ones of the Earth solar wind interacting at two locations (at the Earth's bow shock Slavin and Holzer (1981); Bale et al. (2003); Liebert et al. (2018); Stasiewicz and Eliasson (2020); Balogh and Treumann (2013) and at the termination shock outside the solar system Richardson et al. (2008); Burlaga et al. (2008)) and of the mixed morphology SNRs interacting with a dense molecular cloud (i.e., W28 Velàzquez et al. (2002); Hoffman et al. (2005); Brogan (2007); Li and Chen (2010); Abdo et al. (2010); Vaupré et al. (2014); Okon et al. (2018); Phan et al. (2020), Kes. 78 Miceli et al. (2017); Boumis et al. (2009); Koralesky et al. (1998); Lockett et al. (1999), W44 Frail and Mitchell (1998); Claussen et al. (1997), and IC443 Greco et al. (2018); Cesarsky et al. (1999); Reach et al. (2019)). Ion species are dominated by protons. For the SNRs with velocity less than 400 km/s, ion temperatures are assumed to be equal to electron temperatures (Ghavamian et al. 2006), which refer to immediate post-shock values. Since the typical radiative cooling length is much larger than the Larmor radius for cosmic rays (Kaufman and Neufeld 1996), the temperatures used here should not be affected by it. Numbers in bold are the primary ones, either measured in our experiment or inferred from the cited publications for the natural plasmas. Numbers in light are derived from the averaged primary numbers. The thermal (resp. dynamic) beta parameter is the ratio of the plasma thermal (resp. ram) pressure over the magnetic pressure. The Mach number is the ratio of the flow velocity over the sound velocity, the Alfvénic Mach Number is the ratio of the flow velocity over the Alfvén velocity, and the Magnetosonic Mach number is the ratio of the flow velocity over the Magnetosonic velocity.*

physical interest. They are typically produced by a laser-driven piston creating a collisionless shock in the ambient secondary plasma (Schaeffer et al. 2019) in the presence of an externally applied homogeneous and highly reproducible magnetic field. Such a high-strength magnetic field (Albertazzi et al. 2013) we use is key to ensuring the collisionless nature of the induced shock.
The key parameters of the laboratory created shock are summarized in Table 3.2, which shows that they result similar to the parameters of the Earth's bow shock (Ellison et al. 1990; Turner et al. 2018), the solar wind termination shock (Richardson et al. 2008; Burlaga et al. 2008; Decker et al. 2008), and of four different non-relativistic SNRs interacting with dense molecular clouds (see Table 3.3 detailing the considered objects).
More importantly, non-thermal proton spectra are observed, and the underlying acceleration mechanism is identified to be SSA via kinetic simulations, which can remarkably reproduce the experimental proton spectra.
Such experimental efforts in the study of proton acceleration, as well as those for electrons (Rigby et al. 2018; Li et al. 2019; Fiuza et al. 2020), can not only advance our understanding of the shock formation and evolution by complementing spacecraft and remote sensing observations, but also help shed new light on solving the fundamental issue of injection for astrophysically-related collisionless shocks (Lebedev et al. 2019).

Our experimental platform can be tuned in the future to perform a systematical study of magnetized collisionless shocks with different B-field strength and orientation (Fujioka et al. 2013), enabling us to capture the transition of such shocks from the supercritical regime to the subcritical one, and hence to explore the triggering of other acceleration scenarios (e.g., SDA and DSA). Another direction will be to test quantitatively the effect of intentionally rippling the shock front by seeding the piston plasma with modulations (Cole et al. 1982).

Chapter 4

Collision of two magnetized shocks

The interaction between collisionless shocks occurs in a great variety of astrophysical phenomena and is thought to be a possible source of particle acceleration in the Universe. In astrophysics one can find subcritical shocks in a variety of scenarios. When a high-Mach number flow meets a dense medium, it becomes heavily "mass-loaded" and slows down to a velocity that allows the formation of a subcritical shock. This is expected to happen when the solar wind interacts with the interstellar medium and forms the termination shock (Treumann 2009). Moreover, some astrophysical supercritical shocks evolve into subcritical ones in the course of their interaction with the upstream medium and consequent loss of energy, as it happens for solar coronal mass ejections (CMEs; Bemporad and Mancuso 2011a). The collision of subcritical shocks are expected to occur between forward and reverse shocks in the solar wind and also between solar wind shocks and planetary bow shocks (Whang and Burlaga 1985).

Like their counterpart, namely supercritical shocks with $M_{ms} > M_{ms}^{cr}$, where ions can be accelerated through a variety of mechanism (Balogh and Treumann 2013; Marcowith et al. 2016a), subcritical shocks can also accelerate ions and induce thermal heating, although particle acceleration does not play a significant dissipative role in subcritical shocks. Both ion acceleration and heating have been observed in satellite crossings (Mellott 1984a). The underlying ion acceleration mechanism(s) is still up for debate, but it is suggested to include $\mathbf{v} \times \mathbf{B}$ heating (Ohsawa and Sakai 1985), ion reflection to a small degree from the shock front (Lee et al. 1987), and from other wave-particle interactions (Balikhin and Wilkinson 1996). As for particle acceleration from the collision of two subcritical shocks, no significant ion acceleration, with respect to the energies reached by particles accelerated by supercritical shocks, was observed in simulations (Cargill et al. 1986). Accelerated ions with energy in the tens of MeV have been measured from the collision of two subcritical shocks at a small angle

(Dudkin et al. 2000), however their numbers are extremely small and there is still an ongoing effort to determine the acceleration mechanism.

Here, we created in the laboratory subcritical perpendicular collisionless shocks, i.e., inside an external magnetic field perpendicular to the shock propagation direction. We characterized in detail their global spatio-temporal dynamics using multiple diagnostics. Moreover, we investigated the head-on encounter of two such shocks, in order to determine if and how this could modify the conditions under which ions can be energized in such a configuration. The shocks were characterized in the laboratory by interferometry and Thomson scattering (TS) measurements, performed at different times, which provided the electron density map, local electron density, and local ion and electron temperature. We then performed three-dimensional (3D) hydrodynamic simulations with the magnetohydrodynamic (MHD) code FLASH (Fryxell et al. 2000a), which reproduced the global dynamics of both the expanding plasmas driving the shock, as well as the latter. Next, we studied the event using the 1D3V fully kinetic Particle-In-Cell code SMILEI (Derouillat et al. 2018) where we used again the experimentally obtained parameters as initialization values. In these kinetic simulations, we observed acceleration of the ambient protons. The acceleration is initially due to the electrostatic field associated with the shock front E_x, then to the inductive electric field $E_y \sim v_x B_z$, where v_x is the flow velocity and B_z the perpendicular magnetic field. During the interaction between the two subcritical shocks, we note that both the presence of the downstream zone of the second shock and the creation of a downstream zone common for the two shocks play a role in the higher energization of the ambient ions: the characteristics of the perpendicular electric fields of these two areas allow, indeed, certain protons to keep being accelerated or to avoid being decelerated. As a result, ambient ions were energized to 1.5 times the energy of the single shock case. This is consistent with space measurements performed in-situ of ions accelerated ahead of outward propagating interplanetary shocks (Gosling et al. 1984), or in the interaction of an interplanetary shock with the bow shock of the Earth (Hietala et al. 2011).

4.1 Experimental setup and diagnostics

4.1.1 Laser and target conditions

The experiment on the collision between two shocks was performed on the facility LULI2000, with laser-target conditions similar to the ones of the single shock case treated in Chapter 3.
The setup employed in our experiment is shown in Fig. 4.1: we irradiated two Teflon (C_2F_4) targets with two high-power laser pulses (1053 nm wavelength, 1 ns, 100 J, 1.6×10^{13} W/cm^2 each). The

targets were tilted in a way that allowed the laser beams to reach them and such that the two plasma flows would encounter each other, as detailed in Fig. 4.2. The two targets were separated by a 9 mm distance. The region in between the targets was pre-filled with hydrogen at low density ($n_0 \sim 10^{18}$ cm^{-3}) injected by a gas nozzle and magnetized using an externally applied magnetic field of 20 T provided by a pulsed coil (Albertazzi et al. 2013), directed along the z-axis.

The pressure inside the nozzle was set the same as in the single shock case, leading to the gas (and, then, plasma) density profiles shown in Fig. 3.2–3.3.

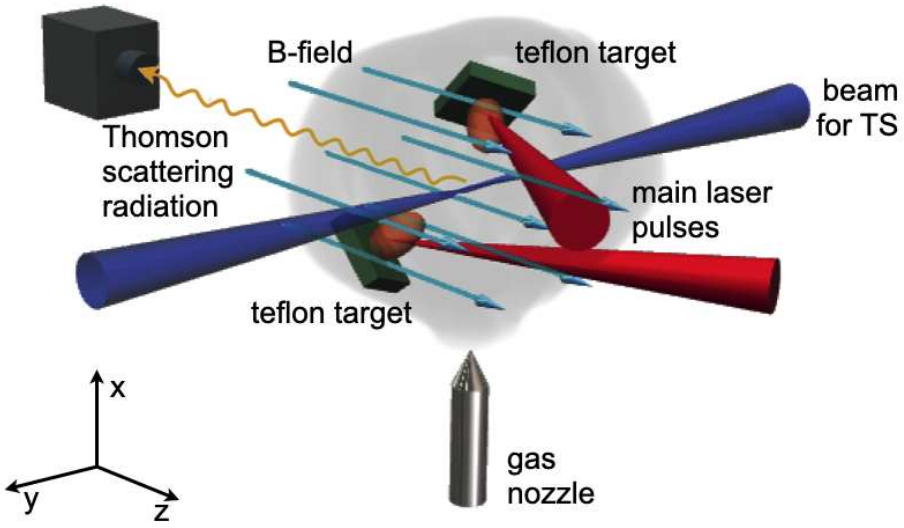

Figure 4.1: *Setup of the experiment, conducted at LULI2000 by having two high-power lasers (1 ns, 100 J at 1ω, 1.6×10^{13} W/cm^2 on target) irradiate two solid (Teflon, C_2F_4) targets to investigate the interpenetration of two magnetized shocks. An auxiliary beam of 15 J was used to perform Thomson scattering (TS) and an additional low energy beam (not shown in the picture for readability reasons) probed the plasma along a line titled 9º upwards with respect to the z-axis in order to measure the integrated plasma electron density.*

4.1.2 Optical probing

The plasma integrated electron density was measured via interferometry. This was performed with an optical probe beam ($\lambda = 530$ nm) passing with a 9° angle with respect to the B-field lines through the interaction zone (see Fig. 4.6). Also in this case, the chosen configuration was the Mach-Zehnder, as described in Sec. 2.2.1.

The presence of the magnetic field breaks once again the symmetry of the system, allowing only for a measurement of the integrated electron density and not a volumetric one.

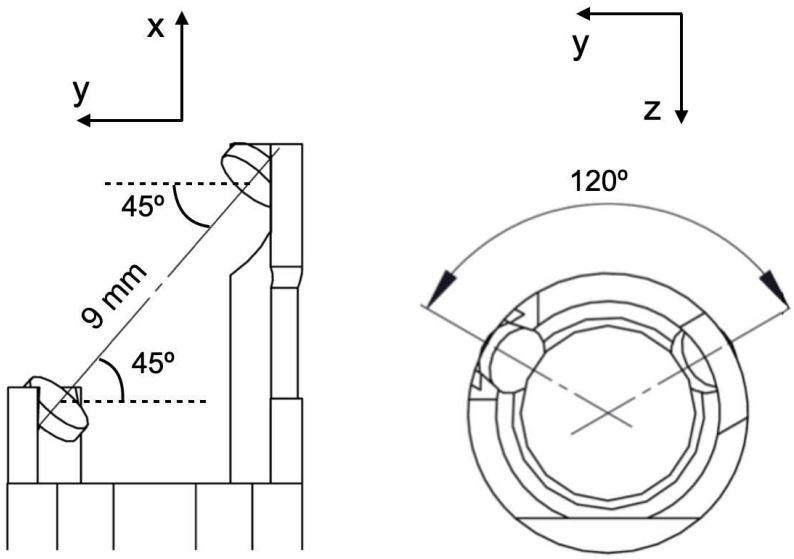

Figure 4.2: *Side (left) and top (right) view of the targets.*

4.1.3 Thomson scattering diagnostic

A high-energy auxiliary beam (527.5 nm wavelength, 1 ns, 15 J, focused over $\sim$ 40 µm along the y-axis and propagated throughout the plasma, see Fig. 4.1) was used to perform Thomson scattering (TS) measurements off the electron and ion waves in the plasma. It was used in a mode where the plasma was sampled in a collective mode (Froula et al. 2011b). The collection of the scattered light was performed at 90° (along the z-axis) from the incident direction of the laser probe (the y-axis). The light scattered off the ion (TSi) and electron (TSe) waves in the plasma was analyzed by means of two different spectrometers, set to different dispersions (3.1 mm/nm for TSi and 7.5×10^{-2} mm/nm for TSe), which were coupled to two streak-cameras (Hamamatsu for TSe, and TitanLabs for TSi, both equipped with S-20 photocathode to be sensitive in the visible part of the spectrum, and both with typical 30 ps temporal resolution), allowing us to analyze the evolution of the TS emission in time. The scattering volumes sampled by the instruments were: 120 µm along the x- and y-axes, 40 µm along the z-axis for TSi; 100 µm along the x- and y-axes, 40 µm along the z-axis for TSe. The analysis of the Thomson scattered light was performed by comparison of the experimental images (recorded by the streak cameras) with the theoretical curves of the scattered spectrum for coherent TS in non-collisional plasmas, with the instrumental function width of 5.9 nm for the electron spectrometer and 0.12 nm for the ion spectrometer taken into account. We remind that the TS laser probe induces some heating in the hydrogen ambient gas (details can be found in Sec. 3.2.2). With TS, we can get a spatially and temporally resolved measurement of the plasma density and temperature.

4.1.4 X-ray spectroscopy

A focusing spectrometer with spatial resolution (FSSR) (Faenov et al. 1994) was employed to register x-ray ion emission of the plasma with and without ambient medium. It allowed to characterize both the plasma initiated by the laser interaction at the surface of each target, and the heating of the ambient medium induced by the expanding plasmas. The spectrometer was equipped with a spherically bent mica crystal, as detailed in Sec. 2.2.5. A spatial resolution about 0.1 mm was achieved along the axis which joins the centers of the two targets (see the blue line in Fig. 4.4 (d)). The presence of Sulfur impurities in the targets allowed us also to register a corresponding He-like doublet (2p–1s transition) in the third order of reflection with a Li-like satellite structure being sensitive in our range of plasma parameters. Spectral resolution was achieved better than $\lambda/d\lambda = 1000$. The spectra were recorded using Fujifilm Image Plates of type TR, which were placed in a cassette holder protected from the visible optical radiation. The signal is time-integrated. The analysis of x-ray spectra was done by comparison of the experimental line ratios with simulated ones using the radiative-collisional code PrismSPECT (MacFarlane et al. 2003) and by comparison of emissivity profiles in different conditions.

4.1.5 Ion spectrometry

Finally, an ion spectrometer with a permanent magnet of 0.5 T, as described in Sec. 2.2.4, was employed along the z-axis in an alternate mode to the TS diagnostic. Its configuration was exactly the same as the one used in the single shock case, since here we were using the same setup and simply shooting two lasers at the same time.

4.2 Experimental results

The electron temperature on the target surface was measured via FSSR by recording the emission of Sulfur lines and by simulating this emission in a steady-state approach using the code PrismSPECT (MacFarlane et al. 2003). This is shown in Fig. 4.3, yielding for the surface plasma a temperature $T_e = 550$ eV at almost critical density $N_e = 7 \times 10^{20}$ cm^{-3}. We point out that this measurement is relative to the laser-target interaction, i.e., to the collisional part of the system.

After the plasmas have been generated at the surface of each target, they expand into the ambient medium. This expansion is monitored by optical probing. This is displayed in Fig. 4.4, which shows the measurements, at successive times, of the integrated (along the line-of-sight of the probe beam) electron density of the plasmas expanding from both targets. We point out that these images were obtained on different shots. As seen in our previous experiment where we created one single magne-

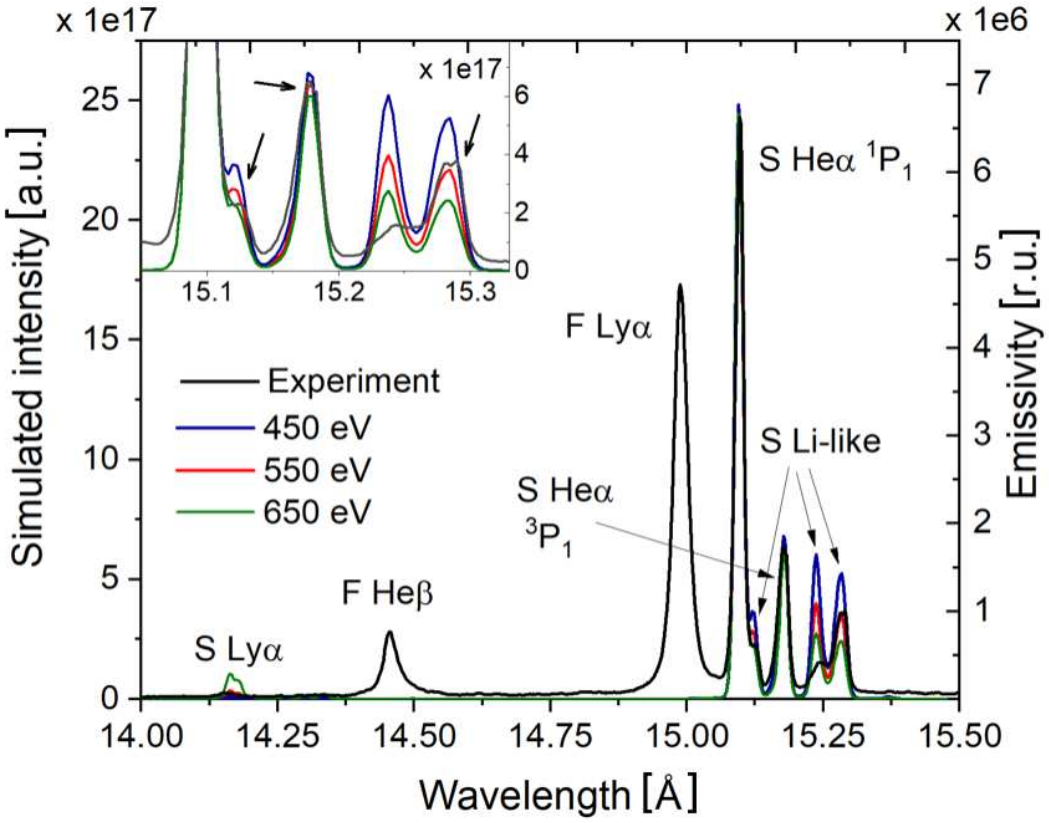

Figure 4.3: *Experimental x-ray spectrum (black line) measured by the FSSR spectrometer as emitted from a CF_2 target. What is recorded is the spectrum of Sulfur impurities in the third order of reflection. Overlaid are simulations performed using the PrismSPECT code (red, olive and blue curves) for the target surface region, using the group of satellites sensitive to the plasma parameters. For all temperatures shown in the figure, the electron density was $N_e = 7 \times 10^{20}$ cm^{-3}. All curves are normalized to the S He$_\alpha$ line. The best fitting corresponds to the red curve. The inset shown in the top left corner demonstrates the detailed fitting of the satellites of the experimental spectrum. The arrows point to the lines having the best fit.*

tized shock (see Chapter 3), two structures develop out of each target: a piston front and a shock front characterized by two separated bumps of higher electron density (identified by arrows in Fig. 4.4 (b) and Fig. 4.5). Each piston is the result of the expansion of the plasma ablated from the solid target by each laser. The plasma flows expand in the low-density ambient hydrogen, which is quickly ionized by the x-rays produced by the irradiated targets, and shocks are generated as a result of the combined action of the supersonic piston expansion and of the externally applied B-field. In fact, the strong external magnetic field of 20 T is critical in providing additional pressure so that a magnetized shock can form in the hydrogen plasma (Yao et al. 2021), as in its absence we would get a shock only in the presence of a denser background plasma. As a result, for early times, i.e., before $\sim$ 12 ns, we observe two well-developed shocks propagating against each other.

In our situation, the shocks are perpendicular, i.e., the angle between the magnetic field and the shock propagation direction is $\theta_{Bn} \approx 90°$, and are characterized by a $\beta = P_{therm}/P_{mag} \approx 0.1$, hence the

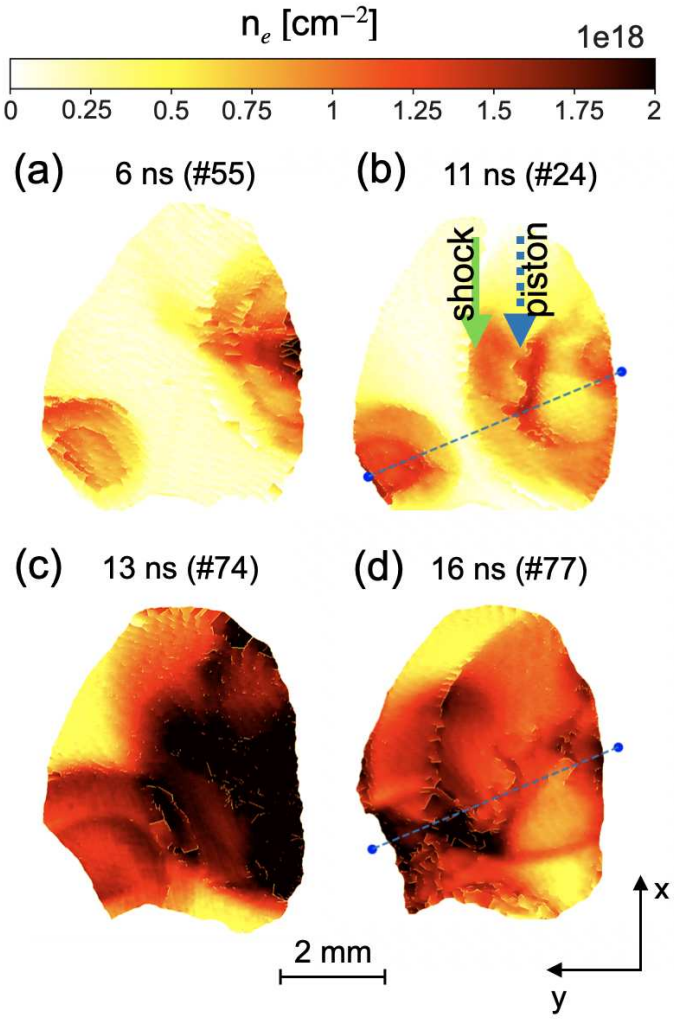

Figure 4.4: *Temporal sequence of integrated (along the z-axis, with a 9° tilt) electron density measurements showing the evolution of the interpenetration of two magnetized shocks, at 6 ns (a), 11 ns (b), 13 ns (c), and 16 ns (d), after the main laser pulses hit the targets. The aperture of the magnetic coil structure restrained the passage of the optical probe, diminishing slightly the field of view (FoV) in (a-d). Before the interpenetration of the two plasma flows, a shock front and a piston develop out of each target, as indicated by the two arrows in (b): the dotted blue arrow points at the left-drifting piston and the solid green arrow at the left-drifting shock front. The profiles of plasma integrated density along the lines in (b) and (d) are reported in Fig. 4.5.*

critical Mach number has a value $M_{ms}^{cr} \sim 2.6$ (Edmiston and Kennel 1984b). The shocks obtained in our experiment are supercritical up to 3-4 ns after the laser beams hit the targets and turn into subcritical for later times (Yao et al. 2021). Indeed, they propagate with an initial velocity of $v_s \approx$ 1500 km/s, which corresponds to $M_{ms} \approx 3.3 > M_{ms}^{cr}$, and when they eventually interact, they have a velocity of a few hundreds of km/s, which gives, for $v_s \approx 500$ km/s, $M_{ms} \approx 1.1 < M_{ms}^{cr}$. We point out that the measurements of shock velocity are obtained from the interferograms by measuring the positions at different times, which correspond also to different shots. As we can observe, the structures developing from the two targets have different sizes: they start forming at the same time, but

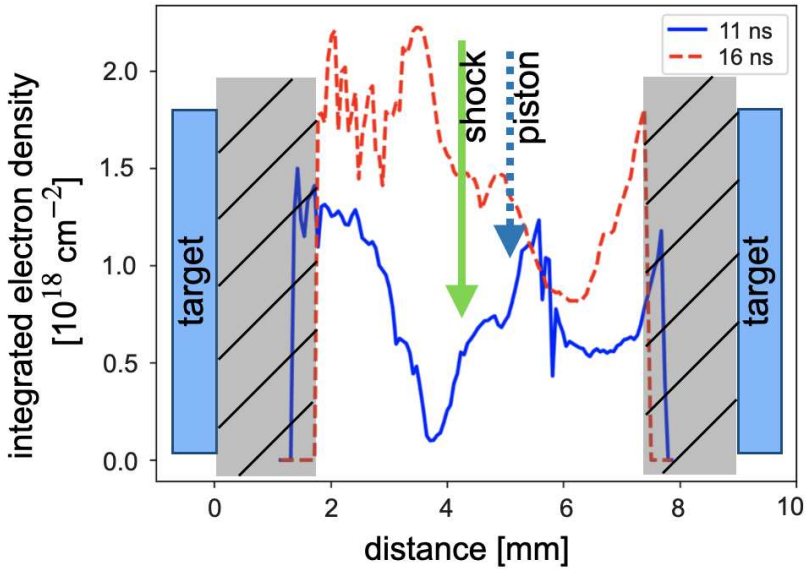

Figure 4.5: *Lineout of the integrated electron density at 11 ns (blue solid line) and at 16 ns (red dashed line), along the lines shown on the relative maps in Fig. 4.4 (b) and (d), respectively; the location of the targets at 9 mm distance from each other is also shown, while the gray dashed areas represents the zones out of the FoV. Before the interpenetration of the two plasma flows, a shock front and a piston develop out of each target, as indicated by the two arrows: the dotted blue arrow points at the left-drifting piston and the solid green arrow at the left-drifting shock front.*

their different distance from the gas nozzle exhaust makes them propagate in a medium of slightly different density which has a visible impact on their propagation velocities. Moreover, the fact that the two shocks do not propagate directly against each other, but perpendicularly to the targets, has also been taken into account while calculating the velocity. Indeed, the interferometry view corresponds to the side view (apart for a $\sim 9°$) of Fig. 4.2, which is a projection of the displacements along the z-axis. Hence, the distances extracted from the interferometry figures have been multiplied by a factor of $1/\cos(60°) = 2$.

As for the collisionality, we find that the mean-free-path of the drifting ions with respect to the ambient ones is $\lambda_{mfp}^{i-i\,(d-a)} \approx 33$ mm (calculated according to Braginskii 1965), which is much larger than the characteristic length over which the interaction takes place ($\sim$ hundreds of μm) and hence makes the shock collisionless.

Moreover, we measured the plasma Thomson scattering of the plasma thermal waves to assess the plasma characteristics. Fig. 4.6 shows two examples of TS spectra from electron plasma waves ((a) and (c)) and from ion acoustic waves ((b) and (d)), corresponding to 15 ns and the period from 13 ns to 16 ns, respectively. The temporal evolution of the electron density, the electron temperature, and ion temperature is shown in Fig. 4.7. We observe that after around 13 ns the TSi signal suddenly broadens, which corresponds to the time of the collision between the two shocks. This broadening is

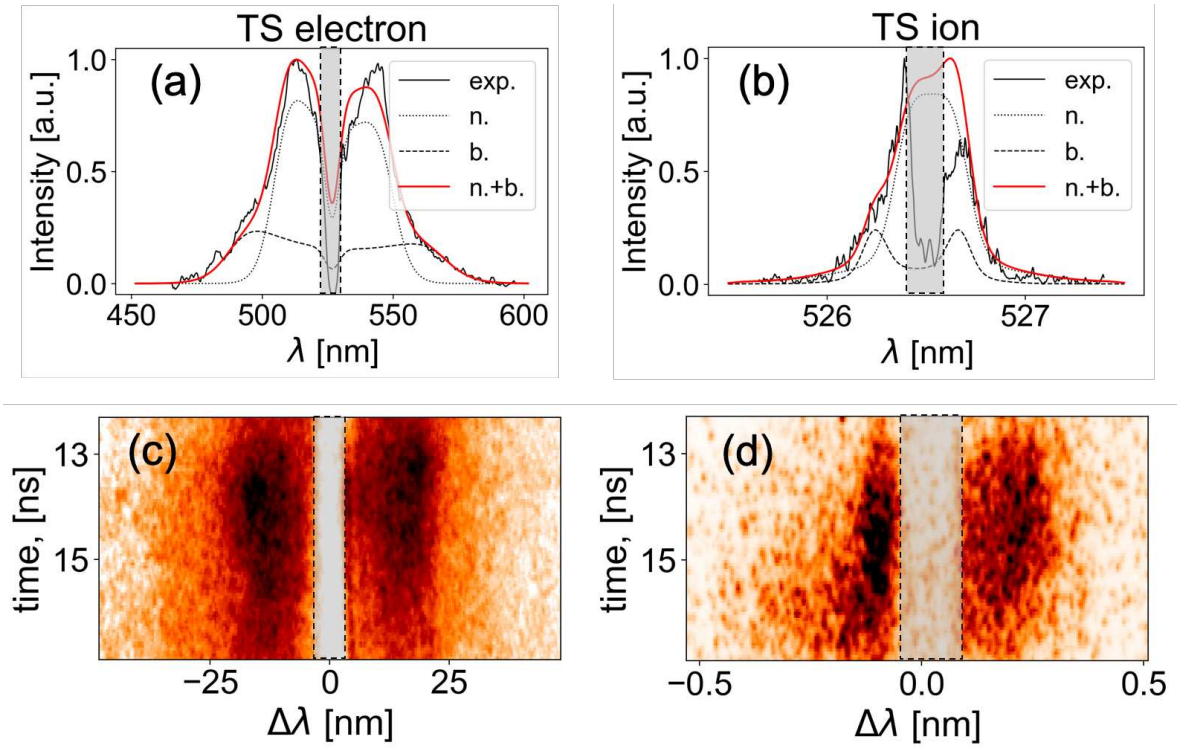

Figure 4.6: *Thomson scattering measurements of the plasma density and temperatures in the region of shock collision. Spectra of Thomson scattering off electron plasma waves ((a),(c)) and ion acoustic waves ((b),(d)). (a) and (b) show the spectra profiles, corresponding to 15 ns, while (c) and (d) show the temporal evolution of the scattering spectra over a time period from 13 ns to 16 ns for the electron plasma and ion acoustic waves, correspondingly. Black solid lines (in (a) and (b)) are for experimental data profiles, while red solid lines are for theoretical spectra, composed of a superposition of narrow (black dotted lines) component relative to the ambient medium, having density 1.5 $\times 10^{18}$ cm^3, electron temperature 100 eV, ion temperature 200 eV, and broad (black dashed lines) component relative to the piston plasma, having density 6 $\times 10^{18}$ cm^3, electron temperature 300 eV, ion temperature 100 eV. The ratio between the magnitudes of the narrow and broad components is 3.5. We note that the deep central dip in the experimental spectra ((a),(b)) and the white vertical region in the streak-camera images ((c),(d)) is related to a filter (a black aluminum stripe) which is positioned right before the entrance of the two streak cameras (recording respectively the light scattered off the electron and ion waves). This filter is used to block the very intense and unshifted laser wavelength (the Rayleigh-scattered light), which otherwise would saturate the cameras. Thus, no signal is recorded in this zone, which is materialized by the grey dashed box.*

attributed to the heating of the ions in the plasma due to the energy released when the two plasma bubbles collide. As is shown in the time evolution in Fig. 4.7, after the collision, the electron density slightly increases, while the electron temperature remains initially unperturbed (around 80 eV). The interpenetration of the two plasma shocks heats the ions up to temperatures ≈ 135 eV, according to an adiabatic gas compression. Electrons are then heated at a slower rate by ion-electron collisions. Further increase of ion and electron temperature as well as electron density is observed when the pistons collide at a later time (~ 14.5 ns). Here, we will only focus on the shock-shock collision, before the encounter of the pistons.

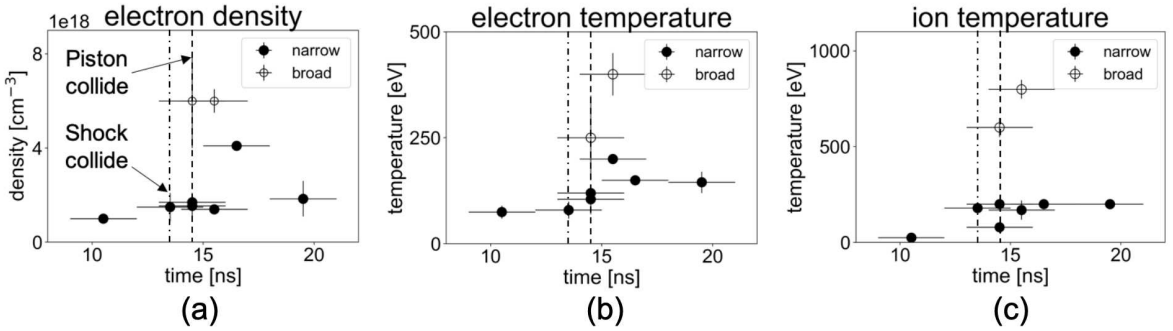

Figure 4.7: *TS measurements of the temporal evolution of electron density* (a)*, electron temperature* (b)*, and ion temperature* (c)*. The narrow and broad configurations are respectively related to the ambient and piston plasmas* (*see caption of Fig. 4.6*)*.*

Characterized Ambient Plasma Conditions	
Upstream Elec. Number Density n_e [cm^{-3}]	1.0×10^{18}
Upstream Elec. Temperature T_e [eV]	80
Upstream Ion Temperature T_i [eV]	20
Downstream Elec. Temperature T_e [eV]	130
Downstream Ion Temperature T_i [eV]	200
Shock Velocity at meeting point v_s [km/s]	~ 500
Upstream Magnetic Field Strength B_z [T]	20
Calculated Parameters	
Ion Collisional mean-free-path $\lambda_{mfp}^{i-i\,(d-a)}$ [mm]	33
Flow Ion Larmor Radius $r_{L,i,fl}$ [mm]	0.26
Upstream plasma Thermal Beta β_{ther}	0.10
Mach Number M	4.42
Alfvénic Mach Number M_A	1.15
Magnetosonic Mach Number M_{ms}	1.12

Table 4.1: *List of parameters extracted from our measurements at* ~ 11 *ns, i.e., right before the interpenetration of the two shock structures.* $\lambda_{mfp}^{i-i\,(d-a)}$ *is the collisional mean free path between drifting and ambient ions.*

Complementary to the TS measurements, Fig. 4.8 shows the x-ray emissivity profiles of the plasma located in between the two targets. We compare three cases: (1) when the applied magnetic field and the ambient medium are present and the plasmas expand from the two targets (thin red line), (2) still with two plasmas, but in the absence of the ambient medium (dashed black line), and (3) when only one plasma is flowing from either the right or the left target, but in the same magnetic field and ambient medium conditions as in case (1) (thin gray lines, with areas filled by patterns). What we observe is that the collision between the two plasma flows results in an emission enhancement in the zone between the two targets (compare the red curve to the filled areas). Here the left target has a lower intensity due to the positioning of the corresponding part of the spectrometer in the "shadow zone" of the right target. The electron temperature was measured in this region as $T_e = 240$ eV (a lower-limit estimate) at an electron density $n_e = 10^{18}$ cm^{-3} using the ratio between the resonance lines Ly$_\alpha$ and He$_\beta$ by the method described in (Khiar et al. 2019a), in reasonable agreement with the

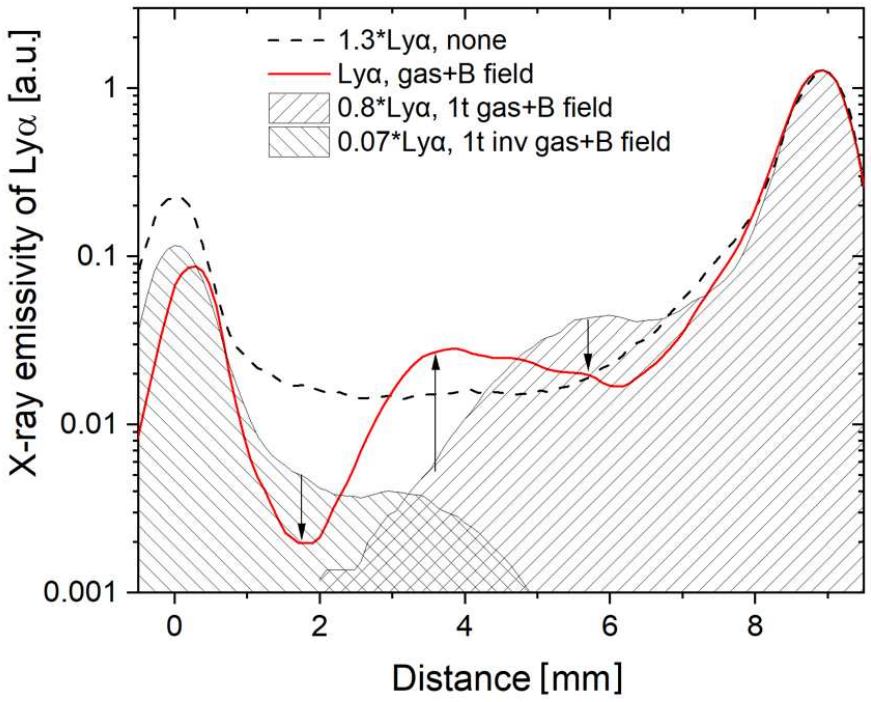

Figure 4.8: *X-ray emissivity profiles measured by the FSSR spectrometer in different cases. First when two plasmas expand from the two targets, either in the absence (dashed black line) or presence (red line) of the ambient medium. The gray curves with a pattern correspond to a single target case as a reference. In all cases, the magnetic field is present. All curves are normalized to the right target emissivity. The emissivity for the left target is the inverted right one with a multiplier taking into account the signal reduction due to the location of a part of the spectrometer in the shadow zone.*

TS measurements, knowing that the x-ray diagnostics is time-integrated. In addition, one can note that the emissivity drops significantly faster between the target and the middle zone in the case when the ambient medium is applied which is most probably related to a faster recombination rate as well as to a higher confinement of particles close to the target (Filippov et al. 2021).

The main plasma parameters extracted from the experimental measurements are summarized in Table 4.1. These values are used to initialize our simulations detailed below, which we use to further investigate the particle acceleration during the shock collision.

4.3 Numerical simulations

Our simulation effort is two-fold: the first step was to undertake MHD simulations of the laser-driven plasma expansion and interaction with the ambient gas and magnetic field, leading to the experimentally observed piston. In the second step, we have used the results of the experimental diagnostics as a starting point for kinetic simulations that allow us to investigate in details the microphysics of the

shocks colliding and the underlying particle acceleration mechanisms.

4.3.1 MHD simulations using the FLASH code

The experiment was first modeled with the 3D MHD code FLASH (Fryxell et al. 2000a). We model the formation and the propagation of pistons and shocks generated by the laser interaction with two Teflon targets having the same arrangement as shown in Fig. 4.2. However, to reduce the computational cost, the separation between the targets is here limited to 6.5 mm, instead of 9 mm as in the experiment. As in the experiment, the targets are embedded inside an ambient hydrogen gas-jet within an external magnetic field. The laser intensity, the hydrogen gas-jet density, and the external magnetic field strength are the same as in the experiment.

Fig. 4.9 shows the electron density time evolution in the case with the external magnetic field (20 Tesla), i.e., before the shocks collision at t = 5.8 ns, at collision time t = 7.2 ns and after the collision at t = 7.8 ns, respectively. Due to the reduced distance between the targets used in the simulation, to scale it with the experiment, the collision time should be scaled by a factor 1.4, resulting in a scaled collision time of 10 ns, which is quite close to the experimentally observed one ($\sim$ 12 ns). When the two shocks collide, the electron density increases only of 20%. The pistons expand more slowly due to the increase of the magnetic pressure behind the shock.

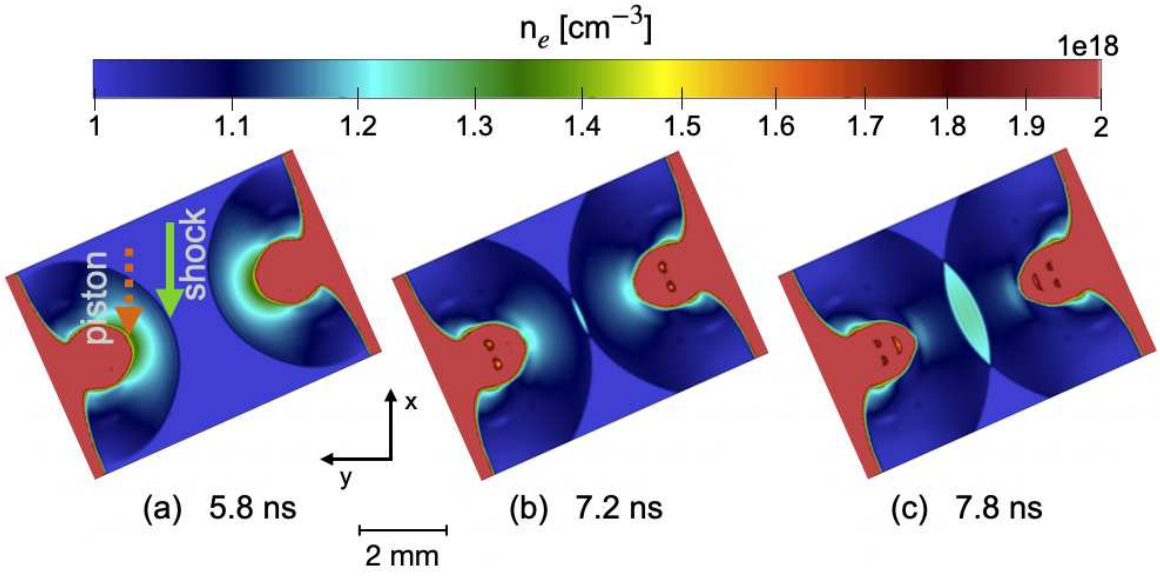

Figure 4.9: *Simulation, using the 3D MHD code FLASH, of the volumetric electron density plotted at $t = 5.8$ ns (a), $t = 7.2$ ns (b), and $t = 7.8$ ns (c), along the laser beams direction, with external magnetic field $B = 20$ T.*

These hydrodynamic simulations performed with FLASH are capable of describing the overall dynamic of the system, but they were not able to quantitatively reproduce the temperatures measured

in the experiment (Yao et al. 2021), likely due to the fact that the kinetic effects associated to our collisionless system cannot be taken into account. That is why we have performed also PIC simulations to take them into account.

4.3.2 PIC simulations using the SMILEI code

The interaction between the two subcritical shocks has been modeled via the fully kinetic Particle-In-Cell code, SMILEI (Derouillat et al. 2018), for which we used the profiles of plasma density, temperature, and the magnetic field extracted from the experimental data as initial conditions (see Table 4.1). We simulated such a system in a 1D3V geometry, as the scale of the shock front interaction with the ambient medium is much smaller across the shock (a few hundreds of microns) than along the shock (a few mm). We point out that our PIC simulations are dedicated to capture only the kinetic effects of the shock colliding process. The laser-target ablation and piston formation are well-reproduced by the FLASH simulations and the shock formation and transition from supercritical to subcritical is detailed in our previous papers (Yao et al. 2021, 2022).

In order to understand the effects of the collision of two shocks, both a single drifting shock con-

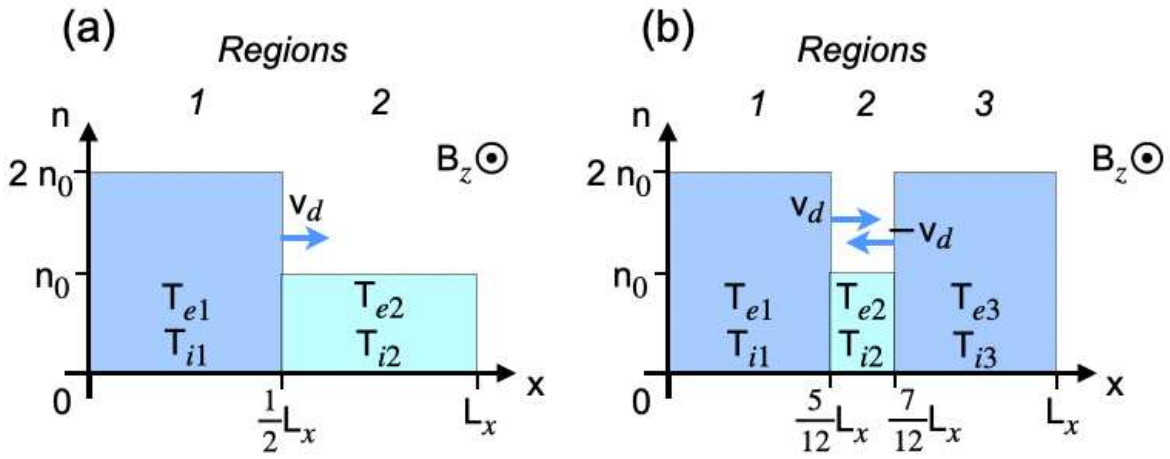

Figure 4.10: *1D PIC simulations initialization setups. (a) Single-shock case: a hydrogen plasma ($n_1 = 2n_0 = 2 \times 10^{18}$ cm^{-3}, $T_{e1} = 130$ eV and $T_{i1} = 200$ eV) drifts through a background hydrogen plasma ($n_1 = n_0 = 1 \times 10^{18}$ cm^{-3}, $T_{e2} = 80$ eV, and $T_{i2} = 20$ eV) with a drifting velocity of $v_d = 350$ km/s (see Table 4.2). (b) Double-shock case: a background plasma ($n_2 = n_0 = 1 \times 10^{18}$ cm^{-3}, $T_{e2} = 80$ eV, and $T_{i2} = 20$ eV) is set at rest between two counter-streaming denser plasmas ($n_1 = n_3 = 2n_0 = 2 \times 10^{18}$ cm^{-3}, $T_{e1} = T_{e3} = 130$ eV and $T_{i1} = T_{i3} = 200$ eV). The drifting velocity $v_d = 350$ km/s imposed to the plasma (in Regions 1 and 3) for both configurations leads to a shock velocity of $v_s \approx 640$ km/s. The simulation is initialized ~ 11 ns after the lasers have started ablating the targets, with a distance of 1.8 mm in between the two shock fronts, while the box has a total length $L_x = 11$ mm.*

figuration and a double counter-streaming shocks scenario have been simulated. The initial configurations are drawn in Fig. 4.10. The box has a length $L_x = 2048\, d_e \approx 11$ mm and the spatial resolution is $d_x = 0.2 d_e \approx 1.1$ µm, where $d_e = c/\omega_{pe} \approx 5.3$ µm is the electron inertial length, and

$\omega_{pe} = \sqrt{n_0 q_e^2/(m_e \epsilon_0)} \approx 5.6 \times 10^{13}$ rad/s is the electron plasma angular frequency. Here, c is the velocity of light, $n_0 = 1.0 \times 10^{18}$ cm^{-3} is the electron (and proton) number density of the ambient plasma, and m_e, q_e and ϵ_0 are the electron mass, the elementary charge, and the permittivity of free space, respectively. We point out that the x-axis we are talking about here in the case of PIC simulation does not correspond to the one relative to the experimental setup (used in Fig. 4.1, 4.2, 4.4, and 4.5) and to the FLASH simulations (Fig. 4.9). In our PIC simulation, the x-axis is the axis along which the two shocks propagate. Each cell has 1024 particles plus 1 tracked particle for each species. Moreover, an external uniform magnetic field $B_{z0} = 20$ T is set in the z-direction perpendicular to the plasma velocity ($\omega_{ce}/\omega_{pe} = 0.06$, where $\omega_{ce} = q_e B_{0z}/m_e$). The simulation lasts for $1.5 \times 10^5 \omega_{pe}^{-1} \approx 2.5$ ns, with an initial time that corresponds to ~ 11 ns in the experiment, i.e., ~ 1 ns before the shocks collide. In short, the simulation covers time between 11 and 13.5 ns of the experiment. These times will be used below for better comparison with the experiment.

We have initialized the system with different portions of plasma, all composed of protons and electrons with $m_p/m_e = 1836$. For a single subcritical shock, we have set from 0 to $\mathrm{L}_x/2$ (Region 1 in Fig. 4.10(a)) a hydrogen plasma drifting towards positive x with a velocity $v_x = v_d = 350$ km/s and density $n_1 = 2n_0 = 2 \times 10^{18}$ cm^{-3}, while between $\mathrm{L}_x/2$ and L_x (Region 2) we put a background hydrogen plasma with density $n_2 = n_0$ at rest. In the case of double shock, we set two counter-streaming hydrogen plasmas with densities $n = 2n_0$ moving in the x-direction at velocities v_d and $-v_d$ between 0 and 5 $\mathrm{L}_x/12$ (Region 1 in Fig. 4.10) and between 7 $\mathrm{L}_x/12$ and L_x (Region 3), respectively. Moreover, a background hydrogen plasma with density n_0 was set at rest in between (Region 2). As for the temperature, we have used the results of the TS diagnostic in the experiment for both simulations, i.e., $T_{e1} = T_{e3} = 130$ eV and $T_{i1} = T_{i3} = 200$ eV for the drifting plasmas, and $T_{e2} = 80$ eV and $T_{i2} = 20$ eV for the background plasma. The list of parameters used to initialize our simulations is summarized in Table 4.2.

Fig. 4.11 shows the spatial profiles of ion density, magnetic field B_z, and electric fields E_x and E_y, for both single shock and double shock simulations. We point out that the profiles relative to the single shock have been shifted by $\Delta x = -\mathrm{L}_x/12$ in order to simplify the comparison. In Fig. 4.11 (a) at 1 ns (≈ 12 ns for the experiment), we clearly see that the shock formation and propagation happens in the same way for both the single shock case and the double shock case, as the profiles relative to the single shock overlap the ones of the right-drifting shock in the double shock case. In other words, the presence of the left-drifting shock has no effect on the evolution of the right-drifting one yet and vice versa. In the downstream regions, we note the spontaneous formation of fast magnetosonic waves propagating away from the shock fronts (Moreno et al. 2019). We point out that in the double-shock

PIC initialization parameters	Regions	
	1 and 3	2
v_d [km/s]	350	0
v_s [km/s]	640	0
B_{z0} [T]	20	20
T_e [eV]	130	80
T_i [eV]	200	20
n_i [10^{18} cm^{-3}]	2	1
v_A [km/s]	308	436
c_s [km/s]	144	102
c_{ms} [km/s]	340	448
r_{Li} [mm]	0.26	0.39
$\lambda_{mfp}^{i-i\,(d-a)}$ [mm]	33	
M_{ms}	1.43	

Table 4.2: *List of parameters we have used to initialize our PIC simulations. Regions 1 and 3 correspond to the drifting hydrogen plasmas, while Region 2 is relative to the background hydrogen plasma at rest. $\lambda_{mfp}^{i-i\,(d-a)}$ is the mean free path relative to the collisions between drifting and ambient ions, while M_{ms} is the magnetosonic Mach number of the shock wave moving at speed $v_s = 640$ km/s in the ambient plasma characterized by a magnetosonic speed $c_{ms} = 448$ km/s. We point out that the values relative to the Regions 1 and 3 refer only to the initial situation, before the shocks completely form, hence they are not to be confused with the parameters of the downstream region at a certain time.*

case the electric field components E_x and E_y of the right-drifting shock and the left-drifting one have opposite direction: the shock coming from the left is characterized by oscillations starting with a positive peak of E_x at the shock front and by a downstream region with $E_y > 0$, while the shock coming from the right has oscillations starting with a peak $E_x < 0$ at the shock front and a field $E_y < 0$ in the downstream region.

In Fig. 4.11 (b) at 1.5 ns ($\approx$ 12.5 ns for the experiment), the interaction of the two shocks has begun: the ion density and magnetic field start overlapping, and, at longer times not shown here, they keep piling up, reaching values of $n_i \approx 5 \times 10^{18}cm^{-3} = 5\, n_0$ and $B_z \approx 50$ T $= 2.5\, B_{z0}$ at ~ 2.2 ns (≈ 13.2 ns in the experiment). The x-component of the electric field E_x fluctuates around 0 and has peaks of ~ 100 MV/m associated with the shocks. After the interpenetration of the two shocks, E_x reaches values of ~ 250 MV/m. The only contributions to the y-component E_y is the inductive electric field $E_y = -(\mathbf{v} \times \mathbf{B})_y = v_x B_z$ (Ilie et al. 2017) and it, too, has a fluctuating profile, centered on 0 in the upstream regions and on $\sim \pm\, 8$ MV/m in the downstream ones. Between these two zones, E_y passes gradually from 8 MV/m (or -8 MV/m) to 0, as the plasma velocity distribution decreases (increases) and the magnetic field increases (decreases), even after the two shocks have met.

By tracking a set of representative protons, we have been able to understand the energization mechanism undergone by the most energetic ones, i.e., the ones reaching a kinetic energy of $E_k > 10$ keV. In Fig. 4.12 (a) and (b) we show the motion in the v_x-v_y space of protons from the drifting

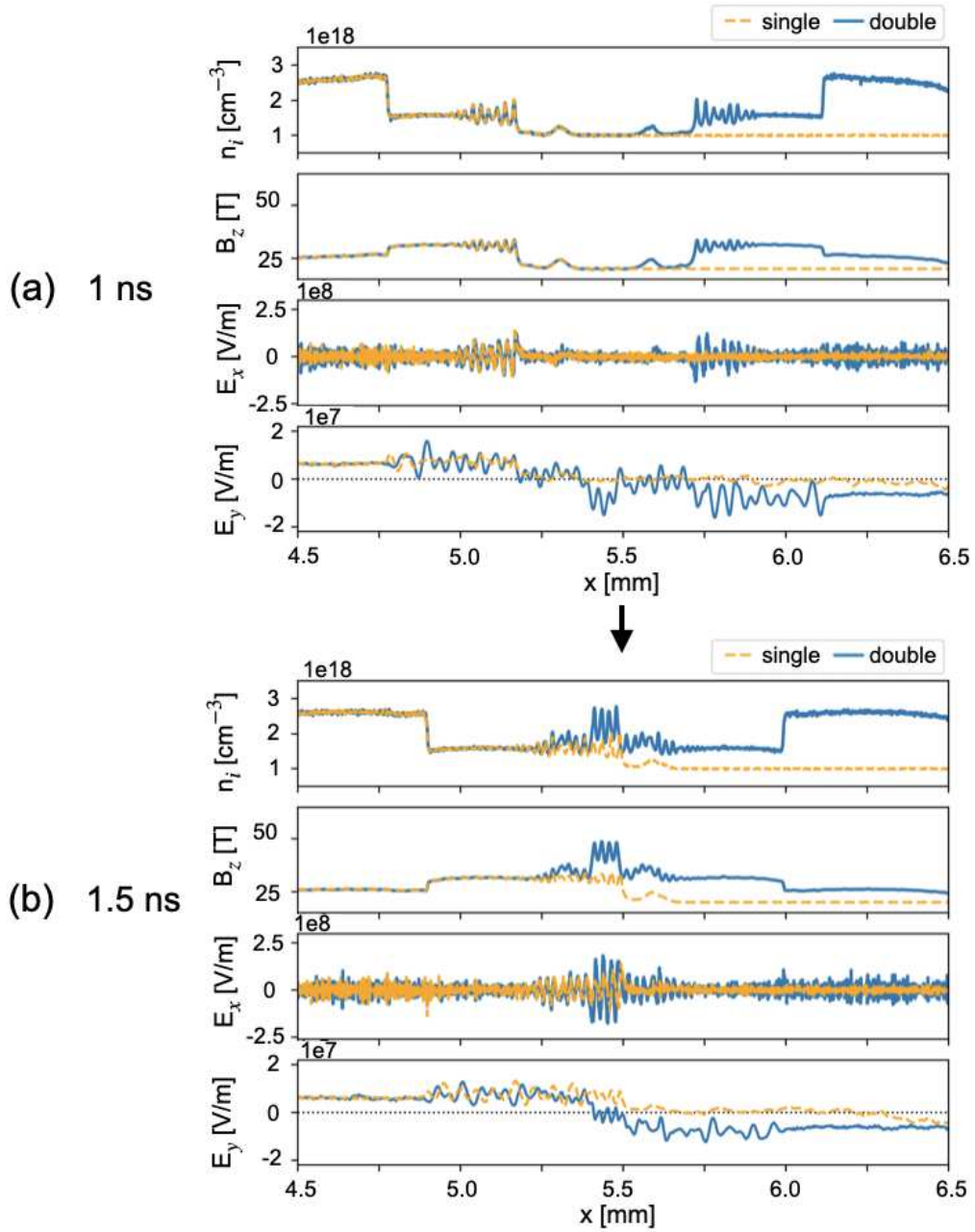

Figure 4.11: *Profiles of ion density, magnetic field B_z, and electric fields E_x and E_y at times 1 ns (a) and 1.5 ns (b) after the beginning of the simulation. At 1 ns ($\approx$ 12 ns for the experiment), the two fast shocks propagate without perturbing each other, as their profiles correspond to the one of the single shock case. At 1.5 ns ($\approx$ 12.5 ns for the experiment), the interaction between the two shocks makes the ion density and the magnetic field B_z increase and pile up in the middle; the electric field E_x presents several spikes also due to the interaction between the downstream fast magnetosonic waves; the inductive E_y does not drastically change structure or magnitude, but it presents opposite signs in the downstream regions depending on the propagation direction of the shock. We point out that the profiles relative to the single shock have been shifted of $\Delta x = -L_x/12$ in order to simplify the comparison.*

and the ambient plasma, respectively. For clarity, we have plotted for each plasma only one particle for each case, but we have checked that these trajectories are well representative of all other tracked

particles coming from the same populations. We observe that the protons of the drifting plasma, having initially a bulk velocity $v_x = 350$ km/s, rotate in the v_x-v_y space, without showing any special difference between the single and double shock cases.

The situation is definitely different for the protons of the ambient plasma: after starting at rest, the protons are accelerated by the shocks up to kinetic energies that, in the double shock case, are around 1.5 times higher than the single shock case. This difference is well presented by the proton spectra at the final simulation time shown in Fig. 4.12 (c) and, zoomed, in Fig. 4.12 (d), where to higher energies are associated higher distribution values in the double-shock case.

By comparing the cases with one and two subcritical shocks, we could understand the reason of the higher energization in the double shock case by analyzing the dynamics of such energetic tracked particles. Let us start considering the protons of the ambient plasma whose dynamics is reported in Fig. 4.12 (b). For the proton from the single shock case, we have analyzed its motion in the in x-t space over a map of E_x and a map of E_y (Fig. 4.13 (a1) and (b1), respectively), and in the v_x-v_y space (Fig. 4.13 (c1)), where the color of the proton trajectory follows a scale based on its kinetic energy K. Moreover, we have compared the temporal evolution of the proton kinetic energy and the work done by E_x and E_y on it as shown in Fig. 4.13 (d1). On these four graphs (a1-d1) we have distinguished the presence of three phases corresponding to different regimes experienced by the proton.

In phase I, the proton is accelerated by the electrostatic field E_x associated with the shock front, it gains a velocity $v_x > 0$ and starts rotating in the upstream plasma. While gyrating clockwise due to the applied magnetic field B_z, its velocity in the x-direction v_x decreases and the proton meets again the shock front. After crossing it, in phase II, the proton is in the downstream region characterized by $E_y > 0$. Since it has a $v_y < 0$, the positive E_y does a negative work on the proton and lowers its kinetic energy, as can be seen in Fig. 4.13 (d1). In phase III, the particle has again a velocity $v_y > 0$, hence the positive $E_y > 0$ does a positive work on the proton and keeps energizing it.

We have conducted a parallel analysis on the proton from the ambient plasma in the double shock case and plotted the results on the right column of Fig. 4.13: (a2) and (b2) show its motion in the x-t space over a map of E_x and E_y, respectively; (c2) shows its trajectory in the v_x-v_y space; (d2) shows the temporal evolution of the particle kinetic energy and the work made on it by E_x and E_y. The color of the proton trajectory in Fig. 4.13 (a2)-(c2) follows the same kinetic energy scale used for the single shock case. We can now distinguish four different regimes for the tracked proton. In phase I, similarly to what happens in the single shock case, the proton is accelerated by the right shock front and rotates in the upstream region. Phase II*a and II*b are due to the presence of the second shock (coming from the right side) and hence are different to phase II in the single shock scenario.

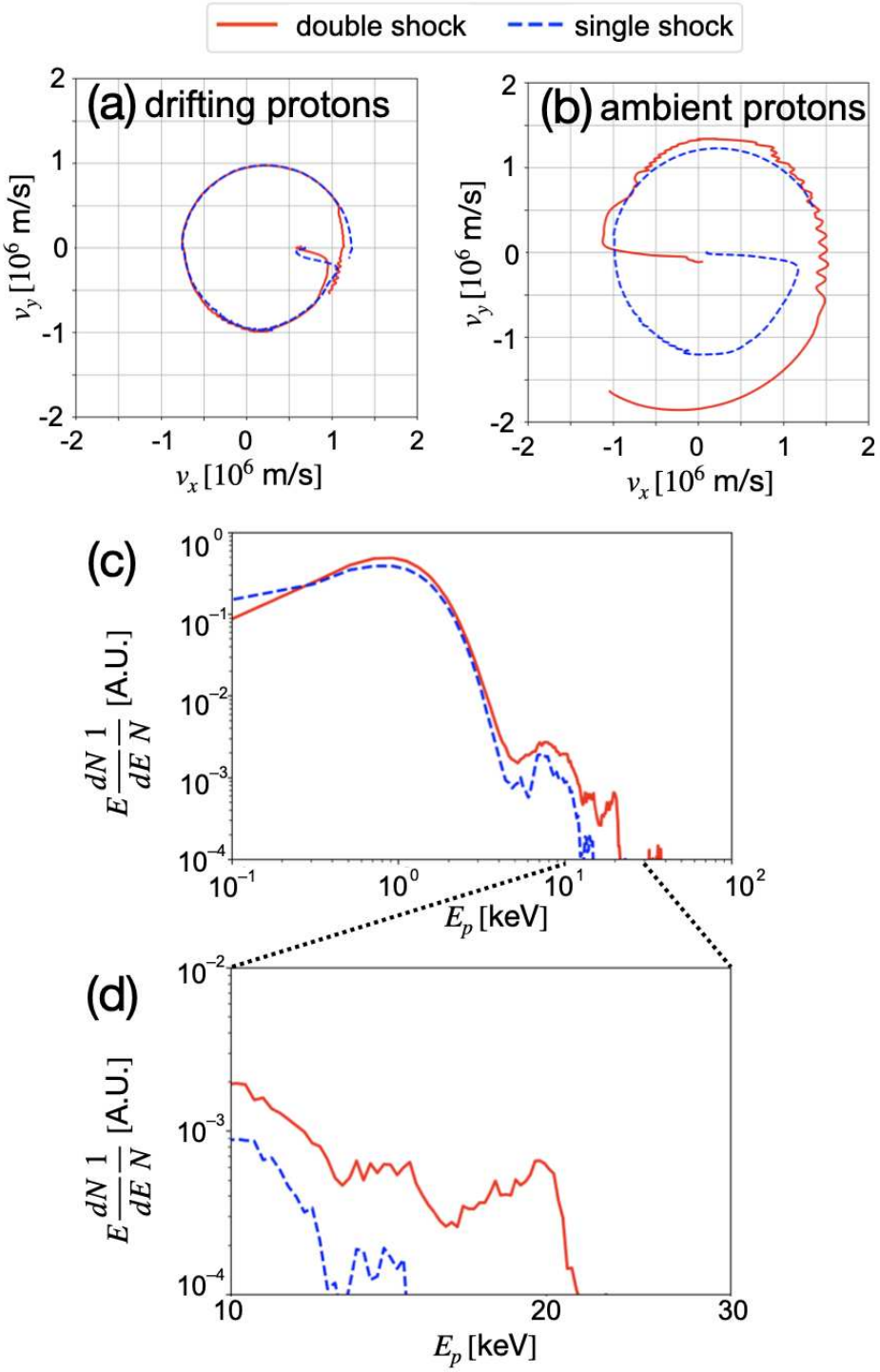

Figure 4.12: *Comparison of the trajectories in the v_x-v_y space of two typical energetic tracked drifting (a) and ambient (b) protons, for the double shock case in red and for the single shock case in blue. (We note that their initial velocities might be different from the species bulk speed ($v_x = 350$ km/s), since the protons are initiated with an initial temperature.) (c) Final energy spectra of the ions for the two configurations and (d) zoom on the range from 10 to 30 keV.*

Specifically, in phase II*a, the proton interacts with the shock front coming from the left, whose E_x oscillates but does a net positive work on the proton, increasing its energy. In phase II*b, the proton

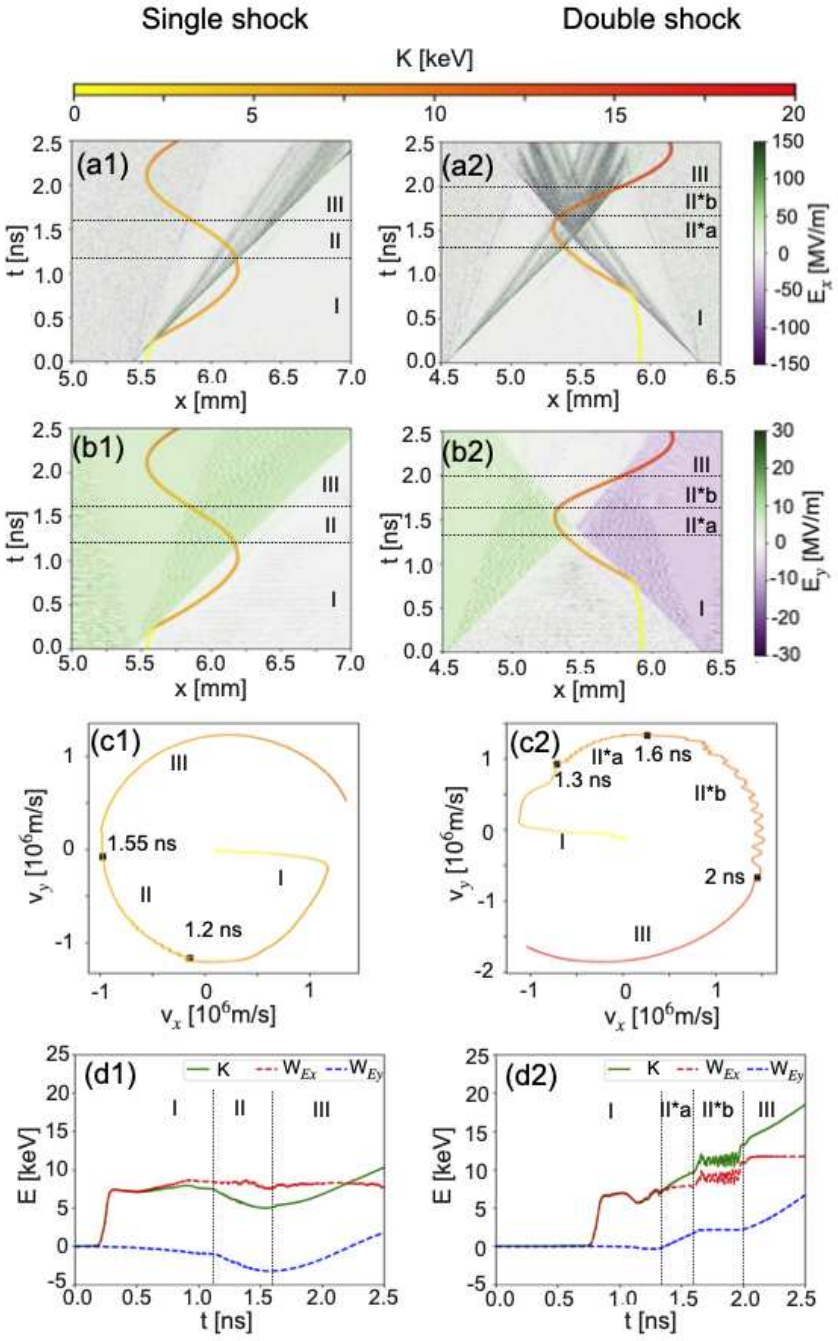

Figure 4.13: *Comparison of the trajectories of two typical energetic protons of the ambient plasma in the single- and double-shock cases in the left column (1) and right column (2), respectively. In their evolution between 0 and 2.5 ns we can distinguish different phases (I, II, II*a, II*b, III), that are detailed in the main text. In (a1-a2) and (b1-b2), the maps of the E_x and of the E_y fields in the x-t space, together with the trajectories of the chosen protons, are shown, respectively. Note the different scales for the electric fields E_x and E_y color maps. In (c1-c2), the proton trajectories in the v_x-v_y space and the temporal points delimiting the different phases, are plotted. The color of the proton trajectories in (a1-a2), (b1-b2), and (c1-c2) follows the evolution of their kinetic energy K on a color scale from 0 to 20 keV. In (d1-d2), are shown the temporal evolution of the kinetic energies of the two tracked protons (full green line), the work done by E_x (dashed red line) and by E_y (dashed blue line).*

encounters the shock coming from the right and finds itself in the region downstream of both shocks, which is characterized by a low E_y (due to the colliding of the two shocks) and by an oscillating E_x (due to the interaction of the two magnetosonic waves), that do not change its energy in a net way. Phase III in the double shock case is similar to the one for the single shock: the proton is in the downstream zone of the shock coming from the right and has a velocity $v_y < 0$, hence the negative $E_y < 0$ makes a positive work and keeps energizing it.
Other energetic protons show a similar behavior: in general, the higher energization in the double shock case is mostly due to the fact that, while gyrating because of the magnetic field, the proton can find areas with E_y directed accordingly to its velocity v_y or zones downstream (of both shocks) with low E_y that does not decelerate it either. These two contributions have the effect of accelerating some of the ambient ions to higher energies in the case of two counter-propagating shocks than in the presence of only one.

Among the tracked background ambient protons, we can compare how many reach, for instance, at least 10 keV in the cases of single and double shock. In the presence of a single shock only 1 proton out of 5120 ($\approx 0.02\%$) reaches 10 keV or higher energies, while with the second shock we have 20 out of 1706 ($\approx 1.17\%$), hence a much higher percentage manages to be accelerated to higher energies. We note that the inequality of number of tracked protons in the two cases comes from the difference of ambient plasma size.

We point out that we are not able to compare the experimental proton spectrum with the simulated one: during the first 3-4 ns of evolution, the shocks are supercritical and the individual interaction of both of them with the background plasma already leads to some high particle energization, as shown in our previous work (Yao et al. 2021, 2022). As the shocks propagate, their velocity drops, leading to an interaction between two subcritical shocks. This interpenetration is indeed the only part that we are simulating here, hence, the resulting spectrum cannot take into account the protons previously accelerated by the supercritical shocks. The protons accelerated by supercritical shocks reach much higher energies, hence in the final spectrum obtained experimentally they "cover" the portion of protons accelerated to lower energies by the interaction between the two subcritical shocks.

Discussion on the limits of validity of our PIC simulations

In our 1D PIC simulations we have not taken the multi-dimensional effects into consideration, e.g., the shock front non-stationarity (Burgess and Scholer 2007), which might affect the proton dynamics due to the rippling along the shock front (Yang et al. 2012). However, we have verified in our former work that the proton acceleration mechanism in the single shock case is not affected by the non-stationarity

in the early few ns (Yao et al. 2022).

Moreover, the 1D geometry approximation has the limit of not considering the hemispherical profile of the shock. This can become a problem if the particles have gone too far in the y-direction and exit the shock. To quantify the maximum length that the protons can travel, we consider the radius and the thickness of the shock right before the collision: from the experimental characterization obtained via interferometry, we estimate a shock front radius $R \approx 2.5$ mm and a shock thickness $\delta R \approx 0.2$ mm.

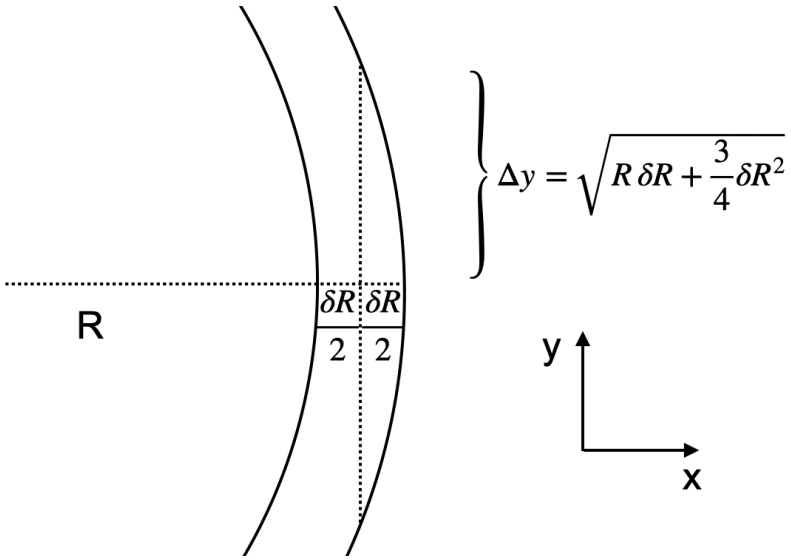

Figure 4.14: *Estimation of the maximum distance that a particle can travel in the y-direction before escaping the shock, considering the hemispherical geometry of the shock front. If we consider a radius $R \approx 2.5$ mm and a shock thickness $\delta R \approx 0.2$ mm, we have $\Delta y \approx 0.73$ mm.*

As shown in Fig. 4.14, we approximate the maximum length Δy for which the particle can still be considered inside the shock as the distance that a particle moving only along the y-axis would travel between the middle of the shock and the external edge of it. This length would result in $\Delta y = \sqrt{R\,\delta R + \frac{3}{4}\delta R^2} \approx 0.73$ mm.

This leads to imposing such a limit to the background protons that have been accelerated by the double shock. Among the 20 protons with energies of 10 keV and higher, only 8 ($= 40\%$) manage to remain confined in the shock all the time. This means that out of the total 1706 tracked ambient protons, only 8 ($\approx 0.47\%$) reach at least 10 keV while remaining confined in the shock. Hence, even considering this limitation, the percentage of protons that are energized to 10 keV and more is considerably higher in the presence of a double shock structure than with a single one (1 out of 5120, i.e., $\approx 0.02\%$).

4.4 Astrophysical interest

Although the vast majority of collisionless shocks in astrophysics are supercritical, the results of our experiment can be relevant for some phenomena observed in both interplanetary and astrophysical plasmas and involving subcritical shocks. In fact, observations of subcritical shocks are sparse and most of them are restricted to the interplanetary space, where colliding shocks can also be observed (e.g., Colburn and Sonett 1966). Examples are the interplanetary forward shocks convected with the solar wind that are expected to propagate with the wind mostly outward into the outer heliosphere, so that they can have a sufficiently low Mach number to be subcritical. Furthermore, subcritical shocks are expected in cometary environments, where the collision between the solar wind and the atmosphere of the comet can reduce the upstream flow velocity, resulting in low Mach number cometary bow shocks. CMEs can also produce subcritical shocks. The observations show that CMEs resulting from x-ray flares of the solar corona associated with type-II radio bursts (the so-called radio-loud CMEs) are, in general, very fast and extended and, initially, they produce supercritical shocks that become subcritical at later times (e.g., Bemporad and Mancuso 2011b, 2013); CMEs resulting from flares not producing a type-II burst (radio-quiet CMEs) produce subcritical shocks at all times (e.g., Bemporad and Mancuso 2011b, 2013). All these subcritical shocks are present in the interplanetary space and can interact with each other or with planetary bow shocks, thus contributing to the acceleration of particles (electrons, protons, ions) up to near-relativistic energies. These shock-shock interactions are reproduced by our experiment which shows that ambient ions can be energized around 1.5 times more than in single shocks and that the particles are accelerated in different ways, depending on the areas of the shock-shock interaction region, where the particles are located. The implication is that the population of high-energy particles in the interplanetary space may depend on the rate of occurrence of shock-shock interactions.

Thanks to the Voyager 1 and 2 missions, since 2012 it was possible to probe the density of the very local interstellar medium with accurate in situ measurements. This has allowed to unveil the presence of several shock waves in the interstellar plasma, most likely interplanetary shocks originated from energetic solar events (e.g., CMEs) that traveled outward through the supersonic solar wind and, after colliding with the heliospheric termination shock, crossed through the heliopause into the interstellar medium (Burlaga et al. 2013; Gurnett et al. 2013; Liu et al. 2014). Burlaga et al. (2013) reported the first in situ measurement of a shock in interstellar plasma, whose characteristics are summarized and compared to the ones relative to our shocks in Table 4.3. Then evidence of multiple shocks was reported in 2015 data collected with Voyager 1 (Ocker et al. 2021). According to the Voyager measurements these shocks are, in general, weak low beta and subcritical shocks (Mellott

and Greenstadt 1984; Burlaga et al. 2013; Mostafavi and Zank 2018). Thus we can argue that the results of our experiment may be applicable to the interactions between these subcritical shocks which populate the very local interstellar medium. Interestingly, these shocks of solar origin are characterized by a precursor consisting of various disturbances in the intensity and anisotropy of galactic cosmic rays (Gurnett et al. 2015). Voyager missions have revealed that these disturbances are typically preceded by bursts of high-energy ($\approx 5 - 100$ MeV) electrons, most likely due to the reflection and acceleration of cosmic-ray electrons by magnetic field jumps at the shock and/or due to interactions with upstream plasma waves/shocks (Gurnett et al. 2021). Our experiment shows that the interaction between these subcritical shocks has a direct effect on the way particles are accelerated by the shocks and on the maximum energization of particles.

Possible shock-shock interactions as those discussed above can also be present (and play a significant role in the acceleration of particles) in the environments around exoplanets. In addition to cases analogous to those we observe in our solar system, the cases of hot-Jupiters (gas giant exoplanets that should be similar to Jupiter but are in close proximity to their stars) are of particular interest, given the strong interaction with their host stars via the stellar wind, the magnetic field and the irradiation. Depending on the parameters of the star-planet system (distance between the two objects, masses of the star and the planet, wind velocity, stellar irradiation, etc.) complex flow structures can form from the colliding planetary and stellar winds, as bow shocks, cometary-type tails, and inspiraling accretion streams (e.g., Matsakos et al. 2015). In particular, the speed of the planetary wind is, in general, only marginally supersonic, so that the Mach number is low (e.g., Tremblin and Chiang 2013). Also the cometary-type tails around the exoplanets are advected by the stellar winds (so that possible shocks can have low Mach numbers to be subcritical) and can be highly perturbed (producing a highly variable complex pattern of shocks), depending on the parameters of the star-planet system. Under these conditions, interactions between subcritical shocks may develop and can be analogous to those produced in our experiment.

Parameters	Our shocks	Shocks as in Burlaga et al. (2013)
B_{DS}/B_{US}	1.5	1.4
$\beta_{ther,US}$	0.1	0.23
$(v_A/c_s)^2_{US}$	4.6	5
θ_{Bn}	90	85
M_{ms}	$1.12^{(\text{exp})} - 1.43^{(\text{sim})}$	≈ 1.9

Table 4.3: *Dimensionless quantities relative to our laser-driven shock and the interstellar medium shock characterized by Voyager in Burlaga et al. (2013), as a weak subcritical resistive laminar shock. DS and US refer to the downstream and upstream zones, respectively.*

The results of our experiment may also be relevant to shed light on the origin of the so-called

suprathermal halo which characterizes the velocity distribution of electrons in the solar wind (e.g., Pierrard et al. 2011). In fact, observational evidence suggests that this electron velocity distribution consists of two components: a dominant low-energy core of thermal (Maxwellian) origin and a high-energy non-thermal tail. The latter component corresponds to a suprathermal halo which is nearly isotropic in the velocity space and can be described by power-law kappa-like distribution functions (Pierrard et al., 2001; Štverák et al., 2009; Maksimovic et al., 2005; Kajdič et al., 2016; Pierrard et al., 2016; Berčič et al., 2019), and a strahl component which appears as a magnetic-field-aligned beam streaming away from the Sun and which is more prominent during solar energetic events (e.g., in the fast component of the solar wind or during CMEs; Pilipp et al. 1987; Anderson et al. 2012). The origin of the high-energy non-thermal tails is widely debated in the literature (e.g., Seough et al. 2015; Boldyrev and Horaites 2019; Horaites et al. 2019). In particular, as it concerns the halo, some authors suggest that it may originate from the solar corona in the form of high-energy electrons which escape from the Sun with velocities much higher than those of the electrons that populate the core. The nearly isotropic distribution in the velocity space may be due to a combination of Coulomb collisions and magnetic de-focusing (e.g., Boldyrev and Horaites 2019). An alternative mechanism that was suggested considers the halo generated from the strahl electrons through strong angular scattering due to local interaction with ambient plasma turbulence (e.g., Štverák et al. 2009; Boldyrev and Horaites 2019). Our work shows that a single event of shock-shock collision can lead to enhanced heating and particle acceleration. An implication could be that such an event, and even more a multiplicity of such events (the interplanetary space is expected to be populated by a multitude of shocklets), could contribute to a turbulent high-energy spectrum of electrons, as observed in the solar wind, thus putting forth a possible explanation for the origin of the halo electrons. More in general, similar effects can be expected in turbulent stellar winds, in supernova remnants in the radiative phase, or in environments in which turbulence is a prominent component. In order to challenge this scenario, however, it is necessary to study the electron energy distribution resulting from a multiplicity of events similar to that investigated here. This would be feasible using advanced laser facilities, like NIF (Moses and Meier, 2008) or LMJ (Casner et al., 2015), offering many individual laser beams. We consider this a promising scenario to investigate in a future work. Complementarily, we will also better characterize turbulence in shock-shock encounters using large-scale 2D PIC simulations, where both longitudinal and transverse kinetic instability (e.g., Bunemann instability and Weibel instability) can be induced, which may lead to the generation of turbulence (Yao et al., 2018).

4.5 Further simulations of supercritical shock collisions

In order to foresee what we could achieve with future experiments, we have simulated the collisions between two supercritical magnetized shocks as well. As we have seen in Chapter 3, the shocks generated in these conditions show a transition from supercritical to subcritical within a few ns, since their speed drops as they propagate. By reducing the distance between the two targets, we could then have supercritical shocks at the meeting point and investigate their interaction. Most of the astrophysical shocks are supercritical and supra-thermal particles are believed to be produced also during the interaction between these structures (Chernin et al. 1995; Ackermann et al. 2011).

We have studied this scenario via PIC simulations on SMILEI, by using a 1D3V setup similar to the

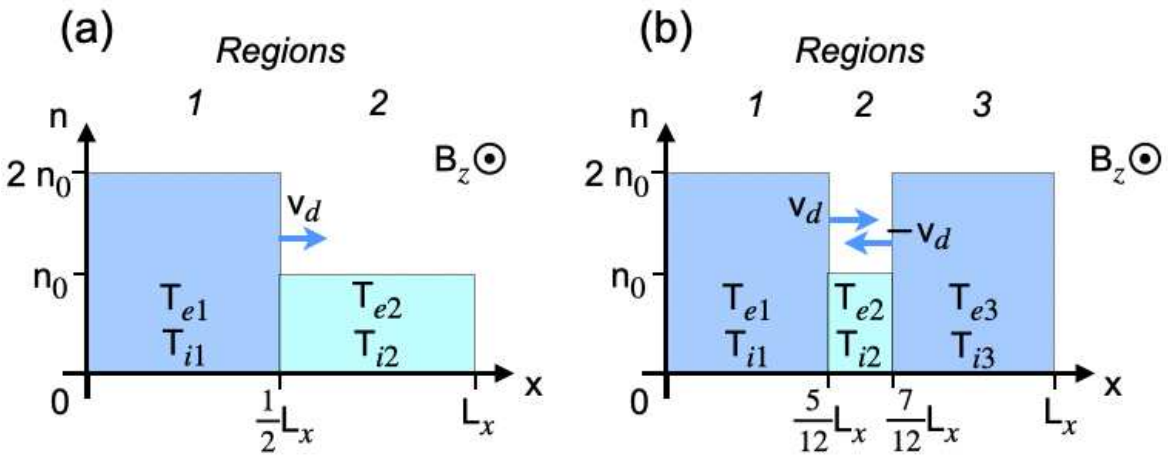

Figure 4.15: *1D PIC simulations initialization setups. (a) Single-shock case: a hydrogen plasma ($n_1 = 2n_0 = 2 \times 10^{18}$ cm^{-3}, $T_{e1} = 130$ eV and $T_{i1} = 200$ eV) drifts through a background hydrogen plasma ($n_1 = n_0 = 1 \times 10^{18}$ cm^{-3}, $T_{e2} = 80$ eV, and $T_{i2} = 20$ eV) with a drifting velocity of $v_d = 350$ km/s (see Table 4.2). (b) Double-shock case: a background plasma ($n_2 = n_0 = 1 \times 10^{18}$ cm^{-3}, $T_{e2} = 80$ eV, and $T_{i2} = 20$ eV) is set at rest between two counter-streaming denser plasmas ($n_1 = n_3 = 2n_0 = 2 \times 10^{18}$ cm^{-3}, $T_{e1} = T_{e3} = 130$ eV and $T_{i1} = T_{i3} = 200$ eV). The drifting velocity $v_d = 1500$ km/s imposed to the plasma (in Regions 1 and 3) makes the shocks supercritical, like seen in Chapter 3. with a distance of 1.8 mm in between the two shock fronts, while the box has a total length $L_x = 11$ mm.*

one employed for the subcritical shock case (see Sec. 4.3.2), as sketched again here in Fig. 4.15.

Here, we have chosen as drifting speed for the downstream plasma the same velocity as in Sec. 3.3.2, $v_d = 1500$ km/s. The other parameters remain the same as in Sec. 4.3.2: the background plasma at rest has a density $n_2 = n_0 = 1 \times 10^{18}$ cm^{-3}, while the drifting plasmas have $n_1 = n_3 = 2n_0$; the ion and electron temperatures are $T_{i1} = T_{i3} = 200$ eV and $T_{e1} = T_{e3} = 130$ eV for the DS regions, and $T_{i2} = 20$ eV and $T_{e2} = 80$ eV for the US region, respectively.

First, let us focus on the evolution of the profiles of proton density n_i, magnetic field B_z, and electric fields E_x and E_y, for both the single shock and double shock configurations. These are shown in Fig. 4.16, for two representative times after the beginning of the simulation, i.e., 0.5 ns and 1ns.

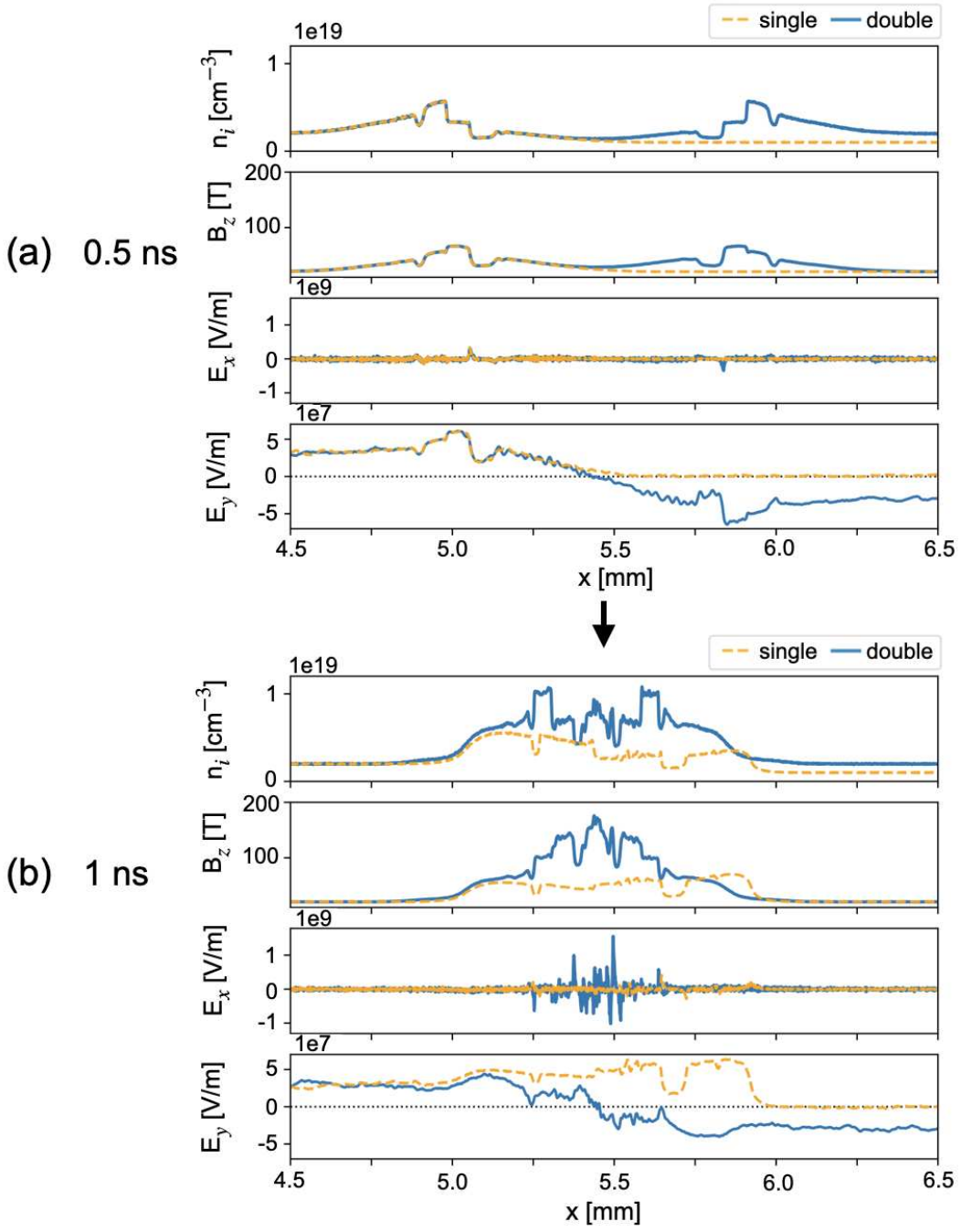

Figure 4.16: *Profiles of ion density, magnetic field B_z, and electric fields E_x and E_y at times 0.5 ns (a) and 1 ns (b) after the beginning of the simulation. Until 0.5 ns, the two fast shocks propagate without perturbing each other, as their profiles correspond to the ones of the single shock case. At 1 ns, the interaction between the two shocks makes the ion density and the magnetic field B_z increase and pile up in the middle, reaching values almost one order of magnitude larger than the initial ones; the electric field E_x presents several intense spikes (both positive and negative); the inductive E_y does not drastically change structure or magnitude, but it presents opposite signs in the downstream regions depending on the propagation direction of the shock. We point out that the profiles relative to the single shock have been shifted of $\Delta x = -L_x/12$ in order to simplify the comparison.*

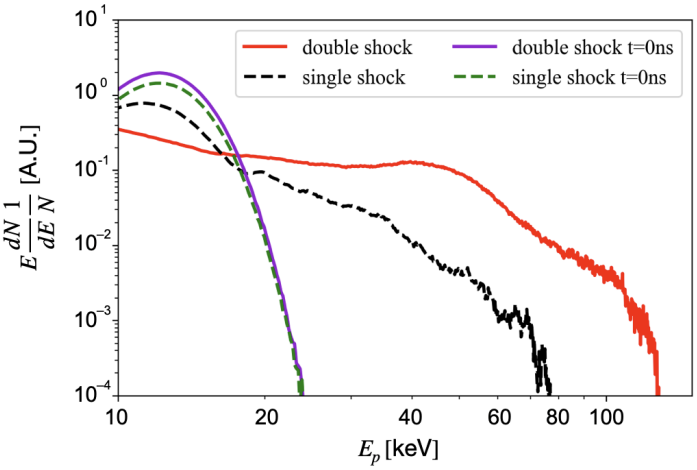

Figure 4.17: *Proton spectra comparison for supercritical single and double shocks. Departing from the initial combinations of maxwellian distributions (full violet line for the double shock and dashed green line for the single shock), the ion spectra widen and supra-thermal protons are produced. While the cutoff energy in the single shock case (dashed black line) is around 75 keV, protons are energized up to about 130 keV in the double shock case (full red line).*

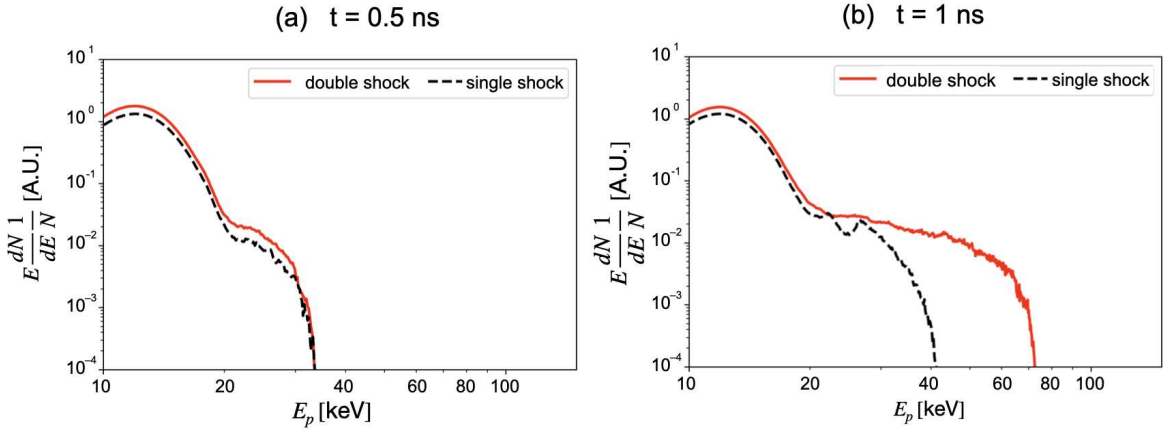

Figure 4.18: *Proton spectra for the single and double shock cases at time 0.5 (a) and 1 ns (b) after the beginning of the simulation.*

We point out that these two times do not coincide to the ones used to plot the same profiles in the subcritical shock case, i.e., 1 ns and 1.5 ns (see Fig. 4.11). Here, the drifting speed v_d is more than four times bigger than in the subcritical shock case, hence a direct comparison at the same times would not mean much, as the shocks would be at different stages of interaction. Similarly, comparing times by simply diving by a factor makes little sense as well, since the distances and the development stage of the shocks are different.

Until around 0.5 ns (Fig. 4.16 (a)), the two fast shocks propagate without perturbing each other, as their profiles correspond to the ones of the single shock case. At 1 ns (Fig. 4.16 (b)), the interaction between the two shocks makes the proton density and the magnetic field B_z increase and pile up in the middle, reaching values almost one order of magnitude larger than the initial ones, that is

densities up to 10^{19} cm^{-3} and B-fields up to 180 T. The electric field E_x presents several spikes (both positive and negative) up to the order of 10^9 MV/m, while the inductive E_y is around ± 50 MV/m in the downstream regions and presents a relatively smooth transition between these two.
If we compare these values with the ones obtained with subcritical shocks (see Fig. 4.11), we note that the compression in ion density n_i, magnetic field B_z, and inductive electric field E_y is around 4-5 times stronger in the case of supercritical shocks, while the electrostatic field E_x has spikes even one order of magnitude bigger than in the subcritical shock case.

Let us now focus on the proton spectrum. At the end of the simulation, i.e., 2.5 ns after the beginning, the proton energy follows the distributions shown in Fig. 4.17, where the initial maxwellians are plotted as well. According to what seen in Sec. 3.3.2, in the presence of one supercritical shock, protons are energized up to around 75 keV. On the other hand, in the presence of a second shock, many more protons are accelerated to these energies and beyond, up to around 130 keV. As expected, this further energization begins as soon as the two shocks start interacting, since their energy distributions are pretty much the same up to around 0.5 ns (as shown in Fig. 4.18).
The value of 130 keV reached with two colliding supercritical shocks is much larger than the one obtained during the collision of two subcritical shocks, which barely exceeded 20 keV (see Fig. 4.12 (d)). One can legitimately wonder whether this higher energization is due to the longer "effective" time over which the protons have interacted with the two shocks, since in the supercritical case the shocks travel faster than in the subcritical one and thus meet earlier. However, this is not the case: as displayed in Fig. 4.18 (b), already 1 ns after the beginning of the simulation protons achieve energies around 70 keV, clearly higher than the 20 keV obtained with subcritical double shocks.

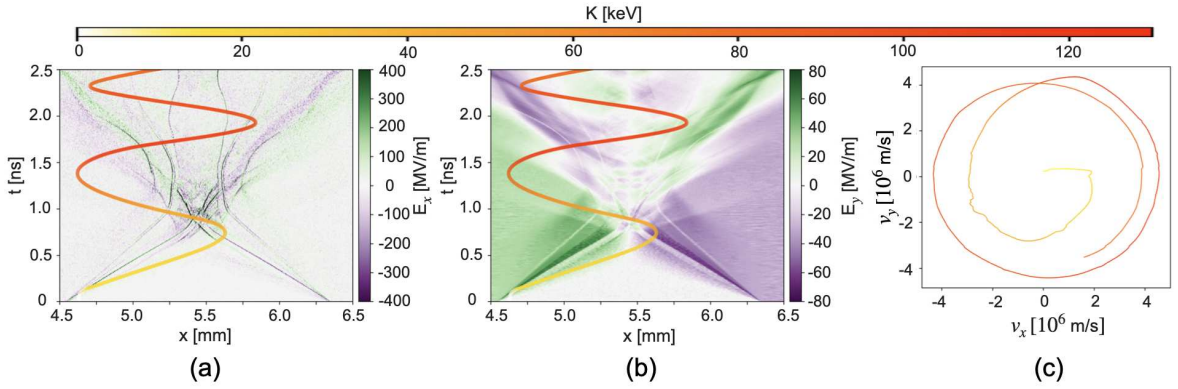

Figure 4.19: *Trajectory of one characteristic energetic background proton plotted over the map of E_x (a) and E_y (b) in the x-t space, and in the v_x-v_y space (c). The color of the trajectory indicates its kinetic energy according to the colorbar raging from 0 to 130 keV at the top.*

Similarly to what we have done in the previous simulations, we have tracked energetic background

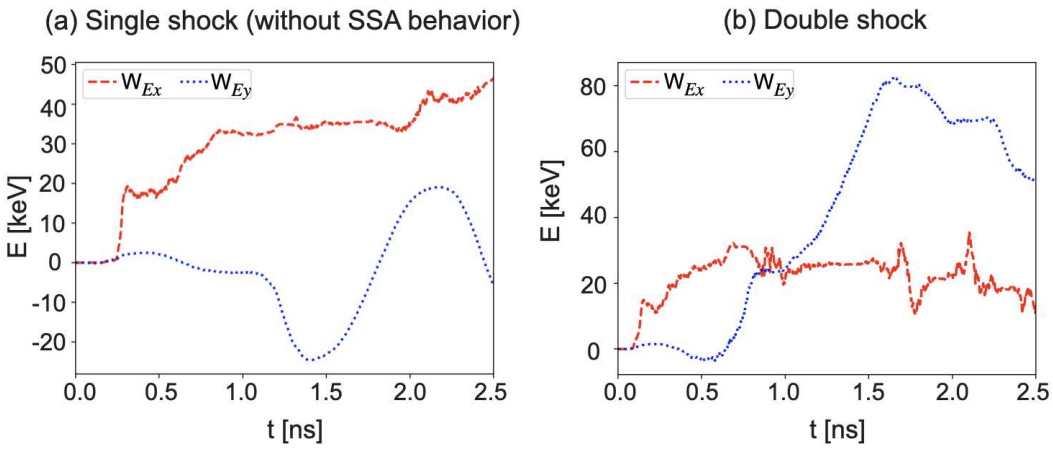

Figure 4.20: *Comparison of the work made along time by the x and y components of the electric field on representative tracked background particles. (a) represents the case of a proton interacting a single supercritical shock (not showing SSA behavior, since treated in the previous chapter): the proton first moves in the upstream region, then in the downstream one, similarly to what happens in the case of single subcritical shock. In (b) are plotted the E_x and E_y works on an ambient proton in the case of double shock.*

protons, i.e., the ones reaching at a certain time energies larger than 50 keV. Among the 77 protons matching this condition, mostly all of them follow the behavior shown in Fig. 4.19: after an initial kick received by the electric field E_x (a), their acceleration is mostly due to the inductive E-field E_y (b), resulting in a trajectory in the v_x-v_y space as shown in (c). This is the same process happening in the case of subcritical colliding shocks, as described in Sec. 4.3.2. At least according to our 1D PIC simulations, it seems that the enhanced acceleration in the case of supercritical shocks is due only to the stronger electric fields associated with the shocks, as seen for example in the comparison between Fig. 4.11 and Fig. 4.16, and not to different physics going on.

Indeed, if we compare what happens in the cases of (supercritical) single and double shock, we witness the same difference as with subcritical shocks. In the double shock case, for certain ambient protons the presence of both the common and individual downstream areas turns out to be advantageous in terms of further energization (see Fig. 4.20).

Regarding the acceleration taking place at the shock front, we have seen in Chapter 3 that under these conditions some protons undergo shock surfing acceleration (SSA). However, in this case we do not observe such a phenomenon occurring before the collision of the two shocks, i.e., at the interface between a supercritical shock and the ambient plasma. This is due to the fact that the two shocks are initialized too close, hence the protons do not have "enough space" to receive the initial kick from E_x, then gyrate upstream, and finally enter the SSA mechanism, without meeting before the shock coming from the opposite side.

Nonetheless, 2 out of the 77 tracked energetic protons shows SSA-like behavior once in the common

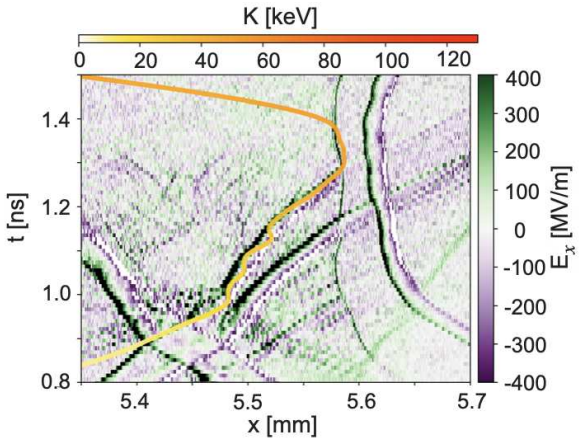

Figure 4.21: *Trajectory of a proton undergoing SSA in the downstream region, plotted over the E_x map in the x-t space.*

downstream region of the two shocks, where strong electric fields E_x spikes are present as well as the motional E_y. The trajectory of one of them over the E_x map in the x-t space is represented in Fig. 4.21.

In conclusion, during the collision of two magnetized supercritical shocks, we obtain proton densities and magnetic and electric fields between 4 to 10 times higher than the ones characterizing the encounter of two subcritical shocks. This leads to a higher energization of the background protons (up to 130 keV, instead of 20 keV), which, similarly to what happens in the subcritical case, is mostly due to the inductive electric field ($E_y \sim v_x B_z$).

Also in this supercritical regime, the presence of a second shock is beneficial to proton energization enhancement: the energy cutoff of the proton spectrum is around 130 keV, that is 50 keV higher than for the single shock case.

It would be interesting to experimentally accomplish the collision of two magnetized supercritical collisionless shocks as well, in order to corroborate (or dismiss) the results obtained with such 1D PIC simulations.

This is possible with the current experimental capabilities by setting the targets closer and directly facing each other. A possible setup is shown in Fig. 4.22, where the targets are set 6 mm apart. This would allow the shocks to be still supercritical when they meet, according to the speed we have measured 3 mm away from the target surface (see Fig. 3.7).

4.6 Conclusions

In our experimental campaign we have investigated the interpenetration of two laser-driven collisionless subcritical shocks, relevant for astrophysical phenomena such as the interplanetary medium and the local interstellar medium. The data obtained from their characterization have been used to feed

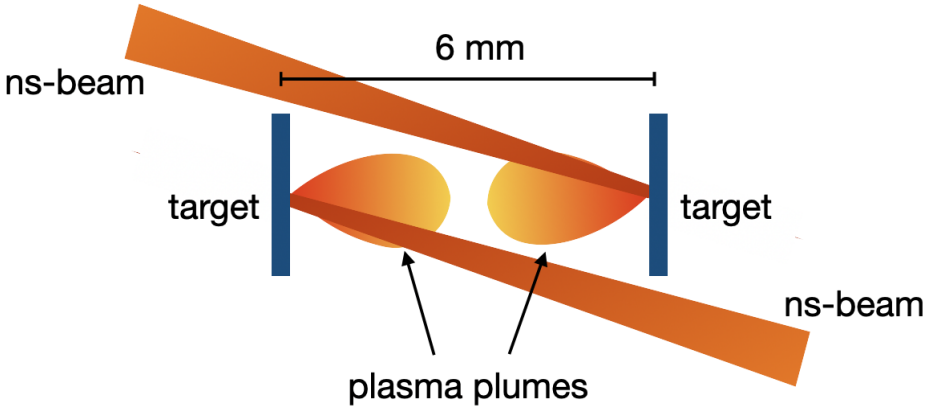

Figure 4.22: *Possible experimental setup to investigate the interpenetration of two supercritical shocks in the laboratory.*

MHD and PIC simulations, respectively run with the FLASH and the SMILEI codes. While the MHD simulations have been used to describe the collisional part of the problem, i.e., the piston, and the overall evolution of the system; PIC simulations have provided insights into the microphysics at play in such a scenario. We compared the cases of single and double shocks and observed an acceleration of the background ions which was up to 1.5 times higher in the case of double shocks. Such acceleration is initially due to the electrostatic field E_x associated with the shock front (injection), followed by a contribution mostly due to the "surfing" effect on the inductive electric field ($E_y \sim v_x B_z$). The presence of a second shock benefits this second mechanism as it allows the existence of zones with E_y directed as the proton v_y, and thus enhance their acceleration. Unfortunately we could not measure such a spectrum during our experimental campaign, as the previously formed supercritical shocks produced higher energy protons whose spectrum covered the one of the particles accelerated by the further stage of double subcritical shock interaction.

Additional PIC simulations employing supercritical shocks have shown that further proton energization can be achieved in this case, allowing for experimental direct investigation as well.

In spite of the fact that most astrophysical collisionless shocks are supercritical, these results can shed light on the less investigated subcritical shocks which are still relevant in various space phenomena. In particular, we have shown that the interaction of two subcritical shocks could lead to a higher energization of the background protons. This is a relevant information when determining the distribution of high-energy particles that populate the interplanetary space and the very local interstellar medium surrounding the heliopause where colliding subcritical shocks are present. Moreover, high-power laser-plasma experiments have demonstrated to be an essential tool allowing us to recreate in the laboratory scaled astrophysical phenomena, whose characterization is crucial to initialize the relative numerical simulations.

Chapter 5

Conclusions and perspectives

The work presented in this thesis concerns the investigation of laser-driven collisionless shocks of astrophysical interest, carried out within the framework of the so-called *Laboratory astrophysics*. In particular, we have been able to experimentally generate and characterize a supercritical quasi-perpendicular magnetized shock by irradiating a solid target of teflon with a $\sim 10^{13}$ W/cm^2 laser pulse. The system was embedded into an externally applied 20 T pulsed magnetic field and a background hydrogen gas, which was converted into an ambient plasma. This interaction lead to the formation of a piston, consisting in the dense ablated plasma expanding from the target, and of a collisionless shock, formed between the hydrogen plasma pushed by the piston and the background plasma.

We have measured various characteristics of the laser-produced plasma at different times: the electron (integrated) density (through interferometry and Thomson scattering), the ion and electron temperatures (through Thomson scattering), the electric field at the shock front (through proton radiography), the time-integrated electron density (through FSSR), and the energy spectrum of the exiting protons (via a proton spectrometer). These measurements allowed us to characterize the shock taking place within the hydrogen plasma as collisionless and to follow its transition from supercritical to subcritical.

The key parameters of the laboratory produced shock are summarized in Table 3.2 in Sec. 3.4, which shows that they result similar to the parameters of the Earth's bow shock, the solar wind termination shock, and of four different non-relativistic SNRs interacting with dense molecular clouds (see Table 3.3 detailing the considered objects).

Our experimental measurements guided us in setting up the numerical simulations that modeled our systems. We simulated the overall scene with the MHD FLASH code, which allowed us to reproduce the global evolution of the system, from the laser energy deposition to the piston and shock forma-

tion and propagation. However, Particle-In-Cell (PIC) simulations with the code SMILEI have been necessary to catch the effects of kinetic processes, out of reach for hydrodynamic or MHD simultions. We used 1D3V (and, to a limited extent, 2D3V) PIC simulations to model only the collisionless shock evolution phase, for which we could probe electromagnetic fields and densities with high spatio-temporal resolution and even track individual particles.
The presence of supra-thermal protons detected experimentally was confirmed by our kinetic simulations. These also showed that most of the energetic protons were undergoing shock surfing acceleration (SSA) when interacting with the shock front. The remarkable match between the simulated and the measured proton spectra identifies SSA as a likely responsible for the particle energization.

In the follow-up experimental campaign, we focused on the interpenetration of two laser-driven shocks. Such collisionless shocks were generated with the same experimental platform as for the single shock case and characterized with the the same diagnostics, but in a different geometry. Also in this case, the data obtained from their characterization have been used to feed MHD and PIC simulations, respectively run with the FLASH and the SMILEI codes. While the MHD simulations have been used to describe the collisional part of the problem, i.e., the piston, and the overall evolution of the system; PIC simulations have simulated the subcritical collisionless shock part, providing insights into the microphysics at play in such a scenario. Here, we directed attention to the comparison between single and double subcritical shock cases. We observed that, in the presence of a double shock, the acceleration of the background protons was up to 1.5 times higher and that the electromagnetic fields and particle densities were piling up in a much stronger way.
Such a proton acceleration is initially due to the electrostatic field E_x associated with the shock front (injection), followed by a contribution mostly due to the "surfing" effect on the inductive electric field ($E_y \sim v_x B_z$). The second shock plays a role by allowing the existence of zones with E_y directed as the proton v_y, and thus it enhances their acceleration.
We did not manage to directly measure the proton spectrum as if only due to the acceleration by subcritical shock interpenetration, since the previously existent supercritical shocks energized much more strongly the protons.
Moreover, additional PIC simulations employing supercritical shocks have shown that further proton energization can be achieved in this case, allowing for future experimental direct measurement as well.
As reported in Sec. 4.4 and made explicit in Table 4.3, these results can shed light on subcritical shocks of astrophysical interest, since they are present for instance in the interplanetary medium and in the local interstellar medium. Indeed, this information might be relevant for determining the energy

spectrum of the particles present in the interplanetary space and the very local interstellar medium around the heliopause (where collisions between subcritical shocks take place).

Hence, high-power laser-plasma experiments have demonstrated to be an essential tool allowing us to recreate in the laboratory scaled astrophysical phenomena, whose characterization is crucial to initialize the related numerical simulations and better interpret astrophysical observations.

Future work

Our experimental platform can be tuned in the future to carry out more systematic studies of collisionless shocks under different conditions and to explore other particle acceleration scenarios. The strength and the orientation of the magnetic field can indeed be adjusted, as well as the density of the background plasma. Moreover, when dealing with more than one shock, the distance and the orientation between the source targets can be regulated (up to a certain limit), with the purpose to investigate interaction between shocks at different stages of their evolution (e.g., when they are still supercritical).

The recent first-stage commissioning campaigns at the Apollon laser facility (on the Saclay campus, France) brought promising results. These are not presented in this thesis, even though I have participated to the related campaign as well, but it is interesting to briefly show the Apollon status and its possible applications within the context of this work.
The Apollon laser will be among the first multi-petawatt user facilities in the world, reaching peak laser intensities over 2×10^{22} W/cm^2. The final goal of the facilities is to provide 10 PW pulses of 150 J energy and 15 fs (FWHM) duration at a repetition rate of 1 shot/minute. In its final configuration, the Apollon laser will comprise two laser beams: F1, with a maximum power of 10 PW, and F2, with a maximum power of 1 PW, will both be available to users in the experimental areas (Papadopoulos et al. 2017).
The first laser-plasma interaction experiments have recently been performed during the commissioning of the beamline F2 at 1 PW in both the long focal (length) area (LFA) and short focal (length) area (SFA). Our group has been in charge, together with other LULI researchers, of the SFA campaign. There, we have achieved a maximum laser energy of 38 J at the last amplification stage, with a $\sim 1.5\%$ rms stability over 6 hours of continuous operation at around 30 J. However, target energy of ~ 10 J has been estimated by taking into account the beam transport losses and the compression efficiency. The laser pulse has wavelength centered at 815 nm, ranging from 750 nm to 880 nm, and is

compressed to about 24 fs. The short f-number parabola (F/3) can focalize the beam into a focal spot of FWHM 2.8 μm, meaning that the on-target peak intensity currently is around 2×10^{21} W/cm^2.
We have characterized the laser-plasma interaction by employing several diagnostics, such as a Thomson parabola, a proton spectrometer, and x-ray spectrometers. A complete description of the SFA commissioning campaign can be found in the recently published paper by Burdonov et al. (2021).
In summary, we observed good laser-target coupling from the measurements of electron, ion, and electromagnetic radiation emission. Performances and temporal contrasts similar to those of other running facilities were achieved. Moreover, TNSA-produced proton beams with cut-off energies around 28 MeV could be generated from 2-3 μm thick Al foils, allowing for applications, such as proton radiography.
The future facility upgrades will allow to deliver powers up to 10 PW and interaction in an ultrahigh constrast regime, thanks to the implementation of plasma mirrors.

Relativistic collisionless shocks are believed to occur in the afterglow phase of gamma-ray bursts (GRBs) and in other astrophysical objects emitting intense radiation and characterized by a narrow transverse size (Bykov and Treumann 2011; Piran 2005). They are thought to form when relativistic flows interact with the interstellar medium and their existence relies on the observation of high-energy cosmic rays of non-solar origin and on the detection of high-energy radiation.
When an intense laser with irradiance $I\lambda^2 \gtrsim 10^{18}$ W μm^2/cm^2 interacts with a plasma, the electrons oscillate in the wave field at relativistic velocities (Wilks et al. 1992). Such a laser-plasma interaction regime allows for strong heating and compression of matter, possibly leading to the formation of relativistic expanding flows and, thus, to relativistic collisionless shocks. Laser facilities providing PW beams with duration of $\sim$ tens of fs are able to accelerate electrons up to multi-GeV energy and protons up to $\sim$ 100 MeV (Leemans et al. 2014; Macchi et al. 2013). Such electron beams can emit up to MeV-photons through betatron radiation, that is, fs-lasting x-rays or gamma-rays suitable to investigate the fine structure or quickly evolving phenomena (Li et al. 2018). On the other hand, Bremmstrahlung radiation (10-100 MeV photons), produced when energetic electrons interact with matter, represents an excellent tool to image dense material (Underwood et al. 2020). High-power lasers can also be applied to the study of quantum electrodynamics (QED) phenomena, allowing – on the long term – the investigation of related astrophysical objects, such as neutron stars and magnetars (Bucksbaum et al. 2021).
Coming back to shocks, it has been shown, for instance, at the 4 PW / 20 fs laser CoReLS (Nam et al. 2018) that a laser-driven near-critical density plasma can lead to shock formation, thanks to its

efficient laser energy absorption. The speed of the developing structure has been measured to be around $0.02c$ (Singh et al. 2020). Even though not yet accomplished, the achievement of collisionless relativistic shocks is thought to be theoretically possible at 10 PW laser facilities, by employing two counter-streaming electron–positron pair plasmas (Jiao et al. 2017).

Seen the previously reported results and the aimed characteristics of the Apollon laser facility, this might be suitable to achieve such a regime and serve in the future to produce relativistic shocks of astrophysical relevance, as well as other space-related processes.

Appendix A

Proton spectrometer calibration

A.1 Method

The proton spectrometer we want to calibrate is the one marked as "2" shown in Fig. A.1 and schematised in Fig. A.2.

After passing through the entrance slit of the collimator, the protons pass between two magnets and are deflected by the magnetic field B. At 86 mm after the beginning of the magnets an imaging plate (IP) is located in order to measure the proton deflection from the 0-order, hence their energy spectrum. The IP holder used was built by a LULI engineer and has the dimensions reported in Fig. A.2 in mm. In order to avoid mistakes due to measuring distances at every use, it is supposed to be inserted from the back side (with respect to the proton flux) of the spectrometer and to be pushed until the end of the metal box: in this way, the IP is going to be located at 26 mm from the end of the magnets every time.

Figure A.1: *Pictures of the proton spectrometer.*

In order to calibrate our proton spectrometer, we put – shot by shot – different filters on the IP, for which we know the proton stopping energy. In this way, by measuring the distance between the 0-order (the point aligned with the target and the spectrometer entrance slit, marked by the x-rays)

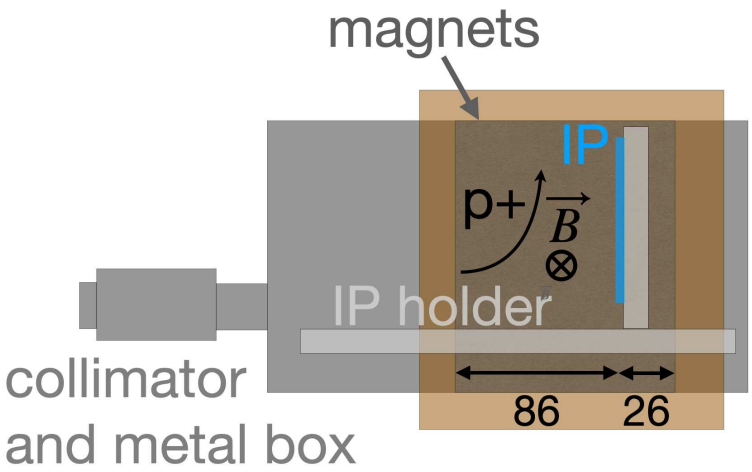

Figure A.2: *Diagram of the proton spectrometer.* (*Lengths in mm.*)

and the position where the least energetic protons start to appear beyond the filter, we get several couples [proton energy ; distance from 0-order]. We fit these data points with the following function:

$$x = \frac{q\,B\,l_B\left(D_B + \frac{l_B}{2}\right)}{\sqrt{2\,m_p\,E_k}} \tag{A.1}$$

where $q = 1.60 \cdot 10^{-19}$ C is the proton charge, B the magnetic field between the magnets, l_B the length of the magnets, D_B the distance between the IP and the back of the magnets, $m_p = 1.67 \cdot 10^{-27}$ kg the proton mass, and the E_k their kinetic energy. B and D_B are not precisely known and are left as free parameters to fit the above function Eq. A.1 with the data points.

In order to estimate the cutoff energy, we have considered the position of the least energetic protons appearing out of the filter, minus half of the FWHM of the slit, as it is an estimation of the error on the proton position, too (Fig. A.3).

For a more precise calibration

Eq. A.1 is the approximated version of

$$x = \frac{\sqrt{2\,E_k\,m_p}}{q\,B_0}\left[\cos\left(\arcsin\left(\frac{q\,B_0\,l_B}{\sqrt{2\,E_k\,m_p}}\right) - 1\right)\right] - D_B\tan\left(\arcsin\left(\frac{q\,B_0\,l_B}{\sqrt{2\,E_k\,m_p}}\right)\right) \tag{A.2}$$

for $\frac{q\,B\,l_B}{\sqrt{2\,E_k\,m_p}} \ll 1$, which corresponds to the condition $\frac{l_B}{r_g} \ll 1$, where $r_g = \frac{v_\perp\,m_p}{q\,B}$ (supposing $v_\perp = v$) is the proton gyroradius. This means that Eq. A.1 is valid in the case of small deflections of the protons over the length of the magnets.

Having measured the magnets length $l_B = 11.2$ cm, this corresponds to $\frac{l_B}{R} \simeq 0.775\frac{B\text{ [T]}}{\sqrt{E_k\text{ [MeV]}}}$.

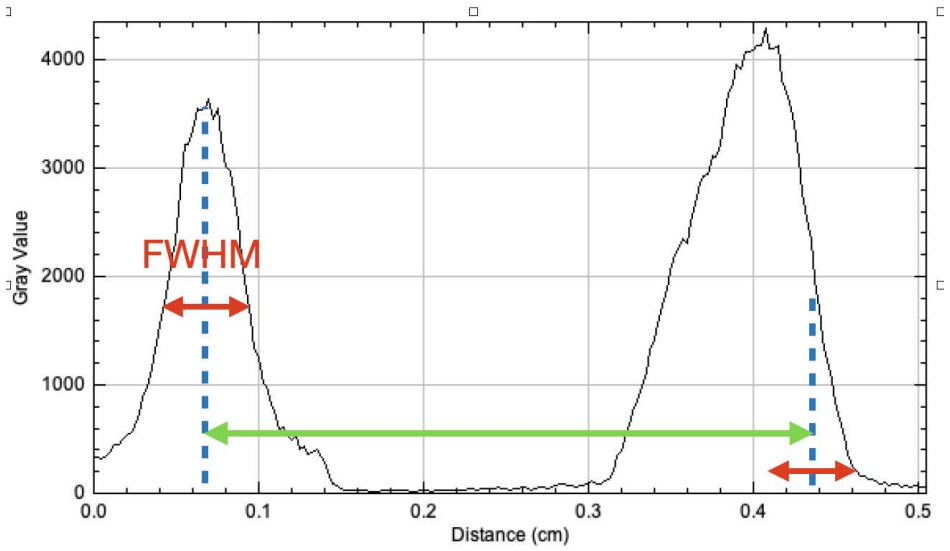

Figure A.3: *Lineout of the image plate of shot 6: 0-order and bunch of protons. The green arrow represents the distance between the 0-order and the least energetic protons passing through the filter. The red arrow is the FWHM, also considered as error bar for the proton position.*

From a calibration done during the experiment run on Titan in 2014, the fit gave as result $B \simeq 0.35$ T. Hence, considering this value as realistic,

$$\frac{l_B}{R} \simeq \frac{0.271}{\sqrt{E_k\,[\text{MeV}]}} \ll 1 \qquad \Longrightarrow \qquad E_k \gg 73 \text{ keV} \tag{A.3}$$

which means that Eq. A.1 is valid for "high" proton energies. As we will see, this condition will be valid for the calibration data points collected on LULI2000, while the energies corresponding to the data from ELFIE will always be less than one order of magnitude bigger than what this condition would impose.

Note also that even the more general Eq. A.2 requires at least $\frac{l_B}{R} \simeq \frac{0.271}{\sqrt{E_k\,[\text{MeV}]}} < 1$.

A.2 Calibration data points

In Tab. A.1 is shown the data collected for the spectrometer calibration during the experimental campaign run on LULI2000 in July-August 2020.

While the calibration with the kapton tape (shots #10 and #11) is accidental, we tried nonetheless to make use of it. In order to find its stopping power, we measured 6 overlapped layers of tape with the calipers and found 300 µm / 6 = 50 µm. From this thickness we can expect a stopping power of around 1.8 MeV.

Additional data points were collected during the experimental campaign run on ELFIE between

shot	filter	energy (MeV)	distance from 0-order (mm)	cutoff energy (MeV)	FWHM (mm)
6	Au 250 μm	12.53	3.7	24 (14)	0.48
7	Al 150 μm	4.357	6.1	33 (20)	0.48
8	Al 25 μm	1.445	11.1	21 (16)	0.38
10	Pb 1 mm	20.89	3.3	28 (20)	0.35
10	Kapton 50 μm	1.8	9.8	28 (20)	0.35
11	Al 300 μm	6.554	5.5	24 (19)	0.45
11	Kapton 50 μm	1.8	10.1	24 (19)	0.45
13	2× Ta 550 μm	26.86	2.7	30 (23)	0.22
14	Cu 1 mm	22.8	2.8	28 (22)	0.22

Table A.1: *Calibration data collected during the campaign on LULI2000 (July-August 2020). For different shots we put a different filter (with a corresponding energy given by simulations on SRIM and tabulated data) and measured the distance between the 0-order and the emerging protons. We add to this table further information that could be useful in other occasions. One is the cutoff energy, i.e., the highest energy that the protons have in that particular shot (by using the calibration done with this data in the table): the first value is found considering the very edge of the proton trace on the IP, the value in brackets is found using the method shown in Fig. A.3. The other is the FWHM, which is the width of the 0-order, considered as to be twice the error (due to the finite opening of the slit) on the measures of distance.*

February and April 2019 in order to calibrate the proton spectrometer for lower energies; they are shown in Tab. A.2.

energy (keV)	distance from 0-order (mm)
186	25.6
448	18.0
448	19.4
610	16.9

Table A.2: *Calibration data collected during the campaign on ELFIE (February–April 2019).*

A.3 Results

We first consider only the data points collected in 2020 on LULI2000 in Tab. A.1 and we fit them with the function in Eq. A.1, leaving D_B and B as free parameters, as they are not considered perfectly fixed or known.

Having measured the distance between the IP and the back of the magnets D_B^{meas} and knowing the estimation of B^{Titan} from a previous calibration (i.e., an experimental campaign on Titan, in November

2014), we chose these values to initialise our fit parameters:

$$D_B^{in} = D_B^{meas} = -26 \text{ mm}, \quad B^{in} = B^{Titan} = 0.35 \text{ T} \tag{A.4}$$

This leads to a first result with $D_B^{fit,1} = -12.1$ mm, $B^{fit,1} = 0.39$ T, where $D_B^{fit,1}$ differs considerably from our measurement. At this point it is worth noticing that in Eq. A.1 D_B and B are strongly correlated for the purposes of the fit, so a small increment of one would directly influence the other one. Hence, trusting more the measured value assigned to D_B^{in}, we try to change B^{in} in order to see if we can have a good fitting curve and go close to the "aimed" $D_B^{meas} = -26$ mm.
By setting now

$$D_B^{in} = D_B^{meas} = -26 \text{ mm}, \quad B^{in} = 0.5 \text{ T} \tag{A.5}$$

as initialisation parameters, we obtain the function plotted in Fig. A.4, where

$$D_B^{fit(L)} = -26.4 \text{ mm}, \quad B^{fit(L)} = 0.58 \text{ T} \tag{A.6}$$

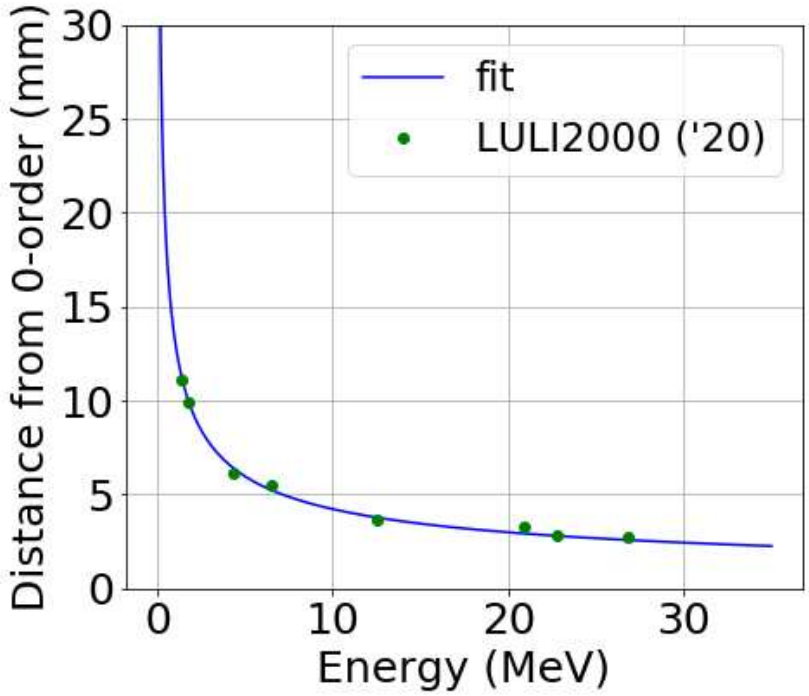

Figure A.4: *Distance from the 0-order on the IP vs cutoff proton energy: calibration data points and fitted function (Eq. A.1 with the fitted parameters in Eq. A.6), obtained by using only the calibration points of the LULI2000 campaign.*

The magnetic field value differs from the previous result, but our curve is reasonably reproducing

all the data point collected and the distance between the IP and the end of the magnets D_B corresponds to the measure.

An improvement would be to consider the errors for the different data points as weights for the fit: indeed, after shot #12, we started using a smaller slit at the entrance of the spectrometer that reduced the uncertainty on the protons position for the two last two measures.

Additional data points

By using the data collected both on LULI2000 and on the ELFIE, we obtain the curve plotted in Fig. A.5, where the fitted parameters are

$$D_B^{fit(L+E)} = -27.1 \text{ mm}, \qquad B^{fit(L+E)} = 0.55 \text{ T} \tag{A.7}$$

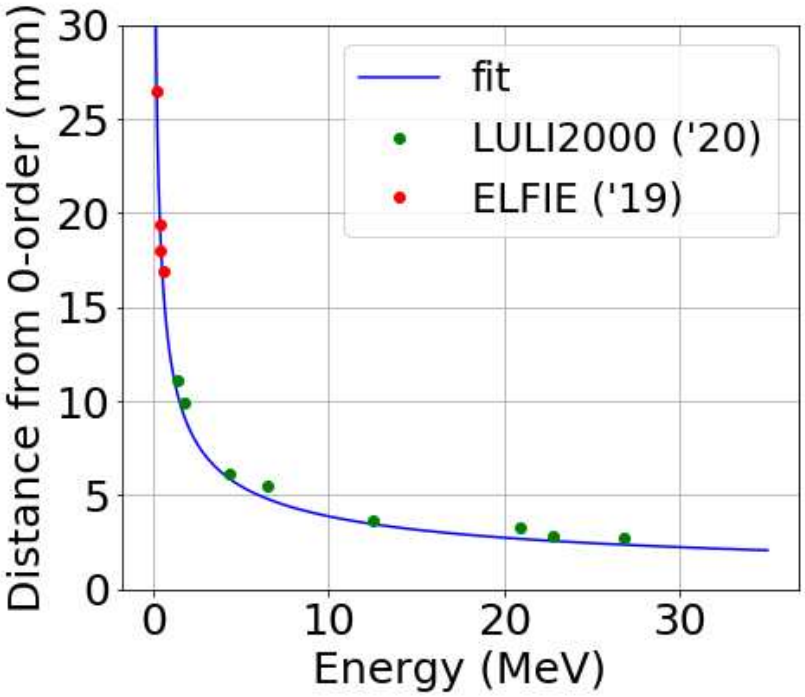

Figure A.5: *Distance from the 0-order on the IP vs cutoff proton energy: calibration data points (from LULI2000 and ELFIE) and fitted function (Eq. A.1 with the fitted parameters in Eq. A.7), obtained by considering the calibrations points both from the LULI2000 and the ELFIE campaigns.*

This curve visibly passes closer to the calibration points at lower energy.

As we mentioned in the previous chapter, Eq. A.1 is not valid for low energy protons, hence we can not expect to find parameters that are valid for a wide spectrum. For this reason and because of the fact that we are mostly interested in proton energies of the order of a few MeVs, we will only considered

the calibration done on LULI2000, whose result is shown in Fig. A.4.

A.4 Proton energy

By inverting Eq. A.1, we obtain

$$E_k = \frac{(q\,B\,l_B)^2\left(D_B + \frac{l_B}{2}\right)^2}{2\,m_p\,x^2} \tag{A.8}$$

which is plotted in Fig. A.6, where we have used the parameters from the fit with only the LULI2000 calibration points, $D_B^{fit} = -26.4$ mm, $B^{fit} = 0.58$ T.

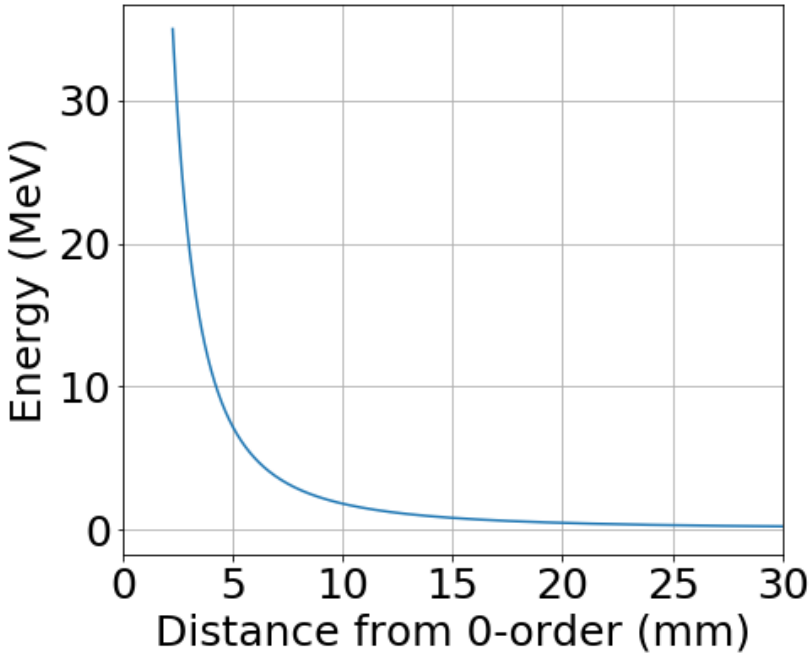

Figure A.6: *Energy of the protons as a function of their distance from the 0-order on the IP (Eq. A.1).*

The error on the energy E_k is retrieved by propagating the error on the position Δx.

$$\Delta E_k = \left|\frac{dE_k}{dx}\right| \Delta x = \frac{2^{3/2}\sqrt{m_p}}{q\,B\,l_B\left(D_B + \frac{l_B}{2}\right)} E_k^{3/2}\,\Delta x \tag{A.9}$$

This leads to an error that increases with the proton energy.

In Fig. A.7 we have plotted the absolute and the relative errors on the energy normalised with the errors on the position.

In Fig. A.10 are plotted the absolute and relative errors for uncertainties on the position $\Delta x = 0.5$ mm and $\Delta x = 0.1$ mm. These are indeed the typical two values relative to the first (until shot #11) and

second (from shot #12) slits used during the experiment.

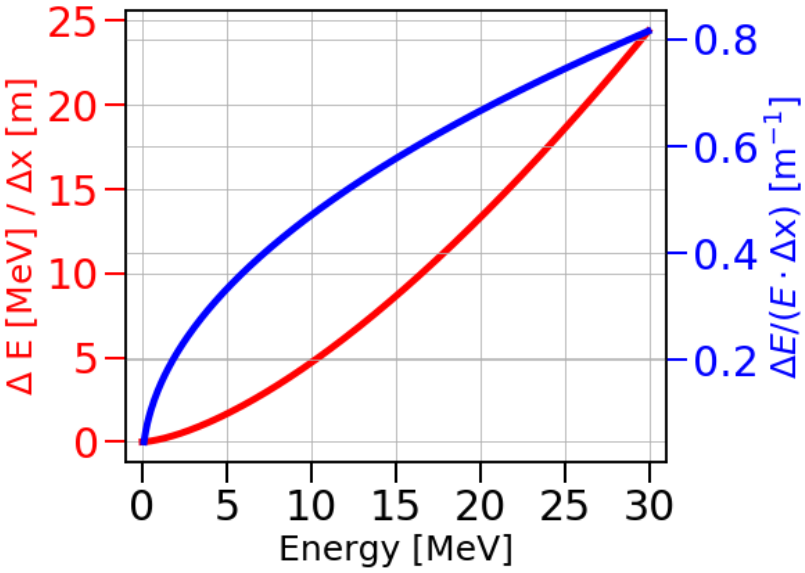

Figure A.7: *Absolute (red) and relative (blue) errors on the energy normalised with the error on the position.*

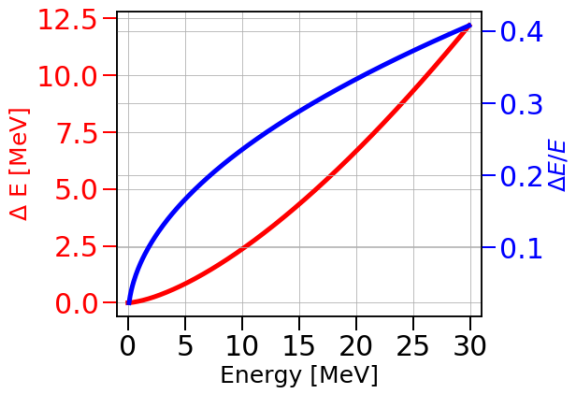

Figure A.8: $\Delta x = 0.5\ mm$ $(FWHM = 1\ mm)$

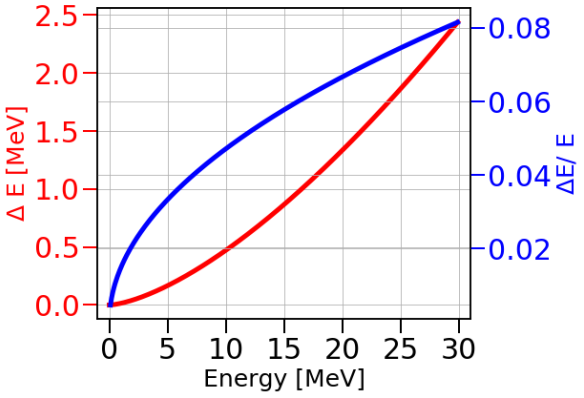

Figure A.9: $\Delta x = 0.1\ mm$ $(FWHM = 0.2\ mm)$

Figure A.10: *Absolute (red) and relative (blue) errors on the energy for two values of the error on the position.*

Bibliography

(1995). LLNL Science & Technology Review.

Abdo, A. A., Ackermann, M., Ajello, M., Allafort, A., Baldini, L., Ballet, J., Barbiellini, G., Bastieri, D., Bechtol, K., Bellazzini, R., et al. (2010). Fermi Large Area Telescope Observations of the Supernova Remnant W28 (G6. 4–0.1). *The Astrophysical Journal*, 718(1):348.

Abraham, J., Abreu, P., Aglietta, M., Aguirre, C., Allard, D., Allekotte, I., Allen, J., Allison, P., Alvarez, C., Alvarez-Muñiz, J., et al. (2007). Correlation of the highest-energy cosmic rays with nearby extragalactic objects. *Science*, 318(5852):938–943.

Ackermann, M., Ajello, M., Allafort, A., Baldini, L., Ballet, J., Barbiellini, G., Bastieri, D., Belfiore, A., Bellazzini, R., Berenji, B., et al. (2011). A cocoon of freshly accelerated cosmic rays detected by fermi in the cygnus superbubble. *Science*, 334(6059):1103–1107.

Ahmed, H., Dieckmann, M. E., Romagnani, L., Doria, D., Sarri, G., Cerchez, M., Ianni, E., Kourakis, I., Giesecke, A. L., Notley, M., et al. (2013). Time-resolved characterization of the formation of a collisionless shock. *Physical Review Letters*, 110(20):205001.

Albertazzi, B., Béard, J., Ciardi, A., Vinci, T., Albrecht, J., Billette, J., Burris-Mog, T., Chen, S. N., Da Silva, D., Dittrich, S., Herrmannsdörfer, T., Hirardin, B., Kroll, F., Nakatsutsumi, M., Nitsche, S., Riconda, C., Romagnagni, L., Schlenvoigt, H.-P., Simond, S., Veuillot, E., Cowan, T. E., Portugall, O., Pépin, H., and Fuchs, J. (2013). Production of large volume, strongly magnetized laser-produced plasmas by use of pulsed external magnetic fields. *Review of Scientific Instruments*, 84(4):043505.

Anderson, B. R., Skoug, R. M., Steinberg, J. T., and McComas, D. J. (2012). Variability of the solar wind suprathermal electron strahl. *Journal of Geophysical Research (Space Physics)*, 117(A4):A04107.

Arran, C., Ridgers, C. P., and Woolsey, N. C. (2021). Proton radiography in background magnetic fields. *Matter and Radiation at Extremes*, 6(4):046904.

Atzeni, S. and Meyer-ter Vehn, J. (2004). *The Physics of Inertial Fusion: BeamPlasma Interaction, Hydrodynamics, Hot Dense Matter*, volume 125. OUP Oxford.

Bale, S. D., Mozer, F. S., and Horbury, T. S. (2003). Density-transition scale at quasiperpendicular collisionless shocks. *Physical Review Letters*, 91(26):265004.

Balikhin, M. A. and Wilkinson, W. P. (1996). Ion heating within the ramp of quasi-perpendicular subcritical collisionless shocks. *Geophysical research letters*, 23(10):1063–1066.

Balogh, A. and Treumann, R. A. (2013). *Physics of collisionless shocks: space plasma shock waves*. Springer New York, New York, NY.

Baraka, S. (2016). Large scale Earth's bow shock with Northern IMF as simulated by PIC code in parallel with MHD model. *Journal of Astrophysics and Astronomy*, 37(2):1–16.

Basko, M. M. and Johner, J. (1998). Ignition energy scaling of inertial confinement fusion targets. *Nuclear Fusion*, 38(12):1779.

Bell, A., Choi, P., Dangor, A., Willi, O., Bassett, D., and Hooker, C. (1988). Collisionless shock in a laser-produced ablating plasma. *Physical Review A*, 38(3):1363.

Belmont, G., Grappin, R., Mottez, F., Pantellini, F., and Pelletier, G. (2013). *Collisionless plasmas in astrophysics*. John Wiley & Sons.

Bemporad, A. and Mancuso, S. (2011a). Identification of super- and subcritical regions in shocks driven by coronal mass ejections. *The Astrophysical Journal Letters*, 739(2).

Bemporad, A. and Mancuso, S. (2011b). Identification of super-and subcritical regions in shocks driven by coronal mass ejections. *The Astrophysical Journal Letters*, 739(2):L64.

Bemporad, A. and Mancuso, S. (2013). Super-and sub-critical regions in shocks driven by radio-loud and radio-quiet CMEs. *Journal of Advanced Research*, 4(3):287–291.

Benuzzi-Mounaix, A., Mazevet, S., Ravasio, A., Vinci, T., Denoeud, A., Koenig, M., Amadou, N., Brambrink, E., Festa, F., Levy, A., et al. (2014). Progress in warm dense matter study with applications to planetology. *Physica Scripta*, 2014(T161):014060.

Berčič, L., Maksimović, M., Landi, S., and Matteini, L. (2019). Scattering of strahl electrons in the solar wind between 0.3 and 1 au: Helios observations. *Monthly Notices of the Royal Astronomical Society*, 486(3):3404–3414.

Berkner, K. and Wells, R. O. (1998). Wavelet transforms and denoising algorithms. In *Conference Record of Thirty-Second Asilomar Conference on Signals, Systems and Computers (Cat. No. 98CH36284)*, volume 2, pages 1639–1643. IEEE.

Blandford, R. and Eichler, D. (1987). Particle acceleration at astrophysical shocks: A theory of cosmic ray origin. *Physics Reports*, 154(1):1–75.

Blasi, P. (2013). The origin of galactic cosmic rays. *The Astronomy and Astrophysics Review*, 21(1):1–73.

Blasi, P., Epstein, R. I., and Olinto, A. V. (2000). Ultra-high-energy cosmic rays from young neutron star winds. *The Astrophysical Journal*, 533(2):L123.

Bockasten, K. (1961). Transformation of observed radiances into radial distribution of the emission of a plasma. *J. Opt. Soc. Am.*, 51(9):943–947.

Bolanos, S., Smets, R., Chen, S. N., Grisolet, A., Filippov, E., Henares, J. L., Nastasa, V., Pikuz, S., Riquier, R., Safranova, M., et al. (2019). Laboratory evidence of the halting of magnetic reconnection by a weak guide field. *arXiv preprint arXiv:1909.01684*.

Boldyrev, S. and Horaites, K. (2019). Kinetic theory of the electron strahl in the solar wind. *Monthly Notices of the Royal Astronomical Society*, 489(3):3412–3419.

Bolton, P., Borghesi, M., Brenner, C., Carroll, D., De Martinis, C., Fiorini, F., Flacco, A., Floquet, V., Fuchs, J., Gallegos, P., Giove, D., Green, J., Green, S., Jones, B., Kirby, D., McKenna, P., Neely, D., Nuesslin, F., Prasad, R., Reinhardt, S., Roth, M., Schramm, U., Scott, G., Ter-Avetisyan, S., Tolley, M., Turchetti, G., and Wilkens, J. (2014). Instrumentation for diagnostics and control of laser-accelerated proton (ion) beams. *Physica Medica*, 30(3):255–270.

Book, D. L. (1980). NRL (Naval Research Laboratory) plasma formulary.

Boumis, P., Xilouris, E. M., Alikakos, J., Christopoulou, P. E., Mavromatakis, F., Katsiyannis, A. C., and Goudis, C. D. (2009). Discovery of optical emission from the supernova remnant G 32.8-0.1 (Kes 78). *Astronomy & Astrophysics*, 499(3):789–797.

Boyd, R., Bernstein, L., and Brune, C. (2009). Studying nuclear astrophysics at nif. *Physics today*, 62(LLNL-JRNL-414484).

Bragg, W. H. (1904). LXXIII. On the absorption of α rays, and on the classification of the α rays from radium. *The London, Edinburgh, and Dublin Philosophical Magazine and Journal of Science*, 8(48):719–725.

Braginskii, S. I. (1965). Transport processes in a plasma. *Reviews of Plasma Physics*, 1:205.

Bret, A., Stockem, A., Fiuza, F., Ruyer, C., Gremillet, L., Narayan, R., and Silva, L. O. (2013). Collisionless shock formation, spontaneous electromagnetic fluctuations, and streaming instabilities. *Physics of Plasmas*, 20(4):042102.

Brogan, C. L. (2007). OH (1720 MHz) masers: signposts of SNR/molecular cloud interactions. *Proceedings of the International Astronomical Union*, 3(S242):299–306.

Brunetti, G. and Lazarian, A. (2007). Compressible turbulence in galaxy clusters: physics and stochastic particle re-acceleration. *Monthly Notices of the Royal Astronomical Society*, 378:245–275.

Bucksbaum, P. H., Dunne, G. V., Fiuza, F., Meuren, S., Peskin, M. E., Reis, D. A., Torgrimsson, G., White, G., and Yakimenko, V. (2021). Probing QED cascades and pair plasmas in laboratory experiments LoI to cosmic frontier. Snowmass.

Burdonov, K., Fazzini, A., Lelasseux, V., Albrecht, J., Antici, P., Ayoul, Y., Beluze, A., Cavanna, D., Ceccotti, T., Chabanis, M., et al. (2021). Characterization and performance of the Apollon Short-Focal-Area facility following its commissioning at 1 PW level. *Matter and Radiation at Extremes*, 6(6):064402.

Burgess, D. and Scholer, M. (2007). Shock front instability associated with reflected ions at the perpendicular shock. *Physics of Plasmas*, 14(1):012108.

Burlaga, L. F., Ness, N. F., Acuna, M. H., Lepping, R. P., Connerney, J. E. P., and Richardson, J. D. (2008). Magnetic fields at the solar wind termination shock. *Nature*, 454(7200):75–77.

Burlaga, L. F., Ness, N. F., Gurnett, D. A., and Kurth, W. S. (2013). Evidence for a shock in interstellar plasma: Voyager 1. *The Astrophysical Journal Letters*, 778(1):L3.

Bykov, A. M., Dolag, K., and Durret, F. (2008). Cosmological shock waves. In *Clusters of Galaxies*, pages 119–140. Springer.

Bykov, A. M. and Fleishman, G. D. (1992). On non-thermal particle generation in superbubbles. *Monthly Notices of the Royal Astronomical Society*, 255(2):269–275.

Bykov, A. M. and Treumann, R. A. (2011). Fundamentals of collisionless shocks for astrophysical application, 2. Relativistic shocks. *The Astronomy and Astrophysics Review*, 19(1):1–67.

Cai, D., Li, Y., Nishikawa, K.-I., Xiao, C., Yan, X., and Pu, Z. (2003). Parallel 3-D electromagnetic particle code using high performance FORTRAN: Parallel TRISTAN. In *Space Plasma Simulation*, pages 25–53. Springer.

Caprioli, D. (2015). Cosmic-ray acceleration and propagation. *arXiv preprint arXiv:1510.07042*.

Caprioli, D. and Spitkovsky, A. (2014). Simulations of ion acceleration at non-relativistic shocks. I. Acceleration efficiency. *The Astrophysical Journal*, 783(2):91.

Cargill, P., Goodrich, C., and Papadopoulos, K. (1986). Interaction of two collisionless shocks. *Phys, Rev. Lett.*, 56(18):1988.

Casner, A., Caillaud, T., Darbon, S., Duval, A., Thfouin, I., Jadaud, J., LeBreton, J., Reverdin, C., Rosse, B., Rosch, R., et al. (2015). LMJ/PETAL laser facility: Overview and opportunities for laboratory astrophysics. *High Energy Density Physics*, 17:2–11.

Cecchetti, C. A., Borghesi, M., Fuchs, J., Schurtz, G., Kar, S., Macchi, A., Romagnani, L., Wilson, P. A., Antici, P., Jung, R., Osterholtz, J., Pipahl, C. A., Willi, O., Schiavi, A., Notley, M., and Neely, D. (2009). Magnetic field measurements in laser-produced plasmas via proton deflectometry. *Physics of Plasmas*, 16(4):043102.

Cesarsky, D., Cox, P., Pineau des Forêts, G., van Dishoeck, E. F., Boulanger, F., and Wright, C. M. (1999). Isocam spectro-imaging of the h2 rotational lines in the supernova remnant ic443. *Astronomy & Astrophysics*, 348:945–949.

Chakraborti, S., Ray, A., Soderberg, A. M., Loeb, A., and Chandra, P. (2011). Ultra-high-energy cosmic ray acceleration in engine-driven relativistic supernovae. *Nature Communications*, 2(1):1–6.

Chalov, S. V., Malama, Y. G., Alexashov, D. B., and Izmodenov, V. V. (2016). Acceleration of interstellar pickup protons at the heliospheric termination shock: Voyager 1/2 energetic proton fluxes in the inner heliosheath. *Monthly Notices of the Royal Astronomical Society*, 455(1):431–437.

Chen, F. F. (2016). *Introduction to Plasma Physics and Controlled Fusion*. Springer.

Chen, M., Sheng, Z.-M., Dong, Q.-L., He, M.-Q., Li, Y.-T., Bari, M. A., and Zhang, J. (2007). Collisionless electrostatic shock generation and ion acceleration by ultraintense laser pulses in overdense plasmas. *Physics of Plasmas*, 14(5).

Chen, S. N., Gauthier, M., Bazalova-Carter, M., Bolanos, S., Glenzer, S., Riquier, R., Revet, G., Antici, P., Morabito, A., Propp, A., Starodubstev, M., and Fuchs, J. (2016). Absolute dosimetric characterization of Gafchromic EBT3 and HDv2 films using commercial flat-bed scanners and evaluation of the scanner response function variability. *Review of Scientific Instruments*, 87(7):073301.

Chernin, A. D., Efremov, Y. N., and Voinovich, P. A. (1995). Superassociations: violent star formation induced by shock–shock collisions. *Monthly Notices of the Royal Astronomical Society*, 275(2):313–326.

Chernukha, Y. (2019). *Investigation of phase transitions triggered by laser-induced focusing shock waves*. PhD thesis, Le Mans.

Chopineau, L., Denoeud, A., Leblanc, A., Porat, E., Martin, P., Vincenti, H., and Quéré, F. (2021). Spatio-temporal characterization of attosecond pulses from plasma mirrors. *Nature physics*, 17(8):968–973.

Claussen, M. J., Frail, D. A., Goss, W. M., and Gaume, R. A. (1997). Polarization observations of 1720 MHz OH masers toward the three supernova remnants W28, W44, and IC 443. *The Astrophysical Journal*, 489(1):143.

Colburn, D. S. and Sonett, C. P. (1966). Discontinuities in the solar wind. *Space Science Review*, 5(4):439–506.

Cole, A. J., Kilkenny, J. D., Rumsby, P. T., Evans, R. G., J., H. C., and Key, M. H. (1982). Measurement of Rayleigh–Taylor instability in a laser-accelerated target. *Nature*, 299(5881):329–331.

Collette, A. and Gekelman, W. (2010). Structure of an exploding laser-produced plasma. *Physical Review Letters*, 105(19):195003.

Cosentino, G., Jiménez-Serra, I., Caselli, P., Henshaw, J. D., Barnes, A. T., Tan, J. C., Viti, S., Fontani, F., and Wu, B. (2019). Interstellar plunging waves: Alma resolves the physical structure of nonstationary mhd shocks. *The Astrophysical Journal Letters*, 881(2):L42.

Cowan, T. E., Fuchs, J., Ruhl, H., Kemp, A., Audebert, P., Roth, M., Stephens, R., Barton, I., Blazevic, A., Brambrink, E., Cobble, J., Fernández, J., Gauthier, J.-C., Geissel, M., Hegelich, M., Kaae, J., Karsch, S., Le Sage, G. P., Letzring, S., Manclossi, M., Meyroneinc, S., Newkirk, A., Pépin, H., and Renard-LeGalloudec, N. (2004). Ultralow emittance, multi-mev proton beams from a laser virtual-cathode plasma accelerator. *Physical review letters*, 92(20):204801.

Croston, J. H. et al. (2009). High-energy particle acceleration at the radio-lobe shock of Centaurus A. *Monthly Notices of the Royal Astronomical Society*, 395(4):1999–2012.

Danson, C. N., Haefner, C., Bromage, J., Butcher, T., Chanteloup, J.-C. F., Chowdhury, E. A., Galvanauskas, A., Gizzi, L. A., Hein, J., Hillier, D. I., et al. (2019). Petawatt and exawatt class lasers worldwide. *High Power Laser Science and Engineering*, 7.

Davidson, P. A. (2002). An introduction to magnetohydrodynamics.

Davis Jr, L. (1956). Modified Fermi mechanism for the acceleration of cosmic rays. *Physical Review*, 101(1):351.

Dean, S. O., McLean, E., Stamper, J., and Griem, H. R. (1971). Demonstration of collisionless interactions between interstreaming ions in a laser-produced-plasma experiment. *Physical Review Letters*, 27(8):487.

Decker, R. B., Krimigis, S. M., Roelof, E. C., Hill, M. E., Armstrong, T. P., Gloeckler, G., Hamilton, D. C., and Lanzerotti, L. J. (2005). Voyager 1 in the foreshock, termination shock, and heliosheath. *Science*, 309(5743):2020–2024.

Decker, R. B., Krimigis, S. M., Roelof, E. C., Hill, M. E., Armstrong, T. P., Gloeckler, G., Hamilton, D. C., and Lanzerotti, L. J. (2008). Mediation of the solar wind termination shock by non-thermal ions. *Nature*, 454(7200):67–70.

Derouillat, J., Beck, A., Pérez, F., Vinci, T., Chiaramello, M., Grassi, A., Flé, M., Bouchard, G., Plotnikov, I., Aunai, N., et al. (2018). Smilei: A collaborative, open-source, multi-purpose particle-in-cell code for plasma simulation. *Computer Physics Communications*, 222:351–373.

Diesing, R. and Caprioli, D. (2021). Steep cosmic-ray spectra with revised diffusive shock acceleration. *The Astrophysical Journal*, 922(1):1.

Dirnberger, L., Dyer, P. E., Farrar, S. R., and Key, P. H. (1994). Observation of magnetic-field-enhanced excitation and ionization in the plume of KrF-laser-ablated magnesium. *Applied Physics A*, 59(3):311–316.

Dizière, A. (2012). *Astrophysique de laboratoire avec les lasers de haute énergie et de haute puissance: des chocs radiatifs aux jets d'étoiles jeunes*. PhD thesis, Physique des plasmas [physics.plasm-ph]. Ecole Polytechnique X.

Drake, J. F., Swisdak, M., Che, H., and Shay, M. A. (2006). Electron acceleration from contracting magnetic islands during reconnection. *Nature*, 443(7111):553–556.

Drake, R. (2006a). *High Energy Density Physics: Fundamentals, Inertial Fusion and Experimental Astrophysics*. Springer-Verlag Berlin Heidelberg.

Drake, R. P. (2006b). *High-Energy-Density Physics*. Graduate Texts in Physics. Springer International Publishing AG.

Drury, L. O. (1983). An introduction to the theory of diffusive shock acceleration of energetic particles in tenuous plasmas. *Reports on Progress in Physics*, 46(8):973.

Drury, L. O. (2012). Origin of cosmic rays. *Astroparticle Physics*, 39:52–60.

Dubey, A., Almgren, A., Bell, J., Berzins, M., Brandt, S., Bryan, G., Colella, P., Graves, D., Lijewski, M., Löffler, F., et al. (2014). A survey of high level frameworks in block-structured adaptive mesh refinement packages. *Journal of Parallel and Distributed Computing*, 74(12):3217–3227.

Dudkin, G. N., Nechaev, B. A., and Padalko, V. N. (2000). Simulation of the formation of accelerating structures and ion acceleration in the collision of magnetosonic shock waves. *Plasma Physics Reports*, 26(6):502–506.

Duţan, I. and Caramete, L. I. (2015). Ultra-high-energy cosmic rays from low-luminosity active galactic nuclei. *Astroparticle Physics*, 62:206–216.

Edmiston, J. P. and Kennel, C. F. (1984a). A parametric survey of the first critical Mach number for a fast MHD shock. *Journal of plasma physics*, 32(3):429–441.

Edmiston, J. P. and Kennel, C. F. (1984b). A parametric survey of the first critical Mach number for a fast MHD shock. *Journal of Plasma Physics*, 32:429–441.

Ellison, D. C., Moebius, E., and Paschmann, G. (1990). Particle injection and acceleration at earth's bow shock-comparison of upstream and downstream events. *The Astrophysical Journal*, 352:376–394.

Faenov, A. Y., Pikuz, S. A., Erko, A. I., Bryunetkin, B. A., Dyakin, V. M., Ivanenkov, G. V., Mingaleev, A. R., Pikuz, T. A., Romanova, V. M., and Shelkovenko, T. A. (1994). High-performance x-ray spectroscopic devices for plasma microsources investigations. *Physica Scripta*, 50(4):333–338.

Falize, É., Bouquet, S., and Michaut, C. (2009a). Scaling laws for radiating fluids - the pillar of laboratory astrophysics. *Astrophysics and Space Science*, 322(1):107–111.

Falize, É., Dizière, A., and Loupias, B. (2011). Invariance concepts and scalability of two-temperature astrophysical radiating fluids. *Astrophysics and Space Science*, 336(1):201–205.

Falize, É., Loupias, B., Dizière, A., Ravasio, A., Gregory, C. D., Cavet, C., Michaut, C., Koenig, M., Leidinger, J. P., Ribeyre, X., Nazarov, W., Barroso, P., Millerioux, M., Chevrot, M., and Leconte, L. (2009b). Similarity concepts and scaling laws of the accreted column in magnetic cataclysmic variables: the polar project. In *SF2A-2009: Proceedings of the Annual meeting of the French Society of Astronomy and Astrophysics*, page 275.

Fermi, E. (1949). On the origin of the cosmic radiation. *Physical review*, 75(8):1169.

Ferrand, G. (2007). *Étude de l'accélération des rayons cosmiques par les ondes de choc des restes de supernovae dans les superbulles galactiques*. PhD thesis, Université Paul Sabatier - Toulouse III.

Ferrand, G. and Marcowith, A. (2010). On the shape of the spectrum of cosmic rays accelerated inside superbubbles. *Astronomy & Astrophysics*, 510:A101.

Filippov, E. D., Makarov, S. S., Burdonov, K. F., Yao, W., Revet, G., Béard, J., Bolaños, S., Chen, S. N., Guediche, A., Hare, J., et al. (2020). Enhanced x-ray emission arising from laser-plasma confinement by a strong transverse magnetic field. *arXiv preprint arXiv:2006.12424*.

Filippov, E. D., Makarov, S. S., Burdonov, K. F., Yao, W., Revet, G., Béard, J., Bolaños, S., Chen, S. N., Guediche, A., Hare, J., Romanovsky, D., Skobelev, I. Y., Starodubtsev, M., Ciardi, A., Pikuz, S. A., and Fuchs, J. (2021). Enhanced x-ray emission arising from laser-plasma confinement by a strong transverse magnetic field. *Scientific Reports*, 11(1):8180.

Filippov, E. D., Skobelev, I. Y., Revet, G., Chen, S. N., Khiar, B., Ciardi, A., Khaghani, D., Higginson, D. P., Pikuz, S. A., and Fuchs, J. (2019). X-ray spectroscopy evidence for plasma shell formation in experiments modeling accretion columns in young stars. *Matter and Radiation at Extremes*, 4(6):064402.

Fiuza, F., Swadling, G. F., Grassi, A., Rinderknecht, H. G., Higginson, D. P., Ryutov, D. D., Bruulsema, C., Drake, R. P., Funk, S., Glenzer, S., Gregori, G., Li, C. K., Pollock, B. B., Remington, B. A., Ross, J. S., Rozmus, W., Sakawa, Y., Spitkovsky, A., Wilks, S., and Park, H.-S. (2020). Electron acceleration in laboratory-produced turbulent collisionless shocks. *Nature Physics*.

Formisano, V. (1974). The earth's bow shock fine structure. In *Correlated interplanetary and magnetospheric observations*, pages 187–223. Springer.

Formisano, V. and Hedgecock, P. C. (1973a). On the structure of the turbulent bow shock. *Journal of Geophysical Research*, 78(28):6522–6534.

Formisano, V. and Hedgecock, P. C. (1973b). Solar wind interaction with the Earth's magnetic field: 3. On the Earth's bow shock structure. *Journal of Geophysical Research*, 78(19):3745–3760.

Fox, W., Fiksel, G., Bhattacharjee, A., Chang, P.-Y., Germaschewski, K., Hu, S. X., and Nilson, P. M. (2013). Filamentation instability of counterstreaming laser-driven plasmas. *Physical review letters*, 111(22):225002.

Frail, D. A. and Mitchell, G. F. (1998). OH (1720 MHz) masers as signposts of molecular shocks. *The Astrophysical Journal*, 508(2):690.

Froula, D., Ross, J., Pollock, B., Davis, P., James, A., Divol, L., Edwards, M., Offenberger, A., Price, D., Town, R., et al. (2007). Quenching of the nonlocal electron heat transport by large external

magnetic fields in a laser-produced plasma measured with imaging thomson scattering. *Physical review letters*, 98(13):135001.

Froula, D. H., Glenzer, S. H., Luhmann, N. C., and Scheffield, J. (2011a). *Plasma scattering of electromagnetic radiation*. Elsevier.

Froula, D. H., Luhmann Jr, N. C., Sheffield, J., and Glenzer, S. H. (2011b). *Plasma scattering of electromagnetic radiation: theory and measurement techniques*. Elsevier.

Fryxell, B., Olson, K., Ricker, P., Timmes, F. X., Zingale, M., Lamb, D. Q., MacNeice, P., Rosner, R., Truran, J. W., and Tufo, H. (2000a). FLASH: An adaptive mesh hydrodynamics code for modeling astrophysical thermonuclear flashes. *The Astrophysical Journal Supplement Series*, 131(1):273.

Fryxell, B., Olson, K., Ricker, P., Timmes, F. X., Zingale, M., Lamb, D. Q., MacNeice, P., Rosner, R., Truran, J. W., and Tufo, H. (2000b). FLASH: An adaptive mesh hydrodynamics code for modeling astrophysical thermonuclear flashes. *The Astrophysical Journal Supplement Series*, 131(1):273.

Fujioka, S., Zhang, Z., Ishihara, K., Shigemori, K., Hironaka, Y., Johzaki, T., Sunahara, A., Yamamoto, N., Nakashima, H., Watanabe, T., Shiraga, H., H., N., and Azechi, H. (2013). Kilotesla magnetic field due to a capacitor-coil target driven by high power laser. *Scientific reports*, 3(1):1–7.

Gabici, S., Evoli, C., Gaggero, D., Lipari, P., Mertsch, P., Orlando, E., Strong, A., and Vittino, A. (2019). The origin of galactic cosmic rays: Challenges to the standard paradigm. *International Journal of Modern Physics D*, 28(15):1930022.

Gales, S. (2015). Laser driven nuclear science and applications: The need of high efficiency, high power and high repetition rate laser beams. *The European Physical Journal Special Topics*, 224(13):2631–2637.

Gao, L., Nilson, P. M., Igumenshchev, I. V., Haines, M. G., Froula, D. H., Betti, R., and Meyerhofer, D. D. (2015). Precision mapping of laser-driven magnetic fields and their evolution in high-energy-density plasmas. *Physical Review Letters*, 114(21):215003.

Gargaté, L. and Spitkovsky, A. (2011). Ion acceleration in non-relativistic astrophysical shocks. *The Astrophysical Journal*, 744(1):67.

Ghavamian, P., Laming, J. M., and Rakowski, C. E. (2006). A physical relationship between electron-proton temperature equilibration and mach number in fast collisionless shocks. *The Astrophysical Journal Letters*, 654(1):L69.

Giagkiozis, S., Walker, S. N., Pope, S. A., and Collinson, G. (2017). Validation of single spacecraft methods for collisionless shock velocity estimation. *Journal of Geophysical Research: Space Physics*, 122(8):8632–8641.

Gibbon, P. (2005). *Short pulse laser interactions with matter*. London Imperial College Press.

Gosling, J. T., Bame, S. J., Feldman, W. C., Paschmann, G., Sckopke, N., and Russell, C. T. (1984). Suprathermal ions upstream from interplanetary shocks. *Journal of Geophysical Research*, 89(A7):5409–5418.

Gould, R. G. et al. (1959). The laser, light amplification by stimulated emission of radiation. In *The Ann Arbor conference on optical pumping, the University of Michigan*, volume 15, page 92.

Grassi, A. (2017). *Collisionless shocks in the context of Laboratory Astrophysics*. PhD thesis, Université Pierre et Marie Curie & Università di Pisa.

Grassi, A., Grech, M., Amiranoff, F., Macchi, A., and Riconda, C. (2017). Radiation-pressure-driven ion weibel instability and collisionless shocks. *Physical Review E*, 96(3):033204.

Graziani, C., Tzeferacos, P., Lamb, D. Q., and Li, C. (2017). Inferring morphology and strength of magnetic fields from proton radiographs. *Review of Scientific Instruments*, 88(12):123507.

Greco, E., Miceli, M., Orlando, S., Peres, G., Troja, E., and Bocchino, F. (2018). Discovery of a jet-like structure with overionized plasma in the snr ic 443. *Astronomy & Astrophysics*, 615:A157.

Greenstadt, E. W., Russell, C. T., Scarf, F. L., Formisano, V., and Neugebauer, M. (1975). Structure of the quasi-perpendicular laminar bow shock. *Journal of Geophysical Research*, 80(4):502–514.

Gurnett, D. A., Kurth, W. S., Burlaga, L. F., and Ness, N. F. (2013). In Situ Observations of Interstellar Plasma with Voyager 1. *Science*, 341(6153):1489–1492.

Gurnett, D. A., Kurth, W. S., Stone, E. C., Cummings, A. C., Heikkila, B., Lal, N., Krimigis, S. M., Decker, R. B., Ness, N. F., and Burlaga, L. F. (2021). A foreshock model for interstellar shocks of solar origin: Voyager 1 and 2 observations. *The Astronomical Journal*, 161(1):11.

Gurnett, D. A., Kurth, W. S., Stone, E. C., Cummings, A. C., Krimigis, S. M., Decker, R. B., Ness, N. F., and Burlaga, L. F. (2015). Precursors to interstellar shocks of solar origin. *ApJ*, 809(2):121.

Haines, M. G. (1986). Magnetic-field generation in laser fusion and hot-electron transport. *Canadian Journal of Physics*, 64(8):912–919.

Harilal, S. S. and Tillack, M. S. (2004). Laser plasma density measurements using interferometry.

Harutyunyan, A. and Sedrakian, A. (2016). Electrical conductivity tensor of dense plasma in magnetic fields. *arXiv preprint arXiv:1607.04541*.

He, S.-K., Jiao, J.-L., Deng, Z.-G., Lu, F., Yang, L., Zhang, F.-Q., Dong, K.-G., Hong, W., Zhang, Z.-M., Zhang, B., et al. (2019). Generation of ultrahigh-velocity collisionless electrostatic shocks using an ultra-intense laser pulse interacting with foil-gas target. *Chinese Physics Letters*, 36(10):105201.

Heil, C. E. and Walnut, D. F. (1989). Continuous and discrete wavelet transforms. *SIAM review*, 31(4):628–666.

Hietala, H., Agueda, N., Andréeová, K., Vainio, R., Nylund, S., Kilpua, E., and Koskinen, H. (2011). In situ observations of particle acceleration in shock-shock interaction. *Journal of Geophysical Research: Space Physics*, 116(A10).

Higginson, D. P., Korneev, P., Ruyer, C., Riquier, R., Moreno, Q., Béard, J., Chen, S. N., Grassi, A., Grech, M., Gremillet, L., et al. (2019). Laboratory investigation of particle acceleration and magnetic field compression in collisionless colliding fast plasma flows. *Communications Physics*, 2(1):1–7.

Higginson, D. P., Revet, G., Khiar, B., Béard, J., Blecher, M., Borghesi, M., Burdonov, K., Chen, S. N., Filippov, E., Khaghani, D., et al. (2017). Detailed characterization of laser-produced astrophysically-relevant jets formed via a poloidal magnetic nozzle. *High Energy Density Physics*, 23:48–59.

Hillas, A. M. (1984). The origin of ultra-high-energy cosmic rays. *Annual review of astronomy and astrophysics*, 22(1):425–444.

Hillas, A. M. (2006). Cosmic rays: Recent progress and some current questions. *arXiv preprint astro-ph/0607109*.

Hoffman, I. M., Goss, W. M., Brogan, C. L., and Claussen, M. J. (2005). The OH (1720 MHz) supernova remnant masers in W28: MERLIN and VLBA polarization observations. *The Astrophysical Journal*, 620(1):257.

Horaites, K., Boldyrev, S., and Medvedev, M. V. (2019). Electron strahl and halo formation in the solar wind. *Monthly Notices of the Royal Astronomical Society*, 484(2):2474–2481.

Huang, Z. and Kim, K.-J. (2007). Review of x-ray free-electron laser theory. *Physical Review Special Topics-Accelerators and Beams*, 10(3):034801.

Hudson, P. D. and Kahn, F. D. (1965). Reflection of charged particles by plasma shocks. *Monthly Notices of the Royal Astronomical Society*, 131(1):23–49.

Huntington, C. M., Fiuza, F., Ross, J. S., Zylstra, A. B., Drake, R. P., Froula, D. H., Gregori, G., Kugland, N. L., Kuranz, C. C., Levy, M. C., et al. (2015). Observation of magnetic field generation via the weibel instability in interpenetrating plasma flows. *Nature Physics*, 11(2):173–176.

Ilie, R., Daldorff, L. K. S., Liemohn, M. W., Toth, G., and Chan, A. A. (2017). Calculating the inductive electric field in the terrestrial magnetosphere. *Journal of Geophysical Research: Space Physic*, 122:5391–5403.

Izumi, N., Snavely, R., Gregori, G., Koch, J. A., Park, H.-S., and Remington, B. A. (2006). Application of imaging plates to x-ray imaging and spectroscopy in laser plasma experiments. *Review of Scientific Instruments*, 77(10):10E325.

Jiao, J., Zhang, B., Yu, J., Zhang, Z., Yan, Y., He, S., Deng, Z., Teng, J., Hong, W., and Gu, Y. (2017). Generating high-yield positrons and relativistic collisionless shocks by 10 PW laser. *Laser and Particle Beams*, 35(2):234–240.

Jiao, J. L., He, S. K., Zhuo, H. B., Qiao, B., Yu, M. Y., Zhang, B., Deng, Z. G., Lu, F., Zhou, K. N., Wang, X. D., Xie, N., Yang, L., Zhang, F. Q., Zhou, W. M., and Gu, Y. Q. (2019). Experimental observation of ion–ion acoustic instability associated with collisionless shocks in laser-produced plasmas. *The Astrophysical Journal*, 883(2):L37.

Jones, F. C. and Ellison, D. C. (1991). The plasma physics of shock acceleration. *Sp. Sci. Rev*, 58(1):259–346.

Kajdič, P., Alexandrova, O., Maksimovic, M., Lacombe, C., and Fazakerley, A. (2016). Suprathermal electron strahl widths in the presence of narrow-band whistler waves in the solar wind. *The Astrophysical Journal*, 833(2):172.

Karsch, S., Düsterer, S., Schwoerer, H., Ewald, F., Habs, D., Hegelich, M., Pretzler, G., Pukhov, A., Witte, K., and Sauerbrey, R. (2003). High-intensity laser induced ion acceleration from heavy-water droplets. *Physical review letters*, 91(1):015001.

Kato, T. N. and Takabe, H. (2008). Nonrelativistic collisionless shocks in unmagnetized electron-ion plasmas. *The Astrophysical Journal*, 681(2):L93.

Kaufman, M. J. and Neufeld, D. A. (1996). Far-infrared water emission from magnetohydrodynamic shock waves. *The Astrophysical Journal*, 456:611.

Kemp, A. J. and Meyer-ter Vehn, J. (1998). An equation of state code for hot dense matter, based on the qeos description. *Nuclear Instruments and Methods in Physics Research Section A: Accelerators, Spectrometers, Detectors and Associated Equipment*, 415(3):674–676.

Khiar, B. et al. (2019a). Laser-produced magnetic-Rayleigh-Taylor unstable plasma slabs in a 20 T magnetic field. *Physical Review Letters*, 123(20):205001.

Khiar, B., Revet, G., Ciardi, A., Burdonov, K., Filippov, E., Béard, J., Cerchez, M., Chen, S., Gangolf, T., Makarov, S., et al. (2019b). Laser-produced magnetic-rayleigh-taylor unstable plasma slabs in a 20 t magnetic field. *Physical Review Letters*, 123(20):205001.

Kirk, J., Melrose, D., Priest, E., Benz, A., and Courvoisier, T. (1994). *Plasma astrophysics*. Springer, Berlin.

Koenig, M., Benuzzi-Mounaix, A., Ravasio, A., Vinci, T., Ozaki, N., Lepape, S., Batani, D., Huser, G., Hall, T., Hicks, D., et al. (2005). Progress in the study of warm dense matter. *Plasma Physics and Controlled Fusion*, 47(12B):B441.

Koenig, M., Faral, B., Boudenne, J. M., Batani, D., Benuzzi, A., Bossi, S., Remond, C., Perrine, J. P., Temporal, M., and Atzeni, S. (1995). Relative consistency of equations of state by laser driven shock waves. *Physical Review Letters*, 74(12):2260.

Koopman, D. W. (1976). High-beta effects and anomalous diffusion in plasmas expanding into magnetic fields. *The Physics of Fluids*, 19(5):670–674.

Koralesky, B., Frail, D. A., Goss, W. M., Claussen, M. J., and Green, A. J. (1998). Shock-excited maser emission from supernova remnants: G32. 8- 0.1, g337. 8- 0.1, g346. 6- 0.2, and the hb 3/w3 complex. *The Astronomical Journal*, 116(3):1323.

Kugland, N., Ryutov, D.D. Plechaty, C., Ross, J., and Park, H.-S. (2012). Relation between electric and magnetic field structures and their proton-beam images. *Review of Scientific Instruments*, 83(10):101301.

Kuramitsu, Y., Sakawa, Y., Morita, T., Ide, T., Nishio, K., Tanji, H., Aoki, H., Dono, S., Gregory, C., Waugh, J., et al. (2012). Laboratory investigations on the origins of cosmic rays. *Plasma Physics and Controlled Fusion*, 54(12):124049.

Lancia, L., Albertazzi, B., Boniface, C., Grisollet, A., Riquier, R., Chaland, F., Thanh, K.-C., Mellor, P., Antici, P., Buffechoux, S., Chen, S., Doria, D., Nakatsutsumi, M., Peth, C., Swantusch, M., Starodubtsev, M., Palumbo, L., Borghesi, M., Willi, O., and Fuchs, J. (2014). Topology of megagauss

magnetic fields and of heat-carrying electrons produced in a high-power laser-solid interaction. *Physical review letters*, 113(23):235001.

Landau, L. D. and Lifshitz, E. M. (1987). *Fluid Mechanics*. Oxford: Pergamon Press.

Lebedev, S. V., Frank, A., and Ryutov, D. D. (2019). Exploring astrophysics-relevant magnetohydrodynamics with pulsed-power laboratory facilities. *Reviews of Modern Physics*, 91(2):025002.

Lee, L. C., Mandt, M. E., and Wu, C. S. (1987). Increase of ion kinetic temperature across a collisionless shock: 2. A simulation study. *Journal of Geophysical Research*, 92:13438.

Lee, M. A., Shapiro, V. D., and Sagdeev, R. Z. (1996). Pickup ion energization by shock surfing. *Journal of Geophysical Research: Space Physics*, 101(A3):4777–4789.

Leemans, W., Gonsalves, A., Mao, H.-S., Nakamura, K., Benedetti, C., Schroeder, C., Tóth, C., Daniels, J., Mittelberger, D., Bulanov, S., et al. (2014). Multi-GeV electron beams from capillary-discharge-guided subpetawatt laser pulses in the self-trapping regime. *Physical review letters*, 113(24):245002.

Lever, E. L., Quest, K. B., and Shapiro, V. D. (2001). Shock surfing vs. shock drift acceleration. *Geophysical research letters*, 28(7):1367–1370.

Li, C. K., Séguin, F. H., Frenje, J. A., Rygg, J. R., Petrasso, R. D., Town, R. P. J., Amendt, P. A., Hatchett, S. P., Landen, O. L., Mackinnon, A. J., Patel, P. K., Smalyuk, V. A., Sangster, T. C., and Knauer, J. P. (2006). Measuring e and b fields in laser-produced plasmas with monoenergetic proton radiography. *Physical review letters*, 97(13):135003.

Li, C. K., Tikhonchuk, V. T., Moreno, Q., Sio, H., D'Humières, E., Ribeyre, X., Korneev, P., Atzeni, S., Betti, R., Birkel, A., et al. (2019). Collisionless shocks driven by supersonic plasma flows with self-generated magnetic fields. *Physical review letters*, 123(5):055002.

Li, H. and Chen, Y. (2010). γ-rays from molecular clouds illuminated by accumulated diffusive protons from supernova remnant w28. *Monthly Notices of the Royal Astronomical Society: Letters*, 409(1):L35–L38.

Li, Y., Feng, J., Li, D., Tan, J., Huang, K., Wang, J., Tao, M., and Chen, L. (2018). Betatron X/γ-Ray Radiation from Wakefield-Accelerated Electrons Wiggling in Laser Fields. In *International Conference on X-ray Lasers*, pages 109–116. Springer.

Liebert, E., Nabert, C., and Glassmeier, K.-H. (2018). Statistical survey of day-side magnetospheric current flow using cluster observations: bow shock. In *Annales Geophysicae*, volume 36, pages 1073–1080. Copernicus GmbH.

Liu, R.-Y., Wang, X.-Y., and Dai, Z.-G. (2011). Nearby low-luminosity gamma-ray bursts as the sources of ultra-high-energy cosmic rays revisited. *Monthly Notices of the Royal Astronomical Society*, 418(2):1382–1391.

Liu, Y. D., Richardson, J. D., Wang, C., and Luhmann, J. G. (2014). Propagation of the 2012 March Coronal Mass Ejections from the Sun to Heliopause. *ApJL*, 788(2):L28.

Lockett, P., Gauthier, E., and Elitzur, M. (1999). Oh 1720 megahertz masers in supernova remnants: C-shock indicators. *The Astrophysical Journal*, 511(1):235.

London, R. A. and Rosen, M. D. (1986). Hydrodynamics of exploding foil x-ray lasers. *The Physics of fluids*, 29(11):3813–3822.

Longair, M. S. (1992). *High energy astrophysics. Vol. 1: Particles, photons and their detection*.

Macchi, A., Borghesi, M., and Passoni, M. (2013). Ion acceleration by superintense laser-plasma interaction. *Reviews of Modern Physics*, 85(2):751.

MacFarlane, J. J., Golovkin, I. E., Woodruff, P. R., Welch, D. R., Oliver, B. V., Melhorn, T. A., Campbell, R. B., Mehlhorn, T. A., and Campbell, R. B. (2003). Simulation of the ionization dynamics of aluminum irradiated by intense short-pulse lasers. *Proceedings of Inertial Fusion and Science Applications (American Nuclear Society, La Grange Park, IL)*, pages 1–4.

Maiman, T. H. et al. (1960). Stimulated optical radiation in ruby.

Maksimovic, M., Zouganelis, I., Chaufray, J. Y., Issautier, K., Scime, E. E., Littleton, J. E., Marsch, E., McComas, D. J., Salem, C., Lin, R. P., and Elliott, H. (2005). Radial evolution of the electron distribution functions in the fast solar wind between 0.3 and 1.5 AU. *Journal of Geophysical Research (Space Physics)*, 110(A9):A09104.

Malkov, M. A. and Drury, L. O. (2001). Nonlinear theory of diffusive acceleration of particles by shock waves. *Reports on Progress in Physics*, 64(4):429.

Mančić, A., Fuchs, J., Antici, P., Gaillard, S. A., and Audebert, P. (2008). Absolute calibration of photostimulable image plate detectors used as (0.5–20 mev) high-energy proton detectors. *Review of Scientific Instruments*, 79(7):073301.

Mancic, A., Robiche, J., Antici, P., Audebert, P., Blancard, C., Combis, P., Dorchies, F., Faussurier, G., Fourmaux, S., Harmand, M., Kodama, R., Lancia, L., Mazevet, S., Nakatsutsumi, M., Peyrusse, O.,

Recoules, V., Renaudin, P., Shepherd, R., and Fuchs, J. (2010). Isochoric heating of solids by laser-accelerated protons : Experimental characterization and self-consistent hydrodynamic modeling. *High Energy Density Physics*, 6(1):21–28.

Marcowith, A., Bret, A., Bykov, A., Dieckman, M. E., Drury, L. O., Lembège, B., Lemoine, M., Morlino, G., Murphy, G., Pelletier, G., et al. (2016a). The microphysics of collisionless shock waves. *Reports on Progress in Physics*, 79(4):046901.

Marcowith, A., Bret, A. Bykov, A., Dieckman, M. E., Drury, L. O., Lembège, B., Lemoine, M., Morlino, G., Murphy, G., Pelletier, G., Plotnikov, I., Reville, B., Riquelme, M., Sironi, L., and Stockem Novo, A. (2016b). The microphysics of collisionless shock waves. *Rep. Prog. Phys.*, 79(4):046901.

Marcowith, A., Ferrand, G., Grech, M., Meliani, Z., Plotnikov, I., and Walder, R. (2020). Multi-scale simulations of particle acceleration in astrophysical systems. *Living Reviews in Computational Astrophysics*, 6(1):1–182.

Marshall, W. (1955). The structure of magneto-hydrodynamic shock waves. *Proc. R. Soc. Lond. A*, 233:367—376.

Matsakos, T., Uribe, A., and Königl, A. (2015). Classification of magnetized star-planet interactions: bow shocks, tails, and inspiraling flows. *Astronomy & Astrophysics*, 578:A6.

Matsukiyo, S. and Scholer, M. (2003). Modified two-stream instability in the foot of high mach number quasi-perpendicular shocks. *Journal of Geophysical Research: Space Physics*, 108(A12).

Matsukiyo, S. and Scholer, M. (2011). Microstructure of the heliospheric termination shock: Full particle electrodynamic simulations. *Journal of Geophysical Research: Space Physics*, 116(A8).

McBride, J. B., Ott, E., Boris, J. P., and Orens, J. H. (1972). Theory and simulation of turbulent heating by the modified two-stream instability. *The Physics of Fluids*, 15(12):2367–2383.

Medvedev, M. V. and Loeb, A. (1999). Generation of magnetic fields in the relativistic shock of gamma-ray burst sources. *The Astrophysical Journal*, 526(2):697.

Meinecke, J., Doyle, H., Miniati, F., Bell, A. R., Bingham, R., Crowston, R., Drake, R., Fatenejad, M., Koenig, M., Kuramitsu, Y., et al. (2014). Turbulent amplification of magnetic fields in laboratory laser-produced shock waves. *Nature Physics*, 10(7):520–524.

Mellott, M. (1984a). The physical mechanisms of subcritical collisionless shock-wave formation. *Advances in Space Research*, 4(2-3):245–253.

Mellott, M. M. (1984b). The physical mechanisms of subcritical collisionless shock-wave formation. *Adv. Space Res.*, 4(2-3):245–253.

Mellott, M. M. and Greenstadt, E. W. (1984). The structure of oblique subcritical bow shocks: ISEE 1 and 2 observations. *Journal of Geophysical Research*, 89(A4):2151–2161.

Miceli, M., Bamba, A., Orlando, S., Zhou, P., Safi-Harb, S., Chen, Y., and Bocchino, F. (2017). Xmm-newton observation of the supernova remnant kes 78 (g32. 8-0.1): Evidence of shock-cloud interaction. *Astronomy & Astrophysics*, 599:A45.

Moreno, Q., Dieckmann, M. E., Ribeyre, X., and D'Humières, E. (2019). Failed self-reformation of a sub-critical fast magnetosonic shock in collisionless plasma. *Plasma Research Express*, 1(3):035001.

Moses, E. I. and Meier, W. R. (2008). The national ignition facility and the golden age of high energy density science. *IEEE transactions on plasma science*, 36(3):802–808.

Mostafavi, P. and Zank, G. P. (2018). The Structure of Shocks in the Very Local Interstellar Medium. *ApJL*, 854(1):L15.

Mulser, P. and Bauer, D. (2020). *Hot Matter from High-Power Lasers*. Springer.

Nam, C. H., Sung, J. H., Lee, H. W., Youn, J. W., and Lee, S. K. (2018). Performance of the 20 fs, 4 PW Ti: sapphire laser at CoReLs. In *2018 Conference on Lasers and Electro-Optics (CLEO)*, pages 1–2. IEEE.

Nava, L., Recchia, S., Gabici, S., Marcowith, A., Brahimi, L., and Ptuskin, V. (2019). Non-linear diffusion of cosmic rays escaping from supernova remnants - II. Hot ionized media. *Monthly Notices of the Royal Astronomical Society*, 484(2):2684–2691.

Niemann, C., Gekelman, W., Constantin, C. G., Everson, E. T., Schaeffer, D. B., Bondarenko, A. S., Clark, S. E., Winske, D., Vincena, S., Van Compernolle, B., et al. (2014). Observation of collisionless shocks in a large current-free laboratory plasma. *Geophysical Research Letters*, 41(21):7413–7418.

Nobukawa, K. K., Hirayama, A., Shimaguchi, A., Fujita, Y., Nobukawa, M., and Yamauchi, S. (2019). Neutral iron line in the supernova remnant ic 443 and implications for mev cosmic rays. *Publications of the Astronomical Society of Japan*, 71(6):115.

Ocker, S. K., Cordes, J. M., Chatterjee, S., Gurnett, D. A., Kurth, W. S., and Spangler, S. R. (2021). Persistent plasma waves in interstellar space detected by Voyager 1. *Nature Astronomy*, 5:761–765.

Ohsawa, Y. and Sakai, J. (1985). Ion acceleration in quasi-perpendicular collisionless magnetosonic shock waves with subcritical Mach number. *Geophysical research letters*, 12(9):617–619.

Okon, H., Imai, M., Tanaka, T., Uchida, H., and Tsuru, T. G. (2020). Probing cosmic rays with fe k-α line structures generated by multiple ionization process. *Publications of the Astronomical Society of Japan*, 72(4):L7.

Okon, H., Uchida, H., Tanaka, T., Matsumura, H., and Tsuru, T. G. (2018). The origin of recombining plasma and the detection of the fe-k line in the supernova remnant w 28. *Publications of the Astronomical Society of Japan*, 70(3):35.

Oliveira, D. M. (2017). Magnetohydrodynamic shocks in the interplanetary space: A theoretical review. *Brazilian Journal of Physics*, 47(1):81–95.

Olver, P. J. (1995). *Equivalence, invariants and symmetry*. Cambridge University Press.

Onsager, T. and Thomsen, M. (1991). The Earth's foreshock, bow shock, and magnetosheath. *Reviews of Geophysics and Space Physics;(United States)*, 29(CONF-910878-).

Palmroth, M., Honkonen, I., Sandroos, A., Kempf, Y., von Alfthan, S., and Pokhotelov, D. (2013). Preliminary testing of global hybrid-vlasov simulation: Magnetosheath and cusps under northward interplanetary magnetic field. *Journal of Atmospheric and Solar-Terrestrial Physics*, 99:41–46.

Papadopoulos, D., Ramirez, P., Genevrier, K., Ranc, L., Lebas, N., Pellegrina, A., Le Blanc, C., Monot, P., Martin, L., Zou, J., et al. (2017). High-contrast 10 fs OPCPA-based front end for multi-PW laser chains. *Optics letters*, 42(18):3530–3533.

Park, H.-S., Huntington, C. M., Fiuza, F., Drake, R. P., Froula, D. H., Gregori, G., Koenig, M., Kugland, N. L., Kuranz, C. C., Lamb, D. Q., et al. (2015). Collisionless shock experiments with lasers and observation of weibel instabilities. *Physics of Plasmas*, 22(5):056311.

Paul, J., Goldenbaum, G., Iiyoshi, A., Holmes, L., and Hardcastle, R. (1967). Measurement of electron temperatures produced by collisionless shock waves in a magnetized plasma. *Nature*, 216(5113):363–364.

Paul, J., Holmes, L., Parkinson, M., and Sheffield, J. (1965). Experimental observations on the structure of collisionless shock waves in a magnetized plasma. *Nature*, 208(5006):133–135.

Peterson, B. M. (1997). *An introduction to active galactic nuclei*. Cambridge University Press.

Petrosian, V. (2012). Stochastic acceleration by turbulence. *Space science reviews*, 173(1):535–556.

Pfotenhauer, S. M., Jäckel, O., Sachtleben, A., Polz, J., Ziegler, W., Schlenvoigt, H. P., Amthor, K. U., Kaluza, M. C., Ledingham, K. W. D., Sauerbrey, R., et al. (2008). Spectral shaping of laser generated proton beams. *New journal of physics*, 10(3):033034.

Phan, V. H. M., Gabici, S., Morlino, G., Terrier, R., Vink, J., Krause, J., and Menu, M. (2020). Constraining the cosmic ray spectrum in the vicinity of the supernova remnant w28: from sub-gev to multi-tev energies. *Astronomy & Astrophysics*, 635:A40.

Pierrard, V., Lazar, M., Poedts, S., Štverák, Š., Maksimovic, M., and Trávníček, P. (2016). The electron temperature and anisotropy in the solar wind. Comparison of the core and halo populations. *Solar Physics*, 291(7):2165–2179.

Pierrard, V., Lazar, M., and Schlickeiser, R. (2011). Evolution of the electron distribution function in the whistler wave turbulence of the solar wind. *Solar Physics*, 269(2):421–438.

Pierrard, V., Maksimovic, M., and Lemaire, J. (2001). Core, Halo and Strahl Electrons in the Solar Wind. *Astrophysics and Space Science*, 277:195–200.

Pilipp, W. G., Miggenrieder, H., Montgomery, M. D., Mühlhäuser, K. H., Rosenbauer, H., and Schwenn, R. (1987). Characteristics of electron velocity distribution functions in the solar wind derived from the helios plasma experiment. *Journal of Geophysical Research: Space Physics*, 92(A2):1075–1092.

Pinter, S. (1980). The thickness of interplanetary collisionless shock waves. *Bull. Astron. Inst. Czechosl.*, 31:368–379.

Piran, T. (2005). The physics of gamma-ray bursts. *Reviews of Modern Physics*, 76(4):1143.

Pritchett, P. L. (2003). Particle-in-cell simulation of plasmas—a tutorial. *Space Plasma Simulation*, pages 1–24.

Reach, W. T., Richter, M., Gusdorf, A., Dewitt, C., et al. (2019). Supernova shocks in molecular clouds: Velocity distribution of molecular hydrogen. *The Astrophysical Journal*, 884(1):81.

Remington, B. A., Drake, R. P., and Ryutov, D. D. (2006). Experimental astrophysics with high power lasers and z pinches. *Rev. Mod. Phys.*, 78:755–807.

Rho, J. and Petre, R. (1998). Mixed-morphology supernova remnants. *The Astrophysical Journal Letters*, 503(2):L167.

Richardson, J. D., Kasper, J. C., Wang, C., Belcher, J. W., and Lazarus, A. J. (2008). Cool heliosheath plasma and deceleration of the upstream solar wind at the termination shock. *Nature*, 454(7200):63–66.

Ridgers, C., Brady, C. S., Duclous, R., Kirk, J., Bennett, K., Arber, T., Robinson, A., and Bell, A. (2012). Dense electron-positron plasmas and ultraintense γ rays from laser-irradiated solids. *Physical review letters*, 108(16):165006.

Rigby, A., Cruz, F., Albertazzi, B., Bamford, R., Bell, A. R., Cross, J. E., Fraschetti, F., Graham, P., Hara, Y., Kozlowski, P. M., et al. (2018). Electron acceleration by wave turbulence in a magnetized plasma. *Nature Physics*, 14(5):475–479.

Ripin, B. H., Huba, J. D., McLean, E. A., Manka, C. K., Peyser, T., Burris, H. R., and Grun, J. (1993). Sub-alfvénic plasma expansion. *Physics of Fluids B: Plasma Physics*, 5(10):3491–3506.

Romagnani, L., Bulanov, S. V., Borghesi, M., Audebert, P., Gauthier, J. C., Löwenbrück, K., Mackinnon, A. J., Patel, P., Pretzler, G., Toncian, T., et al. (2008a). Observation of collisionless shocks in laser-plasma experiments. *Physical review letters*, 101(2):025004.

Romagnani, L., Bulanov, S. V., Borghesi, M., Audebert, P., Gauthier, J. C., Löwenbrück, K., Mackinnon, A. J., Patel, P., Pretzler, G., Toncian, T., and Willi, O. (2008b). Observation of collisionless shocks in laser-plasma experiments. *Phys. Rev. Lett.*, 101:025004.

Ross, J. S., Glenzer, S. H., Palastro, J. P., Pollock, B. B., Price, D., Divol, L., Tynan, G. R., and Froula, D. H. (2010a). Observation of relativistic effects in collective thomson scattering. *Physical review letters*, 104(10):105001.

Ross, J. S., Glenzer, S. H., Palastro, J. P., Pollock, B. B., Price, D., Tynan, G. R., and Froula, D. H. (2010b). Thomson-scattering measurements in the collective and noncollective regimes in laser produced plasmas (invited). *Review of Scientific Instruments*, 81(10):10D523.

Ross, J. S., Higginson, D. P., Ryutov, D., Fiuza, F., Hatarik, R., Huntington, C. M., Kalantar, D. H., Link, A., Pollock, B. B., Remington, B. A., et al. (2017). Transition from collisional to collisionless regimes in interpenetrating plasma flows on the national ignition facility. *Physical Review Letters*, 118(18):185003.

Ryazantsev, S. N., Skobelev, I. Y., Faenov, A. Y., Pikuz, T. A., et al. (2016). Diagnostics of laser-produced plasmas based on the analysis of intensity ratios of He-like Ions X-ray emission. *Phys. Plasmas*, 23(12):123301.

Ryazantsev, S. N., Skobelev, I. Y., Faenov, A. Y., Pikuz, T. A., Grum-Grzhimailo, A. N., and Pikuz, S. A. (2015). X-ray spectroscopy diagnostics of a recombining plasma in laboratory astrophysics studies. *JETP Letters*, 102(11):707–712.

Ryutov, D., Drake, R. P., Kane, J., Liang, E., Remington, B. A., and Wood-Vasey, W. M. (1999). Similarity criteria for the laboratory simulation of supernova hydrodynamics. *The Astrophysical Journal*, 518(2):821.

Ryutov, D. D. (2018). Scaling laws for dynamical plasma phenomena. *Physics of Plasmas*, 25(10):100501.

Ryutov, D. D., Drake, R. P., and Remington, B. A. (2000). Criteria for scaled laboratory simulations of astrophysical MHD phenomena. *The Astrophysical Journal Supplement Series*, 127(2):465–468.

Ryutov, D. D. and Remington, B. A. (2003). A "perfect" hydrodynamic similarity and effect of the reynolds number on the global scale motion. *Physics of Plasmas*, 10(7):2629–2632.

Sagdeev, R. Z. (1966). Cooperative phenomena and shock waves in collisionless plasmas. *Reviews of plasma physics*, 4:23.

Sakawa, Y., Morita, T., Kuramitsu, Y., and Takabe, H. (2016). Collisionless electrostatic shock generation using high-energy laser systems. *Advances in Physics: X*, 1(3):425–443.

Sanderson, J. J. and Uhrig, R. A. (1978). Extended rankine-hugoniot relations for collisionless shocks. *Journal of Geophysical Research: Space Physics*, 83(A4):1395–1400.

Sarri, G., Schumaker, W., Di Piazza, A., Vargas, M., Dromey, B., Dieckmann, M. E., Chvykov, V., Maksimchuk, A., Yanovsky, V., He, Z., et al. (2013). Table-top laser-based source of femtosecond, collimated, ultrarelativistic positron beams. *Physical review letters*, 110(25):255002.

Schaeffer, D. B. (2014). *Generation of quasi-perpendicular collisionless shocks by a laser-driven magnetic piston*. PhD thesis, University of California Los Angeles.

Schaeffer, D. B., Fox, W., Follett, R., Fiksel, G., Li, C., Matteucci, J., Bhattacharjee, A., and Germaschewski, K. (2019). Direct observations of particle dynamics in magnetized collisionless shock precursors in laser-produced plasmas. *Physical Review Letters*, 122(24):245001.

Schaeffer, D. B., Fox, W., Haberberger, D., Fiksel, G., Bhattacharjee, A., Barnak, D. H., Hu, S. X., and Germaschewski, K. (2017a). Generation and evolution of high-mach-number laser-driven magnetized collisionless shocks in the laboratory. *Physical Review Letters*, 119(2):025001.

Schaeffer, D. B., Fox, W., Haberberger, D., Fiksel, G., Bhattacharjee, A., Barnak, D. H., Hu, S. X., Germaschewski, K., and Follett, R. K. (2017b). High-mach number, laser-driven magnetized collisionless shocks. *Physics of Plasmas*, 24(12):122702.

Schaeffer, D. B., Fox, W., Matteucci, J., Lezhnin, K. V., Bhattacharjee, A., and Germaschewski, K. (2020). Kinetic simulations of piston-driven collisionless shock formation in magnetized laboratory plasmas. *Physics of Plasmas*, 27(4):042901.

Schenck, A., Park, S., and Post, S. (2016). A chandra study of the interstellar metallicity in the large magellanic cloud using supernova remnants. *The Astronomical Journal*, 151(6):161.

Seough, J., Nariyuki, Y., Yoon, P. H., and Saito, S. (2015). Strahl formation in the solar wind electrons via whistler instability. *The Astrophysical Journal Letters*, 811(1):L7.

Shapiro, V. D. and Üçer, D. (2003). Shock surfing acceleration. *Planetary and Space Science*, 51(11):665–680.

Singh, P. K., Pathak, V. B., Shin, J. H., Choi, I. W., Nakajima, K., Lee, S. K., Sung, J. H., Lee, H. W., Rhee, Y. J., Aniculaesei, C., et al. (2020). Electrostatic shock acceleration of ions in near-critical-density plasma driven by a femtosecond petawatt laser. *Scientific reports*, 10(1):1–10.

Slavin, J. A. and Holzer, R. E. (1981). Solar wind flow about the terrestrial planets 1. modeling bow shock position and shape. *Journal of Geophysical Research: Space Physics*, 86(A13):11401–11418.

Snavely, R. A., Key, M. H., Hatchett, S. P., Cowan, T. E., Roth, M., Phillips, T. W., Stoyer, M. A., Henry, E. A., Sangster, T. C., Singh, M. S., et al. (2000). Intense high-energy proton beams from petawatt-laser irradiation of solids. *Physical review letters*, 85(14):2945.

Stasiewicz, K. and Eliasson, B. (2020). Quasi-adiabatic and stochastic heating and particle acceleration at quasi-perpendicular shocks. *The Astrophysical Journal*, 903(1):57.

Strickland, D. and Mourou, G. (1985). Compression of amplified chirped optical pulses. *Optics communications*, 55(6):447–449.

Štverák, Š., Maksimovic, M., Trávníček, P. M., Marsch, E., Fazakerley, A. N., and Scime, E. E. (2009). Radial evolution of nonthermal electron populations in the low-latitude solar wind: Helios, cluster, and ulysses observations. *Journal of Geophysical Research: Space Physics*, 114(A5).

Sudo, S., Sekiguchi, T., and Sato, K. (1978). Re-thermalisation and flow of laser-produced plasmas in a uniform magnetic field. *Journal of Physics D: Applied Physics*, 11(3):389.

Swadling, G. (2019). First direct experimental observation of weibel-mediated collisionless shock formation and the resulting nonthermal electron acceleration in laboratory experiments. *Bulletin of the American Physical Society*, 64.

Swanson, D. G. (1989). *Plasma Waves*. Elsevier.

Takabe, H. (2001). Astrophysics with intense and ultra-intense lasers - "laser astrophysics". *Progress of Theoretical Physics Supplement*, 143:202–265.

Thomas, A. G. R., Kingham, R. J., and Ridgers, C. P. (2009). Rapid self-magnetization of laser speckles in plasmas by nonlinear anisotropic instability. *New Journal of Physics*, 11(3):033001.

Tremblin, P. and Chiang, E. (2013). Colliding planetary and stellar winds: charge exchange and transit spectroscopy in neutral hydrogen. *Monthly Notices of the Royal Astronomical Society*, 428(3):2565–2576.

Treumann, R. A. (2009). Fundamentals of collisionless shocks for astrophysical application, 1. Non-relativistic shocks. *The Astronomy and Astrophysics Review*, 17(4):409–535.

Tuckfield, R. G. and Schwirzke, F. (1969). Dynamics of a laser created plasma expanding in a magnetic field. *Plasma physics*, 11(1):11.

Turner, D. L., Wilson III, L. B., Liu, T. Z., Cohen, I. J., Schwartz, S. J., Osmane, A., Fennell, J. F., Clemmons, J. H., Blake, J. B., Westlake, J., Mauk, B. H., Jaynes, A. N., Leonard, T., Baker, D. N., Strangeway, R. J., Russell, C. T., Gershman, D. J., Avanov, L., Giles, B. L., Torbert, R. B., Broll, J., Gomez, R. G., A., F. S., and Burch, J. L. (2018). Autogenous and efficient acceleration of energetic ions upstream of earth's bow shock. *Nature*, 561(6554):206–210.

Underwood, C., Baird, C., Murphy, C., Armstrong, C., Thornton, C., Finlay, O., Streeter, M., Selwood, M., Brierley, N., Cipiccia, S., et al. (2020). Development of control mechanisms for a laser wakefield accelerator-driven bremsstrahlung x-ray source for advanced radiographic imaging. *Plasma Physics and Controlled Fusion*, 62(12):124002.

Valencia, D., O'Connell, R. J., and Sasselov, D. D. (2009). The role of high-pressure experiments on determining super-earth properties. *Astrophysics and Space Science*, 322(1):135–139.

Vannoni, G., Aharonian, F., Gabici, S., Kelner, S., and Prosekin, A. (2011). Acceleration and radiation of ultra-high energy protons in galaxy clusters. *Astronomy & Astrophysics*, 536:A56.

VanZeeland, M. and Gekelman, W. (2004). Laser-plasma diamagnetism in the presence of an ambient magnetized plasma. *Physics of Plasmas*, 11(1):320–323.

Vaupré, S., Hily-Blant, P., Ceccarelli, C., Dubus, G., Gabici, S., and Montmerle, T. (2014). Cosmic ray induced ionisation of a molecular cloud shocked by the w28 supernova remnant. *Astronomy & Astrophysics*, 568:A50.

Velàzquez, P. F., Dubner, G. M., Goss, W. M., and Green, A. J. (2002). Investigation of the large-scale neutral hydrogen near the supernova remnant w28. *The Astronomical Journal*, 124(4):2145.

Vlasov, A. A. (1962). *Many-Particle Theory*. US Atomic Energy Commission, Technical Information Service Extension.

Wang, X.-Y., Razzaque, S., and Mészáros, P. (2008a). On the origin and survival of ultra-high-energy cosmic-ray nuclei in gamma-ray bursts and hypernovae. *The Astrophysical Journal*, 677(1):432.

Wang, X.-Y., Razzaque, S., Mészáros, P., and Dai, Z. (2008b). Semi-relativistic Hypernovae as a source of UHE cosmic rays. In *AIP Conference Proceedings*, volume 1000, pages 459–462. American Institute of Physics.

Webb, G. M., Axford, W. I., and Terasawa, T. (1983). On the drift mechanism for energetic charged particles at shocks. *The Astrophysical Journal*, 270:537–553.

Weibel, E. S. (1959). Spontaneously growing transverse waves in a plasma due to an anisotropic velocity distribution. *Physical Review Letters*, 2(3):83.

Whang, Y. and Burlaga, L. (1985). Coalescence of two pressure waves associated with stream interactions. *Journal of Geophysical Research: Space Physics*, 90(A1):221–232.

Wilks, S. C., Kruer, W. L., Tabak, M., and Langdon, A. B. (1992). Absorption of ultra-intense laser pulses. *Physical review letters*, 69(9):1383.

Wilks, S. C., Langdon, A. B., Cowan, T. E., Roth, M., Singh, M., Hatchett, S., Key, M. H., Pennington, D., MacKinnon, A., and Snavely, R. A. (2001). Energetic proton generation in ultra-intense laser–solid interactions. *Physics of plasmas*, 8(2):542–549.

Woods, L. C. (1971). *Shock Waves in Collisionless Plasmas*. Wiley, New York.

Woosley, S. E. and Weaver, T. A. (1986). The physics of supernova explosions. *Annual review of astronomy and astrophysics*, 24(1):205–253.

Wu, C. S. (1982). Physical mechanisms for turbulent dissipation in collisionless shock waves. *Space Science Reviews*, 32(1):83–97.

Xu, S. and Lazarian, A. (2017). Magnetic field amplification in supernova remnants. *The Astrophysical Journal*, 850(2):126.

Yamada, M., Kulsrud, R., and Ji, H. (2010). Magnetic reconnection. *Reviews of Modern Physics*, 82(1):603.

Yang, Z., Lembège, B., and Lu, Q. (2012). Impact of the rippling of a perpendicular shock front on ion dynamics. *Journal of Geophysical Research: Space Physics*, 117(A7).

Yao, W., Fazzini, A., Chen, S., Burdonov, K., Antici, P., Béard, J., Bolaños, S., Ciardi, A., Diab, R., Filippov, E., et al. (2021). Laboratory evidence for proton energization by collisionless shock surfing. *Nature Physics*, 17(10):1177–1182.

Yao, W., Fazzini, A., Chen, S. N., Burdonov, K., Antici, P., Béard, J., Bolaños, S., Ciardi, A., Diab, R., Filippov, E. D., Kisyov, S., Lelasseux, V., Miceli, M., Moreno, Q., Nastasa, V., Orlando, S., Pikuz, S., Popescu, D. C., Revet, G., Ribeyre, X., d'Humières, E., and Fuchs, J. (2022). Detailed characterization of a laboratory magnetized supercritical collisionless shock and of the associated proton energization. *Matter and Radiation at Extremes*, 7(1):014402.

Yao, W., Qiao, B., Xu, Z., Zhang, H., Zhao, Z., Chang, H., Zhou, C., Zhu, S., and He, X. (2018). The baryon loading effect on relativistic astrophysical jet transport in the interstellar medium. *New Journal of Physics*, 20(5):053060.

Yao, W., Qiao, B., Zhao, Z., Lei, Z., Zhang, H., Zhou, C., Zhu, S., and He, X. (2019). Kinetic particle-in-cell simulations of the transport of astrophysical relativistic jets in magnetized intergalactic medium. *The Astrophysical Journal*, 876(1):2.

Zank, G., Pauls, H., Cairns, I., and Webb, G. (1996). Interstellar pickup ions and quasi-perpendicular shocks: Implications for the termination shock and interplanetary shocks. *Journal of Geophysical Research: Space Physics*, 101(A1):457–477.

Zank, G. P., Hunana, P., Mostafavi, P., Le Roux, J. A., Li, G., Webb, G. M., Khabarova, O., Cummings, A., Stone, E., and Decker, R. (2015). Diffusive shock acceleration and reconnection acceleration processes. *The Astrophysical Journal*, 814(2):137.

Zel'dovich, Y. B., Raizer, Y. P., Hayes, W. D., Probstein, R. F., and Gill, S. P. (1967). Physics of shock waves and high-temperature hydrodynamic phenomena, vol. 1.

Résumé de la thèse

Les objets et les phénomènes célestes suscitent l'intérêt de l'humanité depuis des millénaires, faisant de l'astronomie l'un des domaines de recherche les plus anciens. Au fil des siècles, le développement scientifique a permis de passer de l'observation à l'œil nu des corps célestes voisins à des à des investigations de plus en plus détaillées sur des objets astrophysiques lointains. Cependant, la capacité de découvrir et de mieux caractériser de nouveaux phénomènes lointains s'accompagne de l'apparition de nouvelles questions auxquelles l'astronomie seule ne peut pas répondre complètement. En effet, l'étude in situ de certains objets reste impossible en raison des énormes distances qui les séparent de la Terre, ce qui limite les données qui pourraient être collectées. L'échelle de temps caractéristique de nombreux phénomènes est très grande par rapport à l'échelle de temps typique de nos capacités d'observation, rendant difficile l'étude dynamique de ces systèmes.
Les énormes progrès réalisés au cours des dernières décennies dans le développement des lasers de haute puissance ont permis d'accéder, en laboratoire, à des conditions physiques extrêmes d'intérêt astrophysique. L'astrophysique "de laboratoire" est le domaine d'étude qui s'intéresse à l'investigation expérimentale des phénomènes astrophysiques qui, grâce à l'utilisation de lois d'échelle, peuvent être émulés en laboratoire.
Grâce aux progrès récents de la science informatique, le domaine des simulations numériques s'est développé. Celles-ci peuvent représenter un outil important, grâce à leur contrôlabilité et leur reproductibilité (malgré des coûts élevés en termes d'heures de calcul), car elles peuvent décrire un système en détail. Néanmoins, ils ont besoin de modèles analytiques précis sur lesquels se baser et donc à valider, ce qui ne peut pas être fourni par des observations limitées et incomplètes.
L'astrophysique de laboratoire joue donc un rôle crucial dans l'effort de compréhension des systèmes astrophysiques hors de portée et dans l'interprétation complète des observations astronomiques, car elle permet de les reproduire (à l'échelle) de manière contrôlée et bien caractérisée.

Ce travail de thèse est axé sur l'étude des ondes de choc "sans collisions", qui sont des phénomènes

se produisant dans de nombreux contextes astrophysiques, tels que les explosions de supernova et les arcs de choc. Elles sont tenues pour responsables de la production de particules énergétiques (rayons cosmiques), dont les mécanismes d'énergisation ne sont aujourd'hui pas entièrement compris. Un choc peut être considéré comme un changement abrupt de certaines quantités physiques décrivant le système physique, qui, en hydrodynamique, est médié par des effets de collision qui dissipent en chaleur l'énergie cinétique du fluide traversant le choc. Lorsqu'une telle transition se produit sur des échelles de longueur beaucoup plus petites que le libre parcours moyen d'une particule, nous avons affaire à une onde de choc "sans collisions". Dans ce cas, de telles discontinuités peuvent se former par l'émission et l'absorption d'excitations collectives du plasma.
Les expériences réalisées dans des installations laser de haute puissance ont été le principal outil d'investigation. En particulier, deux scénarios ont été explorés : un unique choc super-critique et l'interpénétration de deux chocs sous-critiques. L'analyse de nos données a également été soutenue par des simulations Particle-In-Cell (PIC), qui, avec les simulations magnétohydrodynamiques (MHD) réalisées en collaboration avec le CELIA, nous ont permis de mieux comprendre la microphysique qui se déroule dans nos expériences. Enfin, nos résultats sont considérés dans le contexte astrophysique, ce qui nous permet de déterminer les scénarios astrophysiques pertinents auxquels les chocs créés par laser de notre laboratoire peuvent s'appliquer.

En particulier, nous avons pu générer et caractériser expérimentalement un choc magnétisé super-critique quasi-perpendiculaire en irradiant une cible solide en téflon avec une impulsion laser de $\sim 10^{13}$ W/cm^2. Le système a été intégré dans un champ magnétique pulsé de 20 T appliqué de l'extérieur et dans un gaz d'hydrogène, qui a été converti en un plasma ambiant. Cette interaction a conduit à la formation d'un piston, consistant en un plasma dense ablaté s'étendant à partir de la cible, et d'un choc sans collisions, formé entre le plasma d'hydrogène poussé par le piston et le plasma de fond. Nous avons mesuré différentes caractéristiques du plasma créé par laser à différents moments : la densité (intégrée) d'électrons (par interférométrie et par diffusion de Thomson), les températures des ions et des électrons (par diffusion de Thomson), le champ électrique au front du choc (par radiographie protonique), la densité d'électrons intégrée dans le temps (par spectrométrie FSSR), et le spectre d'énergie des protons sortants (par spectrométrie à protons).
Ces mesures nous ont permis de caractériser le choc se produisant dans le plasma d'hydrogène comme étant sans collisions et de suivre sa transition de super-critique à sous-critique. Certains paramètres clés du choc produit en laboratoire sont similaires aux paramètres de l'arc de choc terrestre, du choc de "terminaison" du vent solaire et de quatre rémanents de supernova (Supernova Remnants, SNRs) non relativistes différents interagissant avec des nuages moléculaires denses. Nos

mesures expérimentales nous ont guidés dans la mise en place des simulations numériques qui ont modélisé nos systèmes. Nous avons simulé la scène globale avec le code MHD FLASH, ce qui nous a permis de reproduire l'évolution globale du système, du dépôt de l'énergie laser à la formation et à la propagation du piston et du choc.
Cependant, des simulations de type PIC avec le code SMILEI ont été nécessaires pour saisir les effets des processus cinétiques, hors de portée des simulations hydrodynamiques ou MHD. Nous avons utilisé des simulations PIC 1D3V (et, dans une mesure limitée, 2D3V) pour modéliser uniquement la phase d'évolution du choc sans collisions, pour laquelle nous avons pu sonder les champs électromagnétiques et les densités avec une haute résolution spatio-temporelle et même suivre des particules individuelles.
La présence de protons supra-thermiques détectés expérimentalement a été confirmée par nos simulations cinétiques. Celles-ci ont également montré que la plupart des protons énergétiques subissaient une accélération "de surf de choc" (Shock Surfing Acceleration, SSA) lors de leur interaction avec le front de choc.
La correspondance remarquable entre les spectres de protons simulés et mesurés identifie la SSA comme un responsable probable de l'énergisation des particules.

Dans la campagne expérimentale suivante, nous nous sommes concentrés sur l'interpénétration de deux chocs créés par laser. Ces chocs sans collisions ont été générés avec la même plateforme expérimentale que pour le cas du choc unique et caractérisés avec les mêmes diagnostics, mais dans une géométrie différente. Dans ce cas également, les données obtenues à partir de leur caractérisation ont été utilisées pour initialiser des simulations MHD et PIC, respectivement exécutées avec les codes FLASH et SMILEI. Alors que les simulations MHD ont été utilisées pour décrire la partie collisionnelle du problème - c'est-à-dire le piston - et l'évolution globale du système, les simulations PIC ont simulé la partie du choc sans collisions sous-critique, fournissant un aperçu de la microphysique en jeu dans un tel scénario.
Ici, nous avons porté notre attention sur la comparaison entre les cas de chocs sous-critiques simples et doubles. Nous avons observé qu'en présence d'un double choc, l'accélération des protons ambiants était jusqu'à 1,5 fois plus élevée et que les champs électromagnétiques et les densités de particules s'accumulaient de manière beaucoup plus forte. Une telle accélération des protons est d'abord due au champ électrostatique E_x associé au front du choc (injection), suivi d'une contribution principalement due à l'effet "surfing" sur le champ électrique inductif ($E_y \sim v_x B_z$). Le second choc joue un rôle en permettant l'existence de zones avec E_y dirigé comme la vitesse des protons v_y, et donc il renforce leur accélération.

Nous n'avons pas réussi à mesurer directement le spectre des protons comme s'il n'était que le résultat de l'interpénétration des chocs sous-critiques, car les chocs super-critiques existants auparavant ont énergisé les protons beaucoup plus fortement que cette collision entre chocs sous-critiques. Néanmoins, d'autres simulations PIC utilisant des chocs super-critiques ont montré qu'il est possible d'obtenir une énergisation supplémentaire des protons dans ce cas, ce qui permet également une mesure expérimentale directe future. Ces résultats peuvent aider à mieux expliquer le sujet des chocs sous-critiques d'intérêt astrophysique, qui sont présents par exemple dans le milieu interplanétaire et dans le milieu interstellaire local. En effet, ces informations pourraient être pertinentes pour déterminer le spectre d'énergie des particules présentes dans l'espace interplanétaire et dans le milieu interstellaire très local autour de l'héliopause (où ont lieu les collisions entre chocs sous-critiques).

Les expériences laser-plasma de haute puissance se sont donc révélées être un outil essentiel pour recréer en laboratoire des phénomènes astrophysiques à l'échelle, dont la caractérisation est cruciale pour initialiser les simulations numériques correspondantes et mieux interpréter les observations astrophysiques.

List of Figures

List of Tables

Role of the author

The work presented in this thesis is the result of a collaboration between different research teams:
The LULI (*Laboratoire pour l'Utilisation des Lasers Intenses*) team, at École Polytechnique, is the groups I have been part of during my PhD. Our SPRINT team has been in charge of carrying out the experimental campaigns, analyzing most of the data, and performing the Particle-In-Cell (PIC) simulations.
The CELIA (*Center for Intense Lasers and Applications*) team in Bordeaux, composed by Emmanuel d'Humières and Xavier Ribeyre, has been responsible for the FLASH simulations and has provided remarkable insights during our frequent online meetings.
The INAF (*Istituto Nazionale di Astrofisica*) team of Palermo (Italy) with Salvatore Orlando and Marco Miceli has strongly contributed for the astrophysical interpretation of our results.
The LNCMI (*Laboratoire National des Champs Magnétiques Intenses*) has provided the essential pulsed magnetic field coil, thanks to the work of Jérôme Béard.
The JIHT (*Joint Institute for High Temperatures of the Russian Academy of Sciences*) team has been responsible for the FSSR spectrometer installation and data analysis, for which the corresponding researchers have been Sergey Pikuz and Evgeny Filippov.

Within the SPRINT group at LULI, my personal contribution has concerned the realization of the experiments, the analysis of part of the data, and the performance and interpretation of some of the PIC simulations.

From the experimental point of view, I run (together with the team) the experiment on subcritical shock interpenetration at LULI2000, while the experiment on the single supercritical shock at Titan had been carried out before my arrival at LULI. However, during this PhD, I have had the occasion to participate to several other experimental campaigns at different laser facilities: ELFIE (at LULI, now shut down), LULI2000 (at LULI), TITAN (at LLNL, in Livermore, USA), Vulcan (at RAL, in the United Kingdom), and Apollon (in Saclay, France). Some of them lead to scientific publications, whose list is presented in the next section. Ahead of the last experiment run at the LULI2000 laser

facilities, I have been in charge of the design of the optical setup for the interferometry and proton radiography diagnostics, as well as for the imaging paths of the main beams and of the Thomson scattering driver beam. During the above mentioned experimental campaigns, I have been – together with the rest of the team – responsible for setting up the experiment, i.e., aligning the lasers, putting in place the diagnostics, preparing the targets, and taking care of the unavoidable unexpected events. All the experimental data we obtained have been the result of a joint effort of the technical staff and of a team of researchers composed typically of ~ 5 people.

After the experiments, I have been in charge of the analysis of part of the data. In detail, I have analyzed the interferometry data through the program Neutrino (developed at LULI by Tommaso Vinci). For some particularly hard to analyze interferograms, Roman Zemskov (from the Institute of Applied Physics of Russian Academy of Sciences) has helped by performing some analysis with the program IDEA (developed at TU Graz). Moreover, I have performed the analysis of the proton radiographs, by employing the ray-tracing program ILZ (previously developed at LULI and CEA) and by making use of personal Python routines. Finally, I took care of the calibration of a proton spectrometer during another campaign at LULI2000.

As for the numerical effort, I have marginally participated to the analysis of the PIC simulations for the single supercritical shocks, mostly performed by our team member Weipeng Yao. On the other hand, I have entirely modeled and analyzed the PIC simulations on the subcritical shock collision case, for which I have employed the code SMILEI and personal Python scripts.

Finally, together with the above mentioned teams, I have participated to the overall interpretation of the experimental and numerical results, to their contextualization into the astrophysical framework, and to the writing of the related scientific publications.

List of publications and presentations

Publications

- A. Fazzini, W. Yao, K. Burdonov, J. Béard, S. N. Chen, A. Ciardi, E. d'Humières, R. Diab, E. D. Filippov, S. Kisyov, V. Lelasseux, M. Miceli, Q. Moreno, S. Orlando, S. Pikuz, X. Ribeyre, M.Starodubtsev, R. Zemskov, *and* J. Fuchs. "Particle energization in colliding subcritical collisionless shocks investigated in the laboratory". *Astronomy & Astrophysics* 665, A87 (2022). https://www.doi.org/10.1051/0004-6361/202243277

- K. Burdonov, A. Fazzini, V. Lelasseux, J. Albrecht, P. Antici, Y. Ayoul, A. Beluze, D. Cavanna, T. Ceccotti, M. Chabanis, A. Chaleil, S. N. Chen, Z. Chen, F. Consoli, M. Cuciuc, X. Davoine, J. P. Delaneau, E. d'Humières, J.-L. Dubois, C. Evrard, E. Filippov, A. Freneaux, P. Forestier-Colleoni, L. Gremillet, V. Horny, L. Lancia, L. Lecherbourg, N. Lebas, A. Leblanc1, W. Ma1, L. Martin, F. Negoita, J.-L. Paillard, D. Papadopoulos, F. Perez, S. Pikuz, G. Qi, F. Quèré, L. Ranc, P.-A. Söderström, M. Scisciò, S. Sun, S. Vallières, P. Wang, W. Yao, F. Mathieu, P. Audebert, *and* J. Fuchs. "Characterization and performance of the Apollon short-focal-area facility following its commissioning at 1 PW level". *Matter and Radiation at Extremes* 6, 064402 (2021). https://www.doi.org/10.1063/5.0065138

- W. Yao, A. Fazzini, S.N. Chen, K. Burdonov, P. Antici, J. Béard, S. Bolaños, A. Ciardi, R. Diab, E. D. Filippov, S. Kisyov, V. Lelasseux, M. Miceli, Q. Moreno, V. Nastasa, S. Orlando, S. Pikuz, D. C. Popescu, G. Revet, X. Ribeyre, E. d'Humières, *and* J. Fuchs. "Laboratory evidence for proton energization by collisionless shock surfing". *Nature Phys.* (2021) 17 (10), pp.1177-1182. https://www.doi.org/10.1038/s41567-021-01325-w

- V. Lelasseux, P.-A. Söderström, S. Aogaki, K. Burdonov, M. Cerchez, S. N. Chen, S. Dorard, A. Fazzini, M. Gugiu, S. Pikuz, F. Rotaru, O. Willi, F. Negoita, *and* J. Fuchs. "Design and commissioning of a neutron counter adapted to high-intensity laser matter interactions". *Review of*

Scientific Instruments (2021) 92, 113303. https://www.doi.org/10.1063/5.0057828

- W. Yao, A. Fazzini, S. N. Chen, K. Burdonov, P. Antici, J. Béard, S. Bolaños, A. Ciardi, R. Diab, E. D. Filippov, S. Kisyov, V. Lelasseux, M. Miceli, Q. Moreno, V. Nastasa, S. Orlando, S. Pikuz, D. C. Popescu, G. Revet, X. Ribeyre, E. d'Humières, *and* J. Fuchs. "Detailed characterization of laboratory magnetized super-critical collisionless shock and of the associated proton energization". *Matter and Radiation at Extremes* (2022) 7, 014402. https://www.doi.org/10.1063/5.0055071

- A. Chien, L. Gao, S. Zhang, H. Ji, E. G. Blackman, W. Daughton, A. Stanier, A. Le, F. Guo, R. Follett, H. Chen, G. Fiksel, G. Bleotu, R. C. Cauble, S. N. Chen, A. Fazzini, K. Flippo, O. French, D. H. Froula, J. Fuchs, S. Fujioka, K. Hill, S. Klein, C. Kuranz, P. Nilson, A. Rasmus, *and* R. Takizawa. "Direct measurement of non-thermal electron acceleration from magnetically driven reconnection in a laboratory plasma". https://www.arxiv.org/abs/2201.10052

- A. Fazzini, W. Yao, K. Burdonov, *et al.* (in preparation). "Numerical study of the particle acceleration dynamics in interpenetrating magnetized collisionless super-critical shocks".

Presentations

- DPG Spring meeting SAMOP (Erlangen, Germany – March 2022). Oral presentation.

- 4th International Symposium on High Power Laser Science and Engineering HPLSE (Suzhou, China – April 2021). Oral presentation.

- NIF&JLF Users' meeting (Livermore, CA, USA – February 2020). Poster presentation.

- Plas@par Young Researchers' Day (Palaiseau, France – June 2019). Poster presentation.

- ICHED (Oxford, United Kingdom – April 2019). Poster presentation.

ECOLE DOCTORALE

Titre : Chocs créés par laser d'intérêt astrophysique

Mots clés : astrophysique de laboratoire, interaction laser-plasma, physique des plasmas, chocs, accélération de particules

Résumé : Les énormes progrès réalisés au cours des dernières décennies dans le développement des lasers de haute puissance ont permis d'accéder, en laboratoire, à des conditions physiques extrêmes d'intérêt astrophysique. L'astrophysique dite "de laboratoire" est le domaine d'étude qui se concentre sur l'investigation expérimentale des phénomènes astrophysiques qui, grâce à l'utilisation de lois d'échelle, peuvent être émulés en laboratoire. En particulier, cet effort expérimental vise à combler les lacunes inévitables dans les mesures des événements astrophysiques lointains, qui sont limitées par les énormes échelles de temps et d'espace en jeu. Ce travail de thèse est axé sur l'étude des ondes de choc sans collisions, qui sont des phénomènes se produisant dans de nombreux contextes astrophysiques, tels que les explosions de supernova et les arcs de choc. Elles sont tenues pour responsables de la production de particules énergétiques (rayons cosmiques), dont les mécanismes d'énergisation ne sont aujourd'hui pas entièrement compris. Un choc peut être considéré comme un changement abrupt de certaines quantités physiques décrivant le système physique, qui, en hydrodynamique, est médié par des effets de collision qui dissipent en chaleur l'énergie cinétique du fluide traversant le choc. Lorsqu'une telle transition se produit sur des échelles de longueur beaucoup plus petites que le libre parcours moyen d'une particule, nous avons affaire à une onde de choc sans collisions. Dans ce cas, de telles discontinuités peuvent se former par l'émission et l'absorption d'excitations collectives du plasma. Les expériences réalisées dans des installations laser de haute puissance ont été le principal outil d'investigation. En particulier, deux scénarios ont été explorés : un seul choc supercritique et l'interpénétration de deux chocs sous-critiques. L'analyse de nos données a également été soutenue par des simulations PIC, qui, avec les simulations MHD réalisées en collaboration avec le CELIA, nous ont permis de mieux comprendre la microphysique qui se déroule dans nos expériences. Enfin, nos résultats sont considérés dans le contexte astrophysique, ce qui nous permet de déterminer les scénarios astrophysiques pertinents auxquels les chocs créés par laser de notre laboratoire peuvent s'appliquer.

Title : Laser-driven shocks of astrophysical interest

Keywords : laboratory astrophysics, laser-plasma interaction, plasma physics, shocks, particle acceleration

Abstract : The huge progress made over the last decades in the development of high-power lasers has allowed the access, in the laboratory, to extreme physical conditions of astrophysical relevance. The so-called "laboratory astrophysics" is the field of study that focuses on the experimental investigation of astrophysical phenomena which, through the use of scaling laws, can be emulated in the laboratory. In particular, such experimental effort aims at filling the inevitable gaps in the measurements of remote astrophysical events, which are limited by the enormous time and space scales at play. This PhD work is focused on the study of collisionless shock waves, which are phenomena taking place in many astrophysical contexts, such as supernova explosions and bow shocks. They are held responsible for the production of energetic particles (cosmic rays), whose energization mechanisms are nowadays not fully understood. A shock can be seen as an abrupt change in some physical quantities describing the physical system, which in hydrodynamics is mediated by collisional effects that dissipate in heat the kinetic energy of the fluid crossing the shock. When such a transition occurs on length scales much smaller than a particle mean free path, we are dealing with a collisionless shock wave. In this case, such discontinuities can form through the emission and absorption of collective excitations of the plasma. Experiments performed at high-power laser facilities have been the main investigation tool. In particular, two scenarios have been explored : a single supercritical shock and the interpenetration of two subcritical shocks. Our data analysis has also been supported by PIC simulations, which, together with MHD simulations run in collaboration with CELIA, made us better understand the microphysics taking place in our experiments. Finally, our results are viewed in the astrophysical context, allowing us to determine the relevant astrophysical scenarios to which our laboratory laser-driven shocks can apply.

Institut Polytechnique de Paris
91120 Palaiseau, France